Alkali Metal-O2 Batteries. Performance and Lifetime Limiting Effects

Knudsen, Kristian Bastholm

Publication date:
2015

Document Version
Publisher's PDF, also known as Version of record

Alkali Metal-O_2 Batteries
Performance and Lifetime Limiting Effects

RISØ, DENMARK 2012-2015

KRISTIAN BASTHOLM KNUDSEN
Department of Energy Conversion and Storage
Technical University of Denmark

SUPERVISORS

SENIOR SCIENTIST JOHAN HJELM
SENIOR SCIENTIST SØREN HØJGAARD JENSEN
PROF. PETER HOLTAPPELS

2015
TECHNICAL UNIVERSITY OF DENMARK

Submitted in candidacy for the degree Doctor of Philosophy

Release data: November 30^{th}, 2015
Revised data: December 7^{th}, 2015

Preface

This thesis is submitted in candidacy for the PhD degree from the Technical University of Denmark (DTU) and is based work carried out at the Department of Energy Conversion and Storage in the period of December 2012 to December 2015. The project was mainly supervised by Senior Scientist Johan Hjelm and co-supervised by Senior Scientist Søren Højgaard Jensen and Prof. Peter Holtappels. The work was funded through the Reliable project (project no. 11-116792) by the Danish Council for Strategic Research, Program Commission on Sustainable Energy and Environment. Four months of the work was carried out through an external stay at The University of California, Berkeley (USA) at the battery group led by Prof. Bryan D. McCloskey. This work included two of the main authoring papers and was made possible through funding from Augustinus fonden and Thrigesfonden.

Acknowledgements

First and foremost, I would like to express my gratitude to my main supervisor Senior Scientist *Johan Hjelm* for guidance and support throughout these three years. Thank you for setting a clear start to my project, giving me the necessary support and help, for your eager interest in my work, introducing me to Python, proof reading, and for later letting me pursue my own ideas. Thank you for being my mentor and for being a great person.

A big thanks to my group leader Prof. *Tejs Vegge* for his ideas, valuable input to papers, always having an overview, and the ability to open doors when needed.

Thank you Senoir Scientist *Poul Norby*, Senior Scientist *Søren Højgaard Jensen*, and Prof. *Peter Holtappels* for inspiration, discussions of more general aspects of electrochemistry, discussion on x-ray diffraction, proof reading, and general guidance.

I would also like to gratefully thank Prof. *Bryan D. McCloskey* for letting me visit his facilities, for his warm welcome, our valuable and fruitfull discussions, and for a very productive four months. Also, a big thanks to Prof. *Alan C. Luntz*, who have given me much insight in to the mechanistic of the topic and for great cooperation. To *Colin*, *Jessica*, *Sarah*, *Hyo*, and *Hilda* for your great hospitability, welcome, and cooperation during my four months at UC Berkeley. To *Lea* and *Christian*, my roommates while I was abroad, for taking care of the practical and for being my family for the period.

Thank you *Andreas* and *Jonathan* for a particular close collaboration, it has been three years of a great many discussions, late nights in the lab, coffee breaks, discussing impedance, for Crete, and for the champagne bets. Thank you *Ane*, *Mie*, *Roberto*, *Reza*, and *Supti* for being great colleagues and always ready to give a helping hand or discuss work and issues over a cup of coffee.

Thank you to my friends and colleagues of the car pool *Christos*, *Phillip*, and *Ragnar* for making it not all about work but also a place to depressurize, also for boat trips, Feuerzangenbowle, müsliboller, and the recently established Evil Elephant.

To *Sailor*, *Buch*, *Martin*, *Carsten*, *Line*, and *Lene* for the good times and taking the initiatives for meeting up, when I have been too swamped with work.

Frankly, I also want to thank my parents and family, because they let me do what I want and always support me. In particular, I want to thank *Charlotte* for being my number one person in the impossible task of finding an apartment in Copenhagen. Thank you for letting me borrow your coach, finding two places of the five places where I have been living the past three years and for taking good care of Luna.

Abstract

The rechargeable Na-O_2 and Li-O_2 batteries are attractive battery technologies as they potentially are very cheap and as they theoretically possess about 3 and 10 times higher energy density than the current Li-ion technologies. This PhD thesis is dedicated to studying the effects that limit cell performance of these two technologies.

The Li-O_2 battery was first introduced in 1996 and focus in the field is still on understanding the fundamental mechanisms controlling discharge and charge. This PhD thesis was mainly dedicated to the Li-O_2 battery and initially charge conduction through the discharge product, Li_2O_2, was investigated. This was done by using of a conventional three electrode cell in which the heterogeneous electron transfer rate of three different redox couples were studied on Li_2O_2 coated glassy carbon electrodes to provide a measure of the conductivity of the Li_2O_2 layers. Charge transport through Li_2O_2 gives further evidence that hole transport dominates charge-transfer through Li_2O_2. Electrochemical impedance spectroscopy was also used to conduct detailed investigations of surface capacitance, ion transport, and charge-transfer reactions in the cathode of the Li-O_2 cell. The capacitance of the cathode was shown to be sensitive to the thickness of the deposited Li_2O_2 layer. These investigations also explored the influence of the composition of the electrolyte and conditions, which favors a solution mediated Li_2O_2 deposition mechanism. On charge, an electrochemical "safe" operating voltage was identified until 3.30 V were an interface layer was formed, which activates side reactions and further increases the cell potential. A number of ionic liquids were also investigated for their oxygen diffusivity and solubility and while these were in the order of currently employed aprotic electrolytes as the ionic liquids significantly decompose under electrochemical operation. Last, the influence of CO_2 was investigated and it was suggested that CO_2 blocks the step valleys of the deposited Li_2O_2 forcing Li_2O_2 growth away from the electrode surface hereby increasing cell capacity, as the discharge becomes less limited by the cathode surface area.

The Na-O_2 battery is an even newer technology as it was first introduced to the scientific community in 2010. The two batteries are experimentally quite similar as the only difference is the choice of anode. However, when one studies the two systems, the mechanisms controlling each type of battery are quite different. The discharge and charge processes of the non-aqueous Na-O_2 battery were studied in this thesis. On discharge, the deposition mechanism of NaO_2 was shown to be highly dependent on the current density and cell limitations could be correlated to the depositions mechanisms. On charge, three regions of NaO_2 oxidation were identified, each corresponding to a different type of NaO_2 oxidation.

Resumé

De genopladelige Na-luft og Li-luft batterier er yderst attraktive batteri teknologier, da de potentielt set er billige og teoretisk har henholdsvis 3 og 10 gange større energitæthed end nuværende Li-ion batterier. Denne Ph.D. afhandling fokuserer på at identificere effekter, som begrænser disse to teknologier.

Li-luft batteriet blev først beskrevet i 1996 og nuværende forskningen omhandler at opnå en bedre forståelse af de fundamentale mekanismer, som begrænser af- og opladninger. Under afladningens processen dækkes katode overfladen af lithium peroxid (Li_2O_2), som oxideres under opladningen. Afladningen blev initialt undersøgt ved at udvikle en klassisk tre-elektrode celle, hvor redox proberes ladningsoverførsel gennem Li_2O_2 blev undersøgt på glassy-carbon elektroders overflade. Ladningsoverførslen gennem Li_2O_2 blev således foreslået at være domineret af hul transport igennem Li_2O_2 laget og at det pludselige potential fald, som ses på afladningen, skyldes ladningsoverførsels begrænsninger gennem Li_2O_2 laget. Elektrokemisk impedans spektroskopi blev også anvendt i en tre-elektrode Li-luft batteri celle til formålet at undersøge effekten af den ioniske modstand inde i den porøse struktur af katoden, kapacitansen, samt ladningsoverførsels modstanden under afladning. Det viste sig, at overflade kapacitansen af katoden var afhængig af tykkelsen på det deponerede Li_2O_2 lag og at der var en stor afhængighed på overfalde kapacitansen og elektrolyttens sammensætning, som blev ydereligere undersøgt, da elektrolytter som favoriserer den såkaldte opløsnings mekanisme også blev undersøgt. Under opladningen blev et elektrokemisk "sikkert" operations potential defineret indtil 3.30 V, hvor et nyt interface lag dannes oven på Li_2O_2, som aktiverer side reaktioner og herefter forøger overpotentialet. Ioniske væskers ilt opløselighed og diffusivitet blev også undersøgt og var i samme størrelsesorden, som aprotiske elektrolytters. De ioniske væsker dekomponerede dog signifikant under celle operation. Kuldioxids indflydelse på Li-lufts batteriets performans blev undersøg og det blev foreslået at CO_2 binder til såkaldte "step valleys", som tvinger Li_2O_2 til at gro væk fra elektrode overfladen, hvormed kapaciteten under afladningen forøges.

Na-O_2 batteriet blev først introduceret i 2010 og eksperimentelt er disse to batterier meget ens, men når man ser mærmere på teknologierne, er det klart at mekanismerne, som kontrollere af- og opladningerne er vidt forskellige. I denne afhandling blev både af- og opladnings processerne undersøgt. Under afladningen ses der en tydelig afhængighed mellem afladningsproduktets morfologi og strøm densiteten og som ydereligere kunne blive sammenkoblet med begrænsninger i batteriets afladningskapacitet. Under opladningen blev der detekteret tre områder af NaO_2 oxidation, hvor hvert område svarende til en forskellig type NaO_2 oxidation.

List of Publications

This thesis is based on the following papers, which are referred to in the text by Roman numerals.

Paper I: Knudsen, K.B., Luntz, A.C., Jensen, S.H., Vegge, T., Hjelm, J., A Redox Probing Study of the Potential Dependence of Charge Transport through Li_2O_2. *J. Phys. Chem. C Just Accepted* (2015)

Paper II: Knudsen, K.B., McCloskey, B.D., Vegge, T., Hjelm, J., An Electrochemical Impedance Spectroscopy Study on the Effects of the Surface- and Solution-Based Mechanisms in Li-O_2 Cells. *In manuscript*

Paper III: Knudsen, K.B., Nichols, J.E., Vegge, T., Luntz, A.C., McCloskey, B.M., Hjelm, J., (2015) An Electrochemical Impedance Study of the Capacity Limitations in Na-O_2 Cells. *In manuscript*

Paper IV: Højberg, J., Knudsen, K.B., Hjelm, J., Vegge T., Reactions and SEI formation during charging in Li-O_2 cells. *ECS Electrochem. Lett.* **4**, A63 (2015)

Paper V: Mekonnen, Y.S., Knudsen, K.B., Myrdal, J.S.G., Younesi, R., Højberg, J., Hjelm, J., Norby, P., Vegge, T., The Influence of CO_2 Poisoning on Overvoltages and Discharge Capacity in Non-Aqueous Li-air Batteries. *J. Chem. Phys.* **140**, 121101 (2014)

Paper VI: Das, S., Højberg, J., Knudsen, K.B., Younesi, R., Johansson, P., Norby, P., Vegge, T., Instabilities of Ionic Liquid-Based Electrolytes in Li-O_2 Batteries. *J. Phys. Chem. C* **119**, 18084 (2015)

Comments on my contribution to the appended papers

Paper I: All of the experimental work, analysis, and main part of writing. The theoretical model was conducted by Prof. Alan C. Luntz. First author of the paper.

Paper II: All of the experimental work, analysis, and main part of writing. First author of the paper.

Paper III: Major part of the experimental work, analysis, and main part of writing. SEM images were conducted by Ph.D. fellow Jessica E. Nichols. First author of the paper.

Paper IV: Planning and co-working of the experimental work, also part of the analysis. Second author of the paper.

Paper V: The experimental part and analysis of the paper, part of writing. Second author of the paper.

Paper VI: Contributed to this paper with the determination of diffusion coefficients and solubility of O_2. Limited part of writing and third author of the paper.

Major Symbols

Listed below are symbols used in this thesis. In most cases, the usage follows the recommendations of the IUPAC Commission on Electrochemistry [1], however some exceptions exists.

ROMAN SYMBOLS

Symbol	Meaning	Usual Units
a	slope in the Randles-Sevcik plot	$\frac{A \cdot s^{1/2}}{V^{1/2}}$
A	area	cm^2
A_w	Warburg coefficient	$\Omega/s^{1/2}$
C	capacitor	F
	capacitance	F
C_i	concentration of specie *i* in solution	mol/cm^3
d	separation between plates of an capacitor	cm
D_i	diffusion coefficient of specie *i*	cm^2/s
E	potential	V
$E^{0'}$	formal potential of an electrode	V
E_0	peak amplitude of an a.c. potential	V
$E_{1/2}$	half-wave potential in voltammetry	V
E_p^i	peak potential in voltammetry	V
E_F	Fermi level	eV
f	frequency	Hz
f_s	characteristic summit frequency	Hz
F	the Faraday constant	C
g_c	amount of carbon	g
I	current	A
I_0	peak amplitude of an a.c. current	A
I_p^i	peak current of specie *i*	A
j	$\sqrt{-1}$	-
j_0	exchange current density	A/cm^2
k^0	standard heterogeneous rate constant	cm/s
k_f	heterogeneous rate constant for reduction	cm/s
n	(a) stoichiometric number of electrons	
	involved in an electrode reaction	-
	(b) exponent in the constant phase element, Q	-
Q	(a) constant phase element	s^n/Ω
	(b) capacity	mAh
r_0	radius of an electrode	μm

ROMAN SYMBOLS

Symbol	Meaning	Usual Units
R	resistor	Ω
R_{CT}	charge-transfer resistance	Ω
R_g	gas constant	J/mol·K or $\frac{L \cdot Torr}{mol \cdot K}$
R_i	ionic resistance	Ω/cm
R_s	series resistance also called	
	the electrolyte resistance	Ω
t	time	s
T	temperature	K
T_m	melting point	^{o}C
W	Warburg element	-
Z	impedance	Ω
Z_{re}	real part of the impedance	Ω
Z_{im}	imaginary part of the impedance	Ω

GREEK SYMBOLS

Symbol	Meaning	Usual Units
α	transfer coefficient	-
ε_0	permitivity of vacuum	F/cm
ε_{Li2O2}	dielectric constant of Li_2O_2	-
ζ	surface impedance	-
η	overpotential, E-E_{eq}	V
λ	(a) wavelength	nm
	(b) a.c. utilization depth	cm
ν	scan rate	V/s
ϕ	phase shift	^{o}
X_i	the resistance per unit length of transport channel	
	in the liquid (i=1) and electrode (i=2), respectively	Ω/cm
ω	angular frequency, $\omega = 2\pi f$	rad/s

ABBREVIATIONS

Abbreviation	Meaning	Usual Units
a.c.	alternating current	-
BET	Brunauer, Emmett, and Teller surface area	cm^2
CB	Conduction Band	-
CE	Counter Electrode	-
CV	Cyclic Voltammetry	-
CEI	Cathode Electrolyte Interface	-
d.c.	direct current	-
DME	1,2-dimethoxyethane	-
DEMS	Differential Electrochemical Mass Spectrometer	-
EV	Electric Vehicle	-
EIS	Electrochemical Impedance Spectroscopy	-
GC	Glassy Carbon	-
IPA	Isopropanol	-
LCO	Lithium Cobalt Oxide	-
LMO	Lithium Manganese Oxide	-
LMNO	Lithium Manganese Nickel Oxide	-
OCV	Open Circuit Voltage	V
PET	Porous Electrode Theory	-
ppm	Parts Per Million	-
PTFE	Polytetrafluoroethylene	-
RE	Reference Electrode	-
RTILs	Room Temperature Ionic Liquids	-
SEI	Solid Electrolyte Interface	-
SEM	Scanning Electron Microscopy	-
VB	Valence Band	-
WE	Working Electrode	-
XPS	X-ray Photoelectron Spectroscopy	-

Contents

Til farmor

Introduction 1

Renewable energy technologies are becoming increasingly important in the energy mix of modern society. The rate with which the fraction of renewable energy increase does not only apply for Europe but also China, Brazil, India, and South Africa starts to account for a large shares of the increased non-fossil fuel market [2]. However, the present energy efficiency of these technologies as well as their rate of increased market share are still below the rates necessary to achieve the sustainable energy goals by 2030, *i.e.* Sustainable Energy for All [2]. In addition, the push for independence of fossil fuels that originate from unstable regions in the world is in fact, or should be, high on the politicians tables around the world. The oil reserves in parts of the Middle East, which are tormented by turmoil, remains the only large source of low-cost oil [3] and the fossil fuels are in general being rapidly consumed. In respect, this should not be understood as the world is running out of its fossil fuel reserves but as the production maximum is being reached while the energy demands keeps growing [4]. It becomes more complex as for each barrel of oil no longer used by OECD countries; two barrels more are used by an non-OECD countries. Predominantly, this is driven by the increased demands for transportation in the non-OCED countries. A sector that consumed 90 billion barrels per day in 2013 and is estimated to increase to 104 barrels per day by 2040 [3].

The current energy situation would be much more serious if not improvements in energy efficiency already were implemented and if not continuous efforts to innovate and reduce the cost of renewable energy technologies, such as photovoltaics, wind-, and hydropower, had already begun. The power sector is due to these innovative decisions currently the leading sector to globally transform the worlds energy production from burning fossil fuels into running entirely on different forms of renewable energy technologies [3]. Pumped hydro accounts for the largest share of renewables in the grid storage sector, but requires water availability, geographical height, and large capital costs [2]. Pumped hydro is therefore not suitable for all regions or countries as some lack in one or another. Photovoltaics and wind power exclusively produce electricity when the sun shines or when the wind blows and a means of energy storage is therefore inevitably needed for both technologies as not all energy produced is imminently consumed. In fact, countries overproducing electricity from wind or solar can be forced to sell electricity at unreasonable low rates or in rare cases pay neighboring countries to accept electricity.

One possibility of reducing the oil consumption in the transportation sectors and gain more energy storage is therefore to make fully electric vehicles (EVs) more attractive. This has been recognized by policy-makers, industry, and other stock holders and practical EVs are now realized. However for the technology to become a true 'people's car'; the driving ranges of an economic class EV needs to be increased. Generally, the driving range of economic class EVs lies between 80-160 km while expensive models such as the Tesla Model S reach $\sim$450 km. But for this to become reality the current battery technologies must be enhanced or new "beyond Li-ion" technologies must be developed. Many battery chemistries exist and depending on the application; one is more suited. For instance one of the more special batteries currently in a car would, *in my mind*, be the silver-zinc batteries currently parked on the moon within the three Lunar Rovers that went with the Apollo missions in the 1970's

[5]. These are primary batteries, *i.e.* disposable, which were designed for a single discharge and therefore not relevant in modern automotives. Here, the secondary battery chemistry, *i.e.* rechargeable, seems the most reasonable candidate. It should however also be mentioned that mechanically rechargeable batteries is another approach.

The challenge that we currently face is how to increase the energy densities of a battery, *i.e.* how to create battery technologies with a specific amount of energy that takes up less volume and weighs less. To put the energy density of batteries into perspective consider the following: Gasoline has a specific energy density of ∼12.3 kWh/kg and an energy density of 9.0 kWh/L. In a car engine, gasoline is mixed with air and the vapors are ignited; this controlled explosion produces heat and pressure, where the latter drives the pistons of the engine and finally the crankshaft and the wheels. In this rather complex process a lot of energy is lost as heat and in fact modern engines have about 25-45 % efficiencies meaning that 55-75 % of the energy is lost as heat [6, 7]. Practical energy densities of gasoline, in respect to internal combustion engines, are therefore more in the order of 3.1-5.5 kWh/kg and 2.3-4.1 kWh/L. The energy density of Li-ion batteries depends on the electrode materials as these rely on insertion of Li^+ into the two electrodes. The positive electrode contains transition metal oxides, while negative electrode contains lithiated graphite [8] and today many different combinations of electrode materials exist and some of these are shown in the Ragone plot in Figure 1.1.

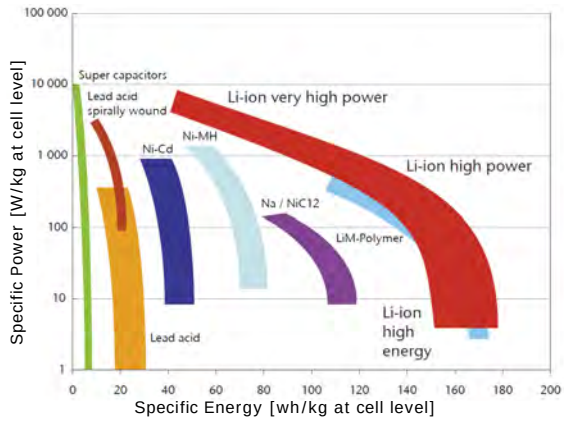

Figure 1.1: A Ragone plot illustrating the specific energy and -power of different battery technologies [9].

The Ragone plot illustrates one of the fundamental concepts of batteries very well, *i.e.* if a higher power is desired; the specific energy will be low and vice versa. In other words, today's batteries are all about compromise, as batteries cannot both have high power and high capacity. In Figure 1.1 numerous battery technologies are shown, lead-acid with a specific energy of ∼15-30 Wh/kg, Nickel-metal hydride (Ni-MH) with ∼45-80 Wh/kg and a range of different Li-ion technologies that span from high power cells to high capacity cells with a specific energy of ∼45-180 Wh/kg. The current Li-ion battery technology is therefore still far from the practical specific energy of gasoline of 2.3-2.7 kWh/L, but also far from the current research goal of 235 Wh/kg and 470 W/kg set by the US council for Automotive Research to be reached by 2020 [10].

An issue is that the theoretical specific energy of the current Li-ion technologies does not allow for sufficient improvements. A branch of new batteries, called "beyond Li-ion", have therefore been suggested as possible candidates to significantly improve the energy densities of batteries. These include the Li-O_2 and Na-O_2 batteries, which popularly are called Li-air and Na-air batteries. These are two very promising candidates as their theoretical specific energy are well beyond that of the Li-ion technologies, as shown in Figure 1.2. In fact, Li-O_2 have a theoretical specific energy close to that of gasoline, if the oxygen of the cell is extracted from the atmosphere upon operation.

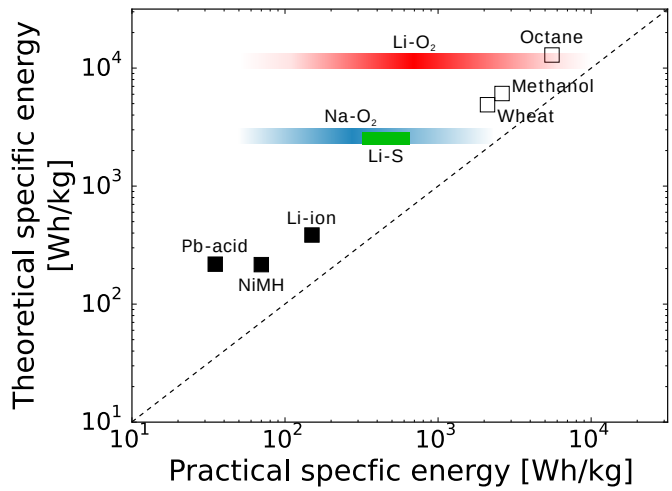

Figure 1.2: Theoretical specific energies of the combustion of active materials (open squares) and of the battery systems (filled squares) versus their practical specific energy. The Li-O_2 and Na-O_2 systems assumes that O_2 is not stored in the cell and their practical specific energy have yet to be determined, hence their fading colors. The lowest practical specific energy of the Li-S system is based on that produced by Sion Power while the highest represents projections of designs currently being developed. Li-ion is exemplified with values of lithium cobalt oxide cells. The straight dashed line illustrates the highest possible practical specific energy for each system. Values are obtained from refs. [7, 11, 12].

The potential of these two battery technologies is enormous, however they suffer from many child diseases and practical energy densities are far from ideal. This thesis is a study of the Li-O_2 and Na-O_2 batteries and their fundamental limitations.

1.1 The Scope of This Thesis

This thesis is a product of three years' work from December 2012 to December 2015. The scope of this thesis was to study and identify the causes of performance and lifetime limiting effects in the Li-O_2 and Na-O_2 cell chemistries. The studies have primarily been focused on the Li-O_2 cell chemistry while a smaller and later part was allocated to Na-O_2. The field has, in this time, moved from questioning the stability of all cell components to understanding the mechanisms of failure and agreeing on previous discrepancies within the field.

The content of this thesis is divided into six chapters. In chapter 1 and 2, an introduction of the motivation for driving the battery technology forward is given, a scope of the thesis is presented, a brief description of the concept of Li-ion cells is shown, and more detailed description of the current understandings of the cell chemistries in Li-O_2 and Na-O_2 is given. The thesis is the cumulation of main-authoring three papers, one peer-reviewed and two in manuscripts; and the co-authoring of three peer-reviewed papers. The papers are a consequence of close collaboration with a number of colleagues and my contribution to each paper is presented in the list of publications.

Chapter 3 describes the experimental characterization techniques applied to electrodes or cells. A brief introduction and the relevance in respect to the published work is also given.

Chapter 4 describes the experimental setups used in this work. This includes cell designs, assembly, and drying procedures.

Chapter 5 presents a summary of the results obtained, from the papers, during this thesis. This include a summary on the cause of sudden-death in Li-O_2 and Na-O_2 as a result of **paper I** and **III**; a summary of the limiting processes in the porous carbon cathode when two separate reactions mechanism are activated on discharge, as a results of **paper II**; a summary of the reactions and SEI formation on charge in Li-O_2 as a result of **paper IV**; a summary of the influence of CO_2 on the Li-O_2 performance as a result of **paper V**; and summary of determination of oxygen diffusivity and solubility in ionic liquid electrolytes, as a result of **paper VI**.

Chapter 6 gives a conclusion and outlook based on the presented results.

Li-ion and Beyond 2

2.1 The Basic Principles of Li-ion Batteries

A Li-ion battery consists of a positive and a negative electrode that are referred to as the cathode and anode, respectively. In Li-ion, both electrodes materials are insertion materials that reversibly host Li^+ ions. Most Li^+ is therefore stored inside the anode material in a charged cell while the cathode material hosts most of the Li^+ in discharged cells. In operation, the Li^+ ions move from one electrode to the other, through a separator and the electrolyte, while e^- move through the outer circuit, generating a current. The principle is sketched in Figure 2.1.

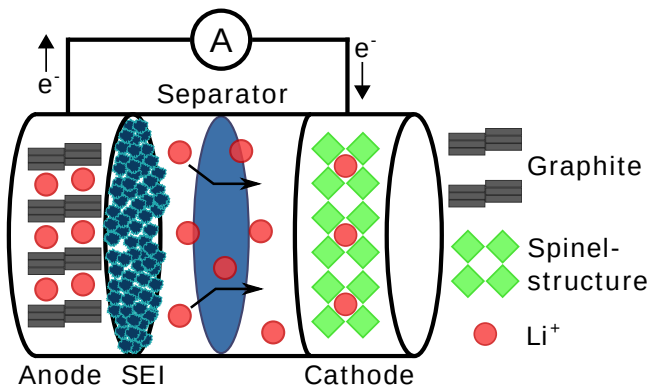

Figure 2.1: A schematic drawing of a Li-ion battery operated in discharge mode.

In order to improve the energy density of a battery and move a new technology to the right-hand side of Figure 2.2 and 1.2; two directions can be taken. First, the potential energy (cell potential) of the cell can be increased or the capacity of the cell can be improved. The two approaches are illustrated in Figure 2.2 and given by eq. 2.1.

$$U = \int_0^t E_{cell} \cdot I_{cell}(t)dt \tag{2.1}$$

Where U is the energy, E_{cell} is the cell voltage, I_{cell} is the current flowing, and t is the time. In terms of Li-ion technologies, the first approach has previously been done for Lithium Manganese oxide (LMO) by adding an additional transition metal, Ni, that increased the cell potential to 4.7-4.9 V [13]. The second approach can be exemplified as the difference between lithium cobalt oxide (LCO) and lithium nickel manganese cobalt oxide (LNMO), where the latter transports more lithium, and energy, per weight than the former.

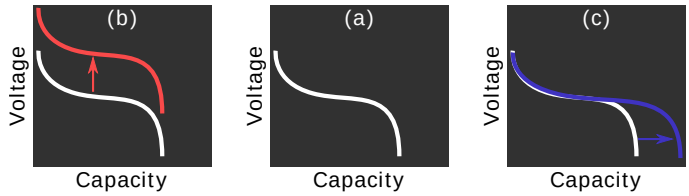

Figure 2.2: Illustrates the concept of improving the energy density of a battery, which can be achieved by either improving the potential of the cell via (b) or improving the capacity of a cell via (c). (a) illustrates the initial, un-improved, battery state.

However, insertion materials used in Li-ion cells does have limiting theoretical capacities far below those of metal-O_2 cells, which therefore are of great interest for drastically improving capacity and the specific energy compared to modern Li-ion cells.

2.2 The Li-O_2 Battery

The non-aqueous Li-O_2 battery was discovered in 1996 by Jiang and Abraham while attempting to study Li^+ intercalation into graphite in a cell with a gel electrolyte that leaked to the atmosphere [14]. Among the beyond Li-ion chemistries, Li-O_2 has the highest theoretical specific energy of 11400 Wh/kg and energy density of 6080 Wh/L, assuming that O_2 is not carried within the battery and metallic lithium as the anode. A sketch of such a system is shown in Figure 2.3.

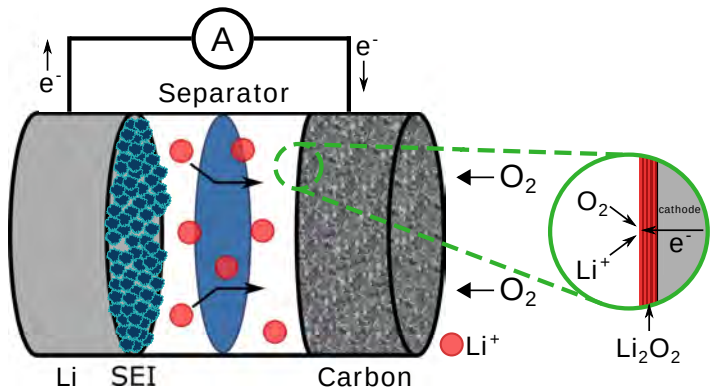

Figure 2.3: A schematic drawing of a Li-O_2 battery operated in discharge mode where Li_2O_2 forms on the cathode surface.

In the non-aqueous Li-O_2 battery, the net electrochemical reaction is $Li + O_2 \rightleftarrows Li_2O_2$, with the forward reaction corresponding to discharge and the reverse direction to charge. Acquiring a truly reversible formation and oxidation of lithium peroxide (Li_2O_2) is the key that can unlock the potential of the technology. The rechargeability is still, 19 years after its discovery, a huge issue. Mainly, this was due to an early trend in the field to use carbonate-based electrolytes that we today know to decompose during electrochemical oper-

ation [15, 16, 17, 18]. This also led the field into catalysis as it was thought that the O-O bond was split/recombined on discharge/charge. Today, we know from $^{18}O_2$ isotopic experiments that the O-O bond of O_2 remains intact [19, 20] and that the fundamental overpotentials (as identified by theoretical calculations) are modest for the Li/O_2 reaction at ∼200 mV [21, 22].

One of the pressing problems is the lack of a fully stable electrolyte during discharge and charge and this severely limits cycle life [23, 24, 25, 26, 27]. Another challenge is the development of a chemically- and electrochemically stable cathode since carbon has been shown to not be fully stable [15, 28, 29]. Finally, the discharge capacity is much smaller than anticipated from complete filling of the pore volume of the cathode. To understand the last challenge requires knowledge of the discharge and charge mechanisms.

2.2.1 Proposed mechanisms

The mechanisms for discharge and charge are highly dependent on the electrolyte. In non-aqueous and water free electrolytes such as 1,2-dimethoxyethane (DME), the main reactions taking place at the anode (negative electrode) and the cathode (positive electrode) are thought to be the following reaction 2.2-2.5.

$$2\,\mathrm{Li} \rightleftharpoons 2\,\mathrm{Li}^+ + \mathrm{e}^- \text{ (anode)} \tag{2.2}$$

$$\mathrm{Li}^+ + \mathrm{e}^- + {\mathrm{O_2}}^* \rightleftharpoons {\mathrm{LiO_2}}^* \text{ (cathode)} \tag{2.3}$$

$$\mathrm{Li}^+ + \mathrm{e}^- + {\mathrm{LiO_2}}^* \rightleftharpoons {\mathrm{Li_2O_2}}^* \text{ (cathode)} \tag{2.4}$$

$$2\,{\mathrm{LiO_2}}^* \rightleftharpoons {\mathrm{Li_2O_2}}^* + \mathrm{O_2} \text{ (cathode)} \tag{2.5}$$

Here the * refers to a surface adsorbed specie. The main discharge product is Li_2O_2. LiO_2 acts a reaction mediate following reaction 2.3-2.5. The LiO_2-like species have in recent studies been proposed to form as the main discharge product [30, 31], however the Raman peaks that are ascribed to the LiO_2 formation have previously been observed from decomposition of the binder (poly-vinylidene difluoride, PVDF) used in the positive electrode during discharge [11, 32].
The final formation of Li_2O_2 has two possible routes as either reaction 2.4 or 2.5, *i.e.* by the electrochemical addition of an superoxide (O_2^-) or chemically where 2 units of LiO_2 disproportionates. However, in reality reaction 2.4 and 2.5 are quite similar, the difference being the source of the final Li^+ as either Li^+ adsorbed to the surface as LiO_2^* or as Li^+ ions from the electrolyte. It is however not possible to differentiate the two routes of Li_2O_2 formation as the rate of both reactions, in galvanostatic mode, implies that $d[LiO_2^*]/dt = 0$. The discharge current (at a constant overpotential) for both reactions are therefore given by $I \propto k_f^{2,3} \cdot [Li^{+*}] \cdot [O_2^*]$. This current dependency of the heterogeneous reactions is therefore valid for both reaction 2.4 and 2.5, so no kinetic measurements will be able to distinguish between the two [11].

The exact discharge morphology of Li_2O_2, and reaction mechanism, has in recent times shown to be the cause of the discrepancy in discharge capacities reported in the field. In

general, two main reaction pathways for Li_2O_2 deposition can take place, referred to as either a surface- or a solution-based mechanism, in which either continuous Li_2O_2 films are formed during discharge, as sketched in Figure 2.5 (of 5-10 nm [22, 33, 34]), or larger Li_2O_2 deposits form in the shape of toroids, respectively. The solution-based mechanism largely circumvents issues related to Li_2O_2-induced electronic insulation of the cathode, resulting in discharge capacities that are approximately six times that, which can be obtained when the surface-based mechanism dominates [35]. The two proposed mechanisms for Li_2O_2 formation are illustrated in Figure 2.4.

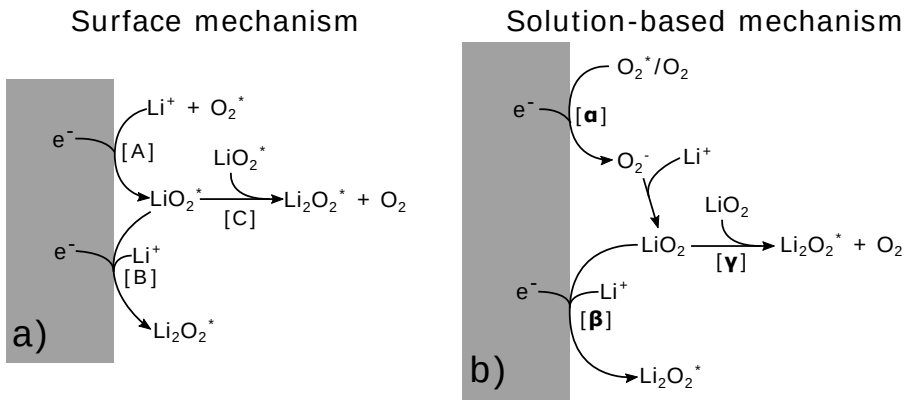

Figure 2.4: Schematic of the two O_2 reduction mechanisms. In (a) the surface-based mechanism described by reaction 2.3-2.5 is depicted while the solution-based mechanism is shown in (b). Species marked with (*) refers to an absorbed specie on the cathode surface. Adapted form **paper II**.

While the surface mechanism in described in the above, the solution-based mechanism initially starts with O_2^* (or O_2) reduction to solubilized LiO_2 [α], which was shown by Johnson et al. [36] to exist as solvated O_2^- and Li^+ immediately after its formation in electrolytes with high Lewis acidity. LiO_2 is then either further reduced [β] or disproportionates in solution [γ] to form $Li_2O_2{}^*$. In both reaction mechanisms, *i.e.* β and γ, diffusion of LiO_2 or O_2^- results in the formation of $Li_2O_2{}^*$ away from the initial O_2 reduction site. $Li_2O_2{}^*$ formation occurs on or close to the carbon cathode as NMR has proven that Li_2O_2 is completely insoluble ($K_{sp} < 10^{-10}$) in most non-aqueous solvents [11]. The latter step in the solution-based mechanism [γ] must be the dominating reaction step in the formation of toroid deposits [23, 24, 35, 36], as the surface-based mechanism is limited by hole transport through Li_2O_2 [22, 33, 34], and thus the reduction of O_2 to form solubilized O_2^- or LiO_2 (reaction [α]) must be the gateway that allows for toroidal Li_2O_2 to form on galvanostatic discharges. **Paper II** will deal with the cathode performance under either the activation of the surface- or solution-based mechanism for Li_2O_2 formation.

However, independent of the discharge mechanism eventually a sudden drop in potential (sudden-death) occurs prematurely with respect to the theoretical discharge capacity, as shown in Figure 2.5.

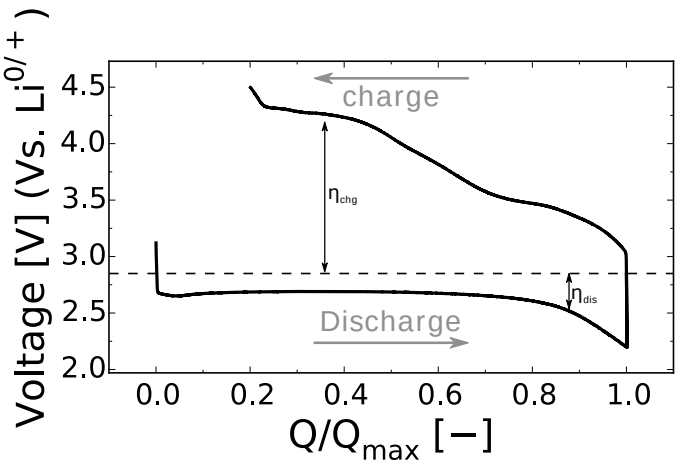

Figure 2.5: The first cycle of the Li-O_2 battery in a 1,2-dimethoxyethane electrolyte containing 1 M LiTFSI with a carbon-based cathode. The dotted line is the equilibrium cell potential of 2.85 V at zero d.c. bias.

Early studies suggested that this sudden-death, in non-aqueous electrolytes, was caused by O_2 diffusion limitations [37, 38]. As this might be true for the specific cells investigated, it is not the fundamental origin of sudden-death but merely an artifact of cell design and today there is a broader agreement that the origin of sudden-death is due to charge transport limitations through the main discharge product, Li_2O_2, that completely covers the active surface [15, 32, 33]. The current understanding of sudden-death is described in full detail in section 5.1 and include the results of **paper I**.

The mechanisms of charge are complex and some disputes still exist in the field. As the chemical reaction 2.5 occurs on discharge it must be exothermic and it is therefore unlikely to occur on charge where it must be endothermic [39, 40, 41]. A simultaneously heterogeneous $2e^-$ charge process was therefore proposed as reaction 2.6, however such a process might seem unreasonable as the entropic barrier for two-electrode processes is much greater than an one e^- transfers [11, 39, 42] and still lack further evidence.

$$Li_2O_2 \longrightarrow 2Li^+ + O_2 + 2e^-(\text{cathode}) \tag{2.6}$$

Usually three potential regions are observed during charging, as also shown in Figure 2.5. Surface delithiation of Li_2O_2 deposits has been suggested as the low overpotential reaction, *i.e.* reaction 2.4, and the mid overpotential-region as a bulk Li_2O_2 oxidation following reaction 2.7.

$$2Li_2O_2 \longrightarrow 2LiO_2 + 2Li^+ + 2e^-(\text{cathode}) \tag{2.7}$$

However, this implies that this mid overpotential-region does not evolve O_2, which is not consistent with pressure decay results of $\sim 2\ e^-/O_2$ reported by McCloskey et al. [15] and in **paper IV**. Section 5.4 and **paper IV** will give a more in-depth description for the increasing charge potential.

2.3 The Na-O_2 Battery

The Na-O_2 technology is based on the same principles of the Li-O_2 technology with the difference being the choice of anode; in the former as Li and in the latter as Na. The obvious benefit of this exchange is the lower cost of Na compared to Li due to a higher natural abundance of Na. Other differences (not necessarily positive) include (i) a lower melting point of Na (T_m^{Na} = 98^{o}C, T_m^{Li} = 181^{o}C) making a molten anode easier to realize; (ii) Na is less reducing than Li; (iii) Na is softer than Li making it more difficult to handle; and (iv) Na dendrites have shown to more readily form [12, 43].

The non-aqueous Na-O_2 battery is considered a "beyond Li-ion technology" as it has a theoretical specific energy of 2643 Wh/kg and 2431 Wh/L, assuming sodium superoxide (NaO_2) as the discharge product, O_2 is excluded from the weight of the battery, and metallic sodium as the anode [12]. A sketch of a Na-O_2 battery is shown in Figure 2.6.

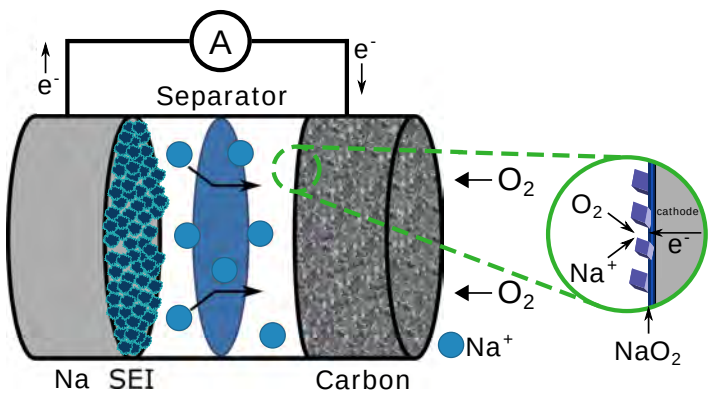

Figure 2.6: A schematic drawing of a Na-O_2 battery operated in discharge mode where NaO_2 forms on the cathode surface as a film and cubic crystals.

The first functioning Na-O_2 electrochemical cell was published by Peled et al. [44] in 2010 and consisted of a Na anode and an oxygen reducing/oxidizing cathode, operated at 105-110^{o}C. Here, the anode was molten Na and the discharge product was assumed to be Na_2O_2. In the following years, multiple authors [44, 45, 46, 47, 48, 49, 50, 51, 52, 53] studied the cell chemistry at room temperature, with a similar cell design of that depicted in Figure 2.6, using various electrolytes, and a range of discharge product was shown to form, *i.e.* NaO_2, sodium peroxide (Na_2O_2), sodium carbonate (Na_2O_3), and hydrated sodium peroxide ($Na_2O_2{\cdot}2H_2O$). Like any secondary battery, the discharge product must be electrochemically reversible, so the identification of reversible and non-reversible products is crucial. Bender et al. [54] compared thermodynamic data of different Na-O_2 phases and found that the theoretical cell voltages with NaO_2 and Na_2O_2 as the product to be 2.27 V and 2.33 V, respectively. As these values are very close, the mechanism of discharge cannot with certainty be derived from thermodynamics. However by 2012, Hartmann et al. [53] reported NaO_2 as the stable and reversible discharge product in the non-aqueous system based on an ether electrolyte. The product was shown to form through a comprehensive study including X-ray diffraction, Raman spectroscopy, pressure monitoring, DEMS, XPS, SEM, and a UV-VIS method also

used in my work and as described in section 3.7. This was further supported by multiple authors [55, 56, 57, 54, 58, 59] who also have shown that NaO_2 formation is independent of the carbon material in the cathode. Results from theoretical studies indicate that the nucleation of NaO_2 is preferred over that of Na_2O_2 and that once NaO_2 is deposited on the cathode surface further reaction to Na_2O_2 is unlikely [12, 60]. The reversible electrochemical reactions, in ether-based electrolytes, can be described by reaction 2.8-2.9 with the forward (or backward) arrow describing discharge (or charge) [55, 56, 57, 61]

$$\mathrm{Na} \rightleftharpoons \mathrm{Na^+ + e^-} \text{ (anode)} \tag{2.8}$$

$$\mathrm{Na^+ + e^- + O_2} \rightleftharpoons \mathrm{NaO_2} \text{ (cathode)} \tag{2.9}$$

In these systems, very large (10-50 μm) cubic crystals of NaO_2 are observed (as sketched in Figure 2.6) and since NaO_2 also is an electronic insulator [61, 62], it is suggested that the NaO_2 crystals also are formed by a solution-based mechanism [61]. A typical first discharge-charge cycle is presented in Figure 2.7 and although the Na-O_2 battery has significant lower energy densities than the Li-O_2 battery, the capacity of Na-O_2 cells, at low currents, is much greater. Furthermore the overpotentials on both discharge and charge are low in the Na-O_2 as the formed NaO_2 is less reactive and hereby less prone induce formation of carbonate-species [12, 57].

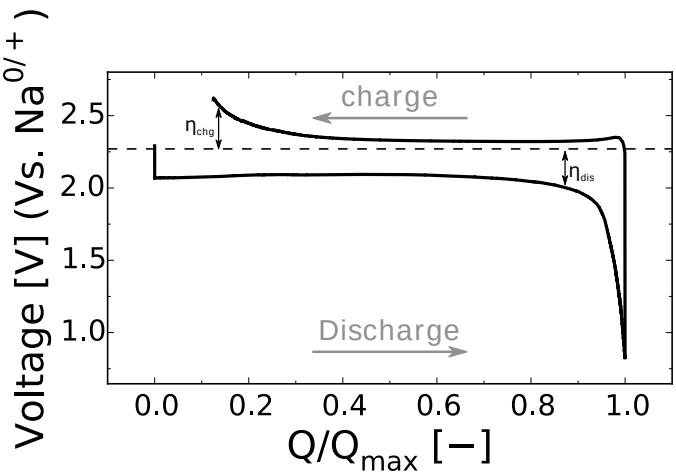

Figure 2.7: The first cycle of the Na-O_2 battery in a 1,2-dimethoxyethane electrolyte containing 0.5 M NaOTf with a carbon-based cathode. The dotted line is the theoretical electrode potential of 2.27 V vs. $Na^{0/+}$ at zero d.c. bias.

The sudden-death on discharge has been suggested to be due to O_2 transport limitations due to a buildup of the large Na-O_2 crystals [55] or due to a blocking of the electrochemistry at the cathode/electrolyte interface as the insulating NaO_2 crystals buildup on the electrochemically active cathode surface [56]. Section 5.2 and **paper III** gives a more in-depth description of the capacity limitations in the non-aqueous Na-O_2 battery.

3 Characterization Techniques

This chapter deals largely with dynamic electrochemistry where processes and factors influencing the transport across the interfaces of *i.e.* an electrolyte and an electrode are studied. The electrolyte and electrodes (containing a collection of interfaces) constitute an electrochemical cell and consists of at least two electrodes between which a potential difference is measured. In the electrochemical cell, one is interested in studying the dynamics of the working electrode (WE) and at the equilibrium electrode potential, a property related to thermodynamics and composition through Nernst equation, which reflects the state of the WE at zero current. Experimentally, dynamic studies are done by controlling either the current or the potential while measuring the other, which will be described in more detail in chapter 4. Electrochemical cells can be divided into two half cells and at equilibrium, the potential of each half-cell is governed by the Nernst eq. given by eq. 3.2, for the redox reaction in reaction 3.1.

$$\mathrm{ox} + \mathrm{ne}^- \rightleftharpoons \mathrm{red} \tag{3.1}$$

where ox is the oxidized specie, red is the reduced specie, and n is the number of electrons transferred.

$$\mathrm{E} = \mathrm{E}^{0'} + \frac{\mathrm{R_g T}}{\mathrm{nF}} \ln\left(\frac{\mathrm{C_{ox}}}{\mathrm{C_{red}}}\right) \tag{3.2}$$

where E is the potential; $\mathrm{E}^{0'}$ is the formal potential, which includes adjustments for the activity coefficients of ox and red; R_g the gas constant; T the temperature; F the Faraday constant; and C_i is the bulk concentration of each specie. In the following five sections, four different methods of studying the dynamics of the WE are described.

3.1 Galvanostatic Discharge and Charge

To initially investigate the performance of a battery galvanostatic cycling is often used. As degradation of the studied aprotic Li-O_2 and Na-O_2 cells is relatively fast, with large changes in capacity and internal resistance over a small number (often <10) of cycles, the assessment of performance metrics was carried out during the first cycle. Discharge and charge is defined by the direction of the current and, a negative and positive current is defined as discharge and charge, respectively. In the field of electrochemistry, the terms anode and cathode are defined by the direction of current but this can be confusing. It is therefore normal procedure to keep these terms constant, independent of the direction of the charge and the cathode and anode is

defined by the state of discharge. Li is therefore defined as the anode while the carbon (O_2) electrode is the cathode. An Example of a galvanostatic discharge and charge for the Li-O_2 cell is shown in Figure 2.5.

3.2 Cyclic Voltammetry (CV)

Cyclic voltammetry is a linear sweep method where the potential of the WE is scanned from E_1 to E_2 and back to E_1 with a known scan rate (ν), as shown in Figure 3.1a. The scan rate (ν) is the slope of the scanned potential and as the potential is scanned the current is measured. Cyclic voltammograms are plotted by E vs. I. Cyclic voltammograms and the ν dependency carries information of the reversibility of reactions (heterogeneous-, and coupled reactions), diffusional transport (homogeneous charge transport), surface capacitance, concentrations, and the potentials at which processes occur.

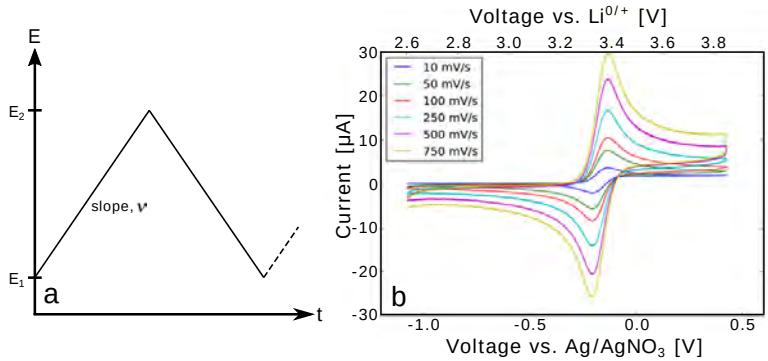

Figure 3.1: (a) Potential-time profile for cyclic voltammetry (b) Cyclic voltammograms of ferroceniuim/ferrocene at six different scan rates. Adapted from **paper I**.

Figure 3.1b illustrates the cyclic voltammograms of ferroceniuim/ferrocene with increasing ν. Cyclic voltammograms and their scan rate dependency is a function of the electrode are (A), C_i, D_i, T, n, the heterogeneous rate constant (k^0), and the geometrics of the electrode. The diagnostic criteria of electrochemical reversibility are (i) that the ratio of anodic and cathodic peak currents (I_p^a) and (I_p^c) is unity; (ii) the peak potentials (E_p^a and E_p^c) remains constant with increasing ν; (iii) E_p^a-E_p^c = 57 mV; and (iv) Ip^i displays a linear relationship with increasing $\nu^{1/2}$.

In order to determine the form of a voltammogram quantitatively and extract any of the previous mentioned parameters, it is necessary to solve Fick's 2^{nd} law for ox and red with boundary conditions given by the electrode geometry. Detailed descriptions can be found in both Bard and Faulkner [63] and the Southampton group [64] for different electrode geometries. The solution for planar macro disk electrodes is called the Randles-Sevcik equation

given by eq. 3.3 for reaction 3.1.

$$I_p^{ox} = 0.4463 \cdot \left(\frac{F^3}{R_g T} \right)^{1/2} \cdot n^{3/2} \cdot A \cdot D_{ox}^{1/2} \cdot C_{ox} \cdot \nu^{1/2} \tag{3.3}$$

This equation was used in **paper I** to determine the concentration of a range of redox shuttles in solution as their diffusion coefficients previously had been determined by the Randles-Sevcik plot (I_p vs. $\nu^{1/2}$) as shown in Figure 3.2.

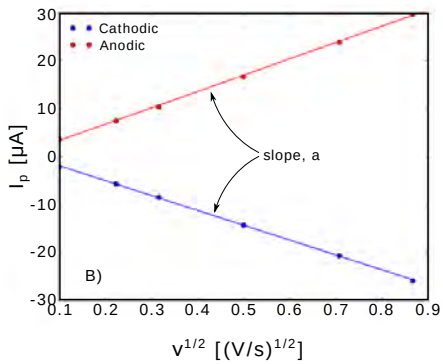

Figure 3.2: The Randles-Sevcik plot of ferroceniuim/ferrocene was a result of the cyclic voltammograms of Figure 3.1b. The peak currents are plotted vs. the square root of the scan rate to obtain the slope, a. Here the anodic and cathodic refers to the currents related to ferroceniuim and ferrocene, respectively. Adapted from **paper I**.

The slope of the Randles-Sevcik plot (a) was used to determine the diffusion coefficients of six redox shuttles with known concentrations using eq. 3.4 in **paper I**.

$$D_i = \frac{a^2 R_g T}{0.4463^2 n^3 A^2 F^3 C_i^2} \tag{3.4}$$

3.3 Microelectrodes

Microelectrodes, also known as ultramicroelectrodes, are electrodes with a critical dimension, *e.g.* radius, in the micrometer range [63, 65]. Microelectrodes used in this thesis were disk microelectrodes used to determine diffusion coefficients and concentrations of electrochemical active species in solution.

The decrease in electrode radius, to the micrometer range, has three important impacts on the electrochemistry. First, the double-layer capacitance is reduced as it is proportional to the area of the electrode and as the electrolyte resistance is proportional to $1/r_0$; the time constant of the cell is decreased. This means that the response time of the electrode is greatly reduced. Second, Faradaic and charging currents that flow between the two electrodes generate a potential that weakens the applied potential, known as the ohmic potential drop (iR

drop). The iR drop is greatly reduced as the currents scale with r_0^2 and are often three to six orders of magnitude smaller than conventional macro disk electrodes. Third, mass transport is significantly altered and two different regimes can occur at the microelectrode depending on the timescale. At sufficient short time scales, the thickness of the layer that is depleted of reactant is smaller than the electrode radius and mass-transport is governed by semi-infinite linear diffusion, which is equivalent to the mass transport occurring at macro disk electrodes. At longer time scales, the depletion layer becomes much larger than the size of the electrode radius and mass transport is governed by semi-infinite hemi-spherical diffusion [63, 65, 66]. Both mass transport modes (type of diffusion fields) are sketched in Figure 3.3 and the effect of the hemisperical diffusion on the cyclic voltammogram is shown in Figure 3.3c, as a steady-state voltammogram is obtained.

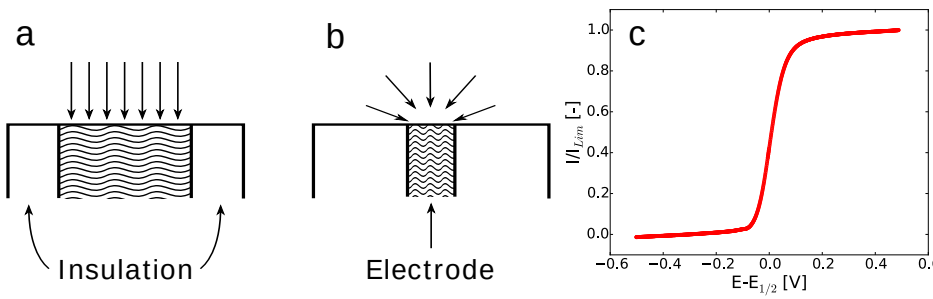

Figure 3.3: The diffusion field of (a) a planar macro electrode with a semi-infinite linear diffusion field, which corresponds to the early time regime for a microelectrode; and (b) a semi-infinite hemi-spherical diffusion field at a microelectrode; and (c) a steady-state voltammogram recorded at 5 mV/s for cobaltocenium/cobaltocene in 1 M LiTFSI-DME at a 12 μm radius glassy-carbon disk electrode.

The concentration and diffusion coefficient of oxygen in room temperature ionic liquids were determined in **paper VI** by a chronoamperometric technique developed by Shoup and Szabo [67]. Numerous numerical models have been proposed over the time to describe the chronoamperometric response observed at a microelectrode. The Shoup and Szabo equation have been widely used and has numerous times been reported to describe the current response at all times, both mass transport regimes, within an error of 0.6 % [67, 68]. For an electrochemical reduction, with an n e^- process, the chronoamperometric response at a microelectrode can be described by eq. 3.5-3.6.

$$\mathrm{i} = \frac{4\mathrm{nFAD_{ox}C_{ox}}}{\pi \mathrm{r_0}} \cdot f(\tau) \tag{3.5}$$

$$f(\tau) = 0.7854 + 0.8862\tau^{-1/2} + 0.2146 \cdot \exp\left(-0.7823\tau^{-1/2}\right) \tag{3.6}$$

A is the area of the microelectrode, D_{ox} and C_{ox} are the diffusion coefficient and concentration of the oxidized specie, respectively. The dimensionless parameter, $\tau = 4D_{ox}t/r_0^2$, represents the squared ratio of the diffusion length to the radius of the disk microelectrode. This technique permits simultaneous determination of either of two following parameters; D_i, n, or C_i if no coupled chemistry operates within the timeframe of the experiment, but if n is known it is possible to determine D_i and C_i simultaneously [63, 67, 69]. C_{ox} and D_{ox} was

fitted to experimental data using least squares minimization to this semi-empirical relationship in a software programmed in Python, which relies on parts of the scientific Python stack [70, 71, 72].

3.4 Electrochemical Impedance Spectroscopy (EIS)

EIS is powerful and non-invasive characterization technique used for electrochemical systems. It is useful as it measures an electrochemical system in terms of the frequency domain, hereby covering a range of timescales (often 5-7 orders of magnitude). This makes it capable of resolving processes, from a single measurement, with respect to their timescale and it is hereby possible to identify and determine interfacial processes, such as: redox reactions, adsorption, coupled reactions, and forced mass transfer. In addition to the quantification of geometrical effects, such as: different types of mass transfer regimes, quantify performance of porous electrodes, double-layer capacitances, and much more.

In EIS, a small amplitude sinusoidal voltage or current is applied to the electrochemical system with a range of frequencies. The response to this is an a.c. voltage or current. A small applied amplitude signal (typical 5 mV or a small percentage of the d.c. current) is often used to ensure that the current-voltage relationship is linear instead of exponential and this ensures that the response signal also is sinusoidal at the same frequency measured, but only shifted in phase angle. The excitation voltage signal and response current, expressed as a function of time, is given by eq. 3.7-3.8.

$$\mathrm{E(t)} = \mathrm{E_0}\cdot\sin\left(\omega\cdot\mathrm{t}\right) \tag{3.7}$$

$$\mathrm{I(t)} = \mathrm{I_0}\cdot\sin\left(\omega\cdot\mathrm{t}+\phi\right) \tag{3.8}$$

The impedance of the system is given by, the analogous expression of Ohm's law, eq. 3.9.

$$\mathrm{Z} = \frac{\mathrm{E(t)}}{\mathrm{I(t)}} = \frac{\mathrm{E_0}\cdot\sin(\omega\cdot\mathrm{t})}{\mathrm{I_0}\cdot\sin(\omega\cdot\mathrm{t}+\phi)} \tag{3.9}$$

Where Z is the impedance; E_0 and $\mathrm{I_0}$ are the peak amplitude of the a.c. potential and current, respectively; ω is the angular frequency; t is the time; and ϕ is the phase shift, which is related to the frequency through $\omega = 2\pi f$. Mathematically, an easy way to deal with the influence of the phase shift is to deal with the impedance in terms of complex numbers. Figure 3.4b illustrates the concept of complex numbers in relation to $\mathrm{Z}(\omega)$, where $\mathrm{Z}(\omega)$ is converted into a vector described by a real and imaginary part that is the relationship between $\mathrm{E}(\omega)$ and $\mathrm{I}(\omega)$ given by eq. 3.10.

$$\mathrm{Z}(\omega) = \mathrm{Z_{re}} - \mathrm{jZ_{im}} \tag{3.10}$$

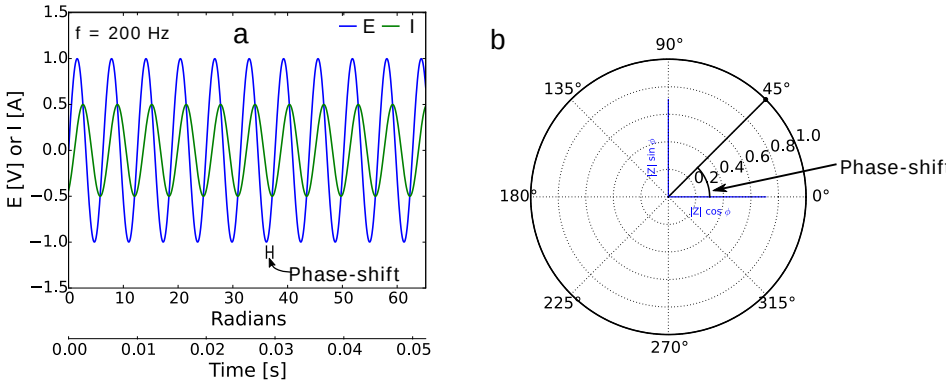

Figure 3.4: (a) A sinusoidal voltage perturbation given by eq. 3.7 and the corresponding output of an a.c. current given by eq. 3.8. (b) Phasor diagram illustrating the relationship between the voltage and current.

A common way to visualize the impedance is by plotting it in the complex plane, in the so called Nyquist plot (Figure 3.5b). Another useful graphical representation is the Bode plot, where the impedance and phase angle (or the real and imaginary parts of the impedance) are shown as a function of the logarithm of the frequency. Electrochemical processes have distinctive and characteristic impedance frequencies, as some processes are faster than others, and it is often possible to *e.g.* distinguish charge-transfers, mass transports, and adsorption processes from a single spectrum.

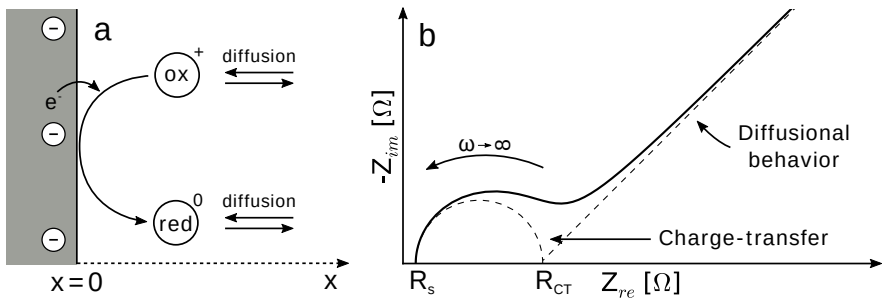

Figure 3.5: (a) A heterogeneous reduction of an electrochemical active specie in solution and (b) the corresponding Nyquist plot, which illustrates the distinctive processes for this system.

In Figure 3.5a, a heterogeneous charge-transfer is illustrated on a macro disk electrode. In the Nyquist plot (Figure 3.5b), the electrolyte resistance is the intercept at high frequencies (R_s), the heterogeneous charge-transfer process can be understood as the semi-circle and quantified as R_{CT} and C (or Q), and the diffusional behavior, which in this case is a semi-infinite linear diffusion expressed at lower frequencies.

3.4.1 Equivalent circuits

To quantify and parameterize the impedance response of an electrochemical cell an equivalent circuit model can be used. The model can be fitted to the data using complex non-linear least squares minimization algorithms. This method is known as equivalent circuit fitting. Data validation can be carried out using the linearized Kramers-Kronig test suggested by Boukamp [73] to ensure a good adherence to the requirements of causality, linearity, stability, and finiteness of the experimental data. In the following the equivalent circuit models used in this work will be described and discussed in relation to their general applicability and how they have been used in this work.

Resistor

An ohmic resistor is the simplest element, as it is independent of frequency and therefore has no complex part. It is used to model *e.g.* series resistance and is given by eq. 3.11 and the impedance response is shown in the Nyquist plot of Figure 3.6.

$$Z_R(\omega) = R \tag{3.11}$$

Capacitor

An ideal capacitor has no real part and is therefore resistance free; it is used to describe interfaces or non-Faradaic reactions such as redistribution of surface charges. The impedance of a capacitor is expressed as a negative complex number and given by eq. 3.12 and its response is shown in Figure 3.6.

$$Z_C(\omega) = \frac{1}{j \cdot \omega \cdot C} \tag{3.12}$$

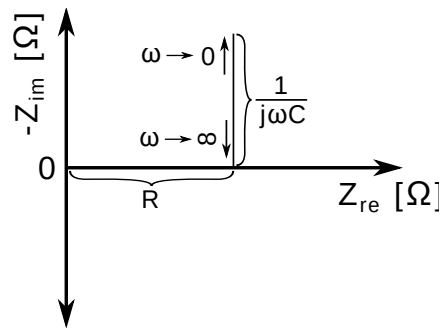

Figure 3.6: Nyquist plot of a resistor and a capacitor connected in series.

Warburg Element

The Warburg element is often used to model semi-infinite linear diffusion, such as the one illustrated in Figure 3.5, where a redox specie diffuses to and from the surface after a heterogeneous charge-transfer. In the Nyquist plot it displays a constant phase of 45^o and is given by an is given eq. 3.13 for reaction 3.1.

$$Z_W(\omega) = \left(\frac{2}{\omega}\right)^{1/2} \cdot A_w \tag{3.13}$$

The Warburg coefficient (A_w) can, among other, be used to determine the diffusion coefficients of species reacting with the surface by eq. 3.14.

$$A_w = \frac{R_g T}{n^2 F^2 A\sqrt{2}} \cdot \left(\frac{1}{D_{ox}^{1/2} \cdot C_{ox}} + \frac{1}{D_{red}^{1/2} \cdot C_{red}}\right) \tag{3.14}$$

Constant Phase element

The constant phase element (Q) has no direct electrical equivalent and the physical interpretation depends on the exponent n. For n = 1, the Q element equals a capacitor, at n = 0 the Q element is a resistor, at n = -1 an inductor, and at n = 0.5; Q is the Warburg element. However, in general, the Q element is used to model situations where a distribution of time constants is associated with the process, such as charging of a rough surface. Most interfaces in electrochemical cells display some degree of time constant dispersion and the surface capacitance is therefore often modeled using a constant phase element, Q, instead of a pure capacitor, C. The impedance of the Q element is given by eq. 3.15.

$$Z_Q(\omega) = \frac{1}{Q_0(j\omega)^n}\ , \ n = 0...1 \tag{3.15}$$

RC and RQ circuit

An RC (or RQ) circuit is a parallel connection of a resistor and a capacitor (or a constant phase element), as illustrated in Figure 3.7a. A parallel RC (or RQ) element is frequently used to model double-layer capacitance of an electrode surface in parallel with the charge-transfer resistance at that interface when a Faradaic reaction or other charge-transfer process (e.g. ion transport) takes place.

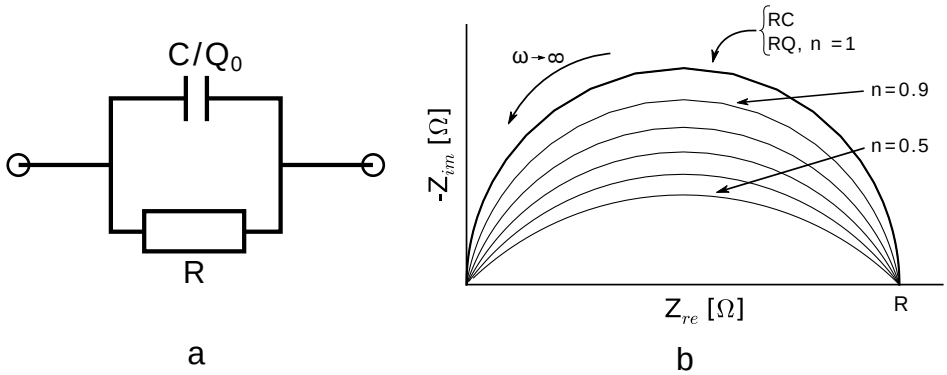

Figure 3.7: (a) The equivalent circuit of an RC element (b) The Nyquist plot of an RC and RQ circuit with varying n values.

The two circuits take the form of a semi-circle in the Nyquist plot (Figure 3.7b) and the behavior of the real and imaginary parts reveal certain characteristics of the electrochemical system. **At very high frequencies**, the current can pass through the C (or Q) without any loss by bypassing the resistor in parallel. **At high frequencies**, the capacitive behavior of the system becomes evident as the complex impedance decreases rapidly from zero with an angle of 90^o from the real part. As charge begins to pass through the resistor the real part also increases. **At low frequencies**, the capacitive behavior becomes less important as more charge runs through the resistor as the impedance of the capacitor moves toward infinite. **At very low frequencies** (approaching zero), the systems behaves more like an d.c. circuit as the capacitive behavior is neglectable and the current almost completely runs through the resistor. The intercept at the real axis, at low frequencies, is therefore R in the RC (or RQ) circuit. The impedance of the RC and RQ elements are given by eq. 3.16-3.17, respectively.

$$\mathrm{Z_{RC}}(\omega) = \frac{\mathrm{R}}{1 + \mathrm{j} \cdot \omega \cdot \mathrm{C}} \tag{3.16}$$

$$\mathrm{Z_{RQ}}(\omega) = \frac{\mathrm{R}}{1 + \mathrm{R} \cdot \mathrm{Q_0} \cdot (\mathrm{j} \cdot \omega)^{\mathrm{n}}} \text{ , n = 0...1} \tag{3.17}$$

Randles circuit

The Randles circuit is usually used to model the heterogeneous charge-transfer in presence of semi-infinite linear diffusion of the electrochemical active specie on flat disk electrodes. The equivalent circuit is illustrated in Figure 3.8 and a sketch of the reaction and the corresponding Nyquist plot is depicted in Figure 3.5.

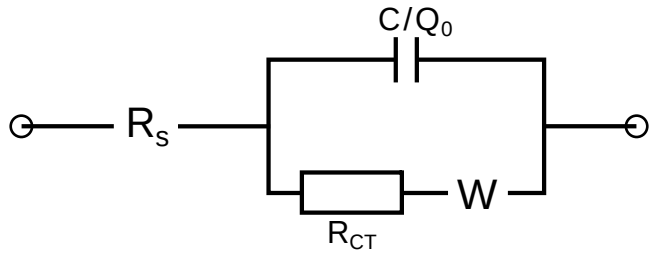

Figure 3.8: The Randles circuit is comprised of R_s the solution resistance, R the charge-transfer resistance, Q the constant phase element, and W the Warburg element that describes the diffusion of the reacting specie.

It is a combination of the RC (or RQ) element with the Warburg element in series with R_s and thus is given by eq. 3.18.

$$Z_{Q(RW)}(\omega) = \frac{R_{CT} + 2^{1/2} \cdot A_w}{\omega^{1/2} + Q_0 \cdot (j \cdot \omega)^n} \text{ , } n = 0...1 \tag{3.18}$$

This equivalent circuit was used in **paper I** to probe the charge-transfer resistance of redox shuttles on glassy-carbon disk electrodes to determine k^0 as a function of the thickness of Li_2O_2. The relationship between R_{CT} and k^0 under these circumstances is given by eq. 3.19 for reaction 3.1 [63, 74].

$$k^0 = \frac{R_g T}{n^2 \cdot F^2 \cdot R_{CT} \cdot A \cdot C_{ox}^{1-\alpha} \cdot C_{red}^{\alpha}} \tag{3.19}$$

Where α is the transfer coefficient, A is the electrode area, and R_{CT} is the charge-transfer resistance.

Porous Electrode Models (PET)

The impedance model that describes an electronically conducting porous electrode immersed in and filled with a liquid electrolyte is known as the porous electrode theory and was first developed by de Levie and Delahay [75]. This model was applied to the impedance of Li-O_2 and Na-O_2 cells of **paper II** and **III**, respectively. The porous electrode is modeled as a cylindrical pore containing electrolyte and the pore wall corresponds to the surface of the solid conducting electrode. The impedance model has frequently been used, among other to describe ideal polarized gold- and Ni- based electrodes [76, 77, 78], composite solid state fuel cell electrodes [79, 80], super capacitors [81, 82], Li-ion batteries [83, 84, 85], nano-porous TiO_2 electrode [86, 87] and in conducting polymer electrodes [88, 89].

The impedance of porous electrodes depends on the pore geometry, the pore size distribution, the presence and concentration of redox species, and can be further complicated by the presence of potential and concentration gradients that may arise when a d.c. current is applied. In the absence of a Faradaic reaction only double-layer charging takes place and the surface impedance can be modelled with a capacitor, or more generally, with a constant phase element and when Faradaic reactions take place; the surface impedance must include

a resistor in parallel to the capacitor/constant phase element (RC or RQ). For more complex situations, such as with ion intercalation into the electrode particles one or more additional impedance elements need to be included in the surface impedance, *e.g.* a finite space Warburg diffusion element, depending on the presence of any surface layers [90]. In the case of the presence of significant potential or concentration gradients in the porous electrode this can further complicate the resulting impedance and using this model neglects such effects, possibly over estimating the double-layer capacitance of the porous electrode [74]. The porous electrode model can be described by a general transmission line model [86, 89] represented by eq. 3.20-3.21.

$$Z_{tot}(\omega) = \frac{X_1 \cdot X_2}{X_1 + X_2} \cdot \left(L + \frac{2 \cdot \lambda}{\sinh(L/\lambda)} \right) + \lambda \cdot \frac{X_1^2 + X_2^2}{X_1 + X_2} \cdot \coth(L/\lambda) \tag{3.20}$$

with

$$\lambda = \sqrt{\frac{\zeta}{X_1 + X_2}} \tag{3.21}$$

Here, λ is the characteristic a.c. penetration depth [cm], which is equivalent to the electrochemical utilization thickness of the electrode, and L is the thickness of the electrode [cm], which is usually determined from cross sectional micrographs of the electrode (ignoring tortuosity of the percolating phases). Eq. 3.20 represents the impedance model of a single pore [Ω] as illustrated in Figure 3.9.

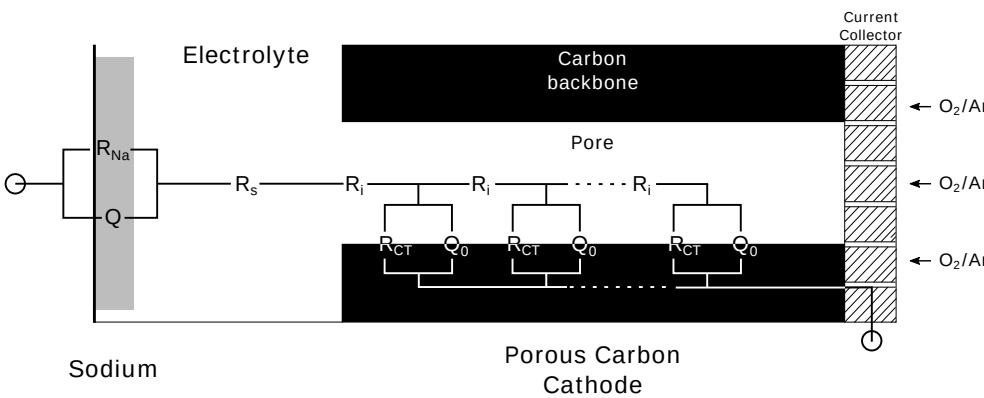

Figure 3.9: Illustrates the equivalent circuit for a two terminal cell and a single pore of the porous electrode with a reacting RQ element included as the ζ. Adapted from **paper III**.

X_1 and X_2 describe the resistance per unit length of transport channel in the liquid and electrode, respectively [Ω/cm]. Eq. 3.20 and 3.21 in principle describes the impedance of a single pore [Ω], however, the porous electrode consists of many pores and although the number of pores is difficult to obtain, a convenient and equally informative approach is to consider the porous electrode as a single pore, as it is depicted in Figure 3.9. This enables eq. 3.20-3.21 to be simplified to eq. 3.22-3.24 by also considering that practical carbon

electrodes have an electronic conductivity that is much greater than that of the electrolyte ($X_2 \ll X_1$).

$$Z_{tot}(\omega) = \lambda \cdot X_1 \cdot \coth(L/\lambda) \tag{3.22}$$

$$\lambda = \sqrt{\frac{\zeta}{X_1}} \tag{3.23}$$

Then, the transport of ions in the flooded pores can be modeled as the resistance per unit length of the electrode [Ω/cm] - i.e. the ionic resistance R_i, as shown in Figure 3.9.

$$X_1 = R_i \tag{3.24}$$

The surface impedance, ζ, of the flooded pores will, (i) in the absence of Faradaic reactions, be modeled as a constant phase element, Q, to describe double layer charging and (ii) in the presence of Faradaic reactions as an RQ circuit with R and Q denoted R_{CT} and Q_0, as shown in Figure 3.9. The surface impedance, ζ, is then described by eq. 3.25-3.26, for (i) and (ii), respectively.

$$\zeta = Z_Q(\omega) \tag{3.25}$$

$$\zeta = Z_{RQ}(\omega) \tag{3.26}$$

The shape of the impedance of the flooded porous electrode gives valuable insight into the balance between the resistance of the electrolyte in the pores and the pore surface impedance. To demonstrate this, simulations of the impedance spectra for selected key cases using either eq. 3.25 or 3.26 and is shown in Figure 3.10. The impedance simulations depicted in Figure 3.10a-b illustrate the shape of **the impedance in absence of Faradaic reactions**. Here, a characteristic high frequency linear region is observed, which is due to the ionic resistance (R_i) within the porous structure, as sketched in Figure 3.9. As stated by Lasia and others [74, 76, 91] this is the simplest evidence to confirm whether the electrode displays any porous impedance character.
Figure 3.10c-d illustrates the shape of **the impedance in the presence of a surface reaction** similar to the equivalent circuit within the porous cathode in Figure 3.9. Here four situations are depicted, where the a.c. penetration depth (λ) is much smaller than the thickness of the electrode ($\lambda \ll L$), the a.c. penetration depth is similar to the thickness of the electrode ($\lambda \sim L$), the a.c. penetration depth is larger than the thickness of the electrode ($\lambda > L$), and where the a.c. penetration is much greater than the thickness of the electrode ($\lambda \gg L$). As the a.c. penetration depth (λ) is smaller or equal to the thickness of the electrode, a skewed semicircle forms in the complex-plane as the impedance is dominated by the ionic resistance, R_i. As λ increases, the complex semicircle becomes more ideal as the surface reaction starts to dominate the impedance.

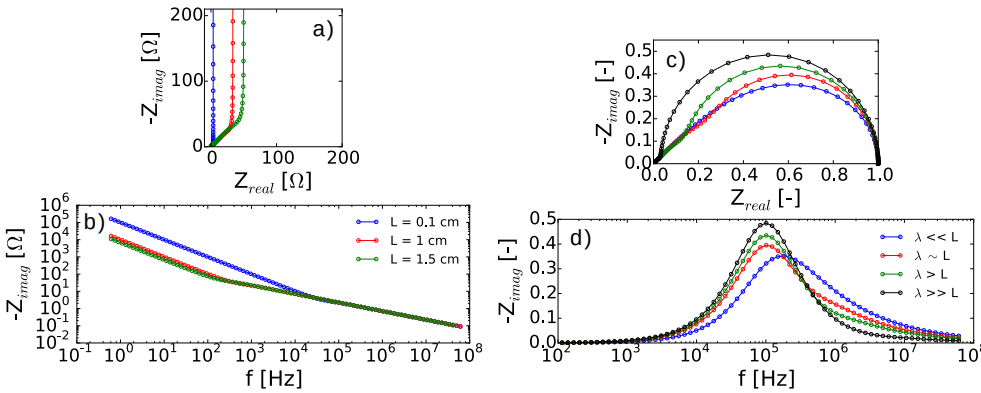

Figure 3.10: Impedance simulations of the PET model using two equivalent circuit elements: -Q- in (a-b) and -RQ- in (c-d). A Nyquist and Bode plot is shown for each system in (a and c) and (b and d), respectively. The simulations for (a-b) was done by varying L to 0.1, 1, and 1.5 cm while R_i, Q_0, and n were kept at 100 Ω/cm, 100 μF/cm, and 1, respectively. The simulations for (c-d) were done by varying R_i to 100, 10, 5, and 1 Ω/cm, while R_{CT}, L, Q_0, and n were constant at 0.1 Ω·cm, 0.1 cm, 100 μF/cm, and 1, respectively. Adapted from **paper II**.

3.5 Differential Electrochemical Mass Spectrometer (DEMS)

The DEMS is a very useful tool for studying side-reactions that leads to gas evolution in batteries and was in this work was used for investigation of the charge process in the Li-O_2 cell. Ideally, as described by reaction 2.3-2.5 for the Li-O_2 battery and by reaction 2.9 for the Na-O_2 battery, O_2 should only evolve on charge. However, in reality also CO_2, H_2O, and H_2 have shown to form [15, 92, 93].

DEMS was, in this thesis, applied for **paper IV** and a brief description will in the following be given, while a more detailed description can be found in ref. [92].

A metal-O_2 battery is connected to a six port, two way, valve with two positions, as shown in Figure 3.11. In position 1, the cell is isolated so that any gas products formed accumulate in the headspace of the cell ($V_{discharge}$) that is isolated from the atmosphere. In position 2, the cell is connected to a small evacuated capillary (V_{MS}), which has with a known volume and as the system is switched back to position 1, the sampled gas is sent to a mass spectrometer, where the sampled gas is detected on the basis of the m/z ratios. The quantification of the gasses was possible as the intensities of the m/z ratios were calibrated to the volume of V_{MS} using 5 v/v % O_2, 5 v/v % CO_2 gas mixtures in Ar.

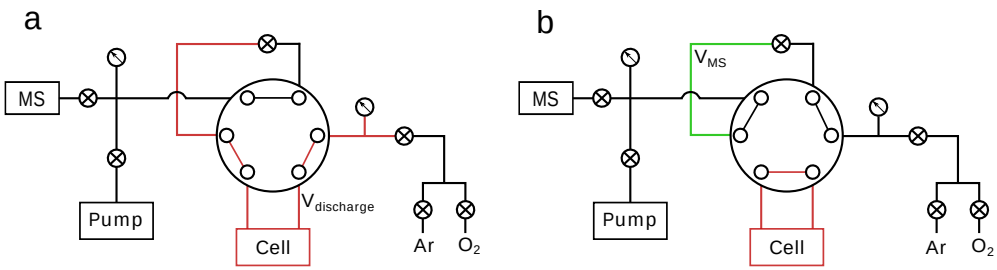

Figure 3.11: Schematic of the DEMS setup at DTU Energy. Position 1 that is used for discharge is illustrated in (a) while (b) is position 2 that is used for charge. The calibrated volumes are marked V_{MS} and $V_{discharge}$. Inspired by ref. [94].

3.6 Number of Electrons per Oxygen Molecule (e^-/O_2)

As the reversibility of metal-O_2 batteries cannot solely be evaluated by the means of columbic efficiencies a simple approach was reported by McCloskey et al. [92]. The effective method measures the gas usage by having a pressure transducer connected to hermetically sealed battery and thus monitors the cell pressure as the battery operates. Using eq. 3.27, it is possible to estimate the number of e^- used per O_2 molecule.

$$\Delta e^-/O_2 = \frac{V_{cell} F \Delta P}{\Delta Q R_g T} \tag{3.27}$$

This is an effective simple tool to evaluate the extent of parasitic reactions and was applied in **paper II**, **III**, **IV**, and **VI**.

3.7 Spectrophotometric Quantification of Li_2O_2

To chemically quantify the amount of Li_2O_2 a spectrophotometrical method introduced to the metal-O_2 community by Hartmann et al. [55] was used. It relies on a Ti-complex (Ti-complex (Ti(IV)OSO_4)) which is chemically oxidized by H_2O_2 to $H_2Ti(VI)O_4$ following reaction 3.29. H_2O_2 is formed by soaking cathodes with Li_2O_2 in water as it rects in a 1:1 ratio, as described by reaction 3.28. The formed $H_2Ti(VI)O_4$ complex strongly absorbs at 408 nm [95].

$$Li_2O_2 + 2H_2O \longrightarrow 2LiOH + H_2O_2 \tag{3.28}$$

$$Ti(IV)OSO_4 + H_2O_2 + 2H_2O \longrightarrow 4H^+ + H_2Ti(VI)O_4 + {OSO_4}^{4-} \tag{3.29}$$

After a Li-O_2 battery had been tested, the cell was purged with argon and transferred to a glovebox. The cell was carefully disassembled and the cathode was extracted. Each cathode was washed with DME dried using 4 Å molecular sieves (Sigma-Aldrich), and the cathodes were subsequently dried in vacuum. The cathodes were taken from the glovebox and immediately put into a 4.00 mL 0.063-0.07 % $TiOSO_4$ aqueous solution and the colored oxidized Ti-complex was immediately seen. The solutions were left to react for 15-30 min and to remove carbon particles, which otherwise would interfere with the spectrophotometric measurement, samples were centrifuged and the supernatant was extracted yielding a clear colored liquid that was characterized using a Shimadzu UV-3600 PharmaSpec with 1 nm resolution and medium scan in absorbance mode. An example of the results is given in Figure 3.12-3.13 including a image of the actual samples, which were used in for **paper IV**.

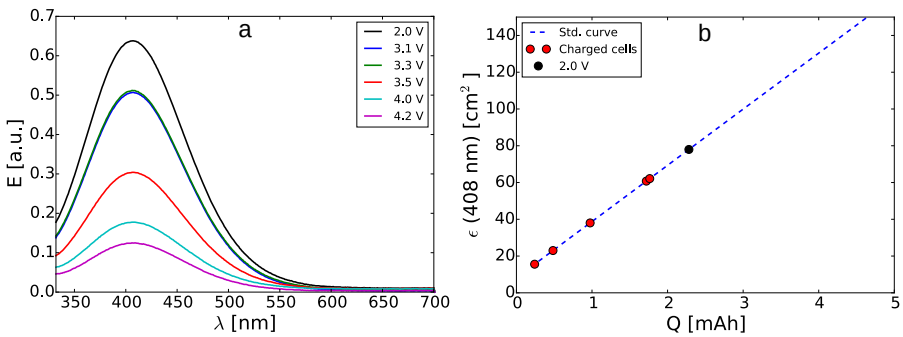

Figure 3.12: (a) Optical absorption spectroscopy for the washed Li_2O_2 coated electrodes. The extinction of the $H_2Ti(VI)O_4$ complex in aqueous solutions illustrating the amount of detected Li_2O_2. (b) Lambert-Beer type calibration curve used to determine the amount of Li_2O_2 in the cathodes. The curve is made by measuring the absorbance of solutions with a known amount of peroxide (–). In the graph, the amount of Li_2O_2 is represented by a capacity equivalent using Faraday's law of electrolysis. Adapted from **paper IV**.

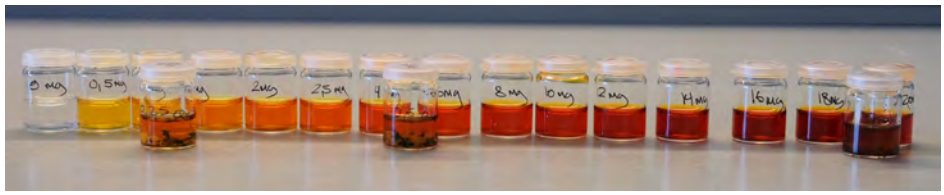

Figure 3.13: Ti-complex samples with known Li_2O_2 concentrations and three samples with post-mortem cathodes. The image is taken prior to centrifugation of the latter samples and the carbon particles from the cathode are seen in suspension.

This method assumes that Li_2O_2 reacts with water forming LiOH and H_2O_2, following reaction 3.28, however reaction 3.30 is also possible.

$$Li_2O_2 + 2H_2O \longrightarrow 1/2O_2 + 2LiOH \tag{3.30}$$

If this reaction takes place, the amount of Li_2O_2 would be underestimated, since the Ti-complex is oxidized by H_2O_2 that only forms through reaction 3.28. Experimentally, O_2 evolution from cathodes submerged in H_2O was not observed and reaction 3.30 therefore seems unreasonable.

3.8 Scanning Electron Microscopy (SEM)

Microscopy is an important tool for investigation of interfaces and morphology of discharge products in *e.g.* batteries. Optical microscopy is based on visible light and is useful for images with a low magnification. Electron beam techniques gives much higher resolutions where it is possible to observe thin films, such as the SEI, nanoparticles, and other product morphologies formed on the electrodes. A range of different electron microscopy techniques exist. In this thesis, scanning electron microscopy was exclusively used and a short description is here given, but more detailed descriptions can be found in Goodhew et al. [96].

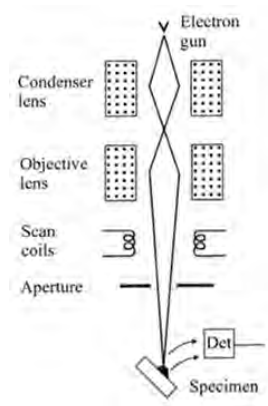

Figure 3.14: Illustrating the working principles of the SEM [96].

The SEM consist of an high-energy electron source that is focused onto the incident sample by a range of lenses, scan coils, objectives and an aperture, as shown in Figure 3.14. As the electron beam hits a sample, a range of electrons are emitted from the surface where two kinds are used to create the SEM image: backscattered- and secondary electrons. Backscattered electrons have lost the least amount of energy, of the two, by interacting with the sample and escape with energies close to the incident beam. Electrons that escape the sample with lower energies are termed secondary electrons, whose energy is lost by inelastic collisions with nuclei or by ejection of high orbitals electrons from the sample atoms. The SEM image is created by scanning the incident beam across the sample and detecting the two former types of emitted electrons by an electron detector. As the low-energy secondary electrons mainly escape the top part of the interaction volume, these electrons contain topographical information of the sample while the energy of backscattered electrons is dependent on the atomic number of the interaction volume and thus can be used to map the chemical information of the sample, as brighter areas corresponds to heavier elements [96].

Cell Designs and Battery Assembly 4

To perform electrochemical experiments certain experimental requirements are needed and one of the most fundamental is the control of the electrode potentials. In order to keep the reference electrode potential stable one must ensure that the composition of the equilibrium half-cell that constitute the reference electrode is maintained. This is possible by use of a so called three-electrode setup. In this setup the current is drawn between the WE and CE, and the voltage is measured between the WE and RE. The RE channel of the potentiostat has a high input impedance hence practically forcing all of the current to flow between the CE and WE, which enables the potential stability of the RE. In a two-electrode cell only the total cell voltage can be measured and the individual electrode potentials cannot be determined. A three-electrode and a two-electrode cell, which are connected to a potentiostat are sketched in Figure 4.1.

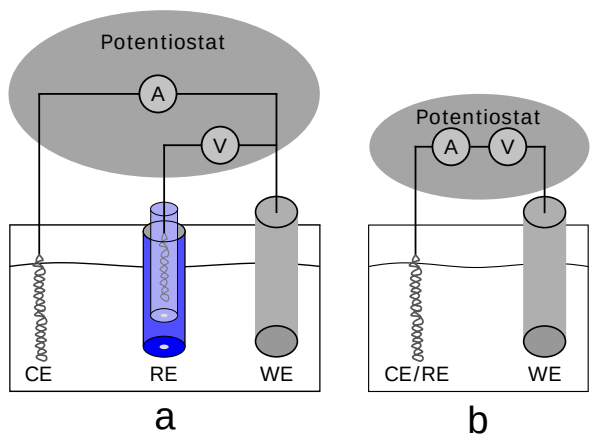

Figure 4.1: (a) A three-electrode system where the potential difference is measured between WE and RE, while the current passes between WE and CE. (b) A two-electrode system, where both the potential difference and current are measured between the WE and the CE/RE.

Typically, to ensure that the measured current is limited by the electrochemistry of the WE, the surface area of CE is often 20 times higher than that of WE. In the experimental setups limited to two electrodes, the CE also acts as the RE and usually very small overpotentials are related to this electrode so that the total cell overpotential is dominated by the overpotential of the WE. In non-aqueous electrolytes this electrode is the anode of the battery (Li or Na). The three-electrode cell design, as the conventional three-electrode cell and the EL-cell, was used in **paper I** and **II**, respectively; while the two-electrode cell design, as the Swagelok cell, was used for **paper III-VI**.

4.1 The Conventional Three-Electrode Cell

The conventional three-electrode cell illustrated in Figure 4.2 was used to study the charge-transfer through Li_2O_2 films in **paper I**. The electrochemical cell was assembled with four working electrodes, a Pt counter electrode, and a dual-reference electrode consisting of a double-junction Ag/0.01 M $AgNO_3$-1 M LiTFSI-DME//1 M LiTFSI-DME// in parallel with a 0.1 μF capacitor connected to a second Pt wire in solution.

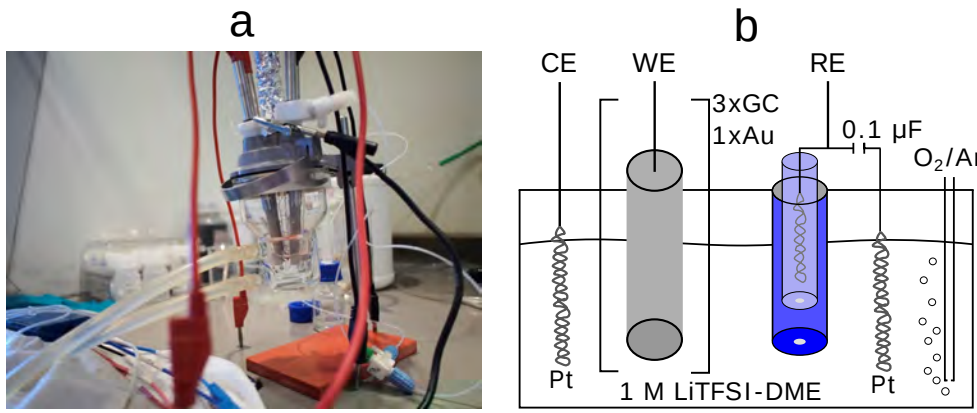

Figure 4.2: (a) The electrochemical cell used in **paper I**. The cell contains four WE's, the dual-RE positioned in the center of the cell, and a Pt CE. In an outer compartment the temperature was controlled to 25^{o}C and the gas inlet is shown on the right hand side of the cell (b) A schematic of the electrochemical cell shown in (a).

The reference electrode was constructed to maintain a stable d.c. potential at all times from the double-junction Ag/$AgNO_3$-1 M LiTSFI-DME//1 M LiTFSI// part, as the Ag^+ leakage rate of a single junction was too great. This is seen from the cyclic voltammetry of ferroceniuim/ferrocene with a single- and double-junction RE in Figure 4.3a-b as a neglectable voltage-drift within 24 hrs is observed from the latter design. The high-frequency by-pass Pt-wire of the RE made it possible to obtain high quality electrochemical impedance data also at high frequencies (f > 100 Hz) as shown in the Kramers-Kronig-residuals from experiments conducted with the ferroceniuim/ferrocene at $E_{1/2}$ in Figure 4.3c-e. A similar RE has previously been reported in refs. [74, 97, 98].

The four WE's were used one at a time. Three of these were glassy-carbon (GC) disk embedded electrodes (d = 1.6 mm) and the fourth was an Au disk embedded electrode in polyether ether ketone (PEEK, d = 1.6 mm) resin from Bio-Logic. All electrodes were all polished using aqueous suspensions of 0.05 μm aluminium oxide (MicroPolish, Buehler). The electrochemical cell was assembled in an Ar-filled glovebox with O_2 and H_2O levels below 2 ppm. After assembly, the electrochemical cell was transferred out of the glovebox with minimal exposure to ambient conditions, placed in a Faraday cage, and flushed with O_2 (purity 6.0, Air Liquid) or Ar (purity 6.0, Air Liquid) that passed through 4 Å molecular sieves (Sigma-Aldrich) followed by dried DME (BASF) before entering the cell to minimize water impurities. Increases in the H_2O and O_2 levels were monitored by examining the cyclic voltammogram of an Au electrode immersed in the electrolyte and experiments with increasing levels of H_2O were discarded. All electrochemical experiments were performed

using a SP-200 Bio-Logic potentiostat or a Gamry REF600.

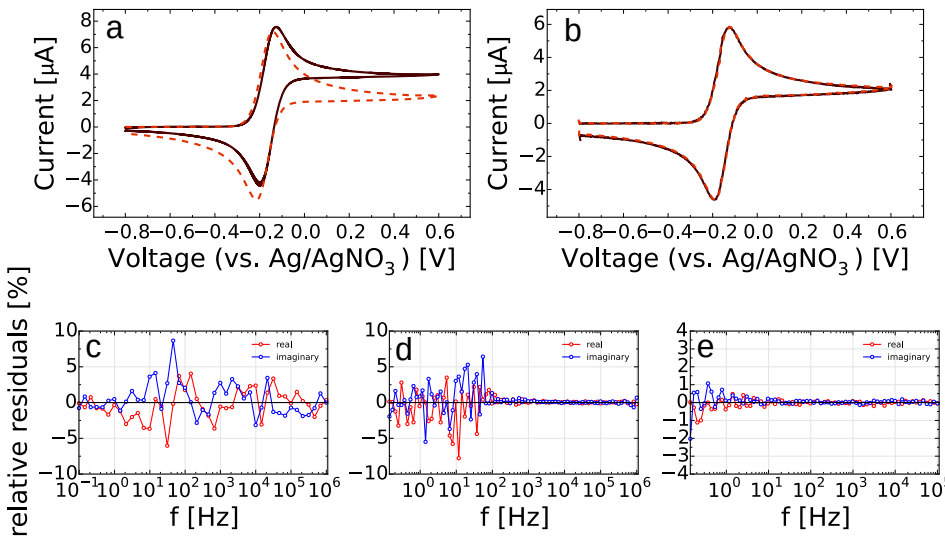

Figure 4.3: Optimization of RE (a) CV of ferroceniuim/ferrocene in Ar with the single-junction RE. The solid line is the initial CV and the dotted a CV 24 hrs later (b) Same experiment as in (a), but with the double-junction RE (c) Kramers-Kronig-residuals from the impedance of ferroceniuim/ferrocene with the single-junction RE and in (d) with the double-junction RE with the Pt by-pass wire, and in (e) with the Pt wire positioned close to the RE's frit.

4.2 The Swagelok Cell

The Swagelok cell is a two-electrode hermetically sealed cell and two Swagelok cell designs have been used in this thesis. The Swagelok cell design developed at DTU Energy was used for paper **IV-VI** and the Swagelok design currently employed at Prof. Bryan McCloskey's lab at UC Berkeley was used for **paper III**. The largest difference being a design, of the latter, that allowed the O-rings to be compressed, which makes for a better seal. A detailed description of this cell can be found in ref. [92].

The Swagelok cell, used at DTU Energy, is shown in Figure 4.4 with its components except the Li or Na anode. Experiments were conducted with an 11 mm anode; either 12.7 mm Celgard 2500 separators or one 12.7 mm Whatman GF/A glass fiber separator; either an XC72 carbon black (Vulcan XC72, Cabotcorp, GA) cathode with 33.3 wt/wt % polytetrafluoroethylene (PTFE, Sigma-Aldrich) or P50 (AvCarb) carbon paper cathode; a 316SS stainless steel 150 mesh (WestCoast, Esbjerg, Denmark); and 60-90 μL electrolyte. These components were stacked between the SS-mesh and the anode inside a fused silica glass tube which was sealed between two O-rings (KZ6375, M-Seals) connected to the anode and cathode current-collectors. Hereafter the gas inlet/outlet was connected by a 1/16" M4 thread mount that had two DESO quick-connects.

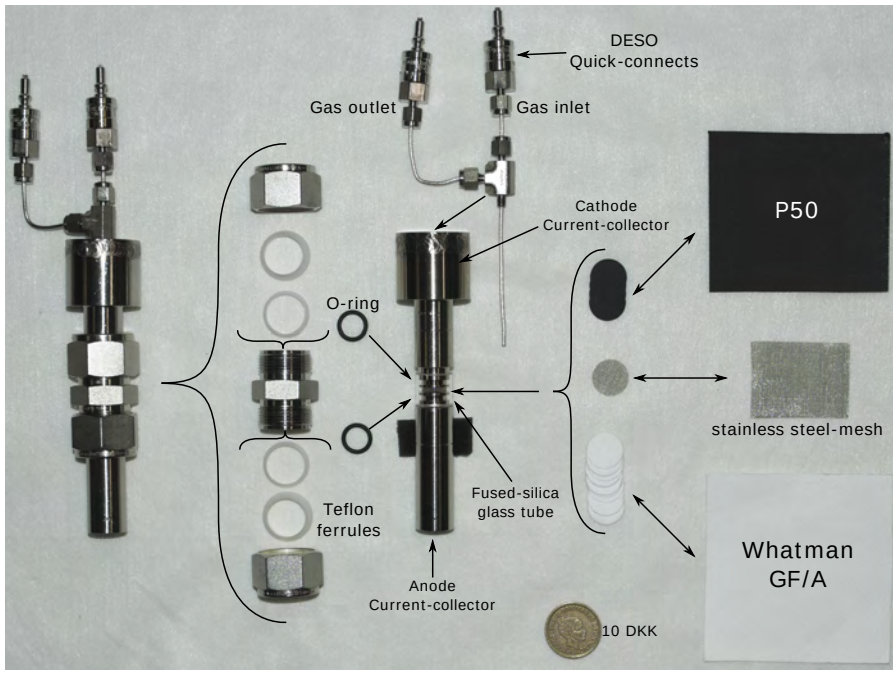

Figure 4.4: The Swagelok cell developed at DTU Energy. The components and assembly is illustrates and should be read from the right to left, finishing with the assembled and sealed cell.

The cells were assembled and sealed in an Ar-filled glovebox and transferred out where the cathode head-space (10 mL) was flushed and filled with O_2 (purity 6.0, Air Liquid) to a partial pressure of 1.8 bar. The cells were leak tested empty and typical leak rate were found in the range of 5-10 mbar/hr, corresponding to a 10 % O_2 loss in 9 hrs, sufficient to perform most experiments.

4.3 The EL-Cell

The EL-cell (EL-cell, Germany) is a hermitically sealed three-electrode setup, similar to the Swagelok design. The third electrode allows simultaneously measurement of the electrochemical response of both anode and cathode in respect to the RE. The cell parts are shown in Figure 4.5 and an assembled cell is shown in Figure 4.6a. The RE is sandwiched inbetween the WE and CE in the PEEK sleeve at the position labeled "RE position" in Figure 4.5. Prior to cell assembly, Li was extruded through the "RE position" hole using a custom tool (RCC-REFload, EL-cell, Germany) and electrical contact was later made by the "RE current-collector". The EL-cell was used in **paper II**.

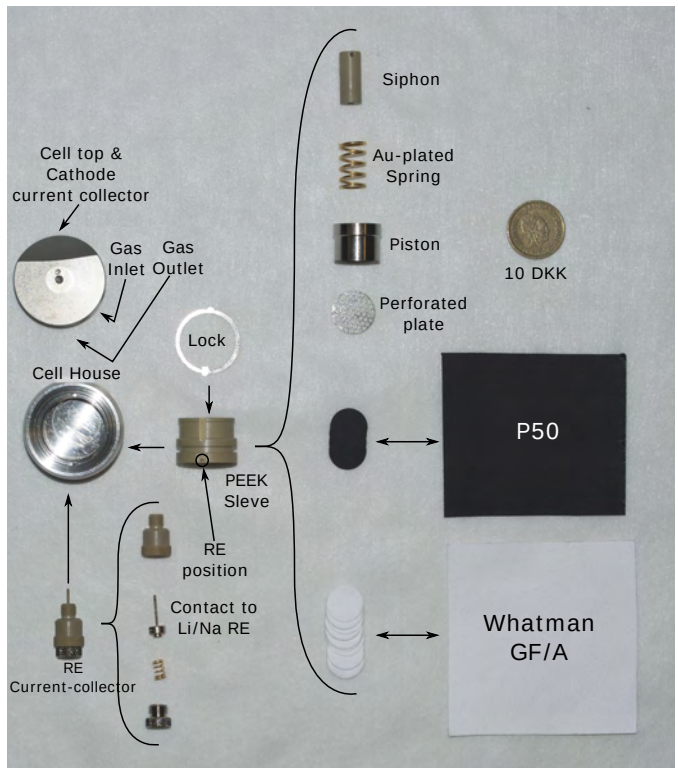

Figure 4.5: The EL-cell parts and assembly procedure sketched from right to left. All cell parts in contact with the active materials are made from stainless steel (SS 315L).

The position of the RE is important, too low or too high and it will short-circuit with the CE or WE, respectively. The optimal position is directly in-between the two electrodes and the position is determined by the height (number of) stacked glass fiber separators. In this work, 8 pieces of stacked Whatman QM-A (VWR) was typically used. The correct positioning could be monitored from the R_s in the Nyquist plot of each electrode in respect to the RE. The cell was assembled, in an Ar-filled glovebox, by first inserting the Li RE in the PEEK sleeve, the PEEK sleeve (ID = 18 mm) was inserted into the cell house, an 16 mm Li anode (HongKong Wisdom Tech Company) was attached to its bottom, 8 pieces of 18 mm stacked Glass fiber separators was added, and one 18 mm XC72 or P50 cathode was put on

top. Hereafter the following cell components were added on top: the perforated plate, piston, Au-plated spring, siphon, and the lock. The RE current-collector was then attached and the cell potentials were tested inside the glovebox using a multimeter. Then, a PE seal was attached to the cell house and the cell top was connected carefully to avoid short-circuits. The assembled cell was then attached in the cell mount and modified stainless steel gas connects were attached to the gas in- and outlet of the cell top. Note, that commercially available EL-cells come with PEEK capillaries that permit H_2O permeation, these were therefore not used in any published work. A fully assembled EL-cell is shown in Figure 4.6a. The cell was flushed with O_2 and for **paper II** a constant pressure of ∼1050 Torr (∼1.4 bar) was kept in the cell. The cell was leak tested by applying a vacuum and leaving it overnight while monitoring the cell pressure. Typical leak rates for empty dry cells were in the order for 1.6 mbar/hr. The volume of the cell, needed for eq. 3.27, was calibrated, containing only dry cell parts, by attaching standard volume loops (Valco Instruments Company Inc.) to the setup in place of the cell. The standard loops were charged with a known Ar pressure and the gas was then expanded into a sample cross (*e.g.* V_{MS} of Figure 3.11) and the pressure decrease was noted. The same was done for the cell and by relating the two, the volume was determined to 5.30 mL.

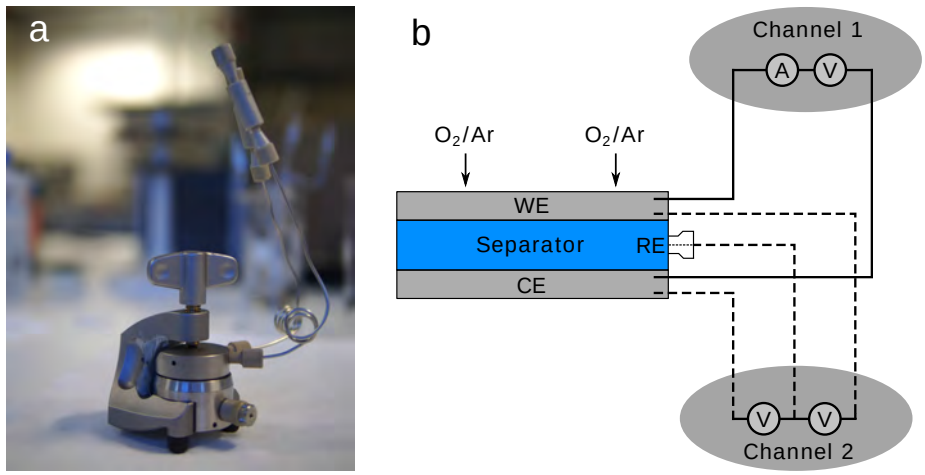

Figure 4.6: (a) Image of an assembled EL-cell (b) A schematic of the sandwich structure of the cell and the position of the RE. It also illustrates how the cell was connected to the potentiostat using two channels.

The study in **paper II** required that the impedance of the WE and CE were measured simultaneously during discharge. This required that two channels of the potentiostat were applied, as sketched in Figure 4.6b. Channel 1 functions as a normal two-electrode setup, and controls the current and potential of the cell while channel 2 only observes the potential difference between WE and RE; and CE and RE. This setup made it possible to experimentally separate the impedance of two electrodes. These experiments were performed using Bio-Logic VSP or VMP3 potentiostats in stack mode.

4.4 Cell Components

As contaminations and even small amounts of H_2O ($\sim$500 ppm) have shown to heavily impact the electrochemistry and performance of the two technologies, a rigorous cleaning and drying procedure of all chemicals, materials (cell + electrodes), and solvents was employed.

Cell parts were cleaned heavily and thoroughly, sonicated in soap-milli-Q H_2O, heavily rinsed with milli-Q H_2O, sonicated in milli-Q H_2O, rinsed three consecutive times with isopropanol (Sigma-Aldrich, IPA) and acetone (Sigma-Aldrich), and dried in vacuum at 110^{o}C.

XC72, carbon black, cathodes (Vulcan XC72, Cabotcorp, GA) were prepared by air spraying carbon/PTFE slurry onto 316SS 100 mesh (TWP, Inc., Berkeley, CA). The slurry was prepared by mixing Vulcan XC72 and PTFE (Sigma-Aldrich) in a 3:1 wt/wt % ratio in IPA and milli-Q H_2O, which were sonicated for 30 min and homogenized for 5 min using an IKA mixer. A Badger model 250 air-sprayer was used to spray the slurry onto the stainless steel mesh, which had been rinsed with IPA and acetone and dried at 150^{o}C. The air sprayed mesh was air-dried and 18 mm disks (for the EL-cell) were punched out, rinsed with IPA and acetone, and dried at 150^{o}C under vacuum for 12 hrs. When the cathodes were transferred to the glovebox, they were stored on a 200^{o}C hot plate. The loadings varied depending on the study, but typical loading were 10-15 mg for an 18 mm disk electrode. P50 (Avcarb, fuelcellstore) cathodes were rinsed with IPA and acetone, dried at 150^{o}C under vacuum for 12 hours and also stored on a 200^{o}C hot plate.

Three types of separators were used in this work; Whatman glass fiber QM-A or GF/A or Celgard 2500. Separators were punched to the desired dimensions, washed in IPA and acetone and dried at 110^{o}C in vacuum. In the glovebox they were stored on a 200^{o}C hot plate.

Lithium (HongKong Wisdom Tech Company) was punched in the desired size and used as received. The lithium is shown in Figure 4.7a. Sodium (Galliumsource) was cut clean as it was covered by a white coating (likely NaOH and Na_2CO_3), a piece was placed between two Celgard separators and was rolled flat, and punched to the desired size.

For the Li-O_2 system, a 1 M bis(trifluoromethane)sulfonimide lithium salt (LiTFSI, Sigma-Aldrich or BASF) in 1,2-dimethoxyethane (DME, BASF) was used. The water content of this electrolyte (LiTFSI from Sigma-Aldrich) was investigated using the conventional three-electrode cell and with an Au disk electrode and it was seen from cyclic voltammograms that the potential window of the electrolyte solution decreased significantly when undried LiTFSI was used as the supporting electrolyte, due to water contamination. A series of drying procedures of the LiTFSI salt were tested and 180^{o}C drying in vacuum was sufficient to reduce the water contamination significantly as indicated by the decreased currents and increased potential window, as shown in Figure 4.7c. DME was dried using 4 Å molecular sieves (Sigma-Aldrich), as shown in Figure 4.7, which were regenerated at 275^{o}C in vacuum prior to being soaked in DME for several days.
The 1 M LiTFSI-DME electrolytes produced from LiTFSI from BASF, contained less than 30 ppm H_2O, determined by Karl-Fisher titration at UC Berkeley. The electrolyte used for Na-O_2 studies was 0.5 M sodium trifluoromethanesulfonate (Sigma-Aldrich) in DME, which was used as received.

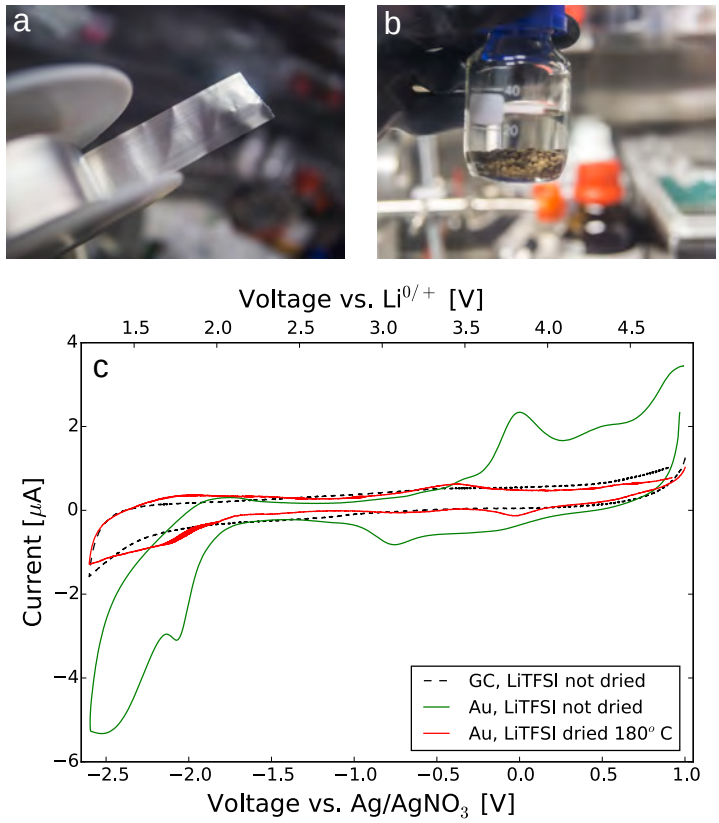

Figure 4.7: (a) Lithium (b) DME with 4 Å molecular sieves (c) Cyclic voltammograms using the conventional three-electrode cell with an Au and GC WE in 1 M LiTFSI from Sigma-Aldrich in DME. The experiments were conducted in Ar inside the glovebox. Adapted from **paper I**.

Summary of Results and Discussion

5

5.1 A Redox Probing Study of the Potential Dependence of Charge Transport Through Li_2O_2

In **paper I**, an extensive redox probing study of the electron conduction through thin, continious, and dense Li_2O_2 layers on glassy carbon electrodes was studied. Here, the potential dependence of the attenuation of charge-transfer through Li_2O_2 layers that was deposited on GC disk electrodes was studied using three different outer-sphere redox shuttles. This corresponds to probe Li_2O_2 at three different potentials. The selected redox shuttles were cobaltocene/cobaltocenium ($[Co(Cp)_2]^{0/+}$), decamethylferrocene/decamethylferrocenium ($[Fe(DMCp)_2]^{0/+}$), and ferrocene/ferroceniuim ($[Fe(Cp)_2]^{0/+}$). These redox shuttles were used as they ensure that a wide potential window could be probed relative to the valence band (VB) and conduction band (CB) of the wide bandgap of Li_2O_2. The bandgap of Li_2O_2 has been estimated to lie within 5.15-6.37 eV [99] and as VB of Li_2O_2 is only $\sim$0.4 V higher than the Fermi level [100] (E_F); CB must therefore lie at very high energies vs. $Li^{0/+}$, as sketched in Figure 5.1.

The alignment of VB relative to the $Li^{0/+}$ potential is based on the potentials suggested in refs. [22, 100] where the VB is pinned. Therefore, electron conduction is extremely unlikely. Even electron polarons, which are $\sim$2 eV below CB have very high barriers to diffusion and cannot conduct charge readily [101]. Hence, experiments with $[Co(Cp)_2]^{0/+}$ and $[Fe(DMCp)_2]^{0/+}$ probe the conduction path of holes, either by hole tunneling or via localized hole polarons [102], since their potentials are deep inside the bandgap of Li_2O_2, while $[Fe(Cp)_2]^{0/+}$ is inside VB where some other resistive conduction dominates. In principal, both hole tunneling and hole polaron hopping can coexist for charge transport [22]. However, the dominant effect estimated theoretically is a modest reduction in the tunneling current due to the localized holes in the tunneling regime [100].

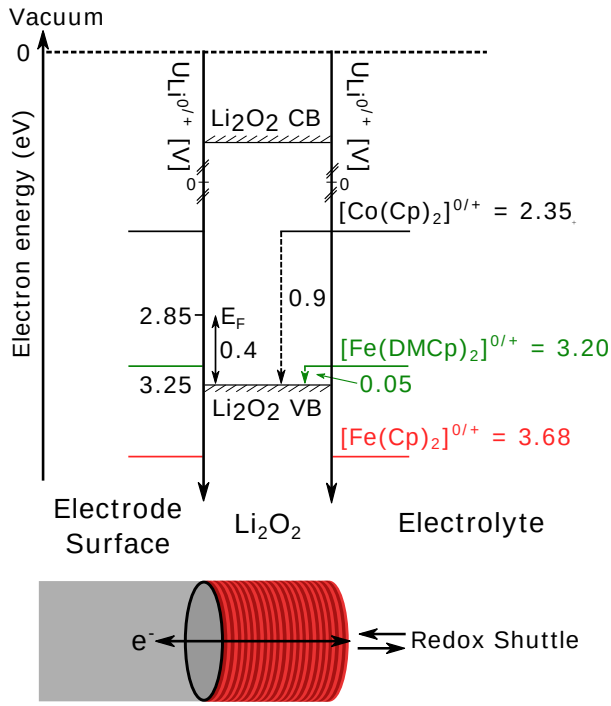

Figure 5.1: A sketch of the electronic structure for Li_2O_2 relative to the energy levels of the three redox shuttle pairs, which were determined from the $E_{1/2}$ calculated from measured cyclic voltammograms, are depicted. The charge-transfer process across the Li_2O_2 has been illustrated analogously to a metal-insulator-metal junction and shows the hole tunneling barriers for $[Co(Cp)_2]^{0/+}$, $[Fe(DMCp)_2]^{0/+}$ as 0.9, and 0.05 V, respectively, while $[Fe(Cp)_2]^{0/+}$ is inside the valence band with an $E_{1/2}$ of 3.68 V. When the charge-transfer process through Li_2O_2 is investigated the potential of the electrode is held at $E_{1/2}$ of the redox shuttle, which is illustrated with energy levels on the "electrode surface" side. The equivalent experimental setup of the sketch is illustrated in the bottom of the figure. Adapted from **paper I**.

The experimental setup used was the conventional three-electrode setup that is described in section 4.1 and it contained three GC electrodes, on which the Li_2O_2 was deposited. The electron transfer from the redox shuttle in solution through the deposited Li_2O_2 and to the electrode surface was studied by quantifying the heterogeneous rate constant (k^0) using eq. 3.19. Therefore, the precise values of C_{ox} and C_{red} were needed and prior to studying the charge-transfer through Li_2O_2, the reversibility, half-wave potentials ($E_{1/2}$), and D_i of each redox shuttle were determined as these were needed to quantify k^0. Cyclic voltammetry was used to determine D_i of the redox shuttles, as described in section 3.2, and a cyclic voltammogram of the three shuttles is illustrated in Figure 5.2.

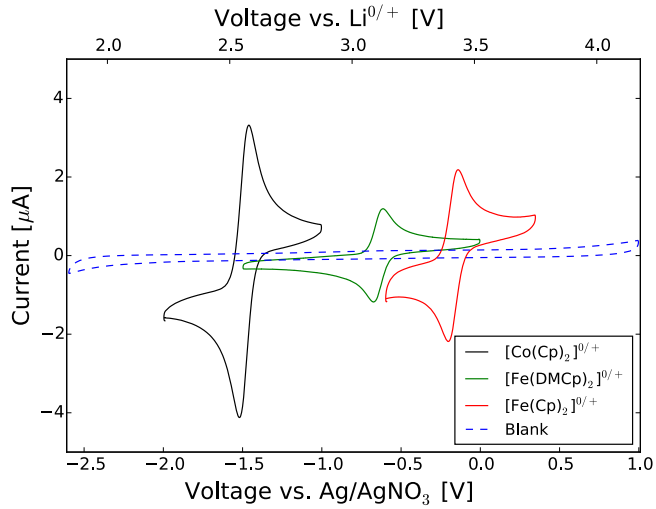

Figure 5.2: Cyclic voltammograms recorded at a scan rate of 100 mV/s of the three different redox shuttles: $[Co(Cp)_2]^{0/+}$, $[Fe(DMCp)_2]^{0/+}$, $[Fe(Cp)_2]^{0/+}$, and including a blank scan. All four voltammograms where recorded in Ar saturated 1 M LiTFSI-DME and have been IR corrected. Note, that only one of the redox shuttles was present in solution at any given time. Adapted from **paper I**.

The diffusion coefficients of the redox shuttles were determined by the Randles-Sevcik relationship (eq. 3.4) and resulted in D_i in the range of (5-8)$\cdot 10^{-6}$ for all six probes, due to their relatively similar size. All positively charged forms displayed lower values compared to their respective neutral forms due to the increased drag from the $TFSI^-$ counter-ion cloud of the electrolyte making the diffusion of the positively charged species diffusion slower. The lowest diffusion coefficients were observed for $[Co(Cp)_2]^{0/+}$ that was approx. 18 % lower than that of $[Fe(Cp)_2]^{0/+}$, which is in line with observations made in ionic liquids reported by Rogers et al. [103]. The diffusion coefficients of the presented redox shuttles has not previously been reported in 1 M LiTFSI-DME, but the diffusion coefficient of $[Fe(Cp)_2]^0$ aligns into a power decay relationship vs. the viscosity, supporting the validity of the determined values (Figure 5 in **paper I**).

The investigation of the limiting charge transport mechanism as a function of the Li_2O_2 thickness was done by determining the charge-transfer resistances (R_{CT}) of the redox shuttles by EIS. The GC electrodes were therefore coated with various thicknesses of Li_2O_2 layers prior to the impedance measurements by a series of galvanostatic discharges on different GC electrodes. The Li_2O_2 coated GC electrode surfaces were probed by EIS in Ar atmosphere at $E_{1/2}$ of each of the redox shuttles. The R_{CT} was determined by fitting a Randles equivalent circuit to the data that, as described in section 3.4, describes a heterogeneous charge-transfer and semi-infinite linear diffusion. The resulting Nyquist-, and Bode plot, and the equivalent circuit model used, are shown in Figure 5.3 for a single electrode probed by $[Co(Cp)_2]^{0/+}$.

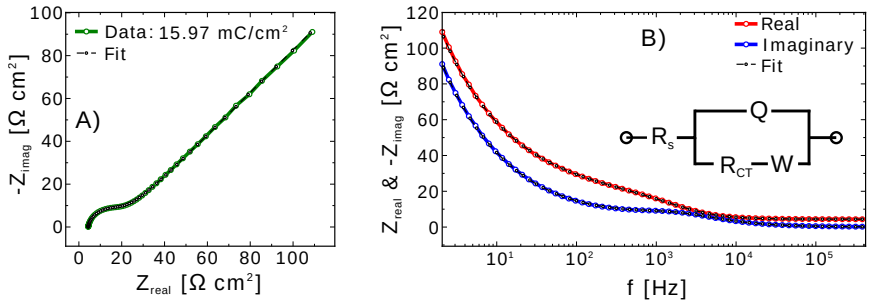

Figure 5.3: (A) Nyquist plot and (B) Bode-like plot for the terminal discharge capacity of 15.97 mC/cm^2 with $[Co(Cp)_2]^{0/+}$ in solution. The equivalent circuit used to model and extract R_{CT} is inserted into (B). Adapted from **paper I**.

To illustrate the dependency of charge transport mechanism as a function of depth-of-discharge ($\sim Li_2O_2$ thickness), k^0 was determined using eq. 3.19 for electron exchange between the glassy carbon electrode and the different redox shuttles in solution with Li_2O_2 sandwiched in between (Figure 5.1). The resulting plot of k^0's as a function of depth-of-discharge and Li_2O_2 thickness is shown in Figure 5.4 and here the redox shuttles acted as a charge source/sink, Li_2O_2 as the insulator, and the GC electrode as the charge source/sink.

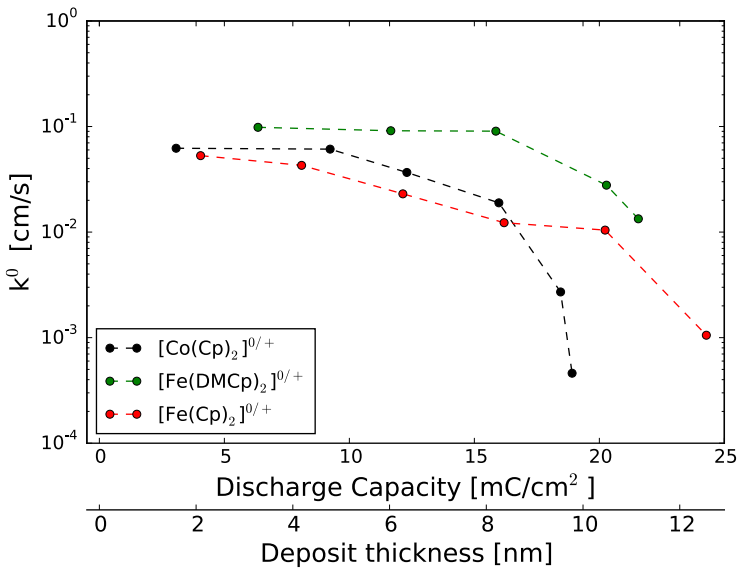

Figure 5.4: The heterogeneous rate constant illustrated as a function of discharge capacity and Li_2O_2 thickness (the thickness was calculated assuming that the Li_2O_2 grows as a dense thin film and that the surface roughness of the electrode was a factor of 2). The k^0's were calculated from R_{CT} obtained from the EIS. The three redox shuttles were probed at their respective $E_{1/2}$ in Ar, *e.g.* $[Co(Cp)_2]^{0/+}$ at 2.35 V, $[Fe(DMCp)_2]^{0/+}$ at 3.2 V, and $[Fe(Cp)_2]^{0/+}$ at 3.68 V vs. $Li^{0/+}$. Adapted from **paper I**.

For $[Co(Cp)_2]^{0/+}$ and $[Fe(DMCp)_2]^{0/+}$ an exponential decrease in k^0 with discharge capacity is observed that mirrors the exponential sudden-death in the Li-O_2 with discharge capacity. This shows that the origin of the sudden-death is due to charge transport limitations. Since $E_{1/2}$ of $[Co(Cp)_2]^{0/+}$ and $[Fe(DMCp)_2]^{0/+}$ both are inside the bandgap of Li_2O_2, as illustrated in Figure 5.1, electronic conduction is likely dominated by a mechanism of hole transport. This transport could be via tunneling [22, 33] or via thermally excited hole polarons [22, 100, 104, 105, 106]. It is suggested that tunneling is the dominant mechanism of hole charge transport in the experiments reported here since relatively high current densities are involved in the impedance measurements (> 9 μA/cm^2), and since this mechanism fits a wide range of experimental results *e.g.* the existence of discharge sudden-deaths and its dependence on current and temperature, asymmetry between discharge and charge sudden-deaths, etc. [11, 22]. One feature that should be noted in Figure 5.4 is the difference in Li_2O_2 thickness/capacity between $[Co(Cp)_2]^{0/+}$ and $[Fe(DMCp)_2]^{0/+}$, with an extended discharge capacity for $[Fe(DMCp)_2]^{0/+}$. This difference is interpreted due to the very different hole transport at 0.9 and 0.05 V relative to the VB, respectively.

The results of Figure 5.4 were compared with a simple semi-classical tunneling model of charge transport and based on assuming trapezoidal barrier shapes (Figure 10 of **paper I**) [22]. The model and the experimental results are qualitatively consistent; suggesting that hole tunneling dominates the process. It is anticipated that if hole polarons were the dominant charge transport mechanism, there should be much larger differences between the $[Co(Cp)_2]^{0/+}$ and $[Fe(DMCp)_2]^{0/+}$ capacities (at which the charge-transfer attenuation becomes significant) since the polaron population and hence conductivity depends exponentially on the energy of the polaron relative to the VB. Since the bulk polaron energy is required to be the same as the electrochemical Fermi energy, *i.e.* the $[Co(Cp)_2]^{0/+}$ and $[Fe(DMCp)_2]^{0/+}$ redox potentials, we would anticipate significantly larger differences. Of course, band bending at the interfaces of the thin films could lessen this effect [106].

In conclusion, these results were interpreted as a reflection of that the exponential decay of k^0 is a result from different hole tunneling barriers highest at which the charge-transfer through Li_2O_2 was probed, hence the smaller the hole tunneling barrier height (or the greater the polaron/hole conductivity), the greater the thickness at which significant attenuation of the heterogeneous exchange rate takes place. The findings reported in **paper I** thus further confirm that sudden-death in the Li-O_2 battery occurs when the charge transport through Li_2O_2 no longer can support the applied electrochemical current.

5.2 An EIS study of the Capactiy Limitations in Na-O_2 Cells

In **paper III**, the charge-transfer resistance and surface capacitances in the Na-O_2 battery was investigated by applying electrochemical impedance spectroscopy to operating Swagelok cells. These results were combined with pressure change measurements (section 3.6) and scanning electron microcopy (SEM) of discharged cathodes to understand the mechanisms of sudden-death that occurs on both discharge and charge. To interpret the impedance, the porous electrode theory model (PET) described in section 3.4 was applied. The PET model includes information about the ionic resistance within the pores of an electrode (R_i) the charge-transfer resistance related to the reaction on the electrode surface (R_{CT}) and the effective surface capacitance $\left(C_{eff}\right)$ and a sketch of model used for this paper is illustrated in Figure 3.9.

To validate the use of the applied PET model, the approach suggested by Lasia and others [74, 76, 91] was used, as the impedance of the cell was measured at open circuit voltage (OCV) and in an Ar atmosphere, *i.e.* in the absence of Faradaic reactions in the porous cathode (Figure 5.5a-b). In Ar, the cell exhibited a high frequency semicircle that is related to the charge-transfer on the Na-anode (Figure 5.5b). At low frequencies, a capacitive behavior was observed from the cathode. The capacitance of the cathode was determined to be 4.1-5.0 μF/cm^2 from fitted EIS spectra. However, between the high frequency semicircle of the sodium anode and the low frequency capacitive cathode response, a linear region was observed (Figure 5.5a-b). This region is strongly dependent on the thickness of the cathode (L) and is observed to increase as L is increased by stacking multiple cathodes together. This linear region is a characteristic of the ionic resistance (R_i) inside the porous structure of the cathode (Figure 3.9) and the observed presence and thickness dependence of this linear region strongly indicates that the impedance is dominated, at mid-frequencies, by the porous nature of the P50 cathode. A similar approach has been used by refs. [74, 79]. This dependency clearly suggests that the PET model gives a physically meaningful parameterization of the cathode impedance for cells used in this study.

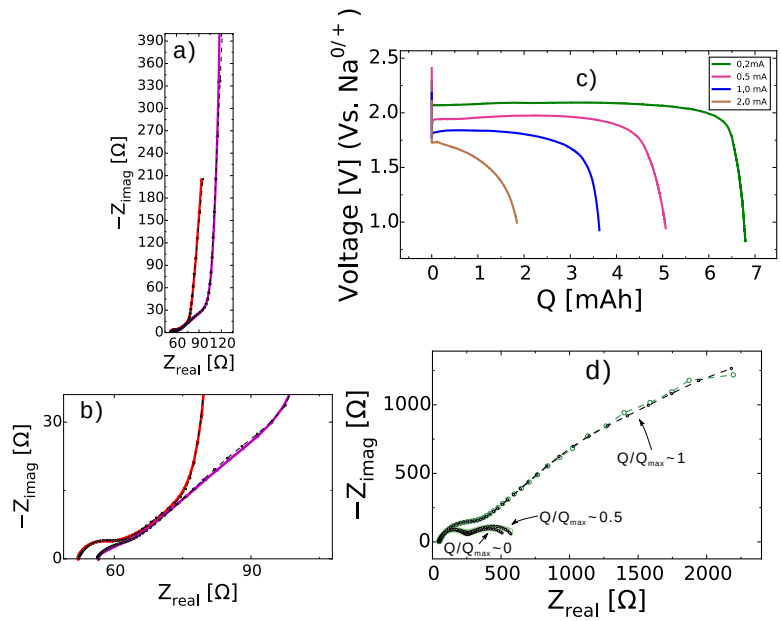

Figure 5.5: (a) Cell impedance in Ar and at OCV of two Na-O_2 cells, where the red curve is a cell with one P50 cathode while the purple curve is a cell with three stacked P50 cathodes. The black dotted lines shows the best fits to the equivalent circuit model: -$(RQ)_{Na}$-PET(Q)- (b) Magnification of (a) where the high-frequency process of the sodium anode is seen, denoted -$(RQ)_{Na}$- in the model, (c) Galvanostatic discharge curves in 0.5 M NaOTf-DME operated under a pressure of O_2 (∼1000 torr) at 0.2, 0.5, 1.0, and 2.0 mA (12 mm P50 cathode diameter). (d) The Nyquist plot of the 0.2 mA discharge with three curves illustrating the impedance at Q/Q_{max}∼ 0, 0.5, and 1. Adapted from **paper III**.

The mechanisms controlling the sudden-death on discharge were studied by galvanostatic discharges at 0.2, 0.5, 1.0 and 2.0 mA under constant pressure of O_2 (∼1000 Torr) as shown in Figure 5.5c. EIS was measured throughout each discharge as illustrated for the 0.2 mA discharge in Figure 5.5d while Nyquist and Bode plots for all current densities can be found in Figure S1 of **paper III**. The fitted impedance parameters, R_{Na}, R_{CT}, R_i, and C_{eff}, are shown in Figure 5.6 for the four current densities. At all discharge currents, NaO_2 crystals are deposited on the cathode surface, as previously reported [56], and an electron count of 1.03-1.08 e^-/O_2 is observed from experiments with cells discharged under a closed headspace using otherwise identical conditions (Figure S2 of **paper III**). At lower discharge currents, 0.2-0.5 mA, R_i dominates the cell impedance throughout the discharge until sudden death while R_{CT} dominates the cell resistance throughout the discharge at higher currents, 1.0-2.0 mA (Figure 5.6). The capacitance of the active cathode surface (C_{eff}), which at lower currents, 0.2-0.5 mA, decreases gradually from an initial value of ∼4.5 μF/cm^2, determined at OCV in pristine cells, to 0.29-0.43 μF/cm^2 at sudden-death. At higher currents, 1.0-2.0 mA, the capacitance immediately drops to a plateau of 0.35-0.37 μF/cm^2.

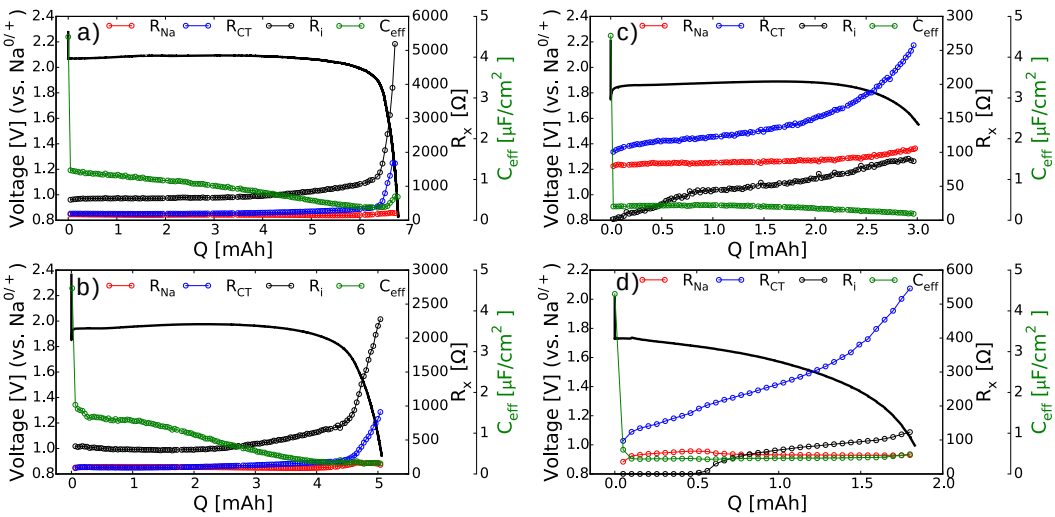

Figure 5.6: Galvanostatic discharge curves of (a) 0.2 mA (b) 0.5 mA, (c) 1.0 mA, and (d) 2.0 mA, which were operated under at a constant pressure of O_2 (∼1000 Torr). The output resistances from the impedance fits are plotted on the two secondary axes marked R_x while the output C_{eff} is plotted in green belongs to the third green axis. The initial C_{eff} value of the carbon cathode (∼4.5 μF/cm^2) was obtained at OCV from Figure 5.5a. Adapted from **paper III**.

The double-layer capacitance of the cathode would be expected to significantly decrease if the surface is coated by a thin film of NaO_2 already at film thicknesses of few nanometers as NaO_2 is a poor electronic conductor [61] and has a low dielectric constant (4.5 [62]). The observed nearly immediate decrease in capacitance upon discharge at higher currents, 1.0-2.0 mA, suggests that the cathode surface is immediately covered by a NaO_2 film at these conditions. SEM images of cathodes discharged to 1.0 V vs. $Na^{0/+}$ shown in Figure 5.7, further shows that a NaO_2 film has formed at these currents, and SEM images of cells discharged to lesser capacities also indicate a thin NaO_2 film has deposited on the electrode surface in be-

tween the larger cubic crystals. At lower currents, 0.2-0.5 mA, the SEM images (Figure 5.7) show that a predominant part of the discharge product formed as cubic NaO_2 crystals, with a thin NaO_2 film covering the electrode surface in-between the larger crystals. The gradual decrease in C_{eff}, observed at these lower currents, (Figure 5.6) also suggests that the rate of surface coverage by NaO_2 is slower. A reasonable explanation of these observations is that as NaO_2 crystals grow, parts of the cathode remains uncoated or gets covered by a thin, possibly porous, NaO_2 film that allows for continued oxygen reduction and consequent NaO_2 crystal growth. Therefore, as the crystals grow and gradually cover the surface, C_{eff} slowly decreases. The differential resistance, at these currents, is dominated by the ionic resistance (R_i) indicating that NaO_2 takes up some part of the pore volume within the porous cathode, which is in agreement with the SEM images that show the presence of a large amount of 3-10 μm NaO_2 crystals at sudden death. R_{CT} also increases dramatically at sudden-death suggesting that the surface is becoming completely blocked by NaO_2, in the form of NaO_2 cubes and/or in the form of a continuous NaO_2 thin film of sufficient density and thickness to be completely blocking to further oxygen reduction.

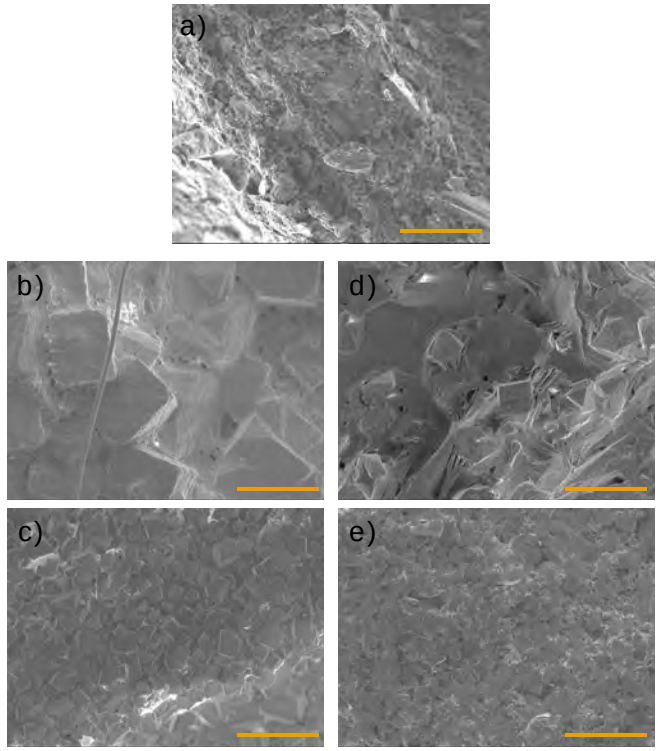

Figure 5.7: SEM images of (a) a pristine P50 cathode and P50 cathodes discharged to 1.0 V vs. $Na^{0/+}$ at (b) 0.2 mA (6.29 mAh), (c) 0.5 mA (4.51 mAh), (d) 1.0 mA (3.79 mAh), and (e) 2.0 mA (2.58 mAh). The scale bar is 10 μm. Adapted from **paper III**.

The origins of the voltage profiles on charge were investigated by galvanostatically discharging cells at 1 mA to 3 mAh and subsequent charging at 0.2, 0.5 and 1 mA while EIS continuously was measured (full description given in SI of **paper III**) at short intervals through-

out discharge and charge. The corresponding Nyquist and Bode plots obtained during charge are shown in Figure S3 of **paper III** and Figure 5.8 shows the evolution of the impedance parameters obtained from the fits of the equivalent circuit to the experimental data. At the beginning of the three charge experiments, the cathode surface was, at 3 mAh, covered by NaO_2 (Figure 5.7). R_{CT} dominates the cell impedance throughout the charge experiments (Figure 5.8); it dramatically increases near sudden death; and decreases with increasing charging currents. R_i initially decreases and reaches a plateau at all currents while C_{eff} displays a rapid linear increase initially, the slope of which depends on the current density. After some time the slope of C_{eff} variation, which occurs earlier the greater the charging current is, and finally reaches a plateau. It is speculated that the reason for the change in C_{eff} slope is related to complete removal of the thin conformal NaO_2 film on the electrode surface, while the larger NaO_2 crystals still remain on the surface at that point during charge. It is important to also note that the charges were halted by short-circuiting due to the penetration of Na dendrites through the separator, influencing the cycle efficiency negatively. Prior to this in each case the cell potential increased showing that the initial state of sudden-death on charge was reached.

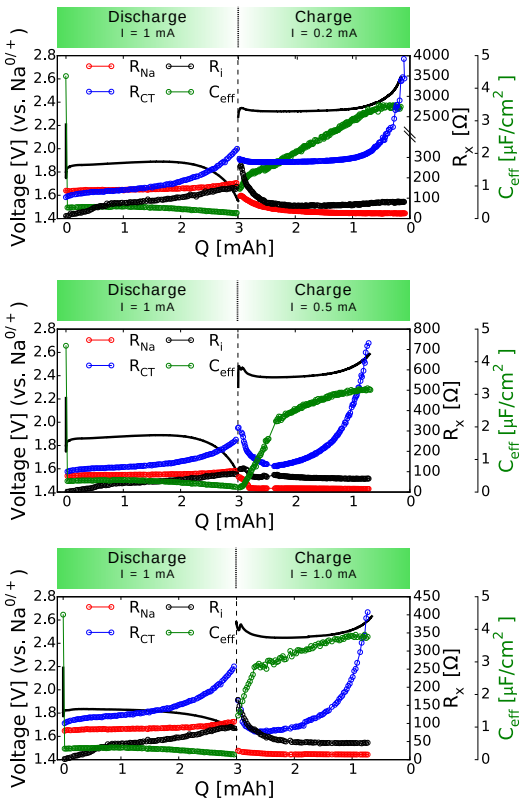

Figure 5.8: The galvanostatic discharges and charges of Na-O_2 cells that were discharged at 1 mA to a capacity of 3 mAh at ~1000 Torr of O_2 and subsequently charged at 0.2 mA, 0.5 mA, and 1.0 mA. The parameters on the two secondary axes are from the impedance fits where the equivalent circuit: -$(RQ)_{Na}$-PET(RQ)- was used. The initial C_{eff} value of ~4.5 μF/cm^2 reported at Q = 0 mAh was determined at OCV from Figure 5.5a. Adapted from **paper III**.

The charge-transfer resistance yields the dominating contribution to the overpotential of the positive electrode on the charging plateau. The decrease of R_{CT} with increasing current density is interpreted as a reflection of the curvature of the current-voltage curve. For a reaction obeying Butler-Volmer type kinetics (kinetic control) a decreasing R_{CT} with increasing overpotential would be expected, as R_{CT} reflects the slope of the current-voltage curve. At very early stages of charge, the initial rapid increase in C_{eff} from $\sim$0.4 μF/cm^2 to 2.15-2.84 μF/cm^2, depending on current rate, could indicate that most of the NaO_2 oxidation, in this region, occurs as removal of the NaO_2 film by exposing some of the conductive carbon cathode surface to the electrolyte. The following monotonous increase in C_{eff} indicates a gradual unblocking of the electrode surface during charge due to continuous oxidation of NaO_2 crystals, mediated by a solution mechanism, would lead to a gradual decrease in the crystal size. The ionic resistance (R_i) is observed to decrease during charge, most likely reflecting that larger NaO_2 crystals are removed from the pore volume in the cathode. At the end of charge, C_{eff} reaches a plateau at 3.11-3.77 μF/cm^2, depending on the current rate, and R_{CT} also dramatically increases. As the final C_{eff}'s after charge are lower than the initial value of a pristine cathode ($\sim$4.50 μF/cm^2), it suggests that some solid NaO_2 still remains on the surface of the cathode, possibly the larger NaO_2 crystals that have not yet been completely dissolved and/or that other low dielectric constant products (*e.g.* sodium carbonates) have accumulated on the electrode surface and blocks soluble NaO_2 oxidation. R_{CT} rapidly increases at sudden-death on charge and is therefore likely a reflection of the depressed amount of dissolved NaO_2 in the electrolyte near the cathode surface as a consequence of the decrease in the amount of remaining solid NaO_2 at the cathode/electrolyte interface, which may have the consequence that an increasing fraction of the oxidation current is due to direct oxidation of NaO_2.

Cell failure, in the presented cells, was caused by short circuits as dendrites formed through the glass fiber separators upon charge. This has previously also been reported by Hartmann et al. [55] and is an issue that limits cycle life. The solid electrolyte interphase (SEI) of the sodium anode, in non-aqueous electrolytes has been observed to be partly soluble, hence decreasing the Na/electrolyte interface stability [43]. The observed decrease in R_{Na}, a concurrent continuous increase in C_{dl}^{Na} and an initial drop in the exponent n of the Q equivalent circuit element indicates that the Na metal surface roughens or that sodium dendrites form during charge, as shown in Figure 5.9. The instability of the sodium anode is further demonstrated by monitoring the cathode and anode potential in relation to a third sodium reference electrode in the EL-cell, where the largest overpotential in the plateau region is accounted for by the ($\sim$250 mV) anode and not the cathode (10 mV), as illustrated in Figure S4 of **paper III**.

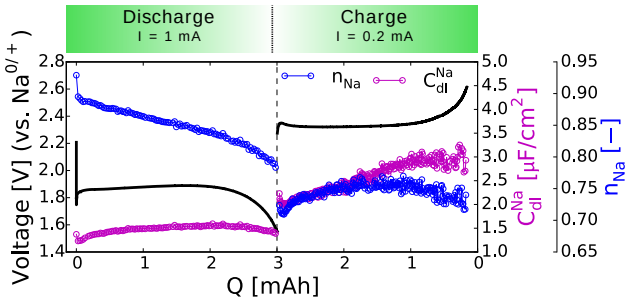

Figure 5.9: The *same* galvanostatic discharge and charge as of Figure 5.8a. Here the double-layer capacitance of the sodium anode is plotted versus the capacity. The exponent of the constant phase element, n, that is used to model the double-layer capacitance of the sodium anode is plotted in blue and the effective double-layer capacitance of the sodium anode under operation is plotted in purple. Adapted from **paper III**.

In summary, electrochemical impedance spectroscopy-, pressure change-, and SEM results are presented that show the degree to which mass transport or kinetic losses dominate the internal resistance of the porous carbon electrode at different stages of discharge and charge in Na-O_2 cells. The results show that the discharge impedances are highly dependent on the current density. At higher current densities, the surface capacitance indicates that NaO_2 immediately covers the surface of the cathode as some form of, possibly porous, NaO_2 film is formed initially. Cubic NaO_2 crystals are observed after discharge at all current densities investigated here. The size of the crystals increases with decreasing discharge currents. At lower discharge current densities, the gradual decrease of the cathode surface capacitance indicates that the cathode surface is coated gradually with NaO_2, probably reflecting that the surface is blocked by growth of cubic crystals of NaO_2 on the electrode with a continuous NaO_2 film stretching in-between at sudden-death as visible from SEM images. The NaO_2 crystals become smaller and more of the deposit appears as a continuous film as the discharge current increases. Interestingly, the cathode surface capacitance decreases very rapidly upon discharge at high current, indicating that much more of the electrode surface is covered with a low dielectric constant product (NaO_2) at an early stage of discharge consistent with formation of some kind of thin film. Considering that the discharge can proceed long after this film is formed, and factoring in that NaO_2 has a very low electronic conductivity, this may be an indication that the film formed at short times at high discharge currents is porous in nature. On charge, three regions could be identified. Initially, a large part of the NaO_2 film is oxidized and removed from the cathode surface; secondly, the NaO_2 crystals are dissolved and oxidized and as the crystals decrease in size more of the initial carbon/electrolyte interface is regained; and lastly, the potential and R_{CT} dramatically increases, possibly due to a decreased amount of dissolved NaO_2 in the electrolyte near the cathode surface.

5.3 An EIS study on the Effects of the Surface- and Solution-Based Mechanisms in Li-O_2 Cells

In **paper II**, the influence of activating the solution-based mechanism was studied to identify limiting processes of the operating cells. The experiments were carried out using the three-electrode battery cell (EL-cell, section 4.3) to separate the total cell impedance into separate contributions from the cathode and anode, respectively. The work was based on the conventional porous electrode model, described in section 3.4, to parameterize the impedance of the porous carbon cathode. This allows characterization of the surface impedance, and thus the charge-transfer resistance of the oxygen reduction reaction, along with the ionic conductivity inside the pores of the electrode, which here was studied as a function of the electrolyte composition. Note that this work incorporates the same porous impedance model as in section 5.2, but these experiments were conducted in the EL-cell whereas those of section 5.2 were conducted in two electrode Swagelok cells. This means that none of the cathode impedance that is presented in the following arises from the Li anode.

The dependency between discharge capacity and the composition of the electrolyte is shown in Figure 5.10a, where three types of electrolytes were investigated. The discrepancy in capacity is ascribed to activation of the solution-based mechanism (Figure 2.4b). The increased capacity of $LiNO_3$ containing cells was first reported by Burke et al. [35] to be the consequence of an increased donor number of the electrolyte, as Li^+ ions are shielded by the NO_3^- counter-ion, thereby inducing an increased stability of Li^+ in solution, which shifts the equilibrium of LiO_2 solvation and - promote the solution-based Li_2O_2 formation mechanism. The same solution-based mechanism enhancement has been reported for H_2O containing cells, where H_2O is postulated to behave as a strong Lewis acid, thereby increasing the acceptor number of the electrolyte and stabilizing O_2^-, which again allows Li_2O_2 formation through the solution-based mechanism [23]. In both cases, large toroid shaped Li_2O_2 deposits form, and on the basis of the impedance results it is proposed that toroids form through the solution-based mechanism in Figure 2.4, allowing higher discharge capacities compared to an all-surface-based mechanism, as in the 1 M LiTFSI-DME cell, where no toroid formation is observed, indicating that only a thin, conformal, and dense Li_2O_2 film is formed on the cathode surface.

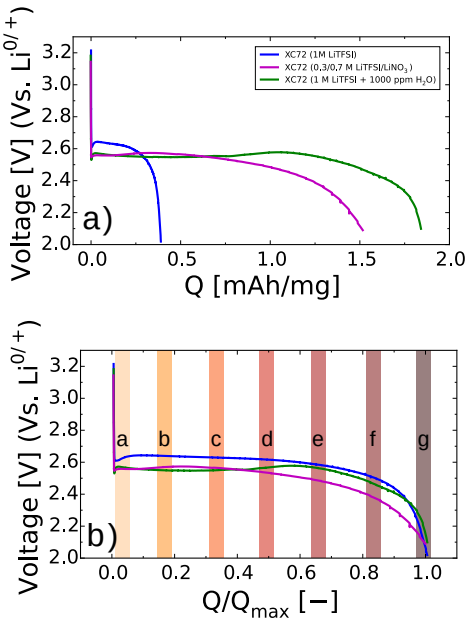

Figure 5.10: (a) Galvanostatic discharge curves for the three XC72 cells with varying electrolyte. (b) The equivalent normalized discharge curves. The partial pressure of O_2 was kept constant at ∼1050 Torr throughout the discharges.

The EL-cell was exclusively used in this study as it allows the impedance to experimentally be measured simultaneously at both electrodes throughout operation, by using the setup shown in Figure 4.6. Figure 5.11 shows the galvanostatic discharge of an 1 M LiTFSI-cell in the EL-cell vs. the reference Li electrode. The electrochemical experiments conducted in this study were exclusively carried out using a three-electrode battery cell (EL-Cell), and together with a multichannel potentiostat this allowed simultaneous measurements of the impedance of both electrodes (anode and cathode). The setup used is shown schematically in figure 4.3.

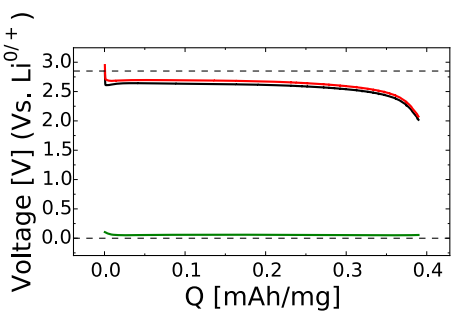

Figure 5.11: A galvanostatic discharge curve of 1 M LiTFSI-DME operated under a constant O_2 partial pressure of ∼1050 Torr. The cell was maintained at constant pressure by keeping it connected to the inlet gas line. The black curve is the cell potential; the red and green curves are the cathode- and anode potentials vs. the reference $Li^{0/+}$ electrode, respectively. The two dotted lines are the theoretical electrode potentials of the cathode and anode (0 V and ∼2.85 V) if no overpotential exists (at zero d.c. bias).

In order to investigate the cathode performance under conditions where either the surface- and/or the solution-based mechanisms are favored; three cells containing XC72 cathodes with 1 M LiTFSI-DME, 0.3/0.7 M LiTFSI/$LiNO_3$-DME, and 1 M LiTFSI-DME with 1000 ppm H_2O were investigated under galvanostatic conditions. The impedance of the cathode was therefore measured under the galvanostatic load of Figure 5.10 and corresponding Nyquist plots are shown in Figure 5.12. Here eight regions, termed a-g, are presented and corresponds to regions a-g of Figure 5.12b.

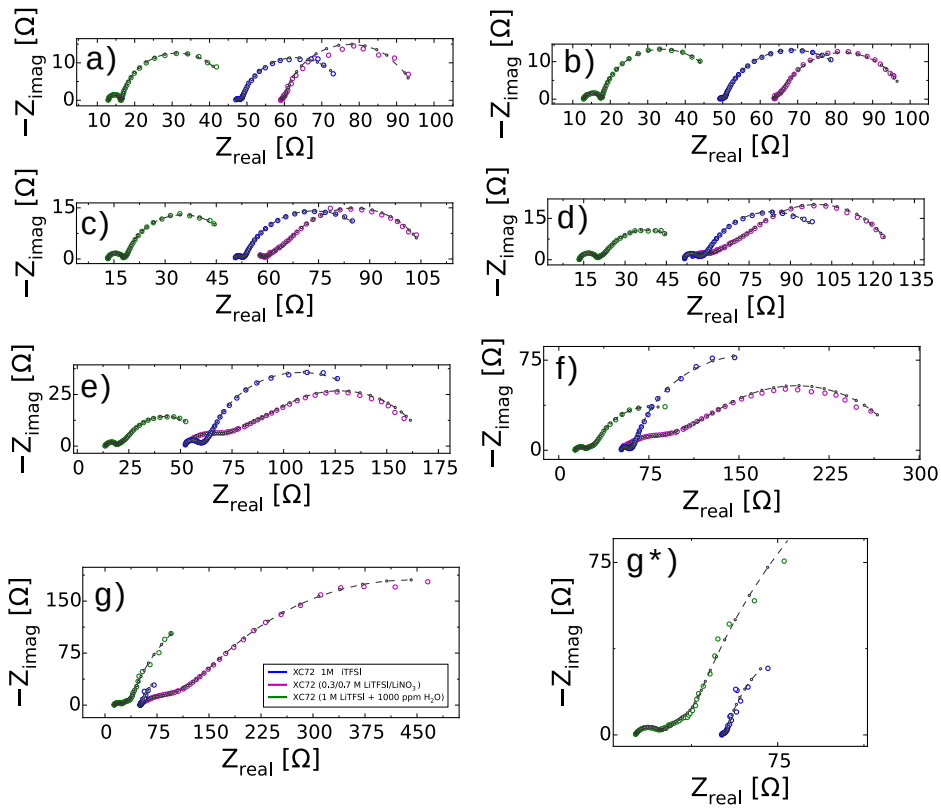

Figure 5.12: The progression of the galvanostatic impedance of the cathode as a function of state-of-discharge: The regions a-g illustrates a specific state of normalized discharge capacity as is depicted in Figure 5.10, while g*) is a magnification of the data in g).

In galvanostatic mode, the impedance measures charge-transfer processes related to the active electrochemical reactions occurring at the electrodes. Two electrochemical processes were detected on the cathode as a high frequency (HF) semicircle and a low frequency (LF) semicircle (Figure 5.12). It is assumed that both processes are related to Li_2O_2 formation as (i) an $\sim$2.0-2.1e^-/O_2 reaction was obtained from pressure measurements while discharging similar cells under a closed headspace filled with O_2 (Figure S3-S5 of the SI of **paper II**); (ii) multiple authors also have reported Li_2O_2 to be the main deposition product in these three solvents [23, 24, 36, 107]; and (iii) an impedance-study of Li-O_2, using two terminal Swagelok cells, observed the same LF semicircle in the same frequency range for 1 M LiTFSI-DME containing cells [108]. In addition, the processes could be controlled, as the impedance of

the same cells measured at OCV is fundamentally different. At OCV under either Ar or O_2, the impedance of the cathodes exhibits behavior expected of non-Faradaic processes, as no electrochemical reactions would occur in the 10 mV impedance amplitude given the modest overpotentials for the Li/O_2 reaction, as shown in Figure 5.13a.

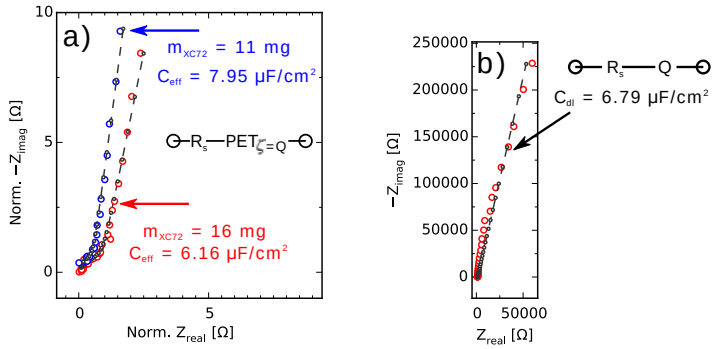

Figure 5.13: a) The impedance of two different loading of XC72 cathodes in 1 M LiTFSI-DME measured in Ar at OCV. The equivalent circuit is also illustrated, where R_s is the series resistance while the PET$_{\zeta=Q}$ is the PET model with ζ=Q, where Q is a constant phase element used to describe the capacitive nature of the porous electrode at these conditions. For easier comparison Z_{real} and Z_{imag} were normalized to start at the origin, (0,0). b) The working electrode impedance from the three-electrode cell (section 4.1) with a 1.6 mm glassy-carbon working electrode in Ar saturated 1 M LiTFSI-DME at OCV.

The linear region at high frequencies observed in Figure 5.13a confirms the use of the porous electrode model, as this linear region resulted from processes occurring in a porous electrode and the origin of a high frequency linear region is in agreement with the predicted by porous electrode theory and is in agreement refs. [74, 76, 91]. Furthermore, increasing the carbon loading increases the high frequency linear region as the pore length and R_i of the cathode is increased. The capacitance of pristine porous cathodes (XC72) were determined by fitting the equivalent circuits to the experimental data in Figure 5.13. The impedance of a flat planar glassy-carbon electrode under similar conditions, *i.e.* at OCV in Ar and without the presence of any redox active species, is shown in Figure 5.13b. The double-layer capacitance was found to be 6.79 μF/cm^2 for the planar GC electrode and 6.16-7.95 μF/cm^2 for the porous cathode (XC72) in 1 M LiTFSI-DME. From the similar double-layer capacitances of the two cathodes, it could be concluded that the areal specific carbon loading does not influence the chemical nature of the cathode processes and that indeed the ionic resistance within the pores was the cause of the high frequency linear region.

In principle, it was possible to isolate capacitive and Faradaic processes and allowing for the conclusion that any semicircles observed in Ar and at OCV (Figure 5.13) was not related to Li_2O_2 formation, while the Nyquist plot semicircles (Figure 5.12) that only were detected in galvanostatic mode under O_2 must be related to the oxygen reduction and consequently Li_2O_2 formation. In addition to the impedance of the XC72 cathode in 1 M LiTFSI-DME at OCV and in Ar (Figure 5.13), similar measurements were conducted for the $LiNO_3$ and H_2O bearing cells (Figure 5c-d of **paper II**). The $LiNO_3$ bearing cell exhibit similar response as the LiTFSI cells, however the H_2O bearing cell exhibit a HF semicircle at OCV and in Ar as H_2O is redox active even at the low potential amplitude of 10 mV.

To understand the contribution of each process of the porous electrode model to the cell performance, as well as to clarify the cause of the low frequency and high frequency semicircles; the impedance of the three cells under galvanostatic conditions were fitted using the equivalent circuit: -$(RQ)_1$-$PET_{\zeta=RQ_2}$-, where $(RQ)_1$ is the high frequency (HF) semicircle observed at 10^2-10^4 Hz and $(RQ)_2$ is the low frequency (LF) semicircle observed at 10^{-2}-10^1 Hz inside of the PET model (similar to Figure 3.9). The fitted impedance parameters are illustrated as a function of the normalized discharge capacity in Figure 5.14.

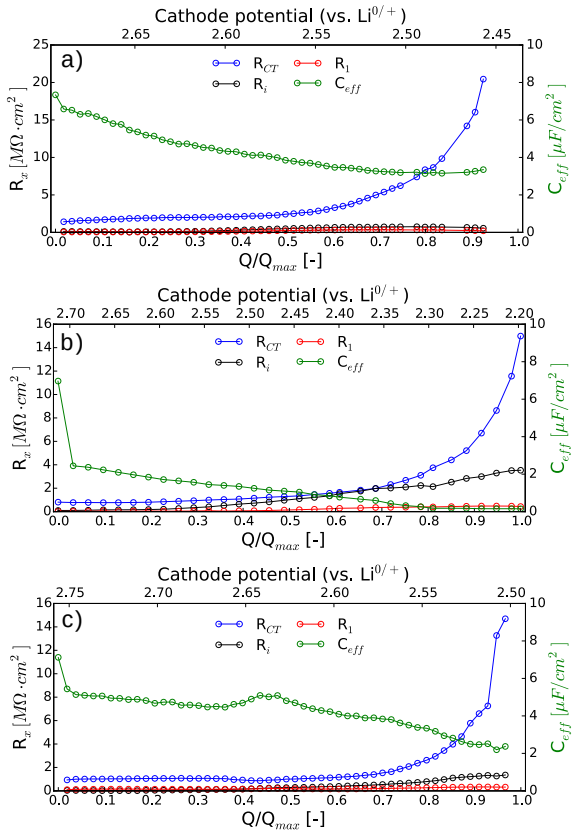

Figure 5.14: Resistances and capacitances from fitting the equivalent circuit -$(RQ)_1$-$PET_{\zeta=RQ_2}$- to the three cells: (a) 1 M LiTFSI-DME, (b) 0.3/0.7 M LiTFSI/$LiNO_3$-DME, and (c) 1 M LiTFSI-DME with 1000 ppm H_2O.

5.3.1 The LF Process

In Figure 5.12, the three cells initially display near-ideal LF semicircles in the initial region a. By relating this observation to the simulations in Figure 3.10, it is understood that the LF process is limited by R_{CT} (the surface charge-transfer resistance) in the PET model. As the state-of-discharge increases, region b-f, the LF semicircle of the three cells in general become more skewed, which the PET model ascribe to an increase in ionic resistance in the pores of the cathode, R_i, as shown in Figure 5.14. Intuitively, this increase in R_i is expected,

as the formed Li_2O_2 is insoluble in DME and accumulates in the pores, causing an increase in R_i. Near sudden-death, region g, the 0.3/0.7 M LiTFSI/$LiNO_3$ cell is significantly more skewed than the other two cells that again display more ideal semicircles. This is interpreted, using the model simulations presented in Figure 3.10, as the former cell being dominated to a larger degree by R_i, where the two latter cells are almost completely dominated by R_{CT}. Similar experiments were also conducted on flat planar GC electrodes (Figure 11 of **paper II**), which revealed that the LF semicircle was the only electrochemical process detected. The LF semicircle was detected in a similar frequency range (10^{-2}-10^{1} Hz) as in the three cells with porous XC72 cathodes. The LF semicircle is therefore suggested to be related to the surface induced formation of Li_2O_2, as Højberg et al. [108] also observed an electrochemical process in 1 M LiTFSI-DME in the same frequency range.

5.3.2 The HF Process

The 0.3/0.7 M LiTFSI/$LiNO_3$-based cell displayed an approximately four-fold discharge capacity increase while maintaining similar Li_2O_2 yields (80-90 %) compared to the other two cells [35]. Burke et al. [35] ascribe the increase in capacity to the increase in the Lewis basicity of the electrolyte with added $LiNO_3$, which results in the promotion of the solubility mechanism.

If the HF semicircle is related to the solution-based mechanism, it is expected that R_1 would be larger compared to R_1 in the 1 M LiTFSI (0 M $LiNO_3$) and the 0.3/0.7 LiTFSI/$LiNO_3$ cells, as Burke et al. [35] identified the LiTFSI/$LiNO_3$ ratio to provide the largest capacity enhancement. In fact, the R_1 was detected to a much larger degree in the cell with 0.3/0.7 M LiTFSI/$LiNO_3$ relative to the two former cells. This may indicate that the resistance associated with the HF semi-circle is the Faradaic charge-transfer resistance of the solution-based mechanism, reaction [α] in Figure 2.4b, but as the HF semicircle also was detected throughout the discharge in the water-containing cell (Figure 5.12) and in Ar and at OCV for this cell (Figure 5c-d in **paper II**); this suggests otherwise. Determining the double-layer capacitance of the HF process, for these two cells, yields area specific capacitance values of 10-50 μF/cm^2 during discharge, pointing to that the HF process likely occurs at the current collector / electrode interface. Therefore it is most likely a concurrent reduction of H_2O (in the case of the cell tested under Ar with water added to the electrolyte), or O_2 and/or NO_3^- reduction taking place at the current collector in the cases where it is observed under an O_2 atmosphere. The HF semicircle was even observed in the 1M LiTFSI cell, where neither H_2O nor $LiNO_3$ should be available. It is suspected that minor water impurities likely contribute to the HF semicircle observed in the 1M LiTFSI cell and to this end, electrolytes were used as received and contained $\sim$25 ppm H_2O as determined via Karl Fischer titration, and although the cathodes used in this study were dried at 200^{o}C in a glovebox, their high surface area porosity could retain small amounts of water. however, note that the magnitude of the HF process is small in the 1M LiTFSI cell and disappears completely as a function of state-of-discharge (Figure 5.12 and 5.14), which possibly could be ascribed to water being consumed at the Li metal anode. However O_2 reduction on the current collector surface could just as likely be ascribed to the HF process.

5.3.3 Rate Limiting Steps

The parameters obtained from the impedance fit are shown in Figure 5.14 describes the cell performance under operation. The three cells can be compared until ∼90 % of the normalized discharge capacity as the Kramers-Kronig relations beyond this no longer were satisfied. In general, it can be seen that R_i increases more with the state of discharge when the solution-based mechanism is favored, which in terms of the PET model can be understood as the insulating, toroidal shaped, Li_2O_2 builds up within the pores forcing R_i to increase. In the PET model, R_{CT} will increase with an increasing thickness of Li_2O_2 on the surface of the electrode, which favors the surface-based mechanism. This is the case for the 1 M LiTFSI-DME cell where R_i also is lowest and R_{CT} the highest, as multiple reports [23, 24, 35, 36, 109, 110] have concluded that only the surface-based mechanism is active in this electrolyte resulting in the formation of a conformal Li_2O_2 deposit. This is further demonstrated by the effective capacitance of the LF semicircle (Figure 5.14) as the capacitance at sudden-death for the 1 M LiTFSI-DME cell is 3.35 μF/cm^2 corresponding to a theoretical Li_2O_2 thickness of 9.25 nm, which was estimated using the dielectric constant of Li_2O_2 of 35 [111] and eq. 5.1.

$$C = \frac{\varepsilon_{Li2O2} \cdot \varepsilon_0 \cdot A/d}{A} \tag{5.1}$$

Where ε_0 is the permittivity of vacuum ($8.854 \cdot 10^{-14}$ F/cm) and d is the separation between the plates of a capacitor, here the thickness of Li_2O_2. The estimated thickness of 9.25 μF/cm^2 is in great agreement with studies on glassy-carbon electrodes that report Li_2O_2 thicknesses of 5-10 nm were conformal deposits are observed [33, 34]. However the $LiNO_3$ and H_2O containing cells obtained C_{eff} of 0.15 and 2.37 μF/cm^2 at sudden-death (Figure 5.14) resulting in the unreasonable theoretical a thicknesses of 206.59 and 13.07 nm. Obviously, this was due to the assumption of conformal Li_2O_2 deposition, which does not apply in these electrolytes as the solution-based mechanism is activated, which is also demonstrated by the higher ionic resistances, R_i, in these cells compared to the 1 M LiTFSI-DME cell (Figure 5.14). The sudden-death of all three cells was still caused by the surface-based mechanism as R_{CT} is the dominating cathode resistance at sudden-death. This is in agreement with the planar electrode experiment, where the charge transport through Li_2O_2 could no longer support the applied electrochemical current, forcing R_{CT} to greatly increase (Figure 11 in **paper II**).

5.4 Reactions and SEI Formation during Charging of Li-O_2 Cells

The discharge process in the Li-O_2 has received a great deal of attention in the past years whereas the process of charge is still less studied as it is complicated since multiple electrochemical and chemical reaction pathways can occur simultaneously. In **paper IV**, the charge in Li-O_2 was studied using differential capacity (dQ/dV), EIS, the spectrophotometric Li_2O_2 quantification, and DEMS. This study led to information about both the chemical and electrochemical processes taking place during charge, and it was possible to quantitatively separate the degradation into chemical and electrochemical contributions. A summary

of the suggested mechanisms reported in this paper and the charge profile of the Li-O_2 battery are shown in Figure 5.15.

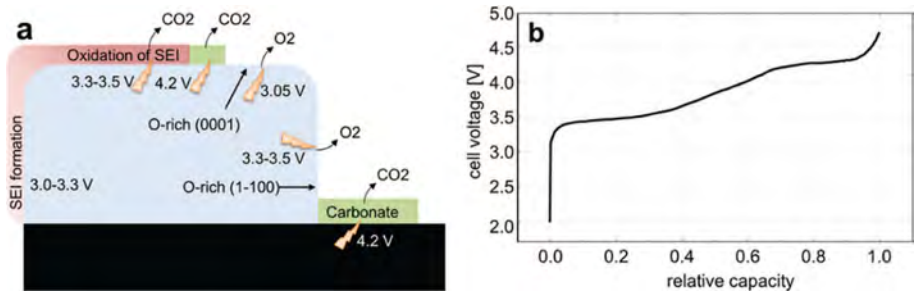

Figure 5.15: (a) A sketch of the reactions and SEI/CEI formation during charge of the Li-O_2 battery for each proposed reaction. The potentials are given as the onset potentials. The initial Li_2O_2 oxidation occurs at 3.05 V and a SEI/CEI formation occurs instantaneously on the fresh surface. At 3.3-3.5 V several reactions occur. (b) Voltage profile of a cell during galvanostatic charging, after galvanostatic discharge to 2.0 V. Adapted from **paper IV**.

Initial experiments were conducted on charge using impedance, which revealed that the overpotential for Li_2O_2 oxidation is low. The initial charge-transfer resistance related to Li_2O_2 oxidation was 500 Ω at a current of 220 μA/cm^2, which is six times lower than the extrapolated charge-transfer resistance of 3 kΩ at 2.0 V at sudden-death, which is in agreement with previous reported studies [22].

Differential capacity (dQ/dV) for the charge is shown in Figure 5.16. Here eight electrochemical processes could be identified at: 3.05, 3.30, 3.40, 3.50, 3.85, 4.20, 4.30, and 4.50 V vs. $Li^{0/+}$.

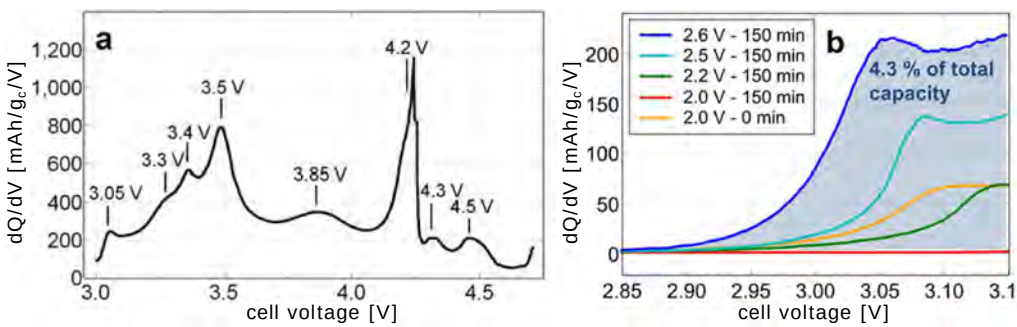

Figure 5.16: (a) The differential capacity (dQ/dV) of a represented battery. Each peak corresponds to the onset of an electrochemical reaction. (b) Differential capacity plot of the initial part of (a) following a galvanostatic discharge at 130 mA/g$_c$ to 2.0, 2.2, 2.5, or 2.6 V vs. $Li^{0/+}$, which was held for 150 min before charge, except the "2.0 V - 0 min" that corresponds to an immediate charge after reaching 2 V on discharge. Adapted from **paper IV**.

In **Paper IV**, it is argued that the first onset potential at 3.05 V is Li_2O_2 oxidation based on three observations: i) From pressure decay experiments a 2.0-2.1 e^-/O_2 is observed in the

potential range of 2.0-3.1 V (as determined using the procedure described in section 3.6). ii) As shown on Figure 5.16b, the onset charge potential at 3.05 V is dependent on the depth-of-discharge and the exposure to lower potentials, however the pressure decay experiments still reveal a $\sim$2.0 e^-/O_2 process and a parasitic reaction is therefore not the case. Instead, it is argued that it is the influence of the Li_2O_2 thickness as the conduction through thicker Li_2O_2 decreases, and iii) as the onset potential correlated with reported values of Li_2O_2 oxidation on GC electrodes reported by Luntz et al. [22].

5.4.1 SEI Formation

The DEMS results shown in Figure 5.17a reveal that all electrons, in the initial potential region 2.0-3.1 V, arise from Li_2O_2 oxidation. In this region, 4.3 % of the total amount of Li_2O_2 formed on discharge is oxidized (Figure 5.16b), and that additional 4.6 % is chemically oxidized (Figure 5.17b).

The 4.6 % chemical oxidized Li_2O_2 was determined from the total amount of Li_2O_2 present at different stages of charge in the cathode using spectrophotometric measurements, described in section 3.7. This means that a chemical reaction is occurring at Li_2O_2/electrolyte interface that cause a 4.6 % Li_2O_2 loss, which cannot be detected either electrochemically or by gas evolution. It was therefore suggested that some sort of SEI/CEI layer forms at the Li_2O_2/electrolyte interface as the amount of Li_2O_2 chemically oxidized is close to one monolayer of Li_2O_2 and thus suggest that the whole Li_2O_2 surface was involved. In addition the impedance measured on charge gives further evidence for the suggested SEI/CEI formation, as will be discussed in the following.

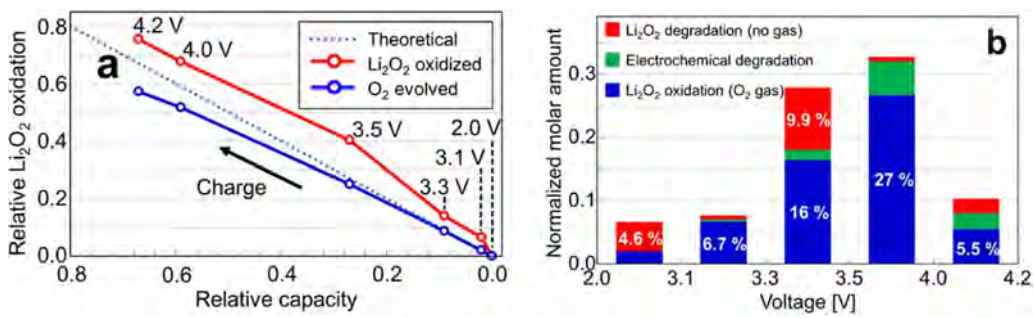

Figure 5.17: (a) Measurements of O_2 evolution using DEMS (blue) and Li_2O_2 removal (either chemical or electrochemical) determined spectrophotometrically (red). The dotted line corresponds to the ideal 2 e^-/O_2 process following reactions 2.2-2.5. (b) The amount of Li_2O_2 oxidation with and without gas evolution and electrochemical degradation in different potential intervals. Values are normalized such that the sum of electrochemical reactions (blue and green) equals the relative change in capacity in each interval and sums to 1 for full charge. Adapted from **paper IV**.

In Figure 5.18b, the resistance and capacitance was determined by EIS. The impedance was fitted to the experimental data using the equivalent circuit R_s-RQ_1-RQ_2-RQ_3-RQ_4-, where RQ_4 was identified as being related to Li_2O_2 oxidation, as it could be activated/de-activated by the applied current, it therefore also suggests that RQ_1-RQ_3 were related to pro-

cesses on the Li anode (Figure S3-S4 in the SI of **paper IV**). The resistance and capacitance shown in Figure 5.18b are those related to Li_2O_2 oxidation, *e.g.* -$(RQ)_4$. A 60 % decrease in surface capacitance is observed from 3.1 to 3.2 V vs. $Li^{0/+}$, which suggests deposition of specie(s) with a low dielectric constant. The monotonous increase in the resistance, related to Li_2O_2 oxidation, until 3.3 V also suggests a decrease of available surface or an increased electronic transport resistance. All of these factors suggests that a capacitive layer, *i.e.* SEI/CEI has formed at the Li_2O_2/electrolyte interface.

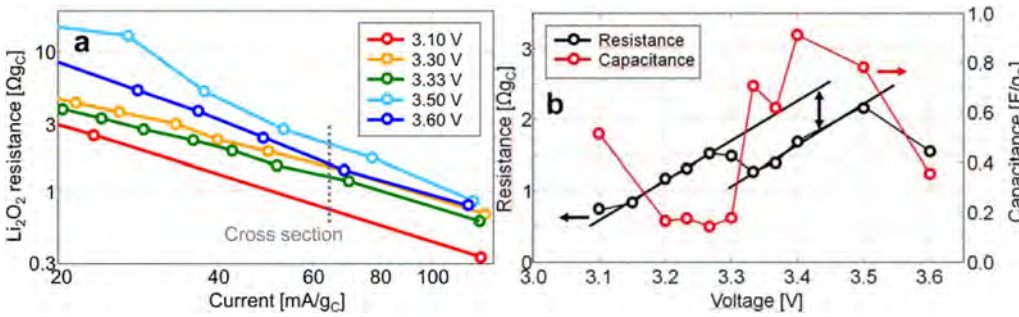

Figure 5.18: (a) The resistance related to Li_2O_2 oxidation measured at different potentials by EIS. The current decreases as a fct. of the duration of the experiment. (b) Resistance and capacitance at different potentials during charge. The guidelines are inserted to illustrate the monotonous increase in the resistance. Adapted from **paper IV**.

5.4.2 Electrochemical degradation

Identification of an electrochemical stable region with an absence of parasitic reactions is important as this could be used to identify a safe operating voltage range (a voltage range where parasitic reactions are minimized leading to better cycle life of the battery). It is proposed that at least one of the electrochemical processes in the potential range of 3.3-3.5 V is a parasitic reaction as the resistance related to Li_2O_2 oxidation (Figure 5.18b) suddenly drops suggesting the activation of a new reaction pathway. At the same time, the capacitance also rapidly increased, suggesting that some low dielectric product was oxidized, *e.g.* Li_2CO_3, possibly making some of the carbon surface available to the electrolyte. This is in agreement with the findings reported by McCloskey et al. [15] where CO_2 evolution originating from electrolyte decomposition was detected in the potential range 3-4 V using isotope labeling experiments.

5.4.3 Charge above 3.5 V

Four additional processes were also detected beyond 3.50 V: 3.85, 4.20, 4.30, and 4.50 V. These processes are due to both electrolyte and cathode decomposition by forming Li_2CO_3 (and other decomposition products) possibly following reaction 5.2, which electrochemically is decomposed to CO_2 at higher potentials [15].

$$Li_2O_2 + C + \frac{1}{2}O_2 \longrightarrow Li_2CO_3 \text{ (cathode)} \tag{5.2}$$

The processes in this region are complex as they are numerous and it is also seen on both the resistance and capacitance, which both significantly decrease at 3.5-3.6 V, *i.e.* a new process occurs to support the applied electrochemical current.

5.5 Influence of Air Contaminants on the Li-O_2 Cell Chemistry

The high specific energy of the non-aqueous Li-O_2 battery rely heavily upon an open system where O_2 is extracted from the air and not contained within the cell. However the purity of all components is extremely important as irreversible parasitic products otherwise can form. A practical Li-*air* battery that utilize the ambient atmosphere is a fascinating idea but as dry air contains 78.08 % N_2, 20.95 % O_2, 0.93 % Ar [112], ~400 ppm CO_2 [113], and a much varying H_2O content of 0.001-5 % [114]; the influence of these species must be investigated. The impact of H_2O and Ar has been covered by section 5.3, **paper I** and **II**, and N_2 is inactive if the Li anode is protected.

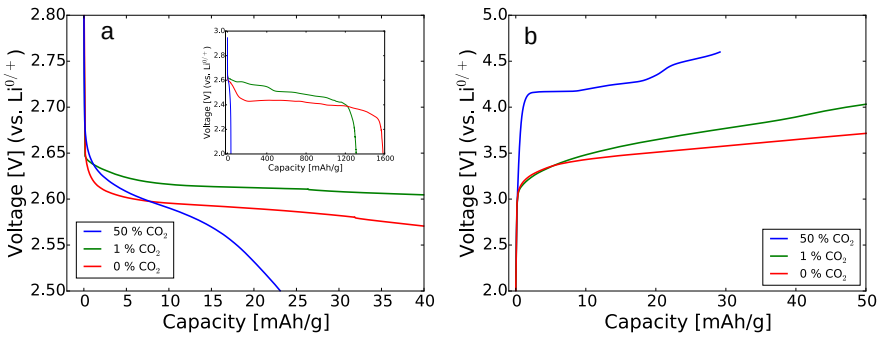

Figure 5.19: (a) Galvanostatic discharge of cells containing 50, 1, and 0 % CO_2 at 127.3 μA/cm^2. The insert is the full discharge profile (b) Galvanostatic charges at 127.3 μA/cm^2. Adapted from **paper V**.

In **paper V**, it was shown that the addition of low CO_2 concentrations increases the discharge capacity, but at higher CO_2 concentrations the discharge capacity decreases again, likely due to the poor Li_2CO_3 electrochemistry. It was suggested, that the CO_2 occupies the stepped (1-100) Li_2O_2 surface forcing Li_2O_2 to grow in another direction in such a way that conformal Li_2O_2 coatings are not formed. A recent paper by Mekonnen et al. [104] also suggests that a low polaron hopping barrier exist in the Li_2CO_3-Li_2O_2-Li_2CO_3 interfaces that could serve as a more efficient conduction path, but the full mechanism is still to be understood. However, as shown on Figure 5.19, overpotential increases at even 1 % CO_2 and is explained by the increased amount of Li_2CO_3 formed in the Li_2O_2. On charge, this is further supported by section 5.4 and **paper IV**, as Li_2CO_3 oxidation drives the increasing overpotential to maintain the applied electrochemical current. Based on these observations, the current state of Li-*air* systems must have a CO_2 purification system.

5.6 Oxygen Solubility and Diffusivity in Electrolytes for Li-O_2 Batteries

One of the great challenge in the current state-of-the-art Li-O_2 batteries, that follows reaction 2.2-2.5, is the instabilities of the electrolyte [20]. As practical batteries should be able to cycle thousands of times, it is crucial to minimize side reactions. The electrolyte should also have a low volatility to avoid evaporation if an open-system is ever to be realized and the O_2 solubility and diffusivity should be sufficient to conduct high currents in addition to a wide electrochemical window. A group of electrolytes that have generated some prospect are the room temperature ionic liquids (RTILs), as they have shown relatively high stability against, the electrochemical generated O_2^- radical [115, 116, 117, 118, 119, 120]. RTILs are salts that are molten at room temperature and in general have an organic cation and an inorganic anion. **Paper VI** was an investigation of the electrochemical stability of five RTILs in operated Li-O_2 cells. This section deals with the O_2 solubility and diffusivity, denoted $[O_2]$ and D_{O_2}, respectively, that was determined in five RTILs.

The $[O_2]$ and D_{O_2} were determined using a two-electrode setup with an GC disk microelectrodes and a Pt reference- and counter-electrode, which were placed in a saturated O_2 RTIL inside a Faraday cage. As Pt was used as the reference and counter-electrode, the potential for O_2 reduction was not known and needed to be identified. This was done by performing cyclic voltammetry, as shown for N,N-diethyl-N-methyl-N-propyl-ammonium FSI (N_{1223}FSI) in Figure 5.20.

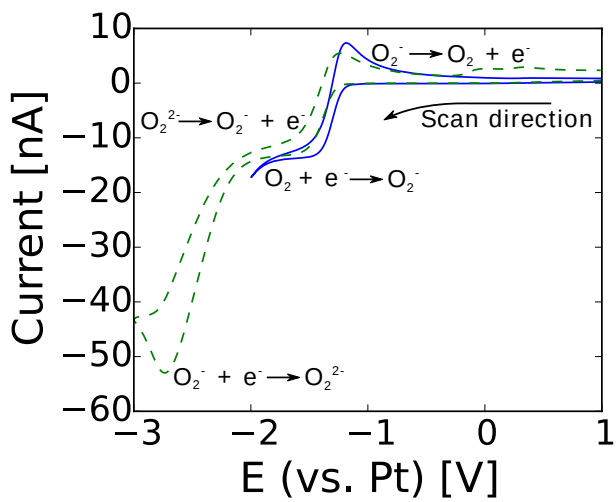

Figure 5.20: Cyclic voltammogram (100 mV/s) of the reduction of O_2 in N_{1223}FSI, at a 33 μm GC microelectrode. The blue curve represents the first scan and the green curve represents the 2^{th} scan with a lower potential limit. Voltammograms were performed in O_2 saturated salts and scanned from positive to negative potentials. Similar voltammograms were obtained in all other RTILs.

Figure 5.20 displays two processes; one at -1.75 V and a second at -2.75 V, which are the formation of O_2^- and O_2^{2-}, respectively. The first reduction ($O_2 \longrightarrow {O_2}^-$) features a steady-state response (hemispherical diffusion) while the latter reduction (${O_2}^- \longrightarrow {O_2}^{2-}$) featured

a peak-shaped response (planar diffusion). This clearly indicates that D_{O_2} is much greater than $D_{O_2^-}$ caused by the associated of cations to the superoxide giving evidence that the generated superoxide is stable within the timeframe of these experiment and is also supported by previous studies [121, 122, 123]. The peak-shaped response of this process occurs as the formed O_2^- stays close to the electrode surface and the diffusion then becomes planar, within the timeframe of the experiment. Reversing the scan rate gives much the same information, however $O_2{}^{2-} \longrightarrow O_2{}^-$ displays hemispherical diffusion, which could also be a consequence of other reactions occurring at these low potentials. The second oxidation ($O_2{}^- \longrightarrow O_2$), again displays planar diffusion, as O_2^- stays in the proximity to the electrode surface.

To determine the concentration of O_2 in N_{1223}FSI, the potential was stepped from OCV (0 V. vs. Pt) to -1.75 V vs. Pt hereby following the one step reduction of $O_2 + e^- \longrightarrow O_2{}^-$ and thus obtaining the chronoamperometric response of Figure 5.21e.

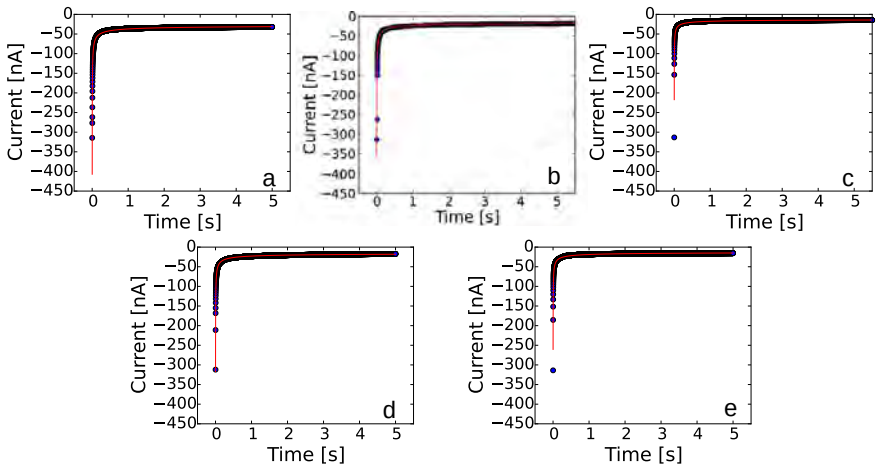

Figure 5.21: Chronoamperometric responses and Shoup-Szabo fit of O_2 saturated (a) N-methyl-N-propyl-piperidinium FSI (P_{13}FSI), (b) N-methyl-N-propyl-pyrrolidinium TFSI (P_{13}TFSI), (c) N-methyl-N-alkyl-pipiridinium TFSI (PP_{13}TFSI), (d) 1-butyl-2,3-dimethyl-imidazolium TFSI (BdIm-TFSI), (e) N_{1223}FSI at a 33 μm GC microelectrode. The blue circles illustrate the current transient and the red lines corresponds to best fit derived from the Shoup and Shabo equations at current transient times of 5 s.

The Shoup-Szabo relation, eq. 3.5-3.6, were fitted to the experimental data using an in-house written python script that iterated $[O_2]$ and D_{O_2} for an optimal fit using the non-linear least squares method of Levenberg-Marquardt. An example of the residuals from the fit is given in Figure 5.22 for N_{1223}FSI, where it is evident that the first data point was not well described by this model but the rest of the data could be described by the model well with relative residuals lower than -0.5 to +4 %.

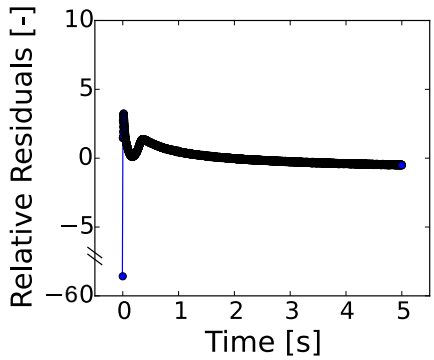

Figure 5.22: The relative residuals from the Shoup-Szabo fit to the experimental data for $N_{1223}FSI$.

A summary of the $[O_2]$ and D_{O_2} obtained from this method is given in Table 5.1.

Table 5.1: Diffusion coefficients and solubilities of O_2 in various RTILs determined from chronoamperometric experiments on a disk microelectrode. Adapted from **paper VI**.

RTIL	D_{O_2} [cm^2/s]	$[O_2]$ [mM]
$P_{13}FSI$	$2.57 \cdot 10^{-6}$	8.17
$P_{13}TFSI$	$9.17 \cdot 10^{-7}$	11.71
$PP_{13}TFSI$	$1.78 \cdot 10^{-6}$	10.58
BdImTFSI	$1.22 \cdot 10^{-6}$	18.81
$N_{1223}FSI$	$1.22 \cdot 10^{-6}$	7.71

6 Concluding Remarks and Future Outlook

The aim of this thesis was to investigate the performance and lifetime limiting effects in the non-aqueous Li-O_2 and Na-O_2 batteries. The main focus has been on Li-O_2 while a smaller part of the project was allocated to the Na-O_2 cell chemistry.

In Li-O_2 battery, the insoluble discharge product, Li_2O_2, forms on the cathode surface during discharge causing a sudden drop in cell potential. This effect was studied on disk electrodes by probing the electron transfer through different thicknesses of Li_2O_2 using three different redox shuttles. The results provide evidence that hole transport is the dominant process for charge-transfer through Li_2O_2. The influence of the discharge mechanism on the cathode performance, in the Li-O_2 battery, was investigated as a function of the depth of discharge and the obtained impedance was parameterized using porous electrode theory (a transmission line equivalent circuit model). Two electrochemical processes were detected and the capacitance of the low frequency process revealed an estimated Li_2O_2 thickness of $\sim$9 nm at sudden death for cells controlled by the surface-based mechanism. The solution-based mechanism was seen to increase the ionic resistance within the porous structure of the cathode indicating that toroid shaped Li_2O_2 formed inside the porous structure. The sudden drop in cell potential on discharge was independent of electrolyte composition and was caused by charge transport limitations through the Li_2O_2 layer formed on the surface of the cathode. On charge for the Li-O_2 battery, an electrochemical safe region with a more pure Li_2O_2 oxidation was identified in the potential region of 3.05-3.30 V in ether-based electrolytes. Above 3.30 V, the formation of an CEI layer is suggested to take place at the Li_2O_2/electrolyte interface, which blocks the cathode surface and in turn activates side reactions, which causes a further increase of the overpotential. To decrease the degree of side reactions formed from electrolyte decomposition, RTILs have been proposed as they prior had shown some promise toward O_2^- stability. Significant decomposition of the five RTILs studied was found to occur via DEMS measurements and none of the studied RTILs would be suitable for long term cycling. However, O_2 diffusivity and solubility have also been an argument against the use of these electrolytes, but the O_2 solubility and diffusion coefficients were found in the order of 10^{-7}-10^{-6} cm^2/s and 7-12 mM, respectively - the same magnitude as in most non-aqueous electrolytes. The diffusion coefficients of the superoxide, O_2^-, was however suggested to be much lower than O_2. The influence of CO_2 was also studied by poisoning cells with 1-50 % CO_2 and combined with DFT calculation, it was suggested that CO_2 poison and block the step valley sites of deposited Li_2O_2 forcing Li_2O_2 to grow much like in the solution-based mechanism and forcing the system away from the surface limited growth.

The capacity limiting effects of the Na-O_2 chemistry on both discharge and charge was also studied using electrochemical impedance spectroscopy, scanning electron microscopy, and pressure change measurements. The effects limiting discharge were found to be highly

dependent on the current density. At lower currents, the cathode surface is gradually covered with cubic NaO_2 crystals and a continuous NaO_2 film is formed in-between. At higher currents, the cathode surface is almost immediately covered by a NaO_2 film, possibly porous, and as the discharge proceeds NaO_2 cubic crystals also cover the surface. On charge, three regions were identified. First, the NaO_2 film is rapidly oxidized, second the NaO_2 cubic crystals are dissolved and oxidized (the plateau), and third the amount of dissolved NaO_2 possibly decreases and forces the potential to increase.

6.1 Outlook

In the last five to ten years, the fundamental mechanisms in the non-aqueous Li-O_2 battery has been studied to understand the limitations of cell performance. This gives us a unique opportunity as there exist a set of proven requirements for further cell design. The most important being the limited charge transport through the deposited Li_2O_2. Furthermore it is also possible to alter the Li_2O_2 discharge morphology by activating the solution-based mechanism and obtaining higher discharge capacities, as it takes longer before the cathode surface is completely covered by Li_2O_2 and that charge transport through Li_2O_2 again limits further discharge. However, as some of these toroid shaped Li_2O_2 particles now are stored far away from the cathode surface, some of the capacity may be lost on charge. In addition, this still has not improved the instabilities of either the electrolyte or the carbon cathode on charge.

One possible route to overcome these issues could be the addition of redox shuttles to the electrolyte. The redox shuttles would on discharge initially be reduced, diffuse from the cathode, reduce O_2, which reacts homogeneously and consequently forms Li_2O_2 in solution. Hereby, the cathode surface would not be blocked by an insulator and capacity not limited by the surface area. On charge, another redox shuttle would be oxidized at the electrode, which consequently oxidizes Li_2O_2 where itself is reduced. The capacity from Li_2O_2 stored in the electrolyte would this way be regained by the shuttle mechanism. Naturally, the Li anode should somehow be protected as it otherwise would reduce the oxidized shuttle.

Bibliography

[1] Parsons, R. *Pure and Applied Chemistry* **37**, 499 (2009).

[2] *Renewables 2014: Global Status Report - Key findings. Production, pages 1-13*. (2014).

[3] *IEA: World Energy Outlook 2014 - Executive Summery*. International Energy Agency, (2014).

[4] Hubbert, M. K. *Nuclear Energy and the Fossil Fuels. Technical report Shell Development Company*. (1956).

[5] *Lunar Roving Vehicle - Apollo XVII*. Boeing Press Suites, (1972).

[6] Baglione, M. L. B. *Development of System Analysis Methodologies and Tools for Modeling and Optimizing Vehicle system Efficiency*. University of Michigan, (2007).

[7] Balsara, N. P. and Newman, J. *J. Chem. Educ.* **90**, 446 (2013).

[8] Etacheri, V., Marom, R., Elazari, R., Salitra, G., and Aurbach, D. *Energy Environ. Sci.* **4**, 3243 (2011).

[9] *Technology Roadmap - Electric and plug-in hybrid electric vehicles*. International Energy Agency (IEA), (2011).

[10] *USABC Goals for Advanced Batteries for EVs - CY2020 Commerializtion*. United States Advanced Battery Consortium, (2013).

[11] Luntz, A. C. and McCloskey, B. D. *Chem. Rev.* **114**, 11721 (2014).

[12] Adelhelm, P., Hartmann, P., Bender, C. L., Busche, M., Eufinger, C., and Janek, J. *Beilstein J. Nanotechnol.* **6**, 1016 (2015).

[13] Amine, K., Tukamoto, H., Yasuda, H., and Fujita, Y. *J. Electrochem. Soc.* **143**, 1607 (1996).

[14] Abraham, K. M. and Jiang, Z. *J. Electrochem. Soc.* **143**, 1 (1996).

[15] McCloskey, B. D., Speidel, A., Scheffler, R., Miller, D. C., Viswanathan, V., Hummelshøj, J. S., Nørskov, J. K., and Luntz, A. C. *J. Phys. Chem. Lett.* **3**, 997 (2012).

[16] Kwabi, D. G., Batcho, T. P., Amanchukwu, C. V., Ortiz-Vitoriano, N., Hammond, P., Thompson, C. V., and Shao-Horn, Y. *J. Phys. Chem. Lett.* **5**, 2850 (2014).

[17] Adams, B. D., Black, R., Williams, Z., Fernandes, R., Cuisinier, M., Berg, E. J., Novak, P., Murphy, G. K., and Nazar, L. F. *Adv. Energy Mater.* **5**, 1400867 (2015).

[18] Freunberger, S. A., Chen, Y., Peng, Z., Griffin, J. M., Hardwick, L. J., Bardé, F., Novák, P., and Bruce, P. G. *J. Am. Chem. Soc.* **133**, 8040 (2011).

[19] McCloskey, B. D., Scheffler, R., Speidel, A., Girishkumar, G., and Luntz, A. C. *J. Phys. Chem. C* **116**, 23897 (2012).

[20] McCloskey, B. D., Bethune, D. S., Shelby, R. M., Mori, T., Scheffler, R., Speidel, A., Sherwood, M., and Luntz, A. C. *J. Phys. Chem. Lett.* **3**, 3043 (2012).

[21] Hummelshøj, J. S., Luntz, A. C., and Nørskov, J. K. *J. Chem. Phys.* **138**, 034703 (2013).

[22] Luntz, A. C., Viswanathan, V., Voss, J., Varley, J. B., Nørskov, J. K., Scheffler, R., and Speidel, A. *J. Phys. Chem. Lett.* **4**, 3494 (2013).

[23] Aetukuri, N. B., McCloskey, B. D., Garcia, J. M., Krupp, L. E., Viswanathan, V., and Luntz, A. C. *Nat. Chem* **7**, 50 (2015).

[24] Schwenke, K. U., Metzger, M., Restle, T., Piana, M., and Gasteiger, H. A. *J. Electrochem. Soc.* **162**, A573 (2015).

[25] Younesi, R., Veith, G. M., Johansson, P., Edström, K., and Vegge, T. *Energy Environ. Sci.* **8**, 1905 (2015).

[26] Younesi, R., Norby, P., and Vegge, T. *ECS Electrochem. Lett.* **3**, A15 (2014).

[27] Das, S., Højberg, J., Knudsen, K. B., Younesi, R., Johansson, P., Norby, P., and Vegge, T. *J. Phys. Chem. C* **119**, 18084 (2015).

[28] Gallant, B. M., Mitchell, R. R., Kwabi, D. G., Zhou, J., Zuin, L., Thompson, C. V., and Shao-Horn, Y. *J. Phys. Chem. C* **116**, 20800 (2012).

[29] Ottakam Thotiyl, M. M., Freunberger, S. A., Peng, Z., and Bruce, P. G. *J. Am. Chem. Soc.* **135**, 494 (2013).

[30] Yang, J., Zhai, D., Wang, H.-H., Chun Lau, K., Schlueter, J., Du, P., Myers, D., Sun, Y.-K., Curtiss, L., and Amine, K. *Phys. Chem. Chem. Phys.* **15**, 3764 (2013).

[31] Zhai, D., Lau, K. C., Wang, H.-H., Wen, J., Miller, D. J., Lu, J., Kang, F., Li, B., Yang, W., Gao, J., Indacochea, E., Curtiss, L. A., and Amine, K. *Nano Lett.* **15**, 1041 (2015).

[32] McCloskey, B. D., Burke, C., Nichols, J. E., and Renfrew, S. *Chem. Commun.* **51**, 12701 (2015).

[33] Viswanathan, V., Thygesen, K. S., Hummelshøj, J. S., Nørskov, J. K., Girishkumar, G., McCloskey, B. D., and Luntz, A. C. *J. Chem. Phys.* **135**, 214704 (2011).

[34] Knudsen, K. B., Luntz, A. C., Jensen, S. H., Vegge, T., and Hjelm, J. *J. Phys. Chem. C Just Accepted* (2015).

[35] Burke, C. M., Pande, V., Khetan, A., Viswanathan, V., and McCloskey, B. D. *Proc. Natl. Acad. Sci. USA* **112**, 9293 (2015).

[36] Johnson, L., Li, C., Liu, Z., Chen, Y., Freunberger, S. A., Ashok, P. C., Praveen, B. B., Dholakia, K., Tarascon, J.-M., and Bruce, P. G. *Nat. Chem.* **6**, 1091 (2014).

[37] Sandhu, S. S., Fellner, J. P., and Brutchen, G. W. *J. Power Sources* **164**, 365 (2007).

[38] Read, J., Mutolo, K., Ervin, M., Behl, W., Wolfenstine, J., Driedger, A., and Foster, D. *J. Electrochem. Soc.* **150**, A1351 (2003).

[39] Laoire, C. O., Mukerjee, S., Abraham, K. M., Plichta, E. J., and Hendrickson, M. A. *J. Phys. Chem. C* **113**, 20127 (2009).

[40] Laoire, C. O., Mukerjee, S., Abraham, K. M., Plichta, E. J., and Hendrickson, M. A. *J. Phys. Chem. C* **114**, 9178 (2010).

[41] Peng, Z., Freunberger, S. A., Hardwick, L. J., Chen, Y., Giordani, V., Barde, F., Novak, P., Graham, D., Tarascon, J.-M., and Bruce, P. G. *Angew. Chem.* **50**, 6351 (2011).

[42] Koper, M. T. M. *J. electroanal. Chem.* **660**, 254 (2011).

[43] Iermakova, D. I., Dugas, R., Palacín, M. R., and Ponrouch, A. *J. Electrochem. Soc.* **162**, A7060 (2015).

[44] Peled, E., Golodnitsky, D., Mazor, H., Goor, M., and Avshalomov, S. *J. Power Sources* **196**, 6835 (2011).

[45] Sun, Q., Yang, Y., and Fu, Z.-W. *Electrochem. Commun.* **16**, 22 (2012).

[46] Das, S. K., Xu, S., and Archer, L. A. *Electrochem. Commun.* **27**, 59 (2013).

[47] Liu, W.-M., Yin, W.-W., Ding, F., Sang, L., and Fu, Z.-W. *Electroch, Commun.* **45**, 87 (2014).

[48] Liu, W., Sun, Q., Yang, Y., Xie, J.-Y., and Fu, Z.-W. *Chem. Commun.* **49**, 1951 (2013).

[49] Li, Y., Yadegari, H., Li, X., Banis, M. N., Li, R., and Sun, X. *Chem. Commun.* **49**, 11731 (2013).

[50] Kim, J., Lim, H.-D., Gwon, H., and Kang, K. *PCCP* **15**, 3623 (2013).

[51] Jian, Z., Chen, Y., Li, F., Zhang, T., Liu, C., and Zhou, H. *J. Power Sources* **251**, 466 (2014).

[52] Yadegari, H., Li, Y., Banis, M. N., Li, X., Wang, B., Sun, Q., Li, R., Sham, T.-K., Cui, X., and Sun, X. *Energy Environ. Sci.* **7**, 3747 (2014).

[53] Hartmann, P., Bender, C. L., Vracar, M., Dürr, A. K., Garsuch, A., Janek, J., and Adelhelm, P. *Nature Mater* **12**, 228 (2012).

[54] Bender, C. L., Hartmann, P., Vrâar, M., Adelhelm, P., and Janek, J. *Adv. Energy Mater.* **4**, 1301863 (2014).

[55] Hartmann, P., Bender, C. L., Sann, J., Dürr, A. K., Jansen, M., Janek, J., and Adelhelm, P. *PCCP* **15**, 11661 (2013).

[56] Hartmann, P., Grübl, D., Sommer, H., Janek, J., Bessler, W. G., and Adelhelm, P. *J. Phys. Chem. C* **118**, 1461 (2014).

[57] McCloskey, B. D., Garcia, J. M., and Luntz, A. C. *J. Phys. Chem. Lett.* **5**, 1230 (2014).

[58] Zhao, N., Li, C., and Guo, X. *PCCP* **16**, 15646 (2014).

[59] Ortiz-Vitoriano, N., Batcho, T. P., Kwabi, D. G., Han, B., Pour, N., Yao, K. P. C., Thompson, C. V., and Shao-Horn, Y. *J. Phys. Chem. Lett.* **6**, 2636 (2015).

[60] Lee, B., Seo, D.-H., Lim, H.-D., Park, I., Park, K.-Y., Kim, J., and Kang, K. *Chem. Mater.* **26**, 1048 (2014).

[61] Hartmann, P., Heinemann, M., Bender, C. L., Graf, K., Baumann, R.-P., Adelhelm, P., Heiliger, C., and Janek, J. *J. Phys. Chem. C* **119** (2015).

[62] Yang, S. and Siegel, D. J. *Chem. Mater.* **27**, 3852 (2015).

[63] Bard, A. J. and Faulkner, L. R. *Electrochemical Methodes: Fundamentals and Applications*. John Riley & Sonc, Inc., 2nd edition, (2001).

[64] Pletcher, D., Greff, R., Peat, R., Peter, L. M., and Robinson, J. *Instrumental Methods In Electrochemistry*. Woodhead Publishing, (2011).

[65] Forster, R. J. *Chem. Soc. Rev.* **23**, 289 (1994).

[66] Hjelm, J. *Conducting Polymers Containing In-Chain Metal Centres*. ACTA Universitatis Upsaliensis, (2003).

[67] Shoup, D. and Szabo, A. *J. Electroanal. Chem. Interfac.* **140**, 237 (1982).

[68] Xiong, L., Aldous, L., Henstridge, M. C., and Compton, R. G. *Anal. Methods* **4**, 371 (2012).

[69] Paddon, C., Silvester, D., Bhatti, F., Donohoe, T., and Compton, R. *Electroanalysis* **19**, 11 (2007).

[70] Hunter, J. D. *Comput. Sci. Eng.* **9**, 90 (2007).

[71] Oliphant, J. O. and Peterson, P. *www.scipy.org* (2001).

[72] Walt, S. V. D., Colbert, S. C., and Varoquaux, G. *Comput. Sci. Eng.* **13**, 22 (2011).

[73] Boukamp, B. A. *J. Electrochem. Soc.* **142** (1995).

[74] Lasia, A. *Electrochemical Impedance Spectroscopy and its Applications*. Modern Aspects of Electrochemistry. Springer US, (2002).

[75] De Levie, R. and Delahay, P. *Advances in Electrochemistry and Electrochemical Engineering*. Wiley-Interscience, New York, 1st edition, (1967).

[76] Hitz, C. and Lasia, A. *J. Electroanal. Chem.* **500**, 213 (2001).

[77] Jurczakowski, R., Hitz, C., and Lasia, A. *Journal of Electroanalytical Chemistry* **572**, 355 (2004).

[78] Jurczakowski, R., Hitz, C., and Lasia, A. *J. Electroanal. Chem.* **582**, 85 (2005).

[79] Nielsen, J. and Hjelm, J. *Electrochim. Acta* **115**, 31 (2014).

[80] Nielsen, J., Klemensø, T., and Blennow, P. *J. Power Sources* **219**, 305 (2012).

[81] Conway, B. *Electrochemical Supercapacitors*. Kluwer Academic/Plenum Publishers, New York, 1st edition, (1999).

[82] Kötz, R. and Carlen, M. *Electrochim. Acta* **45**, 2483 (2000).

[83] Barsoukov, E., Kim, J. H., Kim, J. H., Yoon, C. O., and Lee, H. *Solid State Ionics* **116**, 249 (1999).

[84] Lundqvist, A. and Lindbergh, G. *Electrochimica Acta* **44**, 2523 (1999).

[85] Maja, M., Orecchia, C., Strano, M., Tosco, P., and Vanni, M. *Electrochim. Acta* **46**, 423 (2000).

[86] Bisquert, J., Garcia-Belmonte, G., Fabregat-Santiago, F., Ferriols, N. S., Bogdanoff, P., and Pereira, E. C. *J. Phys. Chem. B* **104**, 2287 (2000).

[87] Fabregat-Santiago, F., Bisquert, J., Garcia-Belmonte, G., Boschloo, G., and Hagfeldt, A. *Sol. Energy Mater. Sol Cells* **87**, 117 (2005).

[88] Bisquert, J., Belmonte, G. G., Santiago, F. F., Ferriols, N. S., Yamashita, M., and Pereira, E. C. *Electrochem. Commun.* **2**, 601 (2000).

[89] Bisquert, J., Garcia-Belmonte, G., Fabregat-Santiago, F., and Compte, A. *Electrochem. Commun.* **1**, 429 (1999).

[90] Meyers, J. P., Doyle, M., Darling, R. M., and Newman, J. *J. Electrochem. Soc.* **147**, 2930 (2000).

[91] De Levie, R. *Electrochim. Acta* **9**, 1231 (1964).

[92] McCloskey, B. D., Bethune, D. S., Shelby, R. M., Girishkumar, G., and Luntz, A. C. *J. Phys. Chem. Lett.* **2**, 1161 (2011).

[93] McCloskey, B. D., Scheffler, R., Speidel, A., Bethune, D. S., Shelby, R. M., and Luntz, A. C. *J. Am. Chem. Soc.* **133**, 18038 (2011).

[94] Højberg, J. *Fundamental Mechanisms in Li-air battery electrochemistry*. Technical Univeristy of Denmark, (2015).

[95] Eisenberg, G. *Ind. Eng. Chem. Anal. Ed.* **15**, 327 (1943).

[96] Goodhew, P. J., Humphreys, J., and Beanland, R. *Electron Microscopy and Analysis*. Taylor & Francis, London, 3th edition, (2001).

[97] Mansfeld, F., Lin, S., Chen, Y. C., and Shih, H. *J. Electrochem. Soc.* **135**, 906 (1988).

[98] Sawyer, D. T., Sobkowiak, A., Roberts, J. L., and Sawyer, D. T. *Electrochemistry for chemists*. Wiley, (1995).

[99] Radin, M. D., Tian, F., and Siegel, D. J. *J. Mater. Sci.* **47**, 7564 (2012).

[100] Varley, J. B., Viswanathan, V., Nørskov, J. K., and Luntz, A. C. *Energy Environ. Sci.* **7**, 720 (2014).

[101] Kang, J., Jung, Y. S., Wei, S.-H., and Dillon, A. C. *Phys. Rev. B* **85**, 035210 (2012).

[102] Garcia-Lastra, J. M., Myrdal, J. S. G., Christensen, R., Thygesen, K. S., and Vegge, T. *J. Phys. Chem. C* **117**, 5568 (2013).

[103] Rogers, E. I., Silvester, D. S., Poole, D. L., Aldous, L., Hardacre, C., and Compton, R. G. *J. Phys. Chem. C* **112**, 2729 (2008).

[104] Mekonnen, Y. S., Garcia-Lastra, J. M., Hummelshøj, J. S., Jin, C., and Vegge, T. *J. Phys. Chem. C* **119**, 18066 (2015).

[105] Mo, Y., Ong, S. P., and Ceder, G. *Phys. Rev. B* **84**, 205446 (2011).

[106] Radin, M. D., Monroe, C. W., and Siegel, D. J. *J. Phys. Chem. Lett.* **6**, 3017 (2015).

[107] McCloskey, B. D., Valery, A., Luntz, A. C., Gowda, S. R., Wallraff, G. M., Garcia, J. M., Mori, T., and Krupp, L. E. *J. Phys. Lett.* **4**, 2989 (2013).

[108] Højberg, J., McCloskey, B. D., Hjelm, J., Vegge, T., Johansen, K., Norby, P., and Luntz, A. C. *ACS Appl. Mater. Interfaces* , 4039 (2015).

[109] Gunasekara, I., Mukerjee, S., Plichta, E. J., Hendrickson, M. A., and Abraham, K. M. *J. Electrochem. Soc.* **162**, A1055 (2015).

[110] Khetan, A., Luntz, A., and Viswanathan, V. *J. Phys. Chem. Lett.* **6**, 1254 (2015).

[111] Gerbig, O., Merkle, R., and Maier, J. *Adv. Mater.* **25**, 3129 (2013).

[112] Mackenzie, F. T. *Our Changing Planet - An Introduction to Earth Science and Global Enviromental change*. Pearson Education, Inc., 4th edition, (2011).

[113] *ESRL Global Monitoring Division - Global Greenhouse Gas Reference Network*. US Department of Commerce, (2015).

[114] Wallace, J. and Hobbs, P. *Atmospheric Science; An Introductory Survey*. Elsevir, 2th edition, (2006).

[115] Elia, G. A., Hassoun, J., Kwak, W.-J., Sun, Y.-K., Scrosati, B., Mueller, F., Bresser, D., Passerini, S., Oberhumer, P., Tsiouvaras, N., and Reiter, J. *Nano Lett.* **14**, 6572 (2014).

[116] Katayama, Y., Sekiguchi, K., Yamagata, M., and Miura, T. *J. Electrochem. Soc.* **152**, E247 (2005).

[117] Kuboki, T., Okuyama, T., Ohsaki, T., and Takami, N. *J. Power Sources* **146**, 766 (2005).

[118] Allen, C. J., Mukerjee, S., Plichta, E. J., Hendrickson, M. A., and Abraham, K. M. *J. Phys. Chem. Lett.* **2**, 2420 (2011).

[119] Monaco, S., Soavi, F., and Mastragostino, M. *J. Phys. Chem. Lett.* **4**, 1379 (2013).

[120] Ara, M., Meng, T., Nazri, G.-A., Salley, S. O., and Ng, K. Y. S. *J. Electrochem. Soc.* **161**, A1969 (2014).

[121] Monaco, S., Arangio, A. M., Soavi, F., Mastragostino, M., Paillard, E., and Passerini, S. *Electrochim. Acta* **83**, 94 (2012).

[122] Buzzeo, M. C., Klymenko, O. V., Wadhawan, J. D., Hardacre, C., Seddon, K. R., and Compton, R. G. *J. Phys. Chem. A* **107**, 8872 (2003).

[123] AlNashef, I. M., Leonard, M. L., Kittle, M. C., Matthews, M. A., and Weidner, J. W. *Electrochem. Solid-State Lett.* **4**, D16 (2001).

Appendix 7

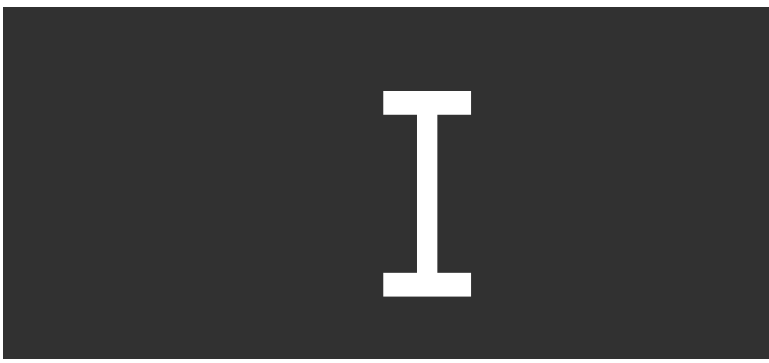

A Redox Probing Study of the Potential Dependence of Charge Transport through Li_2O_2

Kristian B. Knudsen[a], Alan C. Luntz[b,c], Søren H. Jensen[a], Tejs Vegge[a], Johan Hjelm[a,*]

[a] Department of Energy Conversion and Storage, Technical University of Denmark, 4000 Roskilde, Denmark

[b] SUNCAT Center for interface Science and Catalysis, Department of Chemical Engineering, Stanford University, 443 Via Ortega Stanford, California 94305-5025, United States

[c] SLAC National Accelerator Laboratory, 2575 Sand Hill Road, Menlo Park, California 94025, United States

* Corresponding Author: Johan Hjelm, johh@dtu.dk, +45 46 77 58 87

0.0 Abstract

In the field of energy storage devices the pursuit for cheap, high energy density, reliable secondary batteries is at the top of the agenda. The Li-O_2 battery is one of the possible technologies that, in theory, should be able to close the gap, which exists between the present state-of-the-art Li-ion technologies and the demand placed on batteries by technologies such as electrical vehicles. Here we present a redox probing study of the charge-transfer across the main deposition product lithium peroxide, Li_2O_2, in the Li-O_2 battery using outer-sphere redox shuttles. The change in heterogeneous electron transfer exchange rate as a function of the potential and the Li_2O_2 layer thickness (~depth-of-discharge) was determined using electrochemical impedance spectroscopy. The attenuation of the electron transfer exchange rate with film thickness is dependent on the probing potential, providing evidence that hole transport is the dominant process for charge-transfer through Li_2O_2 and shows that the origin of the sudden-death observed upon discharge is due to charge transport limitations.

Keywords: Lithium-air, hole tunneling, redox probing, electrochemical impedance spectroscopy, Li-O_2 charge-transport

1.0 Introduction

The Li-O_2 battery is, in theory at least, a prime candidate for the ultimate generation of beyond Li-ion chemistries, as the theoretical specific energy and energy density for a fully charged battery is 11400 Wh/kg and 6080 Wh/L, respectively[1]. In the Li-O_2 battery, the net electrochemical reaction is $2Li + O_2 \leftrightarrows Li_2O_2$, with the forward reaction corresponding to discharge and the reverse direction to charge. Realizing a practical specific energy of even 1000 Wh/kg with this cell chemistry still requires tremendous efforts in surmounting existing challenges[2].

One of the pressing problems is the lack of a fully stable electrolyte during discharge and charge and this severely limits cycle life[3–8]. Another challenge is the development of a chemically- and electrochemically stable cathode since carbon has been shown to not be fully stable[9–11]. In addition, the charging overpotentials are quite high, although the reasons for this are still controversial[2]. Finally, the discharge capacity is much smaller than anticipated from complete filling of the pore volume of the cathode. To understand the last challenge requires knowledge of the mechanisms of deposition of the main discharge product, Li_2O_2.

In general, Li_2O_2 forms as either toroidal shaped particles or as conformally deposited continuous and dense films on the cathode surface and are referred to as either the solution- or surface-based mechanism[3,12,13]. While the surface electrochemistry always occurs on the cathode, the solution mechanism becomes important when the intermediate LiO_2 is soluble in the electrolyte. The solubility is described well by the electrolyte's donor and acceptor numbers as descriptors for describing the free energy of solution of the Li^+ ion and superoxide, O_2^-, respectively. Ultimately the reaction $Li^+ + O_2^- \leftrightarrows LiO_2$ followed by $2LiO_2 \rightarrow Li_2O_2 + O_2$ takes place to form toroids[3,13,14]. The extent to which these mechanisms dominates the cell electrochemistry has significant impact on the discharge capacity as higher capacities have been reported when toroids are formed[3,4,13,14]. It was shown by Aetukuri et al.[3] that in a rigorously anhydrous electrolyte based on 1,2-dimethoxyethane as the solvent no toroids were formed unless some H_2O is added. It was suggested that this solvent does not have a high enough donor number

and accepter number to give significant solubility of LiO_2. On the other hand, higher donor number anhydrous solvents can produce toroids[3,13,15].

However independent of the mechanism eventually a sudden drop in potential (sudden-death) occurs from the increasing ohmic losses through the formed Li_2O_2 [16]. It has been argued that the origin of this sudden death is due to charge transport through the discharge product Li_2O_2 as Li_2O_2 is a high bandgap insulator[17]. Viswanathan et al.[18] suggested that sudden-death occurs when a hole tunneling current through Li_2O_2 films cannot support the electrochemical current any longer. They studied the charge transport through various film thicknesses of Li_2O_2 using a ferrocene/ferroceniuim redox probe and analyzed the results using a first principles charge transport model.

In this paper, we present a more extensive redox probing study of the electron conduction through thin and dense Li_2O_2 layers on glassy carbon electrodes. We set out to expand on the work by Viswanathan et al.[18] by investigating the potential dependence of the attenuation of charge-transfer through the Li_2O_2 layer in order to shed more light on the mechanism of this important process. Three different outer-sphere redox shuttles were used to probe the charge transport through Li_2O_2 at three different potentials, corresponding closely to the standard reduction potential of each redox couple. The selected redox shuttles are cobaltocene/cobaltocenium ($[Co(Cp)_2]^{0/+}$), decamethylferrocene/decamethylferrocenium ($[Fe(DMCp)_2]^{0/+}$), and ferrocene/ ferroceniuim ($[Fe(Cp)_2]^{0/+}$). These redox shuttles were used since i) they are relatively stable and known to display facile interfacial electron exchange kinetics, yielding a reversible electrochemical response[19–21], and ii) as illustrated in **Figure 1**, they ensure that a wide potential window could be probed relative to the valence- (VB) and conduction band (CB) of the wide bandgap of Li_2O_2. The bandgap of Li_2O_2 has been estimated to lie within 5.15-6.37 eV[22] and as the VB of Li_2O_2 is only ~0.4 V higher than the Fermi level[23], E_F; the CB must therefore lie at very high energies vs. $Li^{0/+}$, as sketched in **Figure 1**. The alignment of the VB relative to the $Li^{0/+}$ potential is based on that suggested in refs.[23,24] where the VB is pinned. Therefore, electron conduction is extremely unlikely. Even electron polarons, which are ~2 eV

below the CB have very high barriers to diffusion and cannot conduct charge readily[25]. Hence, experiments with $[Co(Cp)_2]^{0/+}$ and $[Fe(DMCp)_2]^{0/+}$ probe the conduction path of holes, either by hole tunneling or via localized hole polarons[26], since their potentials are deep inside the bandgap of Li_2O_2, while $[Fe(Cp)_2]^{0/+}$ is inside the VB where some other resistive conduction dominates. In principal, both hole tunneling and hole polaron hopping can coexist for charge transport[24]. However, the dominant effect estimated theoretically is a modest reduction in the tunneling current due to the localized holes in the tunneling regime[23].

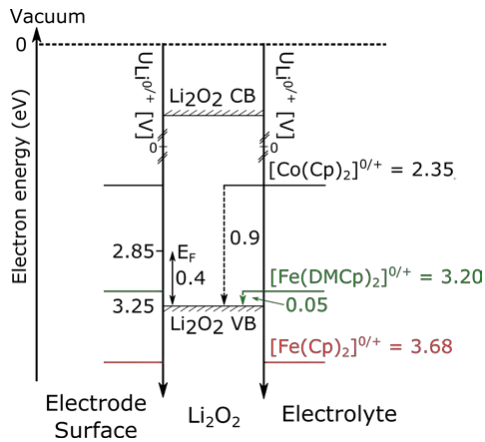

Figure 1: A sketch of the electronic structure for Li_2O_2[23,24] relative to the energy levels of the three redox shuttle pairs, which were determined from the $E_{1/2}$ calculated from measured cyclic voltammograms, are depicted. The charge-transfer process across the Li_2O_2 has been illustrated analogously to a metal-insulator-metal junction and shows the hole tunneling barriers for $[Co(Cp)_2]^{0/+}$, $[Fe(DMCp)_2]^{0/+}$ as 0.9, and 0.05 V, respectively, while $[Fe(Cp)_2]^{0/+}$ is inside the valence band with an half-wave potential ($E_{1/2}$) of 3.68 V. When the charge-transfer process through Li_2O_2 is investigated the potential of the electrode is held at $E_{1/2}$ of the redox shuttle which is illustrated with energy levels on the "electrode surface" side.

2.0 Experimental

2.1 Materials

Bis(trifluoromethane)sulfonamide lithium salt (LiTFSI), tetrabutylammonium perchlorate ($TBAClO_4$), $[Fe(Cp)_2]^0$, $[Fe(Cp)_2]^+PF_6^-$, $[Co(Cp)_2]^0$, $[Co(Cp)_2]^+PF_6^-$, $[Fe(DMCp)_2]^0$, dichloromethane, trifluoroacetic acid, ammonium hexaflurophosphate (99.99 %), acetonitrile, and 4 Å molecular sieves were purchased from Sigma-Aldrich. 1,2-dimethoxyethane (DME) was purchased from BASF and dried over 4 Å molecular sieves that had been dried at 230°C under vacuum, inside a glovebox. $[Fe(DMCp)_2]^+PF_6^-$ was, to the best of our knowledge, not commercially available and was therefore synthesized. This work is reported in the supporting information, **Figure S1**.

2.2 Electrochemical experiments

All electrochemical investigations where conducted at 25°C and the electrochemical cells were assembled in an Ar-filled glovebox with O_2 and H_2O levels maintained below 2 ppm. Electrochemical cells were assembled with four working electrodes, a Pt counter electrode, and a dual-reference electrode consisting of a double-junction Ag/0.01 M $AgNO_3$-1M LiTFSI-DME//1 M LiTFSI-DME// in parallel with a 0.1 µF capacitor connected to a second Pt wire in solution. This reference electrode maintains a stable d.c. potential at all times from the $Ag/AgNO_3$ part and thanks to the high-frequency by-pass Pt-wire makes it possible to obtain high quality electrochemical impedance also at high (f > ~100 Hz) frequencies. Use of a similar RE has previously been reported in refs.[27–29]. All current densities were calculated using the geometric area of the respective electrode. The electrolyte was 1 M LiTFSI-DME, where LiTFSI was dried in vacuum at 180°C for 12 h. The cell contained three (d = 1.6 mm) working glassy-carbon (GC) disc embedded electrodes and one (d = 1.6 mm) Au disc embedded electrode in polyether etherketone (PEEK) resin from Bio-Logic, which were all polished using aqueous suspensions of 0.05 µm aluminium oxide (MicroPolish, Buehler). After assembly; the electrochemical cell was transferred out of the glovebox with minimal exposure to ambient conditions, placed in a Faraday cage, and flushed with O_2 or Ar that passed through 4 Å molecular sieves followed by dried DME

before entering the cell to minimize water impurities. Increases in the H_2O and O_2 levels were monitored by examining the cyclic voltammogram of an Au electrode immersed in the electrolyte and experiments with increasing levels of H_2O were discarded. All electrochemical experiments were performed using a SP-200 Bio-Logic potentiostat or a Gamry REF600.

The diffusion coefficients of $[Co(Cp)_2]^{0/+}$, $[Fe(DMCp)_2]^{0/+}$, and $[Fe(Cp)_2]^{0/+}$ in 1M LiTFSI-DME were determined by using the Randles-Sevcik method on a (d = 1.6 mm) GC electrode. These experiments were conducted in Ar-saturated electrolyte using the previously described cell.

Li_2O_2 was deposited in O_2 saturated 1 M LiTFSI-DME with a continuous flow of dry O_2 as atmosphere. The deposition was performed galvanostatically at a current density of 2.5 $\mu A/cm^2$. The electrodes were discharged sequentially to a given depth-of-discharge ($\sim Li_2O_2$ film thickness). Subsequently, dissolved oxygen was removed from the electrolyte by purging of the electrolyte with Ar until O_2 could no longer be detected on the Au electrode. A blanket of Ar was maintained over the solution after purging. Then, a 1 mM stock solution of each redox shuttle pair, with a supporting 1M LiTFSI-DME electrolyte, was added and subsequently the cell was purged again with Ar to ensure inert conditions. The concentration of the redox shuttle in solution was determined by the Au electrode by the peak current in a cyclic voltammogram, which ranged from 0.02-0.05 mM. The charge transport through Li_2O_2, deposited on each GC electrode, was probed by measuring the charge-transfer resistance (R_{CT}) of each redox shuttle as a function of the depth-of-discharge (*i.e.* the Li_2O_2 film thickness), by performing electrochemical impedance spectroscopy at $E_{1/2}$ of the redox shuttle in the electrolyte. The electrochemical impedance spectroscopy (EIS) was measured using an a.c. amplitude of 10 mV over the frequency range of 100 kHz – 1 Hz with 12 points/decade and two cycles/frequency. The procedure was conducted for each of the three redox shuttles. A sketch of the experimental setup is given in **Figure 2**.

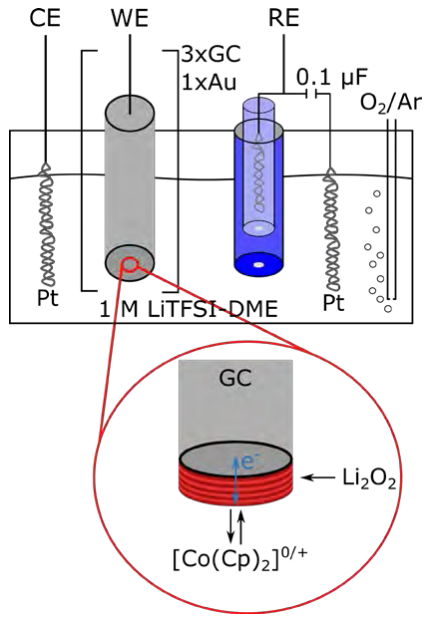

Figure 2: A schematic diagram of the experimental setup using $[Co(Cp)_2]^{0/+}$ to probe the charge-transfer at three different electrodes - each with a certain thickness of Li_2O_2. WE stand for working electrode, CE for counter electrode and RE for reference electrode.

3.0 Results and Discussion

3.1 Electrolyte water content monitoring

Ensuring a water free environment for any non-aqueous metal-air system is crucial, as multiple reports[3,4,13–15,30] have shown that water and different anions will replace DME in the solvation shell of Li^+, thus increasing the capacity of the cell, not only by the extra faradaic route of water reduction, but more importantly by activating a solution-based mechanism for Li_2O_2 formation that in turn can cause the deposition of toroid shaped Li_2O_2 on the electrode surface[3,4,13–15,30]. LiTFSI was therefore dried at 180°C for minimum 12 h in vacuum and the effect is illustrated in **Figure S2**. The voltammograms stress the importance of using a dry salt[5]. Due to high Li salt content in the electrolyte a small water impurity in the salt may still influence the

potential window of the electrolyte solution significantly as seen in **Figure S2**. It should also be stressed that significant water reduction is not observed on GC surfaces in the investigated potential range due to a too low exchange current density and other materials such as Au or (better) Pt can be used for this purpose. In this study, a Au electrode was used to monitor changes in the water content (and other electrochemically active impurities) of the electrolyte.

3.2 Voltammetry of the redox shuttles

The half-wave potentials, reversibility, and the diffusion coefficients of the redox shuttles used in this study were determined using cyclic voltammetry. The diffusion coefficients were used to make concentration determinations in conjunction with the redox probing experiments reported later in this manuscript. The voltammetry of the redox shuttles in 1M LiTFSI in DME was studied using GC electrodes. All voltammograms have been IR corrected by determining the series resistance using EIS and correcting the voltage for the resistive drop ($U = I \cdot R$). A summary of the voltammograms for the three redox shuttles is given in **Figure 3** and illustrates the reasoning behind the choice of these three shuttles as they span a potential window of ~1.3 V (2.35 to 3.68 V vs. $Li^{0/+}$), where each species was present in approximately equimolar amounts.

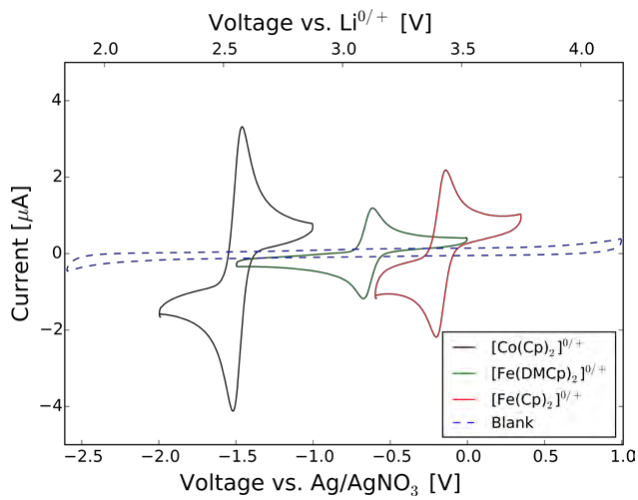

Figure 3: Cyclic voltammograms recorded at a scan rate of 100 mV/s of the three different redox shuttles: $[Co(Cp)_2]^{0/+}$, $[Fe(DMCp)_2]^{0/+}$, $[Fe(Cp)_2]^{0/+}$, and including a blank scan. All four

voltammograms where recorded in Ar saturated 1 M LiTFSI-DME and have been IR corrected. Note, that only one of the redox shuttles was present in solution at any given time.

The electrochemical reversibility of the three redox shuttles was evaluated in the scan rate interval of 10-1000 mV/s based on the peak potential separation between the anodic and cathodic peak potentials (ΔE_p). **Figure 4** depicts the voltammograms of $[Co(Cp)_2]^{0/+}$ as a function of scan rate ($\boldsymbol{v}$) and the Randles-Sevcik plot (I_{peak} vs. $\boldsymbol{v^{1/2}}$) was used to determine the diffusion coefficients for the two species, *e.g.* the neutral and positive specie of the redox shuttle in solution. For $[Co(Cp)_2]^{0/+}$, ΔE_p ranged from 51-64 mV with an average of 57.14±4.43 mV, which in close agreement with the theoretical value of 56.50 mV for a one-electron process[31]. The corresponding plots for $[Fe(DMCp)_2]^{0/+}$ and $[Fe(Cp)_2]^{0/+}$ are illustrated in **Figure S3**, where ΔE_p ranged from 62-72 and 61-72 mV, respectively. A detailed report of the electrochemical reversibility is given in **Table S1-S3**.

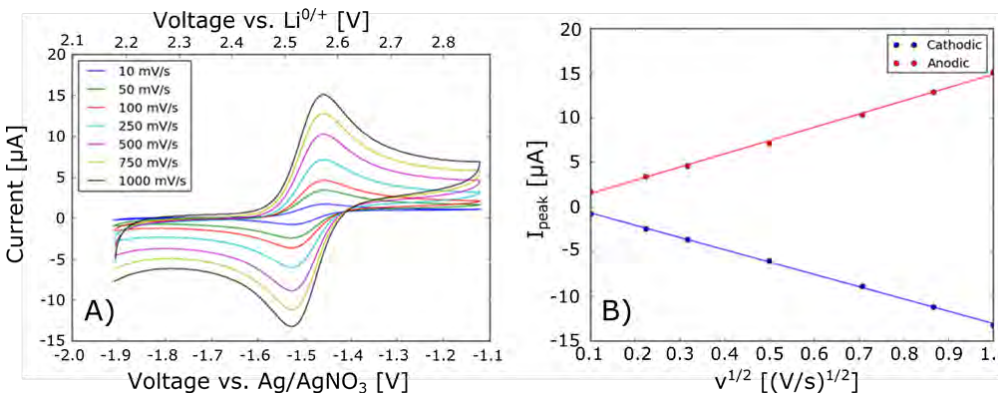

Figure 4: A) illustrates the cyclic voltammogram of $[Co(Cp)_2]^{0/+}$ in 1 M LiTFSI-DME on a GC macro electrode at $\boldsymbol{v}$ from 10 to 1000 mV/s. B) Randles-Sevcik plot of peak current vs. $\boldsymbol{v}^{1/2}$ for the voltammograms in A).

The diffusion coefficients of $[Co(Cp)_2]^{0/+}$, $[Fe(DMCp)_2]^{0/+}$, and $[Fe(Cp)_2]^{0/+}$ were determined by the Randles-Sevcik equation, **eq. 1**, that describes the relationship between peak currents (I_p)

and scan rate ($\boldsymbol{\nu}$) of a reversible electrochemical reaction under semi-infinite linear diffusion conditions.

$$I_p = 0.4463 \cdot \left(\frac{F^3}{R \cdot T}\right)^{\frac{1}{2}} \cdot n^{\frac{3}{2}} \cdot A \cdot D_{ox}^{\frac{1}{2}} \cdot C_{ox} \cdot \nu^{\frac{1}{2}} \quad [1]$$

where n the number of electrons, F Faraday's constant, A electrode area, R gas constant, T temperature, while C_{ox} and D_{ox} is the bulk concentration and diffusion coefficient of the specie, respectively. The presented diffusion coefficients in **Table 1** were determined using the slope found from a least squares linear fits to peak current data obtained from cyclic voltammetry experiments, such as that depicted in **Figure 4B and S3.** Assuming n = 1 the diffusion coefficients for each redox shuttle could be calculated.

Table 1: The diffusion coefficients for the six redox shuttles used to probe the charge transfer through Li_2O_2 on GC electrodes in 1 M LiTFSI-DME at 25°C.

Redox specie	**Diffusion coefficients [cm^2/s]**
$[Co(Cp)_2]^+$	$4.83 \cdot 10^{-6}$
$[Co(Cp)_2]^0$	$5.61 \cdot 10^{-6}$
$[Fe(DMCp)_2]^+$	$6.67 \cdot 10^{-6}$
$[Fe(DMCp)_2]^0$	$6.97 \cdot 10^{-6}$
$[Fe(Cp)_2]^+$	$6.54 \cdot 10^{-6}$
$[Fe(Cp)_2]^0$	$7.90 \cdot 10^{-6}$

All diffusion coefficients are in the range of $(5\text{-}8)\cdot 10^{-6}$ due to their relatively similar size and all positively charged forms have lower values compared to their respective neutral forms due to the increased drag from the $TFSI^-$ counter-ion cloud making the diffusion of the positively charged species diffusion slower. The lowest diffusion coefficients were observed for $[Co(Cp)_2]^{0/+}$ that was approx. 18 % lower than that of $[Fe(Cp)_2]^{0/+}$, which is in line with observations made in ionic liquids reported by Rogers et al.[32]. To the best of our knowledge, no previous reports are available

on the diffusion coefficients of these redox shuttles in 1 M LiTFSI-DME, so in order to verify the diffusion coefficients, one of the most studied redox shuttles, $[Fe(Cp)_2]^0$, was used for comparison with literature values in different non-aqueous solvents. In **Figure 5** the diffusion of $[Fe(Cp)_2]^0$ is illustrated as a function of the viscosity of the solution and here a power decay is observed where the diffusion decreases as the viscosity increases. The diffusion coefficient of $[Fe(Cp)_2]^0$ measured in 1 M LiTFSI-DME aligns into this relationship thus supporting the validity of the values reported in **Table 1**.

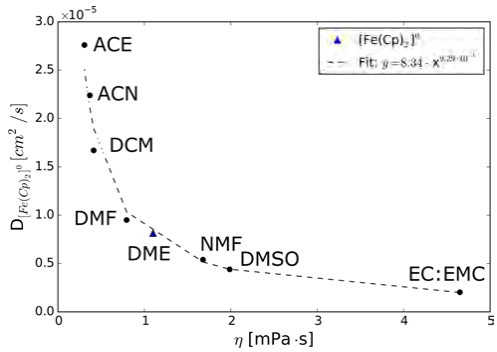

Figure 5: The diffusion coefficient of $[Fe(Cp)_2]^0$ as a function of solvents viscosity. The blue triangle is the diffusion coefficient of $[Fe(Cp)_2]^0$ in 1 M LiTFSI-DME determined by means of Randles-Sevcik. The black dots are literature values, where ACE: Acetone, ACN: Acetonitrile, DCM: dimethylcarbonate, DMF: N,N-Dimethylformamide, DME: 1,2-dimethoxyethane, NMF: N-methylformaide, DMSO: dimethyl sulfoxide, EC:EMC: ethylene carbonate: ethyl methyl carbonate. All values were taken from ref.[33] except EC:EMC which was taken from ref.[34]. The dotted line represents the power-decay fit to the literature values.

3.3 Redox probing of Li_2O_2 surfaces

To investigate the limiting charge transport mechanism as a function of the Li_2O_2 thickness; the charge-transfer resistances of the redox shuttles were measured using EIS. Multiple authors[3,4,13,17], have reported that only conformal films of Li_2O_2 grow in strictly anhydrous 1 M LiTFSI-DME, especially on flat small surface area GC disks. Since we carefully excluded water in our experiments, we claim that only dense thin films of Li_2O_2 are formed on the GC in our

experiments. Our discharge capacities are also similar to those of Viswanathan et al.[18] in anhydrous DME indicating that no toroids or higher capacity structures form. The GC electrodes were therefore coated with various thicknesses of Li_2O_2 layers prior to the impedance measurements. This was performed by a series of galvanostatic discharges onto different GC electrodes as illustrated in **Figure 6** for the experiments conducted with $[Co(Cp)_2]^{0/+}$ while the discharge curves for the Li_2O_2 layers used for the probing experiments with $[Fe(DMCp)_2]^{0/+}$ and $[Fe(Cp)_2]^{0/+}$ are illustrated in **Figure S4 and S6**, respectively.

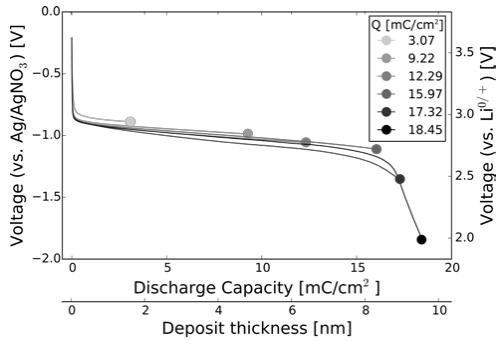

Figure 6: Six galvanostatic discharges were performed on six separate GC electrodes (J = 2.5 μA/cm^2). For the calculation of the deposit thickness a surface roughness factor of two was assumed for the GC electrodes. The dots mark the terminal capacity of each electrode, at which the redox probing was conducted.

The Li_2O_2 coated GC electrode surfaces were probed by EIS in Ar atmosphere at $E_{1/2}$ of each of the redox shuttles. The Nyquist plots for three different depth-of-discharges using $[Co(Cp)_2]^{0/+}$ are illustrated in **Figure 7**, while the Nyquist plots for $[Fe(DMCp)_2]^{0/+}$ and $[Fe(Cp)_2]^{0/+}$ are illustrated in **Figure S5 and S7**.

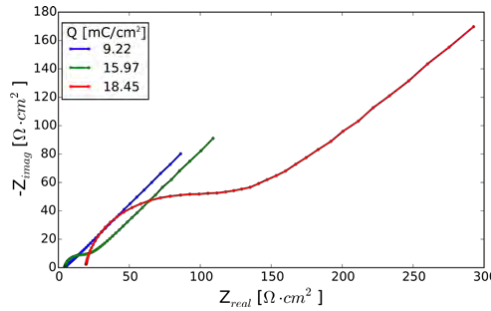

Figure 7: Nyquist plots illustrating the increase in R_{CT} of $[Co(Cp)_2]^{0/+}$ as a function of three different discharge capacities.

These **Figures** illustrate the R_{CT} varies in the impedance spectra as a function of depth-of-discharge (~ Li_2O_2 thickness) and how it greatly increases close to sudden-death. To illustrate the dependency of R_{CT} as a function depth-of-discharge (~ Li_2O_2 thickness), we were interested in quantifying the rate of electron transfer through Li_2O_2 using the heterogeneous rate constant (k^0) since this also made it possible to correct the measured R_{CT} for concentration variations of the redox shuttle in solution. These variations occurred since 5-6 GC electrodes were needed to obtain a sufficient mapping of the discharge. The electrochemical cell, as sketched in **Figure 2**, contained only three GC electrodes, thus two separate experiments were performed, giving rise to small concentration deviations between the two experiments.

The R_{CT} was determined by fitting a Randles equivalent circuit to the data that describes a heterogeneous charge-transfer and semi-infinite linear diffusion and the complex non-linear least squares fitting was carried out using a software package written in Python[35]. Data validation was carried out by using the linearized Kramers-Kronig test (KK) suggested by Boukamp[36]. All data used for determination of R_{CT} here displayed residuals of less than $\pm$ 1 % using this test, indicating good adherence to the requirements of causality, linearity, stability, and finiteness of the data. The resulting Nyquist-, and Bode plots, and the equivalent circuit model used, are shown

in **Figure 8** for $[Co(Cp)_2]^{0/+}$, while the Nyquist plots for $[Fe(DMCp)_2]^{0/+}$ and $[Fe(Cp)_2]^{0/+}$ are illustrated in **Figure S5 and S7**.

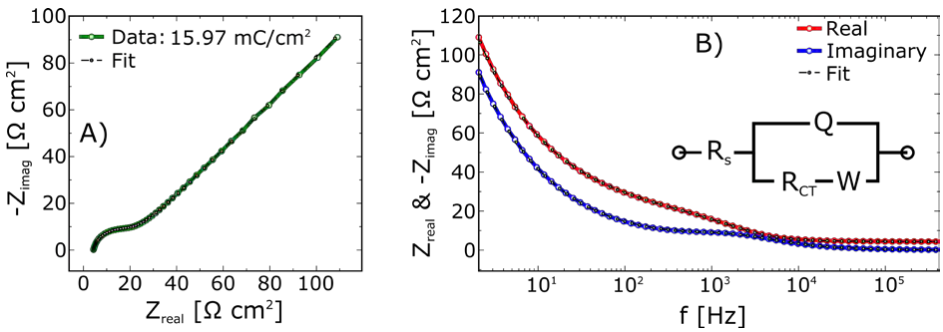

Figure 8: Nyquist plot (A) and Bode-like plot (B) for the terminal discharge capacity of 15.97 mC/cm^2 with $[Co(Cp)_2]^{0/+}$ in solution and corresponds to the green spectrum illustrated in **Figure 7**. The equivalent circuit used to model and extract R_{CT} is inserted into (B).

Figure 8 depicts the EIS spectrum for the 15.97 mC/cm^2 discharged electrode with $[Co(Cp)_2]^{0/+}$ as the redox shuttle and the corresponding fitted equivalent circuit, where it is evident that the model describes charge-transfer and the following diffusion well. At pristine electrodes the R_{CT} of the three redox shuttles could not be detected by EIS as the spectra were completely dominated by the diffusion impedance. In fact, these outer-sphere redox shuttles have very fast heterogeneous exchange rate constants causing the e^- transfer to be so rapid that the electronics used in measuring these systems simply is not fast enough. This is likely the reason for the lack of data in literature of the k^0 on pristine electrodes for these redox shuttles. A few authors have reported k^0's at pristine electrode of larger and more sluggish redox shuttles, such as the 7,7,8,8-Tetracyanoquinodimethane, using specialized higher harmonic techniques or steady-state voltammetry from microelectrodes[37,38]. A similar study using steady-state voltammetry recorded with a microelectrode was conducted here in the hope of obtaining k^0's of the three redox shuttles at pristine surfaces but, as Aoki et al.[37] also concluded, the solution resistance and the currents related to double layer charging of the microelectrode were too great to obtain reliable results and

is therefore not included here. Aoki et al. suggests that $[Fe(Cp)_2]^{0/+}$ and similar molecules have k^0's greater than 10 cm/s at pristine Pt surfaces[37]. Assuming k^0 of 10 cm/s, we can estimate that, as described in the **SI**, the characteristic frequency for the oxidation/reduction of $[Co(Cp)_2]^{0/+}$ is approx. 5 MHz and well beyond the practical frequency range of our equipment.

To illustrate the dependency of charge transport mechanism as a function of depth-of-discharge (~ Li_2O_2 thickness) we determined the k^0 for electron exchange between the glassy carbon electrode and the different redox shuttles in solution with Li_2O_2 sandwiched in between, **Figure 1**. The relationship between k^0 and R_{CT} is given in **eq. 2**[28,31].

$$\boldsymbol{k^0 = \frac{R \cdot T}{n^2 \cdot F^2 \cdot R_{CT} \cdot A \cdot C_{ox}^{1-\alpha} \cdot C_{red}^{\alpha}}} \quad [2]$$

The fourth working electrode in solution, **Figure 2**, was an Au electrode that was used to measure the concentration of each redox species in solution by cyclic voltammetry at 100 mV/s in Ar. From the peak currents it was possible to determine the precise concentrations by rearranging **eq. 1**.

$$\boldsymbol{C_{ox} = \frac{I_p^{ox}}{D_{ox}^{\frac{1}{2}} \cdot A \cdot 0.4463 \cdot n^{\frac{3}{2}} \cdot \nu^{\frac{1}{2}} \cdot \left(\frac{F^3}{R \cdot T}\right)^{1/2}}} \quad [3]$$

In **eq. 3**, the determined diffusion coefficients were used in the determinations of C_{ox} and C_{red} and consequently the k^0's. The concentration correction of the redox shuttles that was used in the calculation of k^0 clearly proved to be significant when compared to the exchange current density (j_0), which does not take C_{ox} and C_{red} into account. This is illustrated in **Figure S8** where a shift in j_0 is clearly observed between two separate experiments, but it is also evident that this shift was caused by a concentration difference of $[Co(Cp)_2]^{0/+}$ between the experiments as this was corrected for by k^0.

The resulting plot of k^0's as a function of depth-of-discharge and Li_2O_2 thickness is illustrated in **Figure 9** and here the redox shuttles acted as charge source/sink, Li_2O_2 as the insulator, and the GC electrode as the charge source/sink.

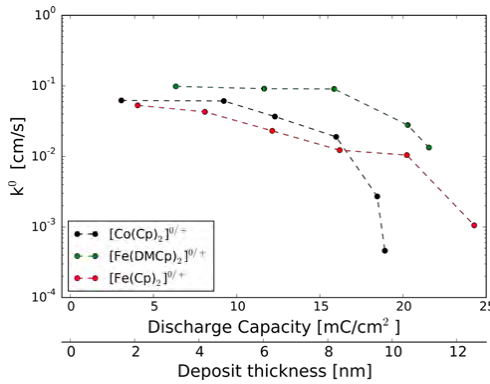

Figure 9: The heterogeneous rate constant illustrated as a function of discharge capacity and Li_2O_2 thickness (the thickness was calculated assuming that the Li_2O_2 grows as a dense thin film and that the surface roughness of the electrode was a factor of 2). The k^0's were calculated from R_{CT} obtained from the EIS. The three redox shuttles were probed at their respective $E_{1/2}$ in Ar, *e.g.* $[Co(Cp)_2]^{0/+}$ at 2.35 V, $[Fe(DMCp)_2]^{0/+}$ at 3.2 V, and $[Fe(Cp)_2]^{0/+}$ at 3.68 V vs. $Li^{0/+}$.

For $[Co(Cp)_2]^{0/+}$ and $[Fe(DMCp)_2]^{0/+}$ we see an exponential decrease in k^0 with discharge capacity that mirrors the exponential sudden death in the Li-O_2 with discharge capacity. This shows that the origin of the sudden-death is due to charge transport limitations. Since $E_{1/2}$ of $[Co(Cp)_2]^{0/+}$ and $[Fe(DMCp)_2]^{0/+}$ both are inside the bandgap of Li_2O_2, as illustrated in **Figure 1**, electronic conduction is likely dominated by a mechanism of hole transport. This transport could be via tunneling[18,24] or via thermally excited hole polarons[23,24,39–41].

We believe that tunneling is the dominant mechanism of hole charge transport in the experiments reported here since relatively high current densities are involved in the impedance measurements (> 9 μA/cm^2), and since this mechanism fits a wide range of experimental results; *e.g.* the existence of discharge sudden deaths and its dependence on current and temperature, asymmetry between discharge and charge sudden deaths, etc.[1,24]. We do note, however, that additional charge transport from hole polarons can also contribute at low current densities (< 1 μA/cm^2)[24]. A very

recent extended hole polaron model by Radin et al.[41] with some adjustable parameters also seem to be able to fit some of the observed aspects of sudden death.

One feature that should be noted in **Figure 9** is the difference in Li_2O_2 thickness/capacity between $[Co(Cp)_2]^{0/+}$ and $[Fe(DMCp)_2]^{0/+}$, with an extended discharge capacity for $[Fe(DMCp)_2]^{0/+}$. We interpret this difference as due to the very different hole transport at 0.9 and 0.05 V relative to the VB, respectively. The predictions of charge transport at 2 $\mu A/cm^2$ current density as a function of the Li_2O_2 film thickness from a simple semi-classical tunneling model of charge transport and based on assuming trapezoidal barrier shapes[24] is presented in **Figure 10**. Therefore, the results of **Figure 9** are qualitatively consistent with hole tunneling. We anticipate that if hole polarons were the dominant charge transport mechanism, there should be much larger differences between the $[Co(Cp)_2]^{0/+}$ and $[Fe(DMCp)_2]^{0/+}$ capacities (at which the charge-transfer attenuation becomes significant) since the polaron population and hence conductivity depends exponentially on the energy of the polaron relative to the VB. Since the bulk polaron energy is required to be the same as the electrochemical Fermi energy, i.e. the $[Co(Cp)_2]^{0/+}$ and $[Fe(DMCp)_2]^{0/+}$ redox potentials, we would anticipate significantly larger differences. Of course, band bending at the interfaces of the thin films could lessen this effect[41].

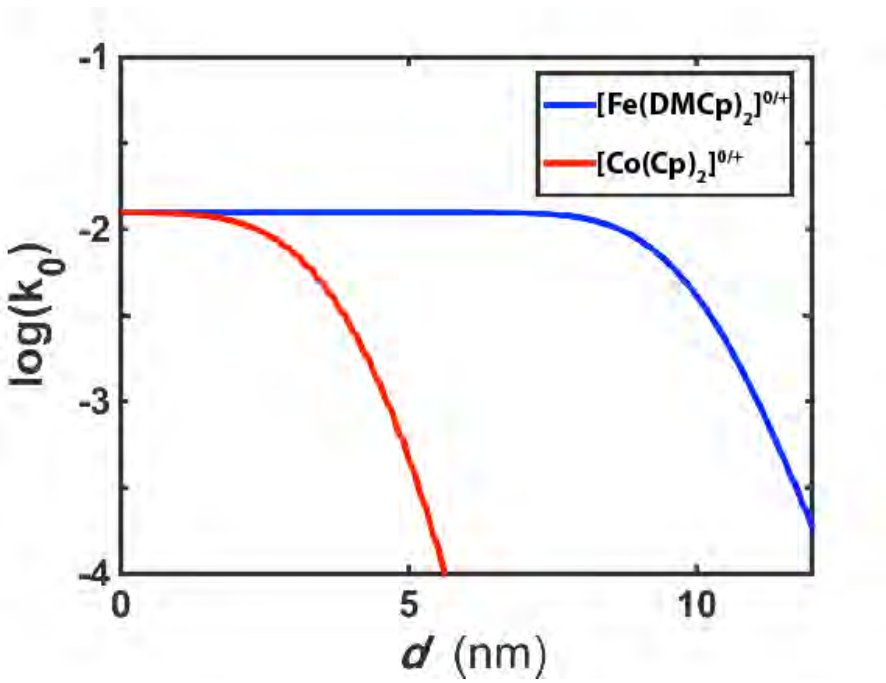

Figure 10: Tunneling charge transport Li_2O_2 films as a function of film thickness *d* assuming the energy levels given in **Figure 1**. Since the absolute value of k^0 at $d = 0$ depends on the exchange current densities of the two different redox species (and is unknown), it is simply scaled to be in rough agreement with experiment.

In this **Figure**, the barrier thickness is given by a nearly uniform Li_2O_2 film thickness *d* (Gaussian roughness of 0.5 nm). This is in reasonable qualitative agreement with the experimental observations in **Figure 9**, although the difference between $[Co(Cp)_2]^{0/+}$ and $[Fe(DMCp)_2]^{0/+}$ is overemphasized. We suspect this may be due to uncertainties in the exact barrier heights for tunneling or due to contributions from hole polaron charge transport.

The experiments with $[Fe(Cp)_2]^{0/+}$ needs a different explanation. The relationship between k^0 and the thickness of Li_2O_2 (or discharge capacity) almost exhibit a linear relationship. The electronic conduction through Li_2O_2 at this potential (3.68 V vs. $Li^{0/+}$) can therefore not be assigned to hole tunneling, since the potential of $[Fe(Cp)_2]^{0/+}$ (3.68 V vs. $Li^{0/+}$) is well inside the VB of Li_2O_2 (3.25

V vs. $Li^{0/+}$) and thereby there is no need for hole tunneling, since electron (hole) conduction though Li_2O_2 should be possible via the VB. Instead, we hypothesize that the observed relationship between k^0 and discharge capacity (~Li_2O_2 thickness), in the case of $[Fe(Cp)_2]^{0/+}$, is a consequence of the increasing R_{CT} as the Li_2O_2 layer thickens, but that the difference in k^0 attenuation and lack of exponential decay (which is the case for tunneling) is due to the charging potential at which $[Fe(Cp)_2]^{0/+}$ was probed. At this potential, Li_2O_2 was oxidized for the entire duration of the EIS measurement (approx. 3.5 min), while probing the surface. Note that, Viswanathan et al.[18] suggested that $[Fe(Cp)_2]^{0/+}$ probed hole tunneling, but with better knowledge of energy level alignments provided here, this is unlikely. Therefore, the k^0 for $[Fe(Cp)_2]^{0/+}$ is a mixture of both hole transport through Li_2O_2 via some ohmic process, Li_2O_2 oxidation and possibly $LiRCO_3$ electrochemical formation, which has been shown to form at these potentials in this specific electrolyte[42–44].

4.0 Conclusion

In this paper, we have performed detailed electrochemical experiments to probe the fundamental limiting processes of e^- transfer through the main deposition product in the Li-O_2 battery, Li_2O_2. The experiments utilized three outer-sphere redox shuttles to probe the charge-transfer through electrochemical grown Li_2O_2 on glassy carbon electrodes.

The results show that i) the attenuation of the heterogeneous rate constants for $[Co(Cp)_2]^{0/+}$ and $[Fe(DMCp)_2]^{0/+}$ displays an exponential decay caused by hole charge transport at the potentials probed as a function of the Li_2O_2 thickness (discharge capacity), and ii) show a clear dependency on the potential probed and the Li_2O_2 thickness (discharge capacity) obtained. We suggest that this results from different hole tunneling barriers at which the charge-transfer through Li_2O_2 was probed, hence the smaller the hole tunneling barrier (or the greater the polaron/hole conductivity), the greater the thickness at which significant attenuation of the heterogeneous exchange rate takes place. The findings reported here thus further confirm that sudden death in the Li-O_2 battery occurs when the charge transport can no longer support the applied electrochemical current.

5.0 Acknowledgments

The authors gratefully acknowledge financial support from the ReLiable project (project No. 11-116792) funded by the Danish Council for Strategic Research, Program Commission on Sustainable Energy and Environment. Dr. Wesley Browne is acknowledged for helpful advice regarding the synthesis and purification of metallocenes.

6.0 Supporting information

Synthesis and characterization of $[Fe(DMCp)_2]^{0/+}$, supporting figures and tables including voltammetry results of the three redox shuttles, water impurities, the impact of redox shuttle concentration on j_0 and the characteristic frequency for the redox shuttles on pristine electrodes.

7.0 References

(1) Luntz, A. C.; McCloskey, B. D. Nonaqueous Li–Air Batteries: A Status Report. *Chem. Rev.* **2014**.

(2) Kundu, D.; Black, R.; Jämstorp Berg, E.; F. Nazar, L. A Highly Active Nanostructured Metallic Oxide Cathode for Aprotic Li–O_2 Batteries. *Energy Environ. Sci.* **2015**, *8* (4), 1292–1298.

(3) Aetukuri, N. B.; McCloskey, B. D.; García, J. M.; Krupp, L. E.; Viswanathan, V.; Luntz, A. C. Solvating Additives Drive Solution-Mediated Electrochemistry and Enhance Toroid Growth in Non-Aqueous Li–O2 Batteries. *Nat. Chem.* **2015**, *7* (1), 50–56.

(4) Schwenke, K. U.; Metzger, M.; Restle, T.; Piana, M.; Gasteiger, H. A. The Influence of Water and Protons on Li_2O_2 Crystal Growth in Aprotic Li-O_2 Cells. *J. Electrochem. Soc.* **2015**, *162* (4), A573–A584.

(5) Younesi, R.; Veith, G. M.; Johansson, P.; Edström, K.; Vegge, T. Lithium Salts for Advanced Lithium Batteries: Li–metal, Li–O_2, and Li–S. *Energy Env. Sci* **2015**, *8* (7), 1905–1922.

(6) Younesi, R.; Hahlin, M.; Björefors, F.; Johansson, P.; Edström, K. Li–O_2 Battery Degradation by Lithium Peroxide (Li_2O_2): A Model Study. *Chem. Mater.* **2013**, *25* (1), 77–84.

(7) Younesi, R.; Norby, P.; Vegge, T. A New Look at the Stability of Dimethyl Sulfoxide and Acetonitrile in Li-O_2 Batteries. *ECS Electrochem. Lett.* **2014**, *3, 3,* A15-A18.

(8) Das, S.; Højberg, J.; Knudsen, K. B.; Younesi, R.; Johansson, P.; Norby, P.; Vegge, T. Instability of Ionic Liquid-Based Electrolytes in Li–O_2 Batteries. *J. Phys. Chem. C* **2015**.

(9) McCloskey, B. D.; Speidel, A.; Scheffler, R.; Miller, D. C.; Viswanathan, V.; Hummelshøj, J. S.; Nørskov, J. K.; Luntz, A. C. Twin Problems of Interfacial Carbonate Formation in Nonaqueous Li–O2 Batteries. *J. Phys. Chem. Lett.* **2012**, *3* (8), 997–1001.

(10) Gallant, B. M.; Mitchell, R. R.; Kwabi, D. G.; Zhou, J.; Zuin, L.; Thompson, C. V.; Shao-Horn, Y. Chemical and Morphological Changes of Li–O_2 Battery Electrodes upon Cycling. *J. Phys. Chem. C* **2012**, *116* (39), 20800–20805.

(11) Ottakam Thotiyl, M. M.; Freunberger, S. A.; Peng, Z.; Bruce, P. G. The Carbon Electrode in Nonaqueous Li–O_2 Cells. *J. Am. Chem. Soc.* **2013**, *135* (1), 494–500.

(12) Black, R.; Oh, S. H.; Lee, J.-H.; Yim, T.; Adams, B.; Nazar, L. F. Screening for Superoxide Reactivity in Li-O_2 Batteries: Effect on Li_2O_2/LiOH Crystallization. *J. Am. Chem. Soc.* **2012**, *134* (6), 2902–2905.

(13) Johnson, L.; Li, C.; Liu, Z.; Chen, Y.; Freunberger, S. A.; Ashok, P. C.; Praveen, B. B.; Dholakia, K.; Tarascon, J.-M.; Bruce, P. G. The Role of LiO_2 Solubility in O_2 Reduction in Aprotic Solvents and Its Consequences for Li–O_2 Batteries. *Nat. Chem.* **2014**, *6* (12), 1091–1099.

(14) Burke, C. M.; Pande, V.; Khetan, A.; Viswanathan, V.; McCloskey, B. D. Enhancing Electrochemical Intermediate Solvation through Electrolyte Anion Selection to Increase Nonaqueous Li–O2 Battery Capacity. *Proc. Natl. Acad. Sci.* **2015**, 201505728.

(15) Khetan, A.; Luntz, A.; Viswanathan, V. Trade-Offs in Capacity and Rechargeability in Nonaqueous Li–O_2 Batteries: Solution-Driven Growth versus Nucleophilic Stability. *J. Phys. Chem. Lett.* **2015**, *6* (7), 1254–1259.

(16) Højberg, J.; McCloskey, B. D.; Hjelm, J.; Vegge, T.; Johansen, K.; Norby, P.; Luntz, A. C. An Electrochemical Impedance Spectroscopy Investigation of the Overpotentials in Li–O_2 Batteries. *ACS Appl. Mater. Interfaces* **2015**, No. 7, 4039–4047.

(17) Albertus, P.; Girishkumar, G.; McCloskey, B.; Sánchez-Carrera, R. S.; Kozinsky, B.; Christensen, J.; Luntz, A. C. Identifying Capacity Limitations in the Li/Oxygen Battery Using Experiments and Modeling. *J. Electrochem. Soc.* **2011**, *158* (3), A343–A351.

(18) Viswanathan, V.; Thygesen, K. S.; Hummelshøj, J. S.; Nørskov, J. K.; Girishkumar, G.; McCloskey, B. D.; Luntz, A. C. Electrical Conductivity in Li_2O_2 and Its Role in Determining Capacity Limitations in Non-Aqueous Li-O_2 Batteries. *J. Chem. Phys.* **2011**, *135* (21), 214704–214704 – 10.

(19) Noviandri, I.; Brown, K. N.; Fleming, D. S.; Gulyas, P. T.; Lay, P. A.; Masters, A. F.; Phillips, L. The Decamethylferrocenium/Decamethylferrocene Redox Couple: A Superior Redox Standard to the Ferrocenium/Ferrocene Redox Couple for Studying Solvent Effects on the Thermodynamics of Electron Transfer. *J. Phys. Chem. B* **1999**, *103* (32), 6713–6722.

(20) Richardson, J. N. Heterogeneous Electron-Transfer Dynamics of Decamethylferrocene from 130 to 181 K. *J. Phys. Chem. A.* **1994**, *98* (50).

(21) Bard, A. J.; Garcia, E.; Kukharenko, S.; Strelets, V. V. Electrochemistry of Metallocenes at Very Negative and Very Positive Potentials. Electrogeneration of 17-Electron Cp_2Co^{2+}, 21-Electron Cp_2Co+, and 22-Electron Cp_2Ni^{2-} Species. *Inorg. Chem.* **1993**, *32* (16), 3528–3531.

(22) Radin, M. D.; Tian, F.; Siegel, D. J. Electronic Structure of Li_2O_2 {0001} Surfaces. *J. Mater. Sci.* **2012**, *47* (21), 7564–7570.

(23) Varley, J. B.; Viswanathan, V.; A. C. Luntz. Lithium and oxygen vacancies and their role in Li2O2 charge transport in Li–O_2 batteries. *Energy Enviorn. Sci.* **2014**, *7*, 720-727

(24) Luntz, A. C.; Viswanathan, V.; Voss, J.; Varley, J. B.; Nørskov, j. K.; Scheffler, R.; Speidel, A. Tunneling and Polaron Charge Transport through Li_2O_2 in Li–O_2 Batteries. *J. Phys. Chem. Lett.,* **2013**, *4 (20)*, 3494-3499.

(25) Kang, J.; Jung, Y. S.; Wei, S.-H.; Dillon, A. C. Implications of the Formation of Small Polarons in Li2O2 for Li-Air Batteries. *Phys. Rev. B* **2012**, *85* (3), 035210.

(26) Garcia-Lastra, J. M.; Myrdal, J. S. G.; Christensen, R.; Thygesen, K. S.; Vegge, T. DFT+U Study of Polaronic Conduction in Li2O2 and Li_2CO_3: Implications for Li–Air Batteries. *J. Phys. Chem. C* **2013**, *117* (11), 5568–5577.

(27) Mansfeld, F.; Lin, S.; Chen, Y. C.; Shih, H. Minimization of High-Frequency Phase Shifts in Impedance Measurements. *J. Electrochem. Soc.* **1988**, *135* (4), 906–907.

(28) Lasia, A. Electrochemical Impedance Spectroscopy and Its Applications. In *Modern Aspects of Electrochemistry*; Conway, B. E., Bockris, J. O., White, R. E., Eds.; Modern Aspects of Electrochemistry; Springer US, 2002.

(29) Sawyer, D. T.; Sobkowiak, A.; Roberts, J. L.; Sawyer, D. T. *Electrochemistry for Chemists*; Wiley, 1995.

(30) Gunasekara, I.; Mukerjee, S.; Plichta, E. J.; Hendrickson, M. A.; Abraham, K. M. A Study of the Influence of Lithium Salt Anions on Oxygen Reduction Reactions in Li-Air Batteries. *J. Electrochem. Soc.* **2015**, *162* (6), A1055–A1066.

(31) Bard, A. J.; Faulkner, L. R. *Electrochemical Methodes: Fundamentals and Applications*, 2nd edition.; John Riley & Sonc, Inc.; Vol. 2001.
(32) Rogers, E. I.; Silvester, D. S.; Poole, D. L.; Aldous, L.; Hardacre, C.; Compton, R. G. Voltammetric Characterization of the Ferrocene|Ferrocenium and Cobaltocenium|Cobaltocene Redox Couples in RTILs. *J. Phys. Chem. C* **2008**, *112* (7), 2729–2735.
(33) CRC Handbook of Chemistry and Physics; CRC Press: Boca Raton, FL; Vol. 2014-2015.
(34) Laoire, C. O.; Plichta, E.; Hendrickson, M.; Mukerjee, S.; Abraham, K. M. Electrochemical Studies of Ferrocene in a Lithium Ion Conducting Organic Carbonate Electrolyte. *Electrochimica Acta* **2009**, *54* (26), 6560–6564.
(35) C. Graves, RAVDAV Data Analysis Software, Version 0.9.7, (2012).
(36) Boukamp, B. A. A Linear Kronig-Kramers Transform Test for Immittance Data Validation. *J. Electrochem. Soc.* **1995**, *142 (6)*, 1885-1894.
(37) Aoki, K. J.; Zhang, C.; Chen, J.; Nishiumi, T. Heterogeneous Reaction Rate Constants by Steady-State Microelectrode Techniques and Fast Scan Voltammetry. *J. Electroanal. Chem.* **2013**, *706*, 40–47.
(38) Bano, K.; Nafady, A.; Zhang, J.; Bond, A. M.; Inam-ul-Haque. Electrode Kinetics Associated with Tetracyanoquinodimethane (TCNQ), $TCNQ^{\bullet-}$, and $TCNQ^{2-}$ Redox Chemistry in Acetonitrile As Determined by Analysis of Higher Harmonic Components Derived from Fourier Transformed Large Amplitude Ac Voltammetry. *J. Phys. Chem. C* **2011**, *115* (49), 24153–24163.
(39) Mekonnen, Y. S.; Garcia-Lastra, J. M.; Hummelshøj, J. S.; Jin, C.; Vegge, T. Role of Li_2O_2@Li_2CO_3 Interfaces on Charge Transport in Nonaqueous Li–Air Batteries. *J. Phys. Chem. C* **2015**, *119* (32), 18066–18073.
(40) Mo, Y.; Ong, S. P.; Ceder, G. First-Principles Study of the Oxygen Evolution Reaction of Lithium Peroxide in the Lithium-Air Battery. *Phys. Rev. B* **2011**, *84* (20), 205446.
(41) Radin, M. D.; Monroe, C. W.; Siegel, D. J. Impact of Space-Charge Layers on Sudden Death in Li/O_2 Batteries. *J. Phys. Chem. Lett.* **2015**, 3017–3022.
(42) McCloskey, B. D. Solvents' Critical Role in Nonaqueous Lithium–Oxygen Battery Electrochemistry. *J. Phys. Chem. Lett.* **2011**, *2* (10), 1161–1166.
(43) McCloskey, B. D.; Valery, A.; Luntz, A. C.; Wallraff, G. M.; Garcia, J. M.; Mori Takashi; Krupp, L. E. Combining Accurate O_2 and Li_2O_2 Assays to Separate Discharge and Charge Stability Limitations in Nonaqueous Li–O_2 Batteries. *J. Phys. Chem. Lett.* **2013**, *4 (17)*, 2989-2993
(44) Højberg, J.; Knudsen, K. B.; Hjelm, J.; Vegge, T. Reactions and SEI Formation during Charging of Li-O_2 Cells. *ECS Electrochem. Lett.* **2015**, *4* (7), A63–A66.

Table of Contents (TOC) Image

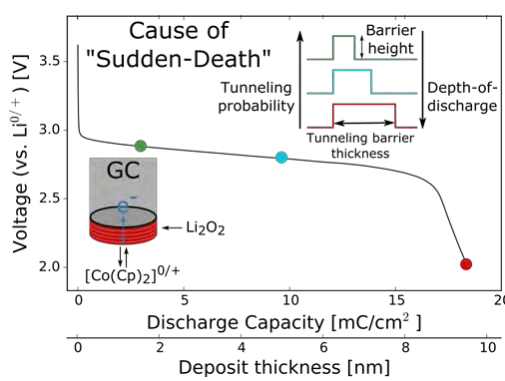

Supporting information

A Redox Probing Study of the Potential Dependence of Charge Transport through Li_2O_2

Kristian B. Knudsen[a], Alan C. Luntz[b,c], Søren H. Jensen[a], Tejs Vegge[a], Johan Hjelm[a,*]

[a] Department of Energy Conversion and Storage, Technical University of Denmark, 4000 Roskilde, Denmark

[b] SUNCAT Center for interface Science and Catalysis, Department of Chemical Engineering, Stanford University, 443 Via Ortega Stanford, California 94305-5025, United States

[c] SLAC National Accelerator Laboratory, 2575 Sand Hill Road, Menlo Park, California 94025, United States

* Corresponding Author: Johan Hjelm, johh@dtu.dk, +45 46 77 58 87

Synthesis and Characterization of decamethylferrocenium hexaflourophosphate

$[Fe(Cp^*)_2]^+PF_6^-$ was synthesized by adding 100 mg $[Fe(DMCp)_2]^0$ and 50 mg of NH_4PF_6 to 50 mL acetonitrile. After complete dissolution of $[Fe(DMCp)_2]^0$, 150 µL of CF_3COOH was added under vigorous mixing. The solution was stirred for 5 h, in which the solution had changed color from bright yellow to dark green and following the addition of 10 mL CH_2F_2 and 20 mL of water, $[Fe(DMCp)_2]^+PF_6^-$ was precipitated from the CH_2F_2/ACN phase by rotary evaporation yielding a dark green powder, which was dried over molecular sieves in vacuum and transferred to a glovebox. IR spectra were recorded using a Bruker Tensor 27 FT-IR spectrometer.

$[Fe(DMCp)_2]^+PF_6^-$ was identified by the strong color change from blue to green during the synthesis and by the FT-IR as signals at: 1023, 1073, 1380, 1389, 1411, 1474, 1674-1700, and 2860-3010 cm^{-1}, which compares well with previous reports [1] [2]. Additional peaks at 713, 800, 877, 1120, 1155, 1195 and 3160-3582 cm^{-1} were identified

as the precursors $[Fe(DMCp)_2]^0$ and NH_4PF_6 while the signal at 560 was associated with C-F_3 from CF_3COOH. The FT-IR spectra's are illustrated in **Figure S1**. Cyclic voltammograms further revealed an approximate 80 % yield and no additional electrochemical active species other than the precursor $[Fe(DMCp)_2]^0$ could be detected.

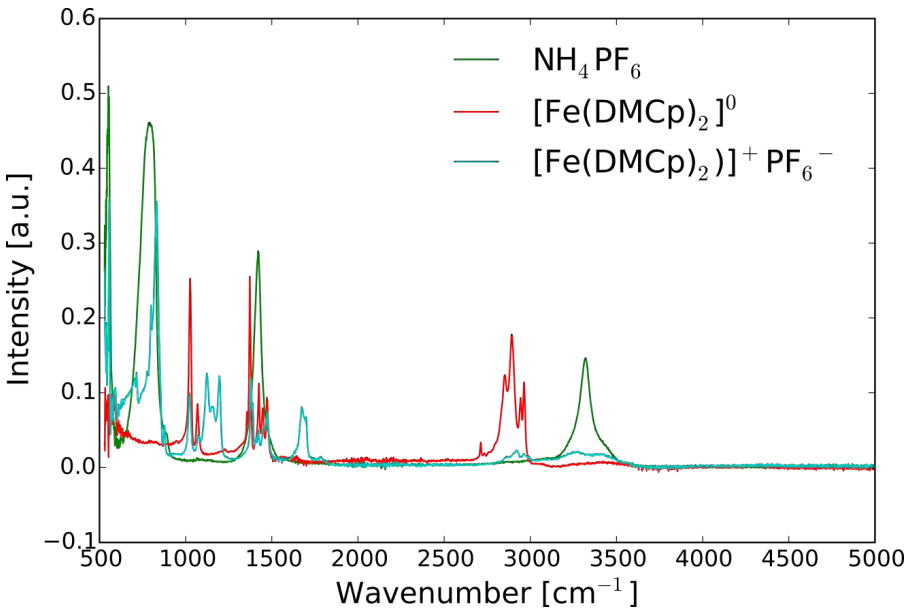

Figure S1: FTIR analysis of NH_4PF_6, $[Fe(DMCp)_2]^0$, and $[Fe(DMCp)_2]^+PF_6^-$.

Voltammetry results

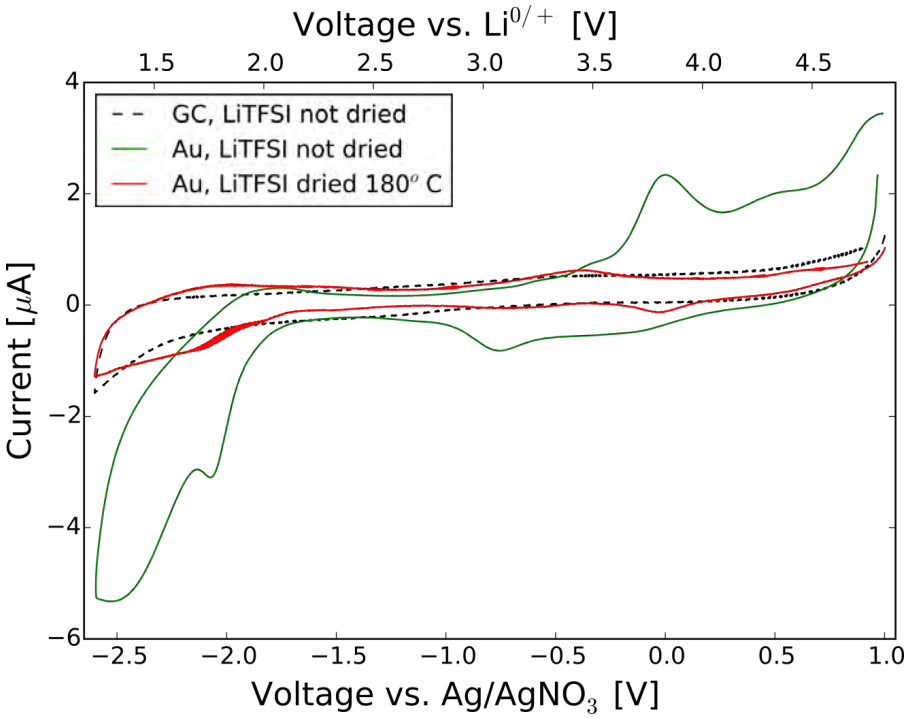

Figure S2: Cyclic voltammograms of 1 M LiTFSI-DME on Au and GC electrodes performed inside a glovebox recorded at a scan rate of 100 mV/s.

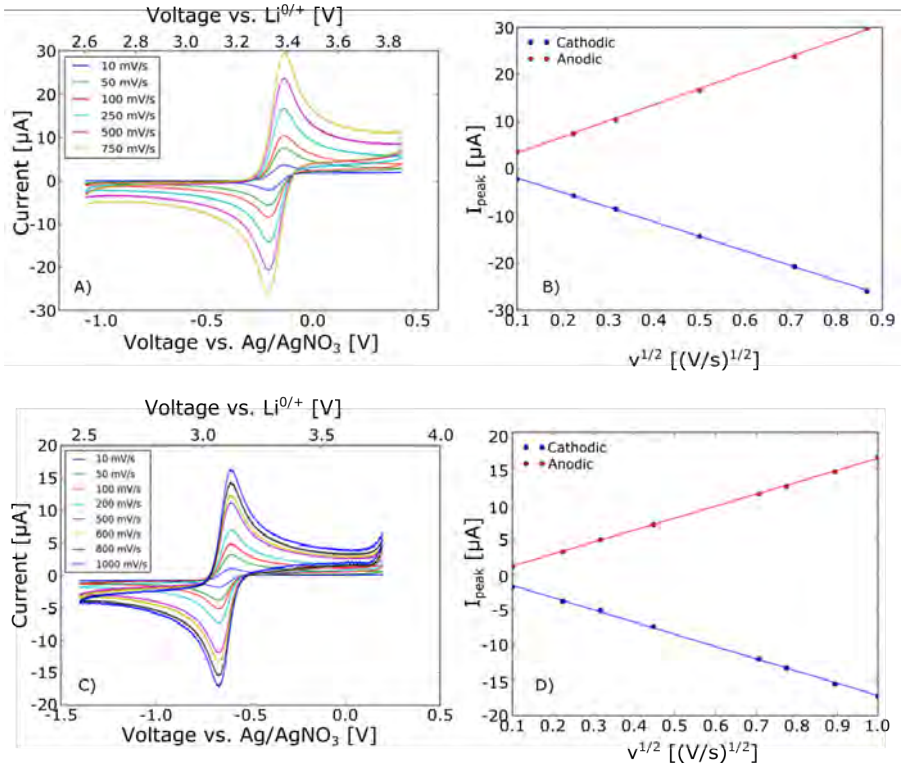

Figure S3: Cyclic voltammetry of $[Fe(Cp)_2]^{0/+}$ (A) and $[Fe(DMCp^*)_2]^{0/+}$ (C) performed in 1 M LiTFSI-DME with 1 mM redox shuttle in separate experiments. The voltammetry was performed on GC electrodes at scan rates from 10-1000 mV/s. The resulting Randles-Sevcik plots from the voltammetry of $[Fe(Cp)_2]^{0/+}$ (B) and $[Fe(DMCp)_2]^{0/+}$ (D).

Table S1: Voltammetric properties of $[Co(Cp)_2]^{0/+}$. All potentials are reported vs. $Li^{0/+}$.

Scan rate [mV/s]	E^{pa} [V]	E^{pc} [V]	ΔE_p [mV]
10	2.575	2.510	64.66
50	2.572	2.511	61.92
100	2.574	2.513	61.51
250	2.571	2.515	56.85
500	2.573	2.510	62.73
750	2.572	2.514	58.21
1000	2.572	2.515	57.38

Table S2: Voltammetric properties of $[Fe(DMCp)_2]^{0/+}$. All potentials are reported vs. $Li^{0/+}$.

Scan rate [mV/s]	E^{pa} [V]	E^{pc} [V]	ΔE_p [mV]
10	3.233	3.164	69.33
50	3.232	3.164	67.39
100	3.232	3.167	65.70
200	3.232	3.164	67.70
500	3.230	3.168	61.66
600	3.233	3.169	72.10
800	3.299	3.161	68.12
1000	3.231	3.166	64.27

Table S3: Voltammetric properties of $[Fe(Cp)_2]^{0/+}$. All potentials are reported vs. $Li^{0/+}$.

Scan rate [mV/s]	E^{pa} [V]	E^{pc} [V]	ΔE_p [mV]
10	3.439	3.367	71.68
50	3.435	3.367	67.96
100	3.438	3.370	67.65
250	3.437	3.372	64.89
500	3.435	3.374	60.77
750	3.437	3.372	65.22

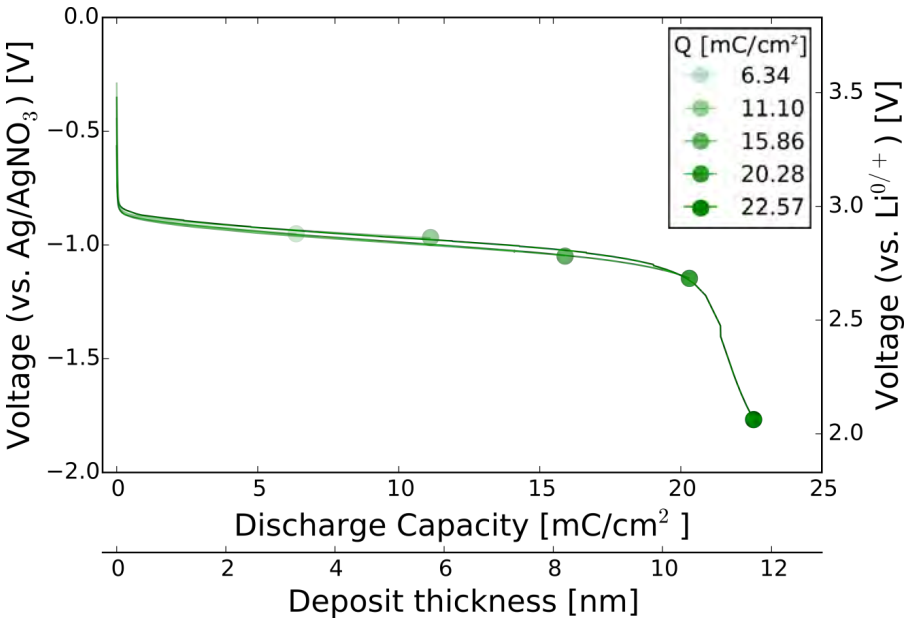

Figure S4: Six galvanostatic discharges on separate glassy carbon disk electrodes for the study of the $[Fe(DMCp)_2]^{0/+}$ charge transfer resistance at 3.20 V vs. $Li^{0/+}$ illustrating the reproducibility of the discharges.

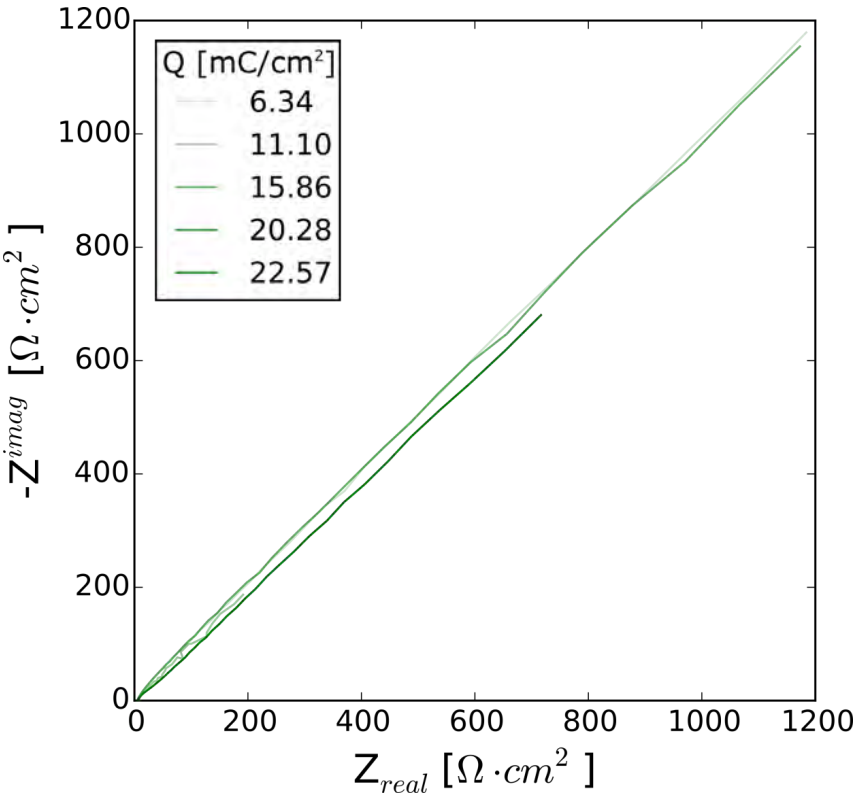

Figure S5: Nyquist plots from five individual glassy carbon electrode with different discharge capacities for the analysis of the charge-transfer resistance of $[Fe(DMCp)_2]^{0/+}$ through the Li_2O_2 layers. Each curve corresponds to a discharge electrode in **Figure S3**.

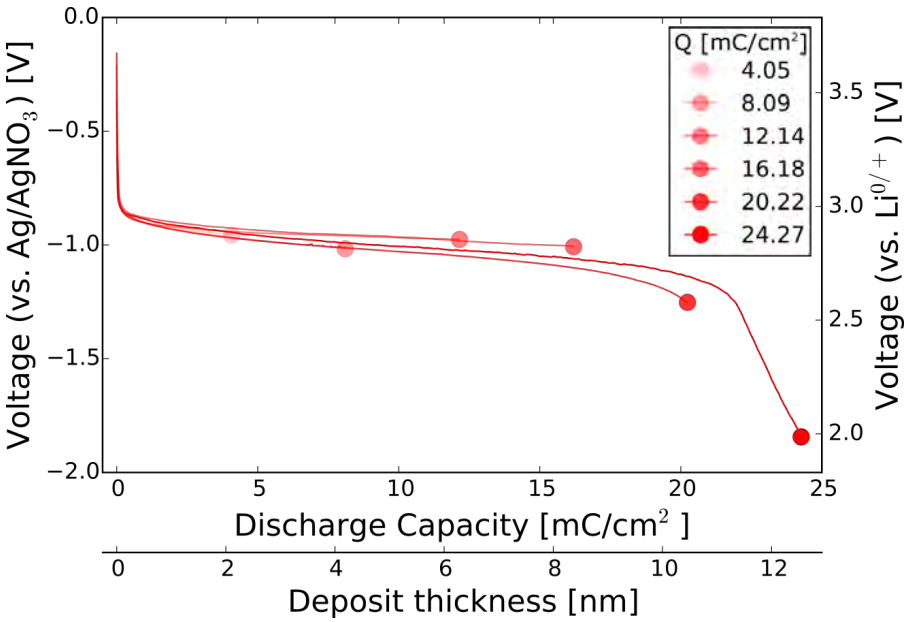

Figure S6: Six galvanostatic discharge curves on separate glassy carbon electrodes used in the study of Li_2O_2 surface with $[Fe(Cp)_2]^{0/+}$.

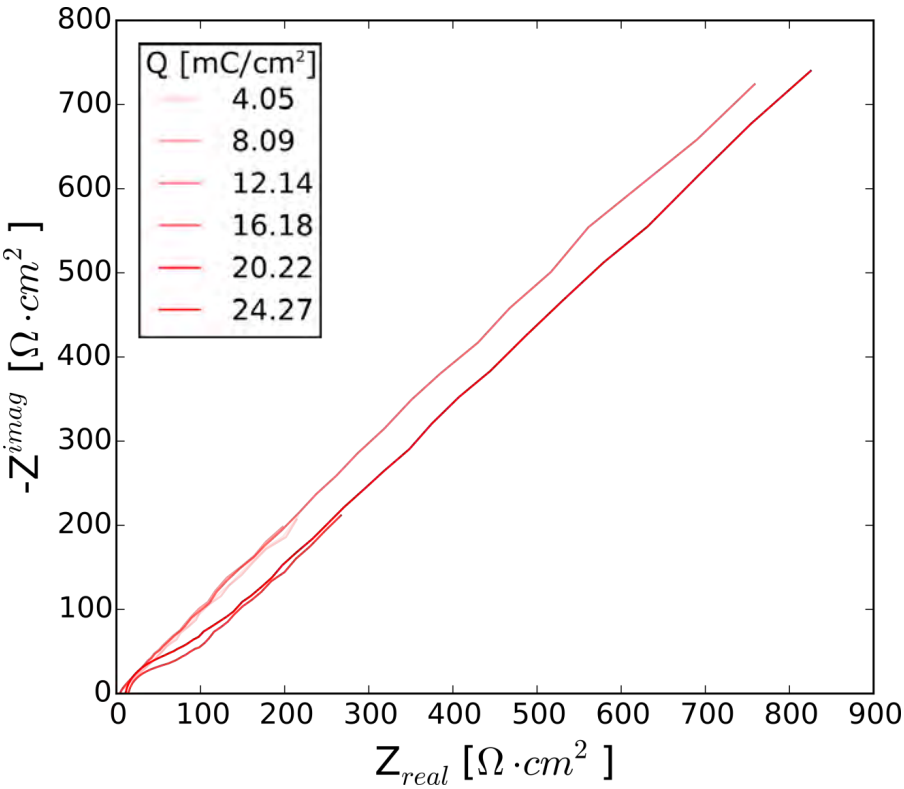

Figure S7: The Nyquist plots of the impedance from probing Li_2O_2 surfaces with $[Fe(Cp)_2]^{0/+}$. The charge-transfer was investigated as a function of discharge capacity and each plot corresponds to a discharged electrode from **Figure S5**.

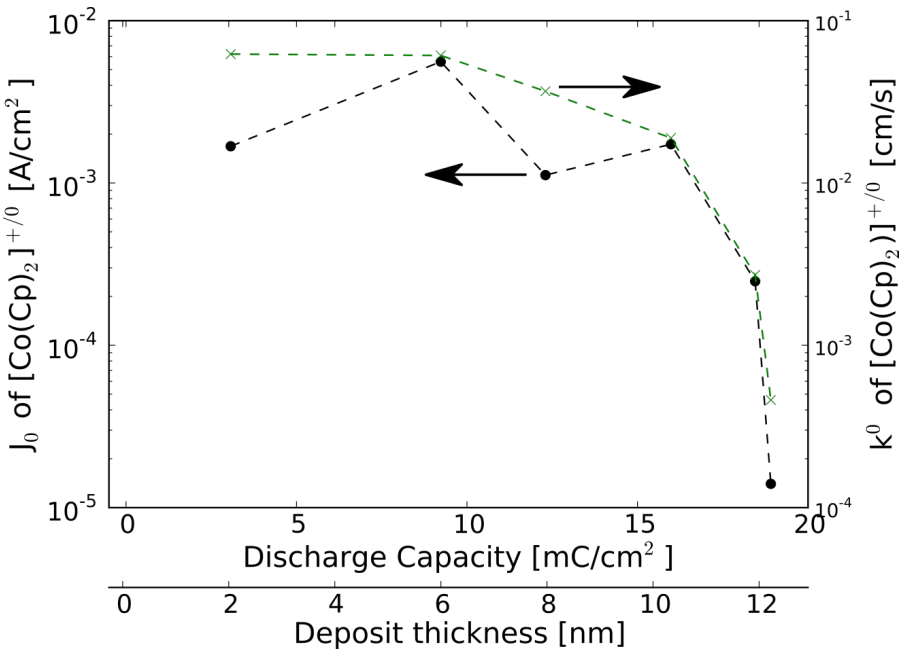

Figure S8: The exchange current density (j_0) (dots) and the heterogeneous rate constant (k^0) (x's) plotted vs. the discharge capacity and thickness of Li_2O_2. The concentration correction used in the calculation of k^0 is seen to correct for misleading results.

The characteristic frequency of $[Co(Cp)_2]^{0/+}$ at pristine electrodes

To evaluate the absence of a charge-transfer in the impedance spectra at pristine electrode, Aoki et al. [3] suggested that the k^0 of similar redox shuttles are greater than 10 cm/s. Knowing the capacitance of the glassy-carbon electrode and assuming a k^0 of 10 cm/s; the time constant (τ) and the characteristic frequency (f_c) at which the electrochemical process is detected in the impedance can be estimated using **eq. 1-3**.

$$R_{CT} = \frac{R \cdot T}{n^2 \cdot F^2 \cdot C_{ox}^{1-\alpha} \cdot C_{red}^{\alpha} \cdot k^0 \cdot A} \quad [1]$$

$$\tau = R_{CT} \cdot C_{dl} \quad [2]$$

$$f_c = \frac{1}{\tau} \quad [3]$$

The capacitance of the pristine electrode was determined by measuring the impedance of the glassy-carbon electrode in Ar at OCV. Here the surface displays a capacitive behavior, since no faradaic species are active as illustrated in **Figure S9**. The equivalent circuit used to fit the data is also illustrated and gave a double-layer capacitance of 6.79 μF/cm^2. Assuming the reasonable conditions of $C_{ox} = C_{red} = 10^{-6}$ mol/cm^3 and $\alpha = 0.5$; the characteristic frequency could be estimated to 5.54 MHz.

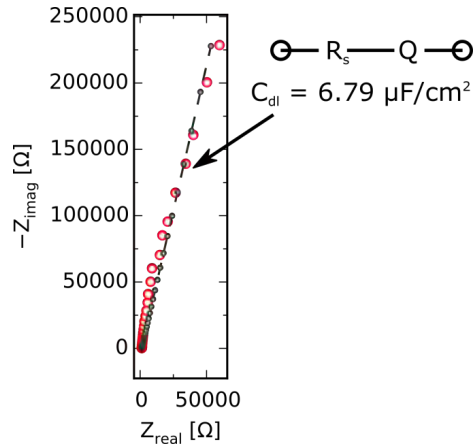

Figure S9: Illustrates the impedance of a glassy-carbon electrode measured at OCV in Ar.

References

(1) Duggan, D. M.; Hendrickson, D. N. Electronic Structure of Various Ferricenium Systems as Inferred from Raman, Infrared, Low-Temperature Electronic Absorption, and Electron Paramagnetic Resonance Measurements. *Inorg. Chem.* **1975**, *14* (5), 955–970.

(2) Hamada, S. Phase Transitions and Thermal Properties of Decamethylferrocenium Salts with Perfluoroalkyl-Sulfonate and -Carboxylate Anions Exhibiting Disorder. *J. Organomet. Chem.* **2012**, *713*, 35–41.

(3) Aoki, K. J.; Zhang, C.; Chen, J.; Nishiumi, T. Heterogeneous Reaction Rate Constants by Steady-State Microelectrode Techniques and Fast Scan Voltammetry. *J. Electroanal. Chem.* **2013**, *706*, 40–47.

II

An Electrochemical Impedance Spectroscopy Study on the Effects of the Surface- and Solution-Based Mechanisms in Li-O_2 Cells

Kristian B. Knudsen[a,b], Bryan D. McCloskey[b,c], Tejs Vegge[a], Johan Hjelm[a,*]

[a] Department of Energy Conversion and Storage, Technical University of Denmark, 4000 Roskilde, Denmark

[b] Department of Chemical and Biomolecular Engineering, University of California, Berkeley, California 94720, United States

[c] Environmental Energy Technologies Division, Lawrence Berkeley National Laboratory, Berkeley, California 94720, United States

* Corresponding Author: Johan Hjelm, johh@dtu.dk, +45 46 77 58 87

0.0 Abstract

The maximum discharge capacity in non-aqueous Li-O_2 batteries has for a while been limited to a fraction of the theoretical value, largely due to a conformal deposition of the insulating discharge product, Li_2O_2, on the cathode surface. However, it has recently been established that additives that increase the shielding of either O_2^- or Li^+ will activate the formation of toroidal shaped Li_2O_2 by a solution-based mechanism. Here, we measure the electrochemical impedance of the cathode and deconvolute it by applying porous electrode theory to investigate the changes in the impedance of the surface and the ionic resistance within the pores under conditions where either the surface-mechanism or the solution-mechanism is favored. Our experimental observations show that (i) an additional charge-transfer process is observed in the impedance spectrum under conditions where the solution-based mechanism is favored, (ii) that the changes in the ionic resistance in the cathode during discharge (related to Li_2O_2 build up in the pores) is much greater in cells where the solution-based mechanism governs and (iii) the observed "sudden-death" during discharge is a consequence of the increasing charge-transfer resistance associated with the surface formation of Li_2O_2 also under conditions where the solution-mechanism is favored.

1.0 Introduction

The Li-O_2 battery has, since its scientific discovery in 1996 by Jiang and Abraham[1], received significant scientific attention due to its high theoretical specific energy and energy density of 11400 Wh/kg and 6080 Wh/L, respectively[2]. These values are based on the overall cell reaction in non-aqueous electrolytes that can be described as $2Li + O_2 \leftrightarrows Li_2O_2$, with the forward reaction corresponding to discharge and the reverse direction to charge. The proposed discharge mechanism for the Li-O_2 system have recently come under great debate since Black et al.[3] and Kwabi et al.[4] independently observed that the main discharge product, Li_2O_2, could also form as toroidal shaped particles on the cathode surface, which both groups attributed to a solution-based reaction. This was, at the time, in contrast to the conformal surface-based deposition of Li_2O_2[5]. This discrepancy has now, to some extent, been described as two independent reaction mechanisms.

Briefly, two main reaction pathways for Li_2O_2 deposition can take place, referred to here as either a surface- or a solution-based mechanism, in which either continuous Li_2O_2 films are formed during discharge (of 5-10 nm[6–8]), or larger Li_2O_2 deposits form in the shape of toroids, respectively. The solution-based mechanism largely circumvents issues related to Li_2O_2-induced electronic insulation of the cathode, resulting in discharge capacities that are approximately six times that, which can be obtained when the surface-based mechanism dominates, with approximately equal Li_2O_2 yield in each case[9]. The two proposed mechanisms for Li_2O_2 formation are illustrated in **Figure 1**.

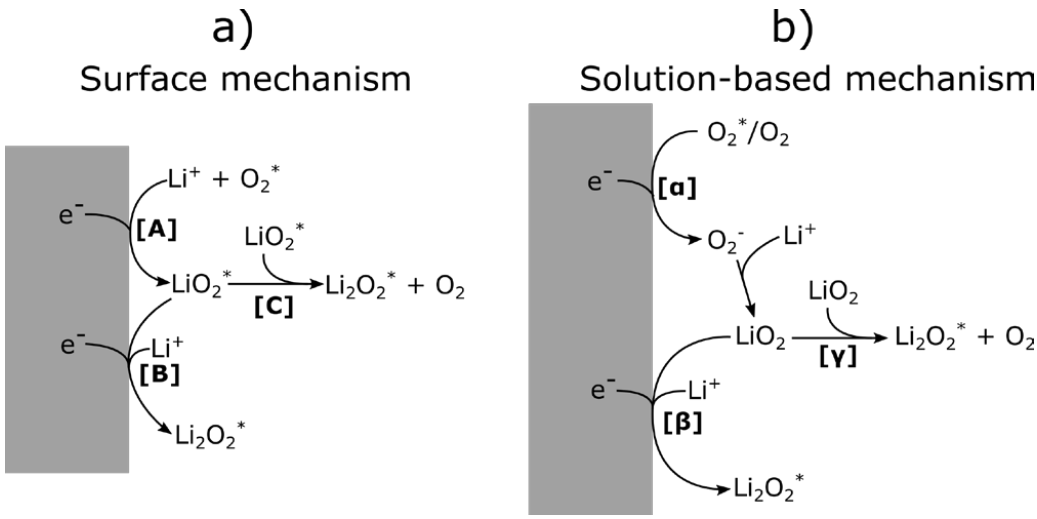

Figure 1: Schematic of the two O_2 reduction mechanisms. In a) the surface-based mechanism is depicted while the solution-based mechanism is shown in b). Species marked with (*) refers to an absorbed specie on the cathode surface.

In the surface mechanism O_2^* is reduced forming LiO_2^* **[A]**. Next $Li_2O_2^*$ is either formed by further reduction **[B]** or disproportionation with another LiO_2^* **[C]**. In the solution-based mechanism O_2^* (or O_2) is reduced to solubilized LiO_2 **[α]**, which was shown by Johnson et al.[10] to exist as solvated O_2^- and Li^+ immediately after its formation in electrolytes with high Lewis, as sketched in **Figure 1**. LiO_2 is then either further reduced **[β]** or disproportionates in solution **[γ]** to form $Li_2O_2^*$. Note that in both reaction mechanisms, *i.e.* β and γ, diffusion of LiO_2 or O_2^- results in the formation of $Li_2O_2^*$ away from the initial O_2 reduction site. $Li_2O_2^*$ formation occurs on or close to the carbon cathode as hard NMR has proven that Li_2O_2 is completely insoluble ($K_{sp} < 10^{-10}$) in most non-aqueous solvents[2]. The latter step in the solution-based mechanism **[γ]** must be the dominating reaction step in the formation of toroid deposits[9–12], as the surface-based mechanism is limited by hole transport through Li_2O_2 [A] or [B][7,8,13], and thus the reduction of O_2 to

form solubilized O_2^- or LiO_2 **[α]** must be the gateway that allows for toroidal Li_2O_2 to form on galvanostatic discharges.

In this paper, we utilize three-electrode Li-O_2 cells to separate the total cell impedance into separate contributions from the cathode and anode, respectively. In this work we have used a conventional porous electrode model to parameterize the impedance of the porous carbon cathode used in the Li-air cell. This allows characterization of the surface impedance, and thus the charge transfer resistance of the oxygen reduction reaction, along with the ionic conductivity inside the pores of the electrode, which here was studied as a function of the electrolyte composition and as a function of the type of carbon electrode. We observe an additional process in cells containing higher donor- (DN) and acceptor number (AN) electrolytes, which we interpret as a further indication of the solution-based mechanism. Lastly, we comment on the rate limiting steps of each system.

2.0 Porous electrode theory

The impedance model that describes an electronically conducting porous electrode immersed in and filled with a liquid electrolyte is known as the porous electrode theory (PET) and was first developed by de Levie and Delahay[14]. The porous electrode is modeled as a cylindrical pore containing electrolyte and the pore wall corresponds to the surface of the solid conducting electrode. This type of impedance model has frequently been used, e.g. to describe ideally polarizable porous gold- and nickel- based electrodes[15–17], composite solid state fuel cell electrodes[18,19], super capacitors[20,21], Li-ion batteries[22–24], nano-porous TiO_2 electrodes[25,26], and in conducting polymer electrodes[27,28].

The impedance of porous electrodes depends on the pore geometry, the pore size distribution, the presence and concentration of redox species, and can be further complicated by the presence of potential and concentration gradients that may arise when a dc current is running. In the absence of faradaic reaction only double-layer charging takes place and the surface impedance can be modelled with a capacitor, or more generally, with a constant phase element. When faradaic reactions take place the surface impedance must include a charge transfer resistance connected in parallel with the capacitive element modelling the double-

layer charging. For more complex situations, such as with ion intercalation into the electrode particles one or more additional impedance elements need to be included in the surface impedance, e.g. a finite space Warburg diffusion element, depending on the presence of any surface layers. In the case of the presence of significant potential or concentration gradients in the porous electrode this can further complicate the resulting impedance, but here (as discussed below) we have interpreted the impedance using a model neglecting such effects, possibly over estimating the double-layer capacitance of the porous electrode somewhat [29]. The porous electrode can be described by a general transmission line model[25,28] represented by **eq. 1-2**.

$$Z_{tot} = \frac{X_1 \cdot X_2}{X_1 + X_2} \cdot \left(L + \frac{2\lambda}{\sinh\left(\frac{L}{\lambda}\right)} \right) + \lambda \cdot \frac{X_1^2 + X_2^2}{X_1 + X_2} \cdot coth\left(\frac{L}{\lambda}\right) \quad [1]$$

with

$$\lambda = \sqrt{\frac{\zeta}{X_1 + X_2}} \quad [2]$$

Here, λ is the characteristic a.c. penetration depth [cm], which is equivalent to the electrochemical utilization thickness of the electrode, and L is the thickness of the electrode [cm], which is usually determined from cross sectional micrographs of the electrode (ignoring tortuosity of the percolating phases). **Eq. 1** represents the impedance model of a single pore (Ω) as illustrated in **Figure 2**.

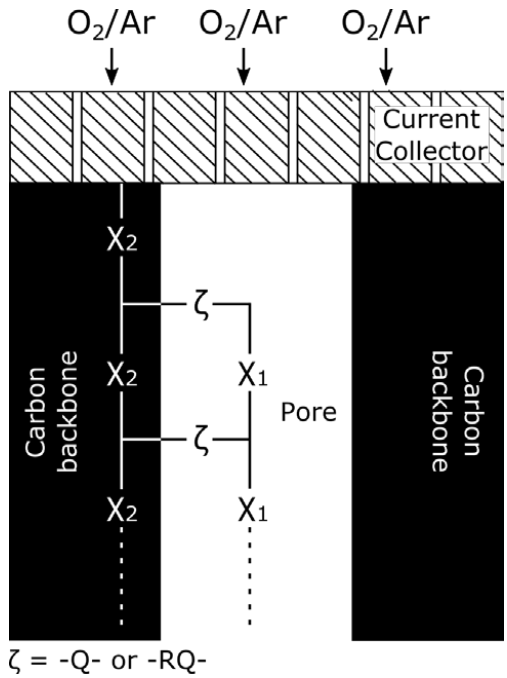

Figure 2: Illustrates a single pore of the electrode of the generalized porous electrode theory, and the equivalent circuit (a transmission line) this corresponds to.

X_1 and X_2 describe the resistance per unit length of transport channel in the liquid and electrode, respectively [Ω/cm]. ζ is the surface reaction of the flooded pores, that is *e.g.* the exchange of electrical charge at the surface related to faradaic reactions at the electrode, but could also describe double-layer charging. **Eq. 1 and 2** in principle describe the impedance of a single pore [Ω], however, the porous electrode consists of *n* columns pr. area. Although the number *n* is difficult to obtain, a convenient and equally informative approach is to consider the porous electrode as one column, as it is depicted in **Figure 2**. This enables **eq. 1-2** to be simplified to **eq. 3-5** by also considering that practical carbon electrodes have an electronic conductivity that is much greater than that of the electrolyte ($X_2 \ll X_1$):

$$Z_{tot} = \lambda \cdot X_1 \cdot coth\left(\frac{L}{\lambda}\right) \quad [3]$$

with

$$\lambda = \sqrt{\frac{\zeta}{X_1}} \quad [4]$$

Then, the transport of ions in the flooded pores can be modeled as the resistance per unit length of the electrode $[\Omega/cm]$ – *i.e.* the ionic resistance R_i.

$$X_1 = R_i \quad [5]$$

The surface impedance, ζ, of the flooded pores will, (i) in the absence of faradaic reactions, be modeled as a constant phase element, Q, to describe double layer charging and (ii) in the presence of faradaic reactions (with oxygen present in the electrolyte) as a parallel combination of a charge-transfer resistance (R_{CT}) and a constant phase element (Q), as also is depicted in **Figure 2.** The surface impedance, ζ, is then described by **eq. 6-7**, for (i) and (ii), respectively.

$$\zeta_Q = \frac{1}{Q_0 \cdot (j\omega)^n} \quad [6]$$

and

$$\zeta_{RQ} = \frac{R_{CT}}{1 + R_{CT} \cdot Q_0 (j\omega)^n} \quad [7]$$

The shape of the impedance of the flooded porous electrode gives valuable insight into the balance between the resistance of the electrolyte in the pores and the pore surface impedance. We simulated impedance data for select key cases using either **eq. 6** or **7** to model the impedance, and the corresponding Bode and Nyquist plots are shown in **Figure 3**. The impedance simulations depicted in **Figure 3a-b** illustrate the shape of the impedance in absence of faradaic reactions in the complex plane when the penetration depth is larger, similar to, or much smaller than the electrode thickness. Here a high frequency linear region is observed that is purely due to the porous nature of the electrode and as stated by Lasia and others[15,29,30] this is the best evidence to confirm whether the electrode displays any porous character. In **Figure 3c-d** the impedance in the presence of faradaic reactions is shown as a function of the ratio between R_i and R_{CT}. When R_{CT}

dominates the complex impedance exhibits an ideal semi-circle with the high frequency linear region illustrating the contribution from the porous nature of the electrode and as R_i starts to dominate the system this high frequency linear regions extends into the -RQ- forcing the complex semi-circle to be skewed. This corresponds to a penetration depth larger than the thickness of the electrode.

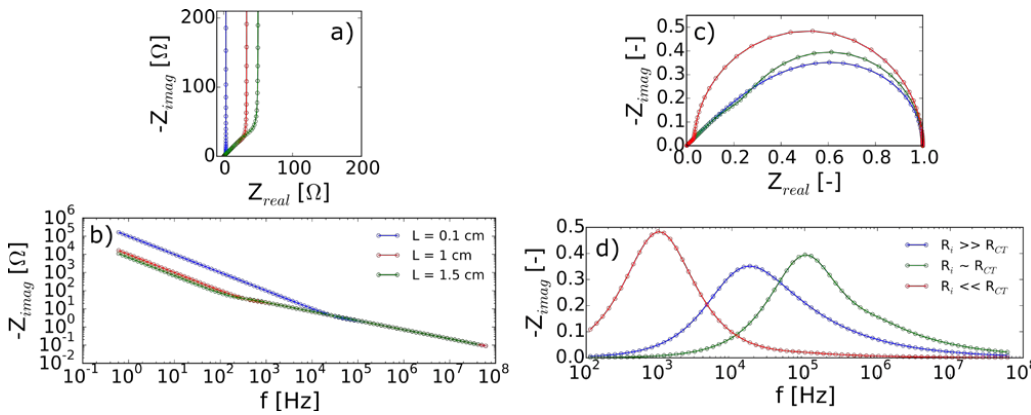

Figure 3: Impedance simulations of the PET model using two equivalent circuit elements: -Q- in (a-b) and -RQ- in (c-d). A Nyquist and Bode plot is shown for each system in (a and c) and (b and d), respectively. The simulations for (a-b) was done by varying L to 0.1, 1, and 1.5 cm while R_i, Q_0, and n were kept at 100 Ω/cm, 100 μF/cm, and 1, respectively. The simulations for (c-d) were done by varying R_i to 100, 10, and 1 Ω/cm, while R_{CT}, L, Q_0, and n were constant at 0.1 Ω ·cm, 0.1 cm, 100 μF/cm, and 1, respectively.

3.0 Experimental

3.1 Cell assembly

Li-O_2 cells were assembled in three-electrode EL-air cells (EL-cell), modified with stainless steel in- and outlets, using XC72 carbon black cathodes (Vulcan XC72, Cabotcorp, GA) or AvCarb P50 carbon paper (Fuelcellstore), mixtures of electrolytes: 1 M LiTFSI (BASF), 0.3/0.7 M LiTFSI/$LiNO_3$ (BASF), and 1 M

LiTFSI-1000 ppm H_2O in 1,2-dimethoxyethane (DME, BASF). A sketch of the RE positioning is given in **Figure S1**. Whatman QM-A glass fiber separators (VWR) and a lithium counter- and reference electrodes (FMC) were used. The carbon cathodes (diameter 18 mm) were manufactured by air-spraying a slurry of XC72 carbon black and PTFE in a wt/wt ratio of 3:1 in a 60:40 V/V ratio of water and isopropanol onto a T316 stainless 120 steel mesh (TWP Inc.). Cathodes and separators were washed in isopropanol and acetone before being dried under vacuum and 110^{o}C for 12 hrs. Cell assembly and electrolyte preparation were carried out in an Ar-filled glovebox with <0.1 ppm O_2 and < 0.1 ppm H_2O. The BET surface area of the XC72 was determined to be 235 cm^2/mg.

3.2 Planar Electrode experiments

Planar glassy-carbon (GC) disc working electrodes (d = 1.6 mm, Bio-Logic) in a glass cell containing 1 M LiTFSI-DME. The measurements were carried out in a three-electrode setup with a Pt CE and a dual-RE consisting of an double junction Ag/0.01 M AgNO3-1M LiTFSI-DME// 1 M LiTFSI-DME// in parallel with a 0.1 μF capacitor connected to a second Pt wire in solution. This RE made it possible to obtain high quality electrochemical impedance also at high (f > ~ 100 Hz) frequencies; similar RE values have previously been reported[29,31,32]. This setup is described in full detail in Knudsen et al.[6].

3.3 Electrochemical Measurements

Electrochemical measurements were performed using Bio-Logic VMP3 and VSP potentiostats. Electrochemical impedance spectroscopy (EIS) was performed potentiostatically at OCV using an a.c. amplitude of 10 mV in the frequency range 100 kHz to 50 mHz with 9 points/decade and 10 cycles/frequency. EIS also was performed galvanostatically during discharge at a d.c. current of 720 μA an a.c. amplitude of 72 μA in the frequency range 100 kHz to 10 mHz with 9 points/decade and 2 cycles/frequency and a lower cut-off electrode potential limit of 2 V vs. $Li^{0/+}$ was applied. The quality of the acquired EIS data was evaluated by a linearized Kramers-Kronig test to ensure that the rules of causality, linearity, stability and finiteness were kept[33]. Equivalent circuit models were fitted to the impedance data

using the Levenberg-Marquardt complex non-linear least squares algorithm using software programmed in Python[34], which relies on parts of the scientific Python stack[35–37].

3.4 Parameter normalization

The output parameters of the PET model fits have units normalized to the electrode thickness – *i.e.* R_{CT} $[\Omega \cdot cm]$, R_i $[\Omega/cm]$, and Q_0 $[s^n/\Omega \cdot cm]$. So to evaluate these parameters relative to each other; each variable was first re-calculated to the total value for the electrode (using the electrode thickness) and then normalized to the surface area. The ionic resistance, R_i, the charge-transfer resistance, R_{CT}, and the effective capacitance (C_{eff}) for a non-blocking porous electrode were normalized using **eq. 8a-8c**.

$$R_i = R_i \cdot L \cdot m_{carbon} \cdot BET_{area} = [\Omega \cdot cm^2] \quad [8a]$$

$$R_{CT} = \frac{R_{CT}}{L} \cdot m_{carbon} \cdot BET_{area} = [\Omega \cdot cm^2] \quad [8b]$$

$$C_{eff} = \left(\frac{1}{R_{CT}/_L \cdot (2\pi f_s)^n}\right)^{1/n} \cdot \left(\frac{R_s \cdot R_{CT}}{R_s + R_{CT}}\right)^{\frac{1-n}{n}} \cdot \frac{1}{m_{carbon} \cdot BET_{area}} = [F/cm^2] \quad [8c]$$

As we use a constant phase element, Q, to describe the capacitance of the surface within the PET model, the parameter Q (an admittance) found from model fits, was recalculated to effective capacitance as described by Brug et al. and Hirschorn et al. [9,38]. For a flat planar electrode, the effective capacitance here denoted C_{dl}, measured in the absence of faradaic reactions, was determined by **eq. 9** [38,39]:

$$C_{dl} = (Q_0 \cdot L \cdot R_s^{1-n})^{1/n} \cdot \frac{1}{m_{carbon} \cdot BET_{area}} = [F/cm^2] \quad [9]$$

3.5 Microscopy

The microstructure of the pristine XC72 cathodes was investigated by inspection of polished cross-sections in a Hitachi TM3000 tabletop scanning electron microscope (SEM), **Figure S2**. The polished cross-sections were prepared by vacuum embedding the electrodes in silicone rubber (Elastosil RT 675 A/B, Wacker Silicones); ground using SiC paper and polished using 6, 3, and 1 μm diamond paste.

4.0 Results

Figure 4 illustrates a galvanostatic discharge curve of an XC72 cathode in 1 M LiTFSI-DME. The 4 curves represented in the figure illustrate the traditional cell (2-terminal) potential, the individual electrode potentials of the cathode and anode vs. the RE, respectively. It is clear that a small part of the cells overpotential (~6 mV) originates from the Li anode whereas the dominant part (~200 mV) originates from the electrochemical reactions on the cathode surface. Also, the sudden drop in potential (sudden-death) towards the end of discharge is purely due to the increase in the overpotential related to the cathode.

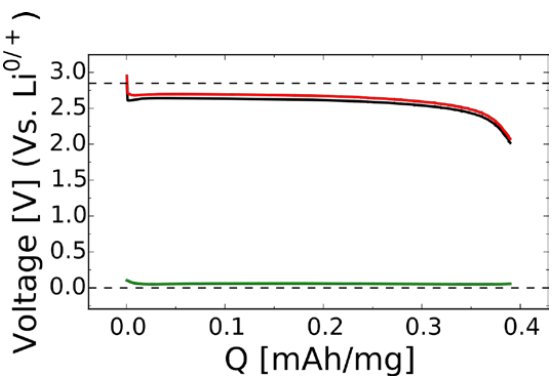

Figure 4: A galvanostatic discharge curve of 1 M LiTFSI-DME operated under a constant pressure of 1060-1080 Torr. The cell was maintained at constant pressure by keeping it connected to the inlet gas line. The black curve is the cell, potential; the red and green curves are the cathode- and anode potentials vs. the reference $Li^{0/+}$ electrode, respectively. The two dotted lines are the theoretical electrode potentials of the cathode and anode (0 V and ~2.85 V) if no overpotential exists (at zero d.c. bias).

4.1 Electrode specific and overall cell impedance

The impedance of the anode, cathode, and the total cell impedance were obtained simultaneously and examples are shown in **Figure 5**, as the impedance of four different cells with three different electrolytes and two types of cathodes, XC72 and P50 are depicted. The impedance presented in **Figure 5** was measured in

pristine cells under an Ar atmosphere, and at OCV (~3.2 V), hence none of the electrochemical processes in **Figure 5** can be related to the reduction of O_2 and the formation of Li_2O_2. The cell impedance is the total 2-terminal impedance (2-terminal) of the cell the cathode impedance is the measured response between the cathode and RE, while the anode impedance is the response between the anode and RE. The three-electrode measurements, along with a measurement configuration that allows simultaneous acquisition of both the overall cell impedance and the individual anode and cathode impedance, are combined with the porous electrode model for the cathode to provide a good overview of all processes taking place in the cell.

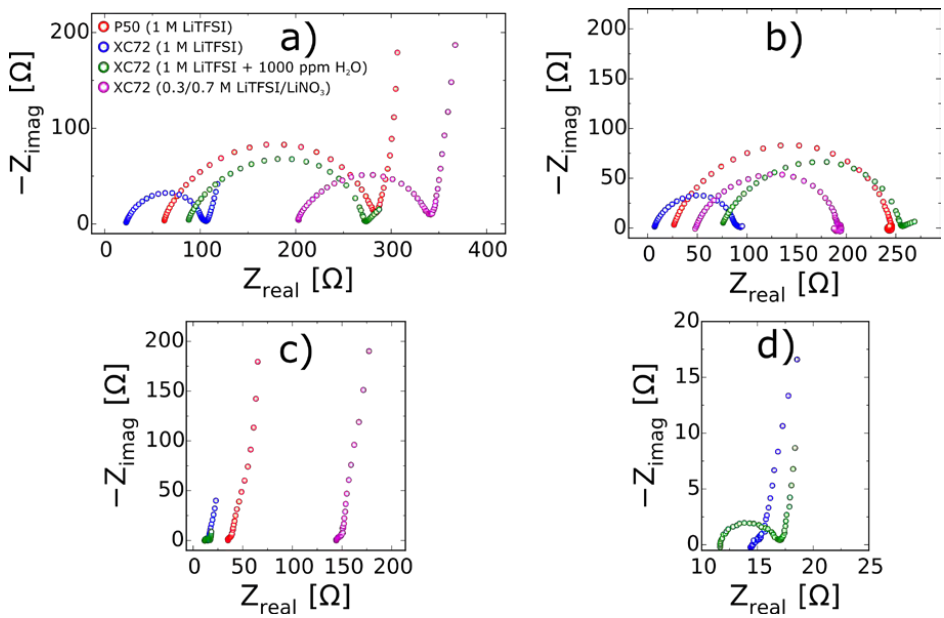

Figure 5: The overall cell impedance spectra (a) and the impedance spectra of the anode (b) and cathode (c), respectively, represented in the Nyquist plot. (d) is a magnification of the cathode impedance in (c). Measurements were taken at OCV under an Ar atmosphere. Red

The impedance of the anode displays depressed high frequency semicircles that were activated by the a.c. perturbation of 10 mV around the OCV. The depressed semi-circle likely consists of multiple contributions,

but is mainly related to Li plating and stripping, with a likely further contribution from Li^+ transport through the solid electrolyte interphase (SEI) on Li[13,40]. It is noteworthy that the high frequency semicircle from the anode is, most often, the only contribution to the high frequency semicircle observed in the cell impedance (2-terminal) at these conditions.

Throughout the remainder of this article, we will focus on the cathode impedance since, as illustrated in **Figure 4**, this is the performance limiting electrode and a detailed analysis of the anode impedance is considered beyond the scope of this paper.

4.2 The cathode impedance at OCV in Ar

The cathode impedance at OCV of the three cells in an Ar atmosphere is presented in **Figure 6** and displays an expected capacitive nature, as no redox active species are present; with the exception of the cell with water added to the electrolyte. To further investigate the nature of the high frequency linear region, two cathodes with different XC72 loadings were analyzed under equivalent conditions as presented in **Figure 6A.**

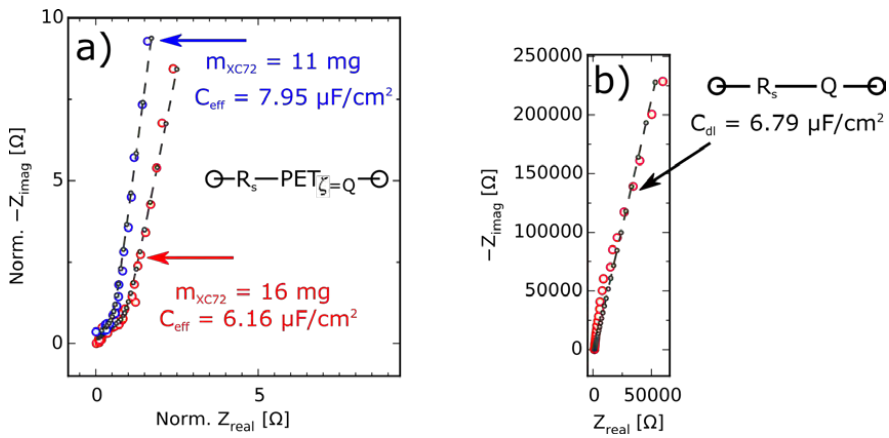

Figure 6: a) The impedance of two different loading of XC72 measured in Ar at OCV is depicted in a Nyquist plot. The equivalent circuit is also illustrated, where R_s is the series resistance while the $PET_{\zeta=Q}$ is the PET model with $\zeta = Q$, where Q is a constant phase element used to describe the capacitive

nature of the porous electrode at these conditions. For easier comparison Z_{real} and Z_{imag} were normalized to start at the origin, (0,0). b) The working electrode impedance from a three-electrode cell with a 1.6 mm glassy-carbon working electrode in Ar saturated 1 M LiTFSI-DME at OCV.

The capacitances shown in the figure were determined by fitting the equivalent circuit depicted in **Figure 6a** to the cathode impedance and the parameters from the fit were used in **eq. 8C** to determine the capacitance of the surfaces and are reported in the figure. For comparison, the impedance of an ideal planar glassy-carbon disc electrode was also investigated. The impedance of a flat planar glassy-carbon electrode under similar conditions, *i.e.* at OCV in Ar and without the presence of any redox active species, is shown in **Figure 6b**. This impedance was fitted using an equivalent circuit consisting of an electrolyte resistance (R_s) in series with a constant phase element (Q) that represents double-layer charging in the surface impedance of the porous electrode model. The equivalent capacitance was calculated using **eq. 9** and is given in **Figure 6**. The capacitance was found to be 6.79 μF/cm^2 for the planar GC electrode and 6.16-7.95 μF/cm^2 (XC72 carbon) for the porous electrodes, in 1 M LiTFSI-DME.

4.3 The cathode impedance in O_2 during galvanostatic discharge

To investigate the impact on the impedance under conditions where either the surface- and/or the solution-based mechanisms are favored; three cells containing XC72 cathodes with 1 M LiTFSI-DME, 0.3/0.7 M LiTFSI/LiNO3-DME, and 1 M LiTFSI-DME with 1000 ppm H_2O, respectively, were investigated under galvanostatic conditions. To ensure that O_2 was not a limiting factor, all cells were kept at a partial pressure of O_2 (pO_2) at 1000-1100 Torr, as presented in **Figure 7a**. The discharge capacities found were, in increasing order, 1 M LiTFSI (~0.4 mAh/mg), 0.3/0.7 M LiTFSI/$LiNO_3$ cell (~1.5 mAh/mg), and 1M LiTFSI with 1000 ppm H_2O (~ 1.8 mAh/mg).

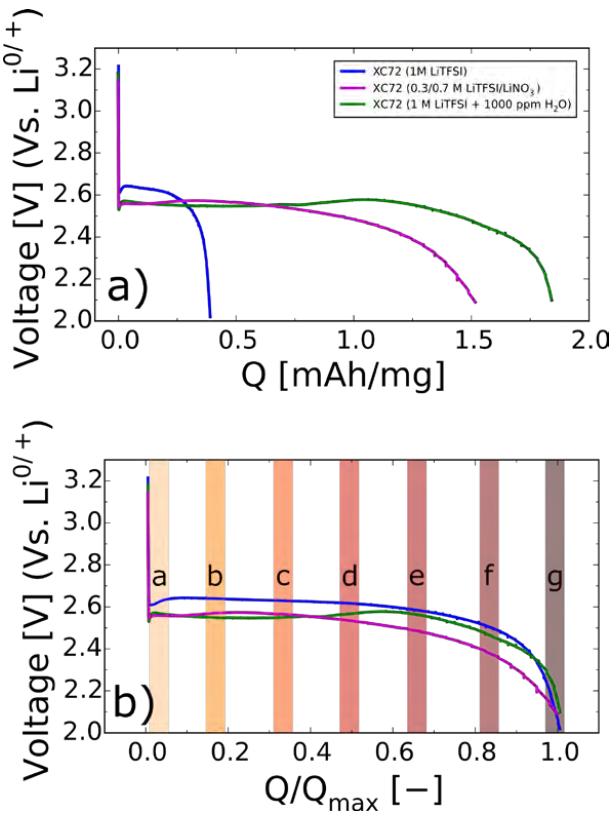

Figure 7: a) Galvanostatic discharge curves for the three XC72 cells with varying electrolyte. b) The equivalent normalized discharge curves. The pO_2 was kept constant at 1000-1100 Torr throughout the discharges.

To evaluate the rate limiting steps in these Li-O_2 batteries, we must understand the impedance of the cathode under operation. The impedance was measured throughout the discharge until sudden-death, but for practical reasons we present only the Nyquist and Bode plots for seven selected spectra, each of which were obtained during discharge in the regions labeled **a-g** in **Figure 7b**. The corresponding Nyquist and Bode-like plots for the seven regions are presented in **Figure 8 and 9**, respectively.

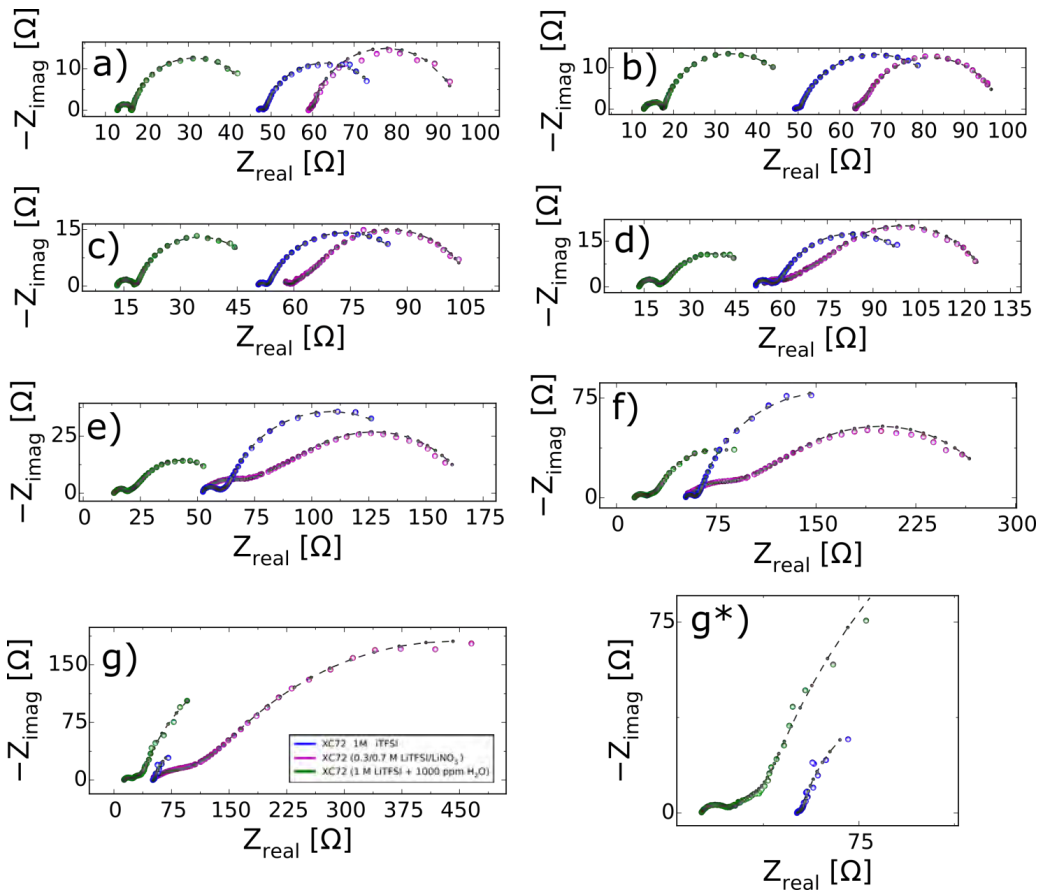

Figure 8: The progression of the galvanostatic impedance as a function of state-of-discharge: The **regions a-g** illustrate a specific state of normalized discharge capacity as is depicted in **Figure 7**, while (g*) is a magnification of the data in (g).

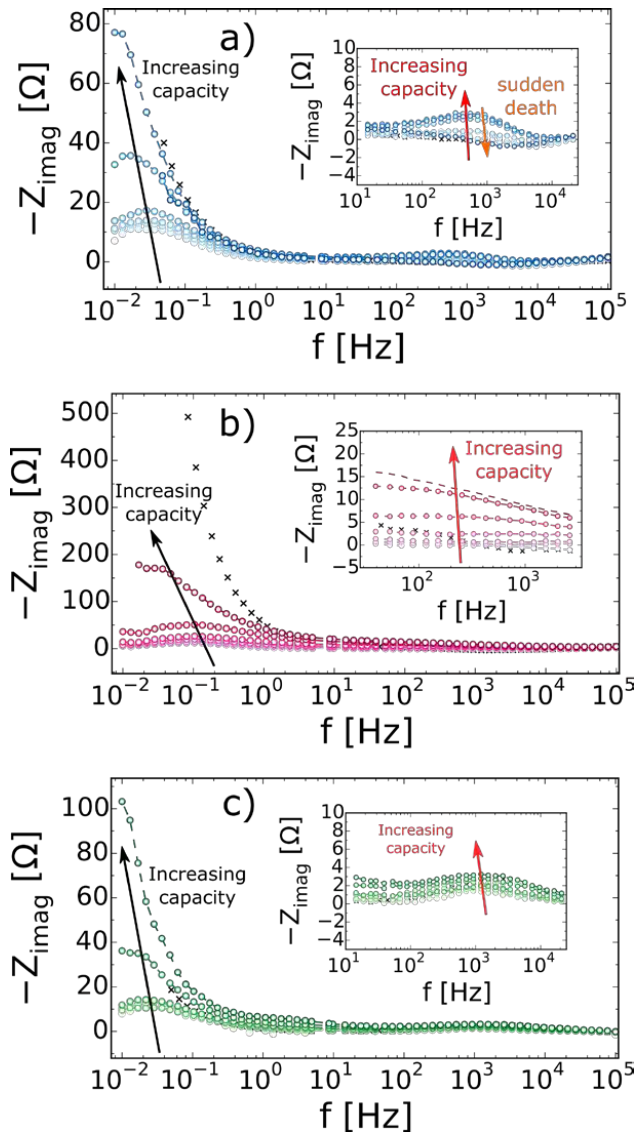

Figure 9: The Bode plot of the three cells containing (a) 1 M LiTFSI-DME, (b) 0.3/0.7 M LiTFSI/$LiNO_3$-DME, and (c) 1 M LiTFSI-DME with 1000 ppm H_2O. The spectra recorded under Ar atmosphere are marked with (x) and the 7 regions of galvanostatic impedance are represented so that the color intensity increases as the impedance progress from **region a-g** with respect to the normalized discharge capacity, as illustrated in **Figure 7b**.

To understand the contribution of each process to the cell performance, as well as to clarify the cause of the low frequency and high frequency semicircles, seen in **Figure 8 and 9**, the impedance of the three cells was fitted using the equivalent circuit: -$(RQ)_1$-$PET_{\zeta=RQ_2}$-, where $(RQ)_1$ is the high frequency (HF) semicircle observed at 10^2-10^4 Hz and $(RQ)_2$ is the low frequency (LF) semicircle observed at 10^{-2}-10^1 Hz inside of the PET model. The resulting parameters were normalized using **eq. 8a-8c** and each parameter is illustrated as a function of the normalized discharge capacity in **Figure 10**.

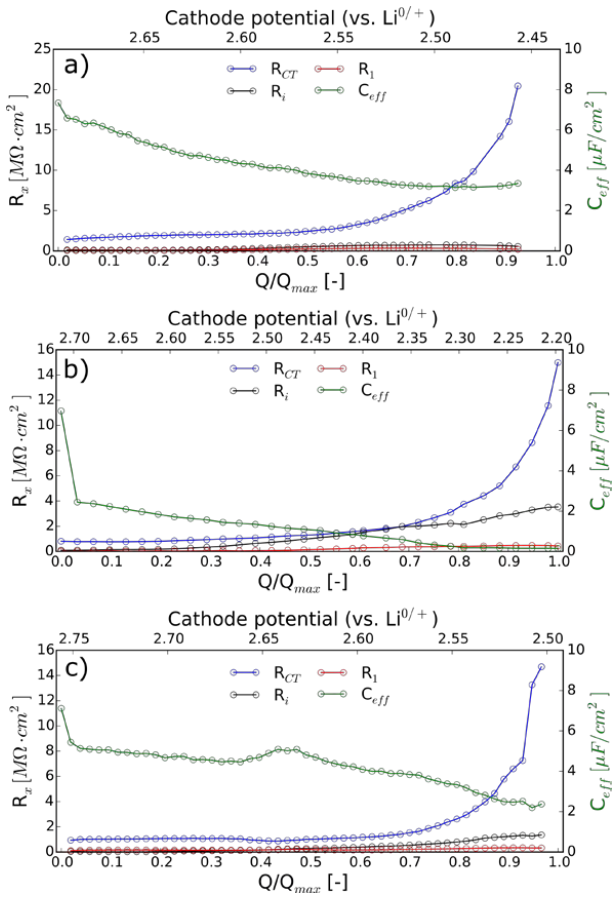

Figure 10: Resistances and capacitances from fitting the equivalent circuit -$(RQ)_1$-$PET_{\zeta=RQ_2}$- to the three different systems: (a) 1 M LiTFSI-DME, (b) 0.3/0.7 M LiTFSI/$LiNO_3$-DME, and (c) 1 M LiTFSI-DME with 1000 ppm H_2O. The parameters were normalized using **eq. 8a-8c.**

4.4 The impedance of a flat planar electrode

The impedance of the faradaic reaction was also investigated using a planar glassy-carbon electrode in O_2 saturated 1 M LiTFSI-DME under similar conditions, and galvanostatic mode. The resulting Nyquist and Bode plot for the initial discharge is shown in **Figure 11**. Here a less complicated impedance spectrum is observed, as the electrode is flat, and the reaction is under kinetic control.

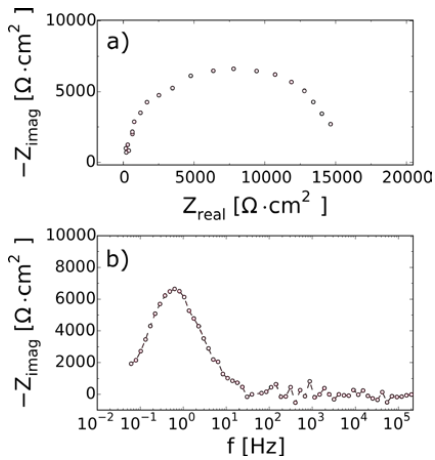

Figure 11: The initial impedance of a glassy-carbon electrode during discharge in 1 M LiTFSI-DME at 2.5 μA/cm^2. The corresponding Nyquist (a) and Bode-like (c) are shown.

5.0 Discussion

Figure 7a show a significant dependency between the discharge capacity and the composition of the electrolyte. In short, this is caused by a change in the Li_2O_2 formation mechanism. The increased capacity of $LiNO_3$ containing cells was first reported by Burke et al.[9] to be the consequence of an increased donor number of the electrolyte, as Li^+ ions are shielded by the NO_3^- counter-ion, thereby inducing an increased stability of Li^+ in solution, which shifts the equilibrium of LiO_2 solvation and-, promote the solution-based Li_2O_2 formation mechanism illustrated in **Figure 1b**. The same solution mechanism enhancement has been reported for H_2O containing cells, where H_2O is postulated to behave as a strong Lewis Acid, thereby increasing the acceptor number of the electrolyte and stabilizing O_2^-, which again allows Li_2O_2 formation through the solution-based mechanism[11]. In both cases, large toroid shaped Li_2O_2 deposits form, and on the basis of the impedance results, we propose that toroids form through the solution-based mechanism in **Figure 1,** allowing higher discharge capacities compared to an all-surface-based mechanism, as in the 1 M LiTFSI-DME cell, where no toroid formation is observed, indicating only thin, conformal Li_2O_2 films are formed on the cathode surface.

We argue that the two activated electrochemical processes detected when applying a current, *i.e.* the LF- and HF semicircles, are mainly related to the formation of Li_2O_2 since (i) we observe a ~2-2.1e^-/O_2 reaction from pressure measurements while discharging similar cells under a closed headspace filled with O_2, illustrated in **Figure S3-S5**; (ii) multiple authors have also reported Li_2O_2 to be the main deposition product in these three solvents[10,11,11,12]; and (iii) an impedance-study of Li-O_2, using two terminal Swagelok cells, observed the same LF semicircle in the same frequency range for 1 M LiTFSI-DME containing cells [41].

5.1 The cathode impedance in Ar and at OCV

The linear region at high frequencies observed before the lower frequency capacitive process in **Figure 6** is in agreement with the predicted by porous electrode theory and is in agreement refs.[16,29,30], where this linear region resulted from processes occurring in a porous electrode. The effect of the carbon loading on the high frequency linear region, which is modeled as an increase in pore length shown in **Figure 2**, is illustrated

in **Figure 6a.** From the similar double-layer capacitances of the two electrodes, we can conclude the areal carbon specific loading does not influence the chemical nature of the cathode processes and that indeed the ionic resistance within the pores was the cause of the high frequency linear region. This high frequency behavior also correlates with impedance simulations performed using the PET, as illustrated in **Figure 3**, where the linear region at high frequencies increased as L is increased. A further argument for attributing this linear region at high frequencies to the pore length was the comparison to the impedance of a planar glassy-carbon electrode, **Figure 6b**, which was performed in the same electrolyte. Here, the impedance is seen as purely capacitive and the high frequency linear region is absent. The impedance and the fit confirm the fundamental difference between the impedance of a planar and porous cathode in Li-O_2 batteries. **Figure 6** also illustrates the similarities of the non-faradaic processes on planar and porous electrodes, as the double-layer capacitance irrespective of the electrode was 6-8 μF/cm^2, which is in good agreement with previous reported double-layer capacitances of 5.25 μF/cm^2 for Vulcan XC72 in non-aqueous electrolytes[42]. The exception of the high frequency linear region was the XC72 cell containing 1M LiTFSI-1000 ppm H_2O (**Figure 5d**), which can clearly be ascribed to the redox active specie H_2O being oxidized and reduced by the 10 mV amplitude. This is confirmed as the double-layer capacitance obtained for this process was determined to a reasonable 8.9 μF/cm^2 using the projected area of the current collector and **eq. 8c**. All of these observations confirm that the PET model can be applied to the Li-O_2 batteries studied in this article.

5.2 The cathode impedance under an O_2 headspace in galvanostatic operation

As shown in **Figure 6 and 8** the impedance of the same cell measured at OCV and galvanostatic mode is fundamentally different. At OCV under either Ar or O_2, the impedance of the cell exhibits behavior expected of non-faradaic processes, as no electrochemical reactions will occur in the 10 mV impedance amplitude given the modest (~200 mV[5]) overpotentials for the Li/O_2 reaction. In galvanostatic mode, impedance measures charge and mass transfer processes related to the active electrochemical reactions occurring at the electrodes. In principle, we can therefore isolate capacitive and Faradaic processes, allowing us to conclude that the semicircles observed in Ar and at OCV (**Figure 5 and 6**) are not related to Li_2O_2 formation, while

the Nyquist plot semicircles (**Figure 8 and 11**) that only are detected in galvanostatic mode under O_2 must be related to the formation of Li_2O_2, as ~2-2.1 e^-/O_2 is observed during these processes, **Figure S4-S6**.

5.2.1 The LF semicircle

In **Figure 8 and 9,** the three cells initially display near-ideal LF semicircles in the initial **region a**. By relating this observation to the simulations in **Figure 3**, we understand that the LF process is limited by R_{CT} (the charge-transfer resistance) in the PET model. As the state-of-discharge increases, **region b-f**, the LF semicircle of the three cells in general become more skewed, which our models ascribe to an increase in ionic resistance in the pores of the cathode, R_i, as shown in **Figure 10**. Intuitively, this increase in R_i is expected, as the formed Li_2O_2 is insoluble in DME[2] and accumulates in the pores, causing an increase in R_i. Near sudden-death, **region g**, the 0.3/0.7 M LiTFSI/$LiNO_3$ cell is significantly more skewed than the other two cells that again display more ideal semicircles. This is interpreted, using the model simulations presented in **Figure 3**, as the former cell being dominated to a larger degree by R_i, where the two latter cells are almost completely dominated by R_{CT}.

The experiments with the flat planar electrode revealed that the LF semicircle was the only electrochemical process detected, since this setup was less prone to water contamination as it contained a larger volume of electrolyte and the electrodes, *i.e.* no separator or highly porous carbon cathodes, **Figure 11**. The LF semicircle was detected in a similar frequency range (10^{-2}-10^{1} Hz) as in the three cells with porous XC72 electrodes. We therefore suggest that the LF semicircle is related to the surface induced formation of Li_2O_2, as Højberg et al.[41] also observed an electrochemical process in 1 M LiTFSI-DME in the same frequency range.

5.2.2 The HF semicircle

The 0.3/0.7 M LiTFSI/$LiNO_3$-based cell displayed an approximately four-fold discharge capacity increase while maintaining similar Li_2O_2 yields (80-90 %) compared to the other two cells [9]. Burke et al. [9] ascribe the increase in capacity to the increase in the Lewis basicity of the electrolyte with added $LiNO_3$, which results in the promotion of the solubility mechanism (**Figure 1b**)[9–12]. We would therefore expect that the resistance

related to the HF semicircle, R_1, which we have speculatively ascribed to a process associated with the solution-mechanism process, should increase in the $LiNO_3$-bearing cell. We therefore compare the 1 M LiTFSI (0 M $LiNO_3$) and the 0.3/0.7 LiTFSI/$LiNO_3$, which Burke et al.[9] identified as the LiTFSI/$LiNO_3$ ratio that provided the largest capacity enhancement and as expected, the HF semicircle was detected to a much larger degree in the cell with 0.3/0.7 M LiTFSI/$LiNO_3$. This may indicate that the resistance associated with the HF semi-circle is the faradaic charge-transfer resistance of the solution-based mechanism, **reaction [A]** in **Figure 1**, but as the HF semicircle also was detected throughout the discharge in the water-containing cell (**Figure 5**) and in Ar and at OCV for this cell; this suggests otherwise. Determining the double-layer capacitance of the HF process, for these two cells, yields area specific capacitance values of 10-50 μF/cm^2 during discharge, pointing to that the HF process likely occurs at the current collector / electrode interface. Therefore it is most likely a concurrent reduction of H_2O (in the case of the cell tested under Ar with water added to the electrolyte), or O_2 and/or NO_3^- reduction taking place at the current collector in the cases where it is observed under an O_2 atmosphere. The HF semicircle was even observed in the 1M LiTFSI cell, where neither H_2O nor $LiNO_3$ should be available. It is suspected that minor water impurities likely contribute to the HF semicircle observed in the 1M LiTFSI cell and to this end, electrolytes were used as received and contained ~25 ppm H_2O as determined via Karl Fischer titration, and although the cathodes used in this study were dried at 200^{o}C in a glovebox, their high surface area porosity could retain small amounts of water. however, note that the magnitude of the HF process is small in the 1M LiTFSI cell and disappears completely as a function of state-of-discharge (**Figure 8-10**), which possibly could be ascribed to water being consumed at the Li metal anode. However O_2 reduction on the current collector surface could just as likely be ascribed to the HF process.

5.2.3 Rate limiting steps

The parameters obtained from the fit that describes the cell performance are illustrated as a function of the normalized discharge capacity in **Figure 10**. The three cells can be compared until approx. 90 % of the normalized discharge capacity as the Kramers-Kronig relations no longer were satisfied. In general it can be seen that R_i increases more with the state of discharge when the solution-based mechanism is favored, which

in terms of the PET model can be understood as the insulating, toroidal shaped, Li_2O_2 builds up within the pores forcing R_i to increase. In the PET model, R_{CT} will increase with an increasing thickness of Li_2O_2 on the surface of the electrode, which favors the surface-based mechanism in **Figure 1**. This is the case for the 1 M LiTFSI-DME cell where R_i also is lowest and R_{CT} the highest, as multiple reports[9–12,43,44] have concluded that only the surface-based mechanism is active in this electrolyte resulting in the formation of a conformal Li_2O_2 deposit. This is further demonstrated by the effective capacitance, determined using **eq. 8c**, of the LF semicircle (**Figure 10**) as the capacitance at sudden-death for the 1 M LiTFSI-DME cell is 3.35 μF/cm^2 corresponding to a theoretical Li_2O_2 thickness of ~9.25 nm, which was estimated using the dielectric constant of Li_2O_2 of 35[45] and **eq. 10**.

$$C = \frac{\varepsilon_{Li2O2} \cdot \varepsilon_0 \cdot A/d}{A} \quad \textbf{[10]}$$

Where ε_0 is the permittivity of vacuum (8.854 x 10^{-14} F/cm). This is in great agreement with studies on glassy-carbon electrodes that report thicknesses of 5-10 nm were conformal deposits are observed[6,8]. However the $LiNO_3$ and H_2O containing cells obtained C_{eff} of 0.15 and 2.37 μF/cm^2 at sudden-death (**Figure 10**) resulting in the unreasonable theoretical a thicknesses of 206.59 and 13.07 nm. Obviously, this was due to the assumption of conformal Li_2O_2 deposition, which does not apply in these electrolytes as the solution-based mechanism is activated in these cells. This is also demonstrated by the higher ionic resistances, R_i, in these cells compared to the 1 M LiTFSI-DME cell (**Figure 10**) as toroidal shaped Li_2O_2 buildup in the porous structure of these cathodes[9,11,12]. The sudden-death of all three cells was still caused by the surface-based mechanism as R_{CT} is the dominating cathode resistance at sudden-death. This is in agreement with the planar electrode experiment, where the charge transport through Li_2O_2, R_{CT}, could no longer support the applied electrochemical current, forcing R_{CT} to greatly increase[6,8], **Figure 11**. Physically, the increase is caused as the hole tunneling barrier in Li_2O_2 increase exponentially and are no longer able to support the applied current, at these current densities[6–8,46].

5.3 O_2 Dependency

All cells presented in the main manuscript where analyzed at a constant pO_2 of 1000-1100 Torr. Initially, we also investigated cells under a closed headspace at an initial pO_2 of 1650 Torr, **Figure S3-S5**, but obtained similar discharge capacities for the 0.3/0.7 M LiTFSI/$LiNO_3$ and the 1000 ppm H_2O containing cell, as the sudden-death was caused by oxygen diffusion. This can be demonstrated as the pO_2 at sudden-death was approximately 50-250 Torr, which corresponds to an approximate decrease of $[O_2]$ from ~22.2 mM at 1650 Torr to ~0.7-3.4 mM at 50-250 Torr as estimated using Henry's constant for O_2 solubility in DME ($K_H = 1.347 \cdot 10^{-5}$ mol/L·Torr) determined by Hartmann et al.[47].

6.0 Summary

In this paper, we have performed electrochemical impedance spectroscopy on Li-O_2 cells and by using different electrolytes; we studied the surface- and solution-based mechanisms of Li_2O_2 growth. Utilizing a 3-electrode configuration it was possible to separate the impedance into a cathodic and anodic contribution. The cathodic impedance displayed 2 electrochemical processes, *i.e.* a high and a low frequency process, respectively.

In general, the two processes were detected in Ar at OCV, but could be activated by applying a current in an O_2 atmosphere. Through comparison with known literature and using similar experimental conditions on a flat planar electrode, we could conclude that the low frequency process was related to the surface formation of Li_2O_2, while the high frequency process was attributed to an additional redox reaction with either H_2O or NO_3^-.

We also successfully applied a porous electrode theory model to understand the impedance of the cathode and we could relate the ionic resistance, of this model, to the increased formation of toroidal shaped Li_2O_2 as it forms in the pores of the cathode, when the solution-based mechanism is activated.

7.0 Acknowledgments

The authors gratefully acknowledge financial support from the ReLiable project (project No. 11-116792) funded by the Danish Council for Strategic Research, Program Commission on Sustainable Energy and Environment.

8.0 References

(1) Abraham, K. M.; Jiang, Z. A Polymer Electrolyte-Based Rechargeable Lithium/Oxygen Battery. *J. Electrochem. Soc.* **1996**, *143* (1), 1–5.

(2) Luntz, A. C.; McCloskey, B. D. Nonaqueous Li–Air Batteries: A Status Report. *Chem. Rev.* **2014**.

(3) Black, R.; Oh, S. H.; Lee, J.-H.; Yim, T.; Adams, B.; Nazar, L. F. Screening for Superoxide Reactivity in Li-O2 Batteries: Effect on Li2O2/LiOH Crystallization. *J. Am. Chem. Soc.* **2012**, *134* (6), 2902–2905.

(4) Kwabi, D. G.; Batcho, T. P.; Amanchukwu, C. V.; Ortiz-Vitoriano, N.; Hammond, P.; Thompson, C. V.; Shao-Horn, Y. Chemical Instability of Dimethyl Sulfoxide in Lithium–Air Batteries. *J. Phys. Chem. Lett.* **2014**, *5* (16), 2850–2856.

(5) Hummelshøj, J. S.; Blomqvist, J.; Datta, S.; Vegge, T.; Rossmeisl, J.; Thygesen, K. S.; Luntz, A. C.; Jacobsen, K. W.; Nørskov, J. K. Communications: Elementary Oxygen Electrode Reactions in the Aprotic Li-Air Battery. *J. Chem. Phys.* **2010**, *132* (7), 071101.

(6) Knudsen, K. B.; Luntz, A. C.; Jensen, S. H.; Vegge, T.; Hjelm, J. A Redox Probing Study of the Potential Dependence of Charge Transport through Li2O2. *J. Phys. Chem. C* **2015**.

(7) Luntz, A. C.; Viswanathan, V.; Voss, J.; Varley, J. B.; Nørskov, j. K.; Scheffler, R.; Speidel, A. Tunneling and Polaron Charge Transport through Li2O2 in Li–O2 Batteries. *J. Phys. Chem. Lett.* **2013**, *4 (20)*, 3494-3499.

(8) Viswanathan, V.; Thygesen, K. S.; Hummelshøj, J. S.; Nørskov, J. K.; Girishkumar, G.; McCloskey, B. D.; Luntz, A. C. Electrical Conductivity in Li2O2 and Its Role in Determining Capacity Limitations in Non-Aqueous Li-O2 Batteries. *J. Chem. Phys.* **2011**, *135* (21), 214704–214704.

(9) Burke, C. M.; Pande, V.; Khetan, A.; Viswanathan, V.; McCloskey, B. D. Enhancing Electrochemical Intermediate Solvation through Electrolyte Anion Selection to Increase Nonaqueous Li–O2 Battery Capacity. *Proc. Natl. Acad. Sci.* **2015**, 9293-9298.

(10) Johnson, L.; Li, C.; Liu, Z.; Chen, Y.; Freunberger, S. A.; Ashok, P. C.; Praveen, B. B.; Dholakia, K.; Tarascon, J.-M.; Bruce, P. G. The Role of LiO2 Solubility in O2 Reduction in Aprotic Solvents and Its Consequences for Li–O2 Batteries. *Nat. Chem.* **2014**, *6* (12), 1091–1099.

(11) Aetukuri, N. B.; McCloskey, B. D.; García, J. M.; Krupp, L. E.; Viswanathan, V.; Luntz, A. C. Solvating Additives Drive Solution-Mediated Electrochemistry and Enhance Toroid Growth in Non-Aqueous Li–O2 Batteries. *Nat. Chem.* **2015**, *7* (1), 50–56.

(12) Schwenke, K. U.; Metzger, M.; Restle, T.; Piana, M.; Gasteiger, H. A. The Influence of Water and Protons on Li2O2 Crystal Growth in Aprotic Li-O2 Cells. *J. Electrochem. Soc.* **2015**, *162* (4), A573–A584.

(13) Koch, V. R.; Nanjundiah, C.; Appetecchi, G. B.; Scrosati, B. The Interfacial Stability of Li with Two New Solvent-Free Ionic Liquids: 1,2-Dimethyl-3-propylimidazolium Imide and Methide. *J. Electrochem. Soc.* **1995**, *142* (7), L116–L118.
(14) De Levie, R.; Delahay, P. *Advances in Electrochemistry and Electrochemical Engineering*; 6; Wiley-Interscience: New York; Vol. **1967**.
(15) Hitz, C.; Lasia, A. Experimental Study and Modeling of Impedance of the Her on Porous Ni Electrodes. *J. Electroanal. Chem. 500* (1–2), 213–222.
(16) Jurczakowski, R.; Hitz, C.; Lasia, A. Impedance of Porous Au Based Electrodes. *J. Electroanal. Chem.* **2004**, *572* (2), 355–366.
(17) Jurczakowski, R.; Hitz, C.; Lasia, A. Impedance of Porous Gold Electrodes in the Presence of Electroactive Species. *J. Electroanal. Chem.* **2005**, *582* (1–2), 85–96.
(18) Nielsen, J.; Hjelm, J. Impedance of SOFC Electrodes: A Review and a Comprehensive Case Study on the Impedance of LSM:YSZ Cathodes. *Electrochimica Acta* **2014**, *115*, 31–45.
(19) Nielsen, J.; Klemensø, T.; Blennow, P. Detailed Impedance Characterization of a Well Performing and Durable Ni:CGO Infiltrated Cermet Anode for Metal-Supported Solid Oxide Fuel Cells. *J. Power Sources* **2012**, *219*, 305–316.
(20) Conway, B. E. *Electrochemical Supercapacitors*; Kluwer Academic/Plenum Publishers: New York, **1999**.
(21) Kötz, R.; Carlen, M. Principles and Applications of Electrochemical Capacitors. *Electrochimica Acta* **2000**, *45* (15–16), 2483–2498.
(22) Barsoukov, E.; Kim, J. H.; Kim, J. H.; Yoon, C. O.; Lee, H. Kinetics of Lithium Intercalation into Carbon Anodes: In Situ Impedance Investigation of Thickness and Potential Dependence. *Solid State Ion.* **1999**, *116* (3–4), 249–261.
(23) Lundqvist, A.; Lindbergh, G. Kinetic Study of a Porous Metal Hydride Electrode. *Electrochimica Acta* **1999**, *44* (15), 2523–2542.
(24) Maja, M.; Orecchia, C.; Strano, M.; Tosco, P.; Vanni, M. Effect of Structure of the Electrical Performance of Gas Diffusion Electrodes for Metal Air Batteries. *Electrochimica Acta* **2000**, *46* (2–3), 423–432.
(25) Bisquert, J.; Garcia-Belmonte, G.; Fabregat-Santiago, F.; Ferriols, N. S.; Bogdanoff, P.; Pereira, E. C. Doubling Exponent Models for the Analysis of Porous Film Electrodes by Impedance. Relaxation of TiO2 Nanoporous in Aqueous Solution. *J. Phys. Chem. B* **2000**, *104* (10), 2287–2298.
(26) Fabregat-Santiago, F.; Bisquert, J.; Garcia-Belmonte, G.; Boschloo, G.; Hagfeldt, A. Influence of Electrolyte in Transport and Recombination in Dye-Sensitized Solar Cells Studied by Impedance Spectroscopy. *Sol. Energy Mater. Sol. Cells* **2005**, *87* (1–4), 117–131.
(27) Bisquert, J.; Belmonte, G. G.; Santiago, F. F.; Ferriols, N. S.; Yamashita, M.; Pereira, E. C. Application of a Distributed Impedance Model in the Analysis of Conducting Polymer Films. *Electrochem. Commun.* **2000**, *2* (8), 601–605.
(28) Bisquert, J.; Garcia-Belmonte, G.; Fabregat-Santiago, F.; Compte, A. Anomalous Transport Effects in the Impedance of Porous Film Electrodes. *Electrochem. Commun.* **1999**, *1* (9), 429–435.
(29) Lasia, A. Electrochemical Impedance Spectroscopy and Its Applications. In *Modern Aspects of Electrochemistry*; Conway, B. E., Bockris, J. O., White, R. E., Eds.; Modern Aspects of Electrochemistry; Springer US, **2002**.

(30) de Levie, R. On Porous Electrodes in Electrolyte solutions—IV. *Electrochimica Acta* **1964**, *9* (9), 1231–1245.
(31) Mansfeld, F.; Lin, S.; Chen, Y. C.; Shih, H. Minimization of High-Frequency Phase Shifts in Impedance Measurements. *J. Electrochem. Soc.* **1988**, *135* (4), 906–907.
(32) Sawyer, D. T.; Sobkowiak, A.; Roberts, J. L.; Sawyer, D. T. *Electrochemistry for Chemists*; Wiley, **1995**.
(33) Boukamp, B. A. A Linear Kronig-Kramers Transform Test for Immittance Data Validation. *J. Electrochem. Soc.* **1995***, 142,* 1885-1894.
(34) C. Graves, RAVDAV Data Analysis Software, Version 0.9.7, (**2012**).
(35) Hunter, J. D. Matplotlib: A 2D Graphics Environment. *Comput. Sci. Eng.* **2007**, *9* (3), 90–95.
(36) Oliphant, J. O.; Peterson, P.; et al. Scipy: Open Source Scientific Tools for Python. ***2001***.
(37) Walt, S. van der; Colbert, S. C.; Varoquaux, G. The NumPy Array: A Structure for Efficient Numerical Computation. *Comput. Sci. Eng.* **2011**, *13* (2), 22–30.
(38) Brug, G. J.; van den Eeden, A. L. G.; Sluyters-Rehbach, M.; Sluyters, J. H. The Analysis of Electrode Impedances Complicated by the Presence of a Constant Phase Element. *J. Electroanal. Chem. Interfacial Electrochem.* **1984**, *176* (1–2), 275–295.
(39) Hirschorn, B. Determination of Effective Capacitance and Film Thickness from Constant-Phase-Element Parameters. *ELECTROCHIMICA ACTA* **2010**, *55* (21), 6218–6227.
(40) Gaberscek, M.; Moskon, J.; Erjavec, B.; Dominko, R.; Jamnik, J. The Importance of Interphase Contacts in Li Ion Electrodes: The Meaning of the High-Frequency Impedance Arc. *Electrochem. Solid-State Lett.* **2008**, *11* (10), A170–A174.
(41) Højberg, J.; McCloskey, B. D.; Hjelm, J.; Vegge, T.; Johansen, K.; Norby, P.; Luntz, A. C. An Electrochemical Impedance Spectroscopy Investigation of the Overpotentials in Li–O2 Batteries. *ACS Appl. Mater. Interfaces* **2015**, 7, 4039–4047.
(42) Barbieri, O.; Hahn, M.; Herzog, A.; Kötz, R. Capacitance Limits of High Surface Area Activated Carbons for Double Layer Capacitors. *Carbon* **2005**, *43* (6), 1303–1310.
(43) Gunasekara, I.; Mukerjee, S.; Plichta, E. J.; Hendrickson, M. A.; Abraham, K. M. A Study of the Influence of Lithium Salt Anions on Oxygen Reduction Reactions in Li-Air Batteries. *J. Electrochem. Soc.* **2015**, *162* (6), A1055–A1066.
(44) Khetan, A.; Luntz, A.; Viswanathan, V. Trade-Offs in Capacity and Rechargeability in Nonaqueous Li–O2 Batteries: Solution-Driven Growth versus Nucleophilic Stability. *J. Phys. Chem. Lett.* **2015**, *6* (7), 1254–1259.
(45) Gerbig, O.; Merkle, R.; Maier, J. Electron and Ion Transport In Li2O2. *Adv. Mater.* **2013**, *25* (22), 3129–3133.
(46) Radin, M. D.; Monroe, C. W.; Siegel, D. J. Impact of Space-Charge Layers on Sudden Death in Li/O2 Batteries. *J. Phys. Chem. Lett.* **2015**, *6 (15),* 3017–3022.
(47) Hartmann, P.; Grübl, D.; Sommer, H.; janek, J.; Bessler, W. G.; Adelhelm, P. Pressure Dynamics in Metal–Oxygen (Metal–Air) Batteries: A Case Study on Sodium Superoxide Cells - J. Phys. Chem. C, **2014**, *118 (3)*, 1461-1471.

Supporting information

Revealing the Surface- and Solution-Based Mechanisms in the Li-O_2 Battery by Electrochemical Impedance Spectroscopy

Kristian B. Knudsen[a,b], Bryan D. McCloskey[b,c], Tejs Vegge[a], Johan Hjelm[a,*]

[a] Department of Energy Conversion and Storage, Technical University of Denmark, 4000 Roskilde, Denmark

[b] Department of Chemical and Biomolecular Engineering, University of California, Berkeley, California 94720, United States

[c] Environmental Energy Technologies Division, Lawrence Berkeley National Laboratory, Berkeley, California 94720, United States

* Corresponding Author: Johan Hjelm, johh@dtu.dk, +45 46 77 58 87

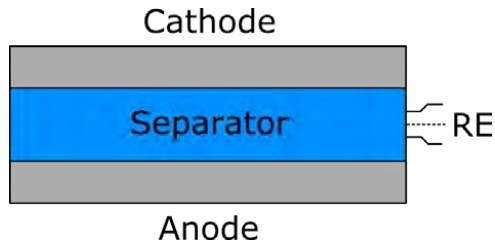

Figure S1: A sketch of the EL-cell and it positioning of the electrodes with respect to each other. This type of configuration is commonly referred to as the sandwich configuration.

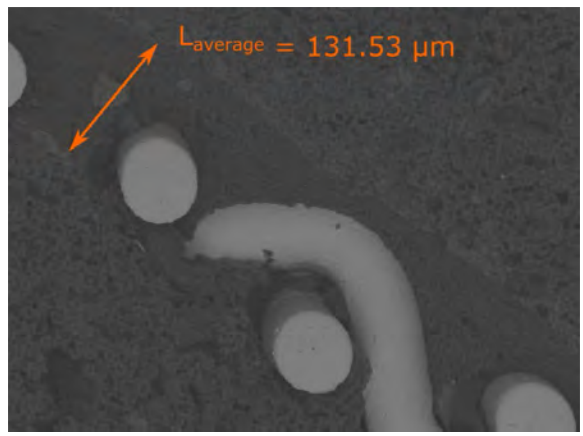

Figure S2: SEM of XC72 cathode. The average electrode thickness was determined by measuring the thickness at approximately 200 positions on three different XC72 cathodes electrode.

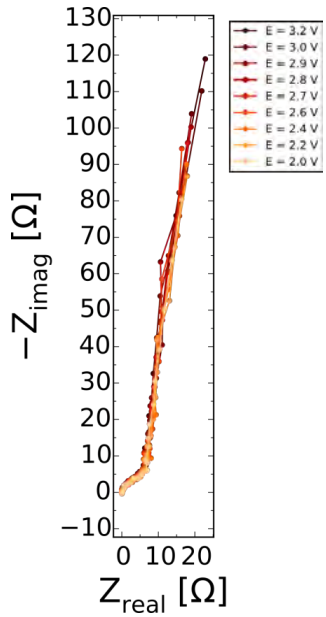

Figure S3: The impedance of an XC72 electrode in 1 M LiTFSI-DME in Ar as a function of the applied overpotential.

Galvanostatic discharges

The galvanostatic discharges presented here were conducted under a closed headspace and the pressure was monitored during the whole duration. This allowed for the analysis of electrons per oxygen, that ideally should be 2 e^-/O_2 following the reaction path, **eq. S1**:

$$2Li^+ + O_2 + 2e^- \rightarrow Li_2O_2 \quad [S1]$$

Experimentally this was performed using **eq. S2-S3**.

$$n_{consumed} = \frac{I \cdot t}{n \cdot F} \quad [S2]$$

$$P = \frac{n_{consumed} \cdot R \cdot T}{V_{cell}} \quad [S3]$$

Where $n_{consumed}$ is the amount of O_2 consumed [mol], I is the current [A], t the time [s], n the number of e^-, R gas constant $\left[\frac{Torr \cdot L}{mol \cdot K}\right]$, T temperature [K], and V_{cell} is the cell volume [L]. The resulting three figures are shown in **Figure S4-S6**.

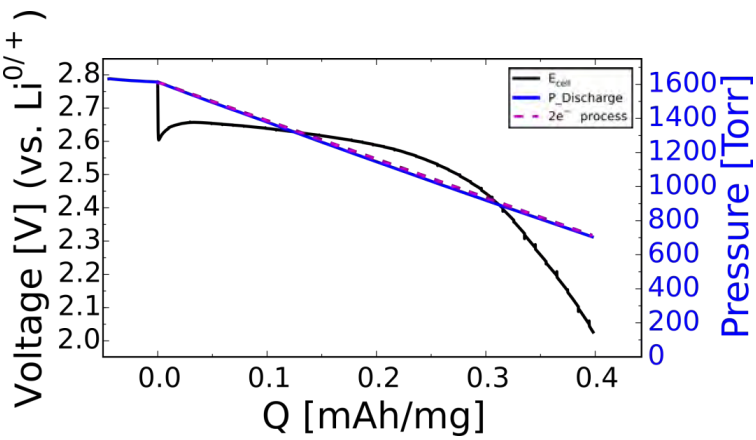

Figure S4: Galvanostatic discharge curve of 1 M LiTFSI-DME.

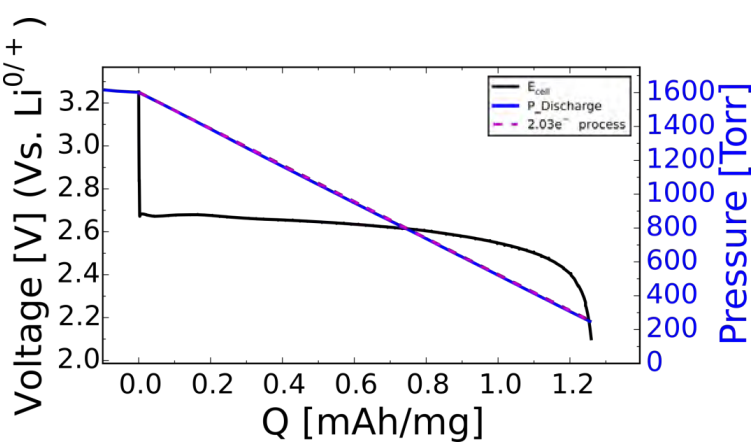

Figure S5: Galvanostatic discharge curve of 0.3/0.7 M LiTFSI/$LiNO_3$-DME.

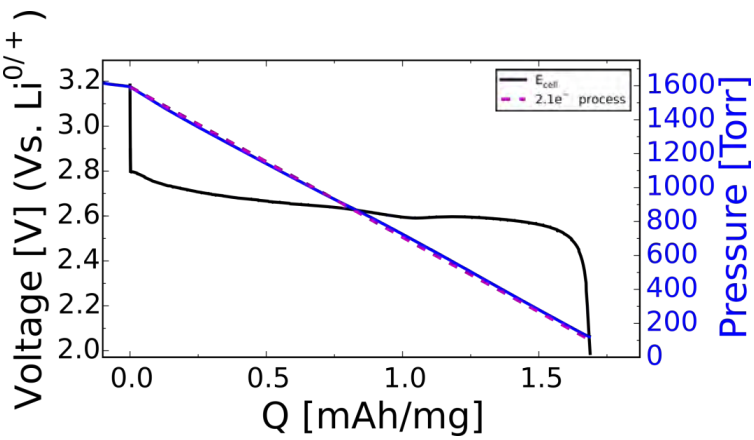

Figure S6: Galvanostatic discharge curve of 1 M LiTFSI –DME with 1000 ppm H_2O.

III

An Electrochemical Impedance Study of the Capacity Limitations in Na-O_2 Cells

Kristian B. Knudsen[a,b], Jessica E. Nichols[b,c], Tejs Vegge[a], Alan C. Luntz[d,e], Bryan D. McCloskey[b,c,*], Johan Hjelm[a,*]

[a] Department of Energy Conversion and Storage, Technical University of Denmark, 4000 Roskilde, Denmark

[b] Department of Chemical and Biomolecular Engineering, University of California, Berkeley, California 94720, United States

[c] Environmental Energy Technologies Division, Lawrence Berkeley National Laboratory, Berkeley, California 94720, United States

[d] SUNCAT Center for interface Science and Catalysis, Department of Chemical Engineering, Stanford University, 443 Via Ortega Stanford, California 94305-5025, United States

[e] SLAC National Accelerator Laboratory, 2575 Sand Hill Road, Menlo Park, California 94025, United States

[*] Corresponding authors: Bryan D. McCloskey, bmcclosk@berkeley.edu, +1 510-642-2295; and Johan Hjelm, johh@dtu.dk, +45 46 77 58 87

Abstract

We use electrochemical impedance spectroscopy, pressure change measurements, and scanning electron microscopy to investigate the reasons for the non-aqueous Na-O_2 cell potential decrease and rise (sudden deaths) on discharge and charge, respectively. To fit the impedance responses from operating cells, an equivalent circuit model was used that takes into account the porous nature of the positive electrode, and is able to distinguish between the electrolyte resistance in the pores and the charge-transfer resistance of the pore walls. The results obtained indicate that sudden death on discharge is caused by, depending on the current density, either accumulation of large NaO_2 crystals that eventually block the electrode surface, and/or by a thin film of NaO_2 forming on the cathode surface at the end of discharge. The commonly observed sudden rise in potential appears to be caused by loss of NaO_2 from the cathode surface.

Content

Metal-O_2 batteries have in recent years received a great deal of attention due to their high theoretical energy densities. However, Li-O_2 and Na-O_2 both suffer from limitations in galvanostatic mode, as the cell potential suddenly drops well before their theoretical energy densities (3456 Wh/kg for Li-O_2 and 1105 Wh/kg for Na-O_2) are achieved[1]. This phenomenon is generally referred to as sudden death and in Li-O_2 batteries is a result of the blocking of charge transport[2–5] through the main discharge product lithium peroxide, Li_2O_2. Li_2O_2 is insoluble in most stable organic electrolytes (e.g. lithium triflourosulfonylimide (LiTFSI) in 1,2-dimethoxyethane (DME)) and deposits as a conformal passivating film on the cathode[6–9]. For other Lewis acidic or basic electrolytes, e.g. dimethylsulfoxide (DMSO) or electrolytes with some H_2O content, the discharge mechanism consists of both an electrochemical process forming Li_2O_2 conformal coatings and a ($Li^+ + O_2^-$) solution mediated mechanism that forms larger toroid shaped particles[6,9]. Even in electrolytes in which Li_2O_2 deposits primarily as large toroids, charge transport limitations through the deposited Li_2O_2 also eventually limits cell capacity[6,9]. In Na-O_2, a sudden death behavior is observed during

both discharge and charge, with the charge sudden death resulting in a dramatic increase in cell potential near the end of charge. The overall Na-O_2 cell chemistry has, e.g. in diglyme[1,10,11] and DME[12], been shown to follow $Na^+_{(solv)} + O_{2(solv)} \rightleftarrows NaO_{2(s)}$, with the forward (or backward) arrow describing discharge (or charge)[1,10–12]. In these systems, very large (10-50 μm) cubic crystals of NaO_2 are observed and since NaO_2 is also an electronic insulator[11,13], it is suggested that the NaO_2 crystals are also formed by a solution mechanism[11]. The sudden death on discharge has been suggested to be due to O_2 transport limitations due to a buildup of the large Na-O_2 crystals[1] or due to a blocking of the electrochemistry at the cathode/electrolyte interface due to a buildup of the insulating NaO_2 crystals on the electrochemically active cathode surface[10].

In this paper, we investigate the charge-transfer resistance and surface capacitances in the Na-O_2 battery by applying electrochemical impedance spectroscopy (EIS) to operating cells (see Supplementary Information for details on the experimental setup). We combine these results with pressure change measurements and scanning electron microcopy (SEM) of discharged cathodes to understand the mechanisms of sudden death that occurs on both discharge and charge.

To interpret the impedance, we applied the porous electrode theory (PET) model, developed by Levie and Delahay[14]. The PET model includes information about the ionic resistance within the pores of an electrode (R_i) the charge-transfer resistance related to the reaction on the electrode surface (R_{CT}) and the effective surface capacitance (C_{eff}). We ignore any potential and concentration gradients that may arise under dc bias which are assumed small because of the low current densities, and used De Levie's model, with the simplifying assumption that the resistance of the ionic conduction in the pores is much greater than the resistance due to electronic conduction in the percolating carbon network. A sketch of the porous electrode model is given in **Figure 1.**

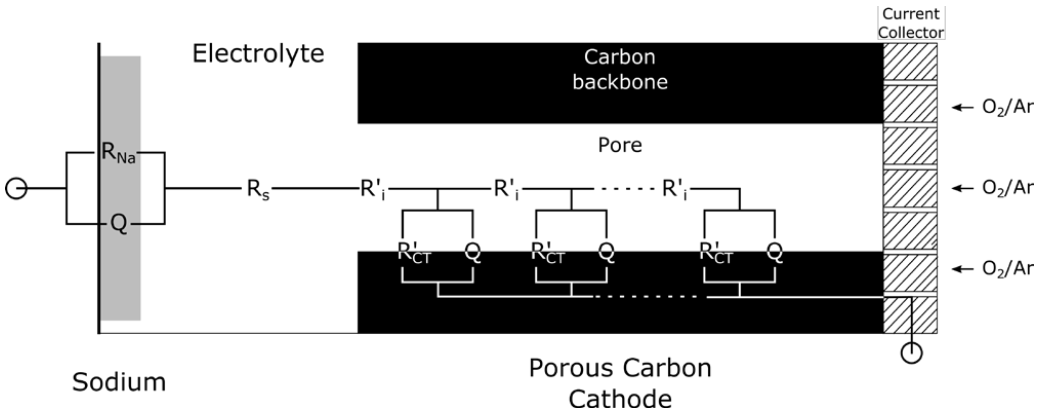

Figure 1: A schematic representation of the equivalent circuit that describes the porous electrode model. R_{Na} is the charge-transfer resistance occurring at the sodium/electrolyte interface, R_s is the electrolyte (series) resistance, $R_i^{'}$ is the ionic resistance within the porous structure of the cathode, $R_{CT}^{'}$ is the charge-transfer resistance at the cathode surface/electrolyte interface, and Q is a constant phase element used to describe the double-layer capacitance of the electrode surfaces, i.e. the pore walls inside the cathode and the surface/electrolyte interface of the sodium anode.

The equivalent circuit can be described as -$(RQ)_{Na}$-$PET_{(RQ)}$-, where the $(RQ)_{Na}$ element models the process occurring on the sodium anode surface and the associated charge-transfer resistance on this surface and double-layer surface capacitance are denoted R_{Na} and C_{dl}^{Na}, respectively. The $PET_{(RQ)}$ portion of the equivalent circuit is the porous electrode theory that contains the elements inside of the porous carbon cathode given in **Figure 1.** As the variables inside the cathode are a function of the cathode thickness, *i.e.* $R_{CT}^{'}$ $[\Omega \cdot cm]$, $R_i^{'}$ $[\Omega/cm]$, and Q $[s^n/\Omega \cdot cm]$[15–18]; each variable was normalized to the total value for the cathode thickness using **eq. 1-3**.

$$R_i = R_i' \cdot L = [\Omega] \quad [1]$$

$$R_{CT} = \frac{R'_{CT}}{L} = [\Omega] \quad [2]$$

$$C_{eff} = \left(\frac{1}{R_{CT}\cdot(2\pi f_s)^n}\right)^{1/n} \cdot \left(\frac{R_s \cdot R_{CT}}{R_s + R_{CT}}\right)^{\frac{1-n}{n}} \cdot \frac{1}{m_{carbon}\cdot BET_{area}} = [F/cm^2] \quad [3]$$

As we use a constant phase element, Q, to describe the capacitance of the reacting surface within the PET model, these are re-calculated to the effective capacitance, as described by both Brug et al.[19] and Hirschhorn et al.[20] The impedance of the cathode is therefore given by the parameters R_i, R_{CT}, and C_{eff}, describing the resistance within the pore volume of the cathode, the charge-transfer resistance of the surface reaction, and the double-layer capacitance of the electrode, respectively. The surface capacitance of pristine electrodes where the impedance were measured at OCV and in Ar, the RQ cicuit inside the porous structure was exchanged with a -Q- element, as the response was non-faradaic. The surface capacitance for pristine cells, were determined using **eq. 4**.

$$C_{eff} = (Q \cdot L \cdot R_s^{1-n})^{1/n} \cdot \frac{1}{m_{carbon}\cdot BET_{area}} = [F/cm^2] \quad [4]$$

The specific experimental procedures and impedance fitting procedures are included in the supplementary information.

To validate the use of the applied PET model, the approach suggested by Lasia[21] was used, as the impedance of the cell was measured at open circuit voltage (OCV) and in an Ar atmosphere, i.e. in the absence of Faradaic reactions in the porous cathode, as seen in **Figure 2a-b**. In Ar, the cell exhibited a high frequency semicircle that is related to the charge-transfer on the Na-anode (**Figure 2b**). At low frequencies, a capacitive behavior was observed from the cathode as O_2 was absent and no Faradaic reaction occurred. The capacitance of the cathode was determined to be 4.1-5.0 μF/cm^2 using **eq. 4**. However, between the high frequency semicircle of the sodium anode and the low frequency capacitive cathode response, a linear region was observed (**Figure 2a-b**). This region is strongly dependent on the thickness of the cathode (L) and is observed to increase as L is increased by stacking multiple cathodes together. This linear region is a

characteristic of the ionic resistance (R_i) inside the porous structure of the cathode and the observed presence and thickness dependence of this linear region strongly indicates that the impedance is dominated, at mid-frequencies, by the porous nature of the P50 cathode. A similar approach has been used by refs.[18,21] This dependency clearly suggests that the PET model gives a physically meaningful parameterization of the cathode impedance for cells used in this study.

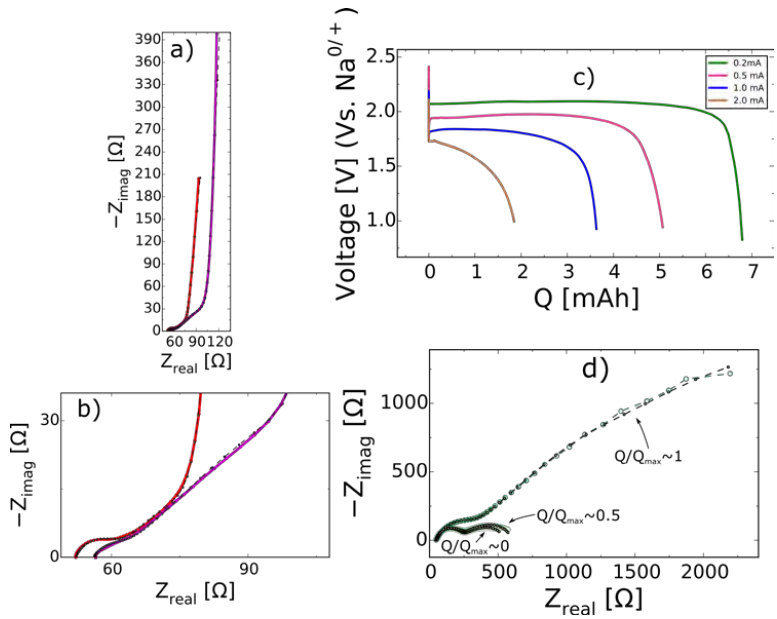

Figure 2: a) Cell impedance in Ar and at OCV of two Na-O_2 cells, where the red curve is a cell with one P50 cathode while the purple curve is a cell with three stacked P50 cathodes. The black dotted lines shows the best fits to the equivalent circuit model: -$(RQ)_{Na}$-$PET_{(Q)}$-. b) Magnification of a) where the high-frequency process of the sodium anode is seen, denoted –$(RQ)_{Na}$- in the model, c) Galvanostatic discharge curves in 0.5 M NaOTf-DME operated under a pressure of O_2 (~1000 torr) at 0.2, 0.5, 1.0, and 2.0 mA (12 mm P50 cathode diameter). d) The Nyquist plot of the 0.2 mA discharge with three curves illustrating the impedance at Q/Q_{max} ~ 0, 0.5, and 1.

The mechanisms controlling the sudden death on discharge were studied by galvanostatic discharges at 0.2, 0.5, 1.0 and 2.0 mA under constant pressure of O_2 (~1000 Torr) as shown in **Figure 2c**. EIS was measured throughout each discharge as illustrated for the 0.2 mA discharge in **Figure 2d** while Nyquist and Bode plots for all current densities can be found in **Figure S1**. The fitted impedance parameters, R_{Na}, R_{CT}, R_i, and C_{eff}, are shown in **Figure 3** for the four current densities. At all discharge currents, NaO_2 crystals are deposited on the cathode surface, as previously reported[10], and an electron count of 1.03-1.08 e^-/O_2 is observed from experiments with cells discharged under a closed headspace (**Figure S2**) using otherwise identical conditions. At lower discharge currents, 0.2-0.5 mA, R_i dominates the cell impedance throughout the discharge until sudden death while R_{CT} dominates the cell resistance throughout the discharge at higher currents, 1.0-2.0 mA (**Figure 3**). The capacitance of the active cathode surface (C_{eff}), which at lower currents, 0.2-0.5 mA, decreases gradually from an initial value of ~4.5 $\mu F/cm^2$, determined at OCV in pristine cells, to 0.29-0.43 $\mu F/cm^2$ at sudden death. At higher currents, 1.0-2.0 mA, the capacitance immediately drops to a plateau of 0.35-0.37 $\mu F/cm^2$.

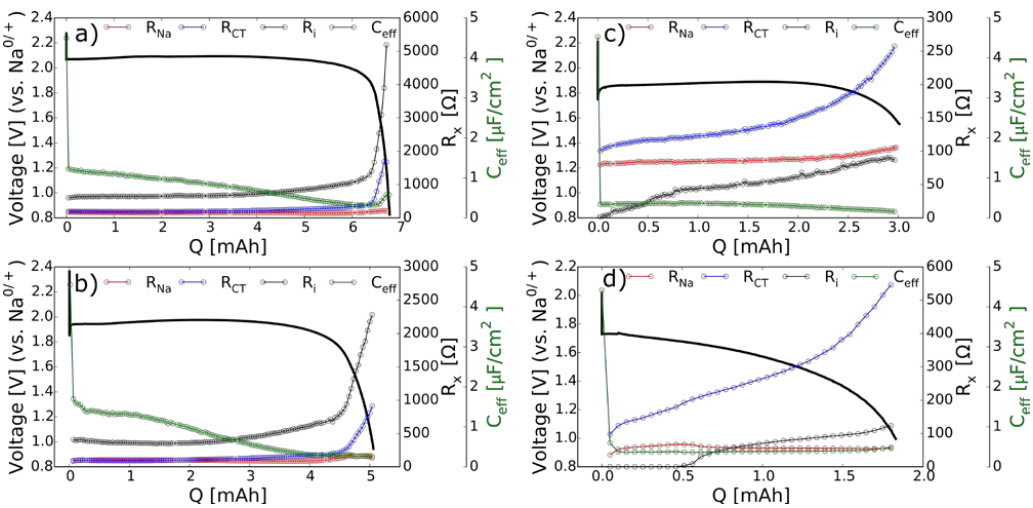

Figure 3: Galvanostatic discharge curves of a) 0.2 mA b) 0.5 mA, c) 1.0 mA, and d) 2.0 mA, which were operated under at a constant pressure of O_2 (~1000 Torr). The output resistances from the impedance fits

are plotted on the two secondary axes marked R_x while the output C_{eff} is plotted in green belongs to the third green axis. The initial C_{eff} value of the carbon cathode (~4.5 μF/cm^2) was obtained at OCV from **Figure 2a**.

The double-layer capacitance of the cathode would be expected to significantly decrease if the surface is coated by a thin film of NaO_2 already at film thicknesses of few nanometers as NaO_2 is a poor electronic conductor[11] and has a low dielectric constant (4.5[13]). The observed nearly immediate decrease in capacitance upon discharge at higher currents, 1.0-2.0 mA, suggests that the cathode surface is immediately covered by a NaO_2 film at these conditions. SEM images of cathodes discharged to 1.0 V vs. $Na^{0/+}$ shown in **Figure 4**, further shows that a NaO_2 film has formed at these currents, and SEM images of cells discharged to lesser capacities also indicate a thin NaO_2 film has deposited on the electrode surface in between the larger cubic crystals. At lower currents, 0.2-0.5 mA, the SEM images (**Figure 4**) show that a predominant part of the discharge product formed as cubic NaO_2 crystals, with a thin NaO_2 film covering the electrode surface in-between the larger crystals. The gradual decrease in C_{eff}, observed at these lower currents, (**Figure 3**) also suggests that the rate of surface coverage by NaO_2 is slower. A reasonable explanation of these observations is that as NaO_2 crystals grow, parts of the cathode remains uncoated or gets covered by a thin, possibly porous, NaO_2 film that allows for continued oxygen reduction and consequent NaO_2 crystal growth. Therefore, as the crystals grow and gradually cover the surface, C_{eff} slowly decreases. The differential resistance, at these currents, is dominated by the ionic resistance (R_i) indicating that NaO_2 takes up some part of the pore volume within the porous cathode, which is in agreement with the SEM images that show the presence of a large amount of 3-10 μm NaO_2 crystals at sudden death. R_{CT} also increases dramatically at sudden death suggesting that the surface is becoming completely blocked by NaO_2, in the form of NaO_2 cubes and/or in the form of a continuous NaO_2 thin film of sufficient density and thickness to be completely blocking to further oxygen reduction.

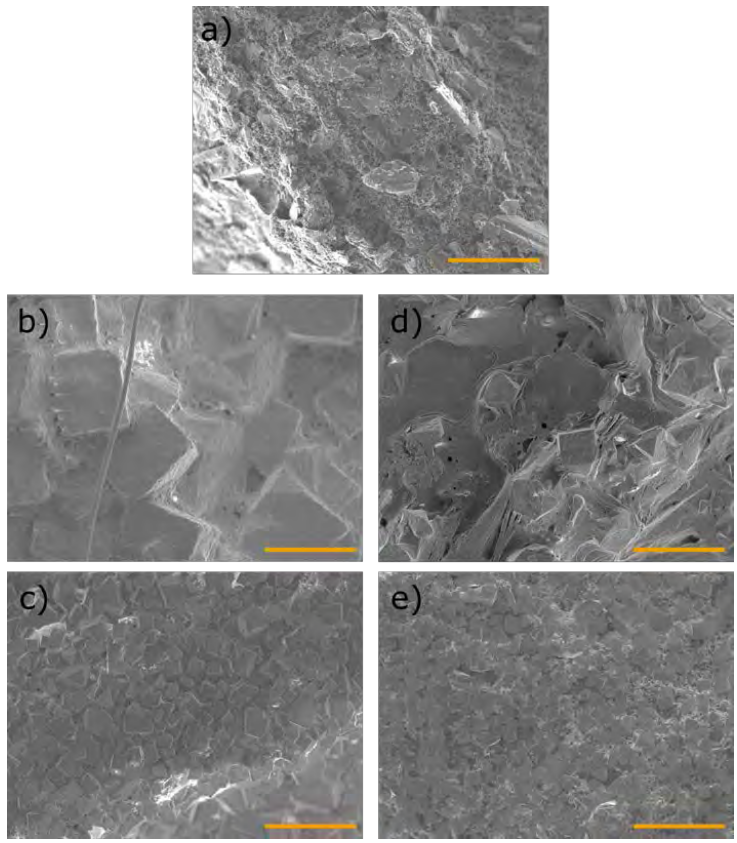

Figure 4: SEM images of a) a pristine P50 cathode and P50 cathodes discharged to 1.0 V vs. $Na^{0/+}$ at b) 0.2 mA (6.29 mAh) c) 0.5 mA (4.51 mAh) d) 1.0 mA (3.79 mAh) e) 2.0 mA (2.58 mAh). The scale bar is 10 μm.

Cells discharged under a closed O_2 headspace were used to determine the number of electrons (1.03-1.08 e^-/O_2) involved in the reaction (**Figure S2**). These cells exhibited lower discharge capacities than cells operated at constant partial pressure of O_2 (~1000 torr, i.e. open headspace) as the partial pressure of O_2 at sudden death had dropped to ~200 Torr. Relating this to the concentration of soluble O_2 is possible using Henry's constant for O_2 solubility in DME ($k_H = 1.347 \cdot 10^{-5}$ mol/L·Torr) determined by Hartmann et al.[10] and a decrease in soluble O_2 from ~13.5 mM (~1000 Torr) to ~2.7 mM (~200 Torr) can be estimated. The

observed decrease in pressure throughout discharge, in the cells of **Figure S2**, leads to significant differences in the concentration of dissolved O_2 in the electrolyte. The decreased concentration of dissolved O_2 may affect the diffusion losses in the cell, and is also expected to lead to a decrease in the surface concentration of O_2 species, leading to greater charge-transfer resistance, and depending on the current density, surface area, and porosity of the cathode this leads to some degree of capacity decrease, consistent with the observations here. There is a possibility that O_2 concentration gradients may influence the polarization resistance of the cathode in particular at the end of discharge and charge and the fact that we neglect the O_2 concentration effect may lead to an overestimate the resistances of the porous electrode. Further studies to lower frequencies should be carried out in the future, however this is a difficult task as the quality of the impedance becomes increasingly poor with decreasing frequency. Diffusion limitation in the porous electrode may lead to the appearance of a low frequency semicircle[22], which we were unable to distinguish in the investigated frequency range.

The origins of the voltage profiles on charge were investigated by galvanostatically discharging cells at 1 mA to 3 mAh and subsequent charging at 0.2, 0.5 and 1 mA while EIS continuously was measured (full description given in supplementary information) at short intervals throughout discharge and charge. The corresponding Nyquist and Bode plots obtained during charge are shown in **Figure S3** and **Figure 5** shows the evolution of the impedance parameters obtained from the fits of the equivalent circuit to the experimental data. At the beginning of the three charge experiments, the cathode surface was, at 3 mAh, covered by NaO_2 (**Figure 4**). R_{CT} dominates the cell impedance throughout the charge experiments (**Figure 5**); it dramatically increases near sudden death; and decreases with increasing charging currents. R_i initially decreases and reaches a plateau at all currents while C_{eff} displays a rapid linear increase initially, the slope of which depends on the current density. After some time the slope of C_{eff} variation changes, which occurs earlier the greater the charging current is, and finally reaches a plateau. We speculate that the reason for the change in C_{eff} slope is related to complete removal of the thin conformal NaO_2 film on the electrode surface, while the larger NaO_2 crystals still remain on the surface at that point during charge. It is important

to also note that the charges were halted by short-circuiting due to the penetration of Na dendrites through the separator, influencing the cycle efficiency negatively. Prior to this in each case the cell potential increased showing that the initial state of sudden death was reached.

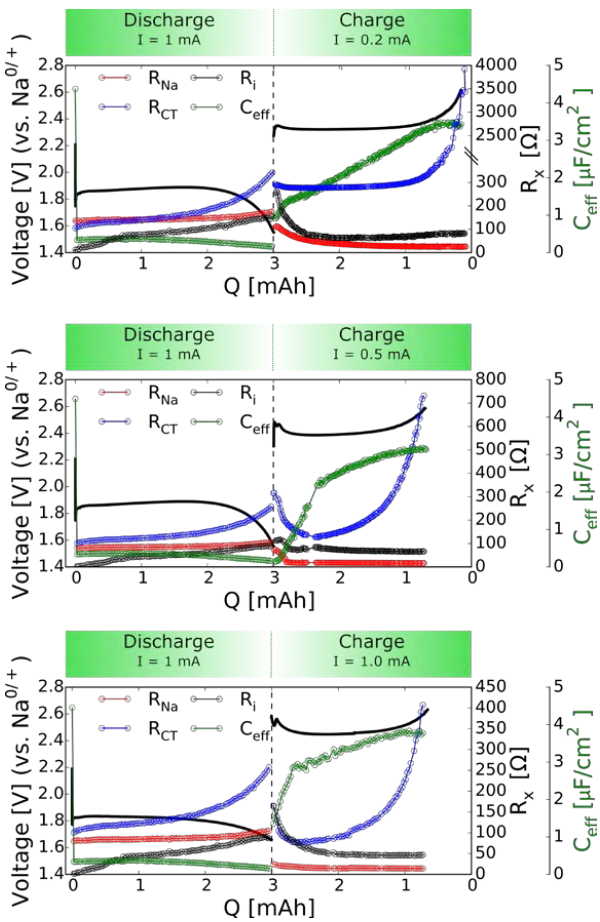

Figure 5: The galvanostatic discharges and charges of Na-O_2 cells that were discharged at 1 mA to a capacity of 3 mAh at ~1000 Torr of O_2 and subsequently charged at 0.2 mA, 0.5 mA, and 1.0 mA. The parameters on the two secondary axes are from the impedance fits where the equivalent circuit: -$(RQ)_{Na}$-$PET_{(RQ)}$- was used. The initial C_{eff} value of ~4.5 μF/cm^2 reported at Q=0 was determined at OCV from **Figure 2a**.

The charge transfer resistance yields the dominating contribution to the overpotential of the positive electrode on the charging plateau. The decrease of R_{CT} with increasing current density is interpreted as a reflection of the curvature of the current-voltage curve. For a reaction obeying Butler-Volmer type kinetics (kinetic control) a decreasing R_{CT} with increasing overpotential would be expected, as R_{CT} reflects the slope of the current-voltage curve. At very early stages of charge, the initial rapid increase in C_{eff} from ~0.4 μF/cm^2 to 2.15-2.84 μF/cm^2, depending on current rate, could indicate that most of the NaO_2 oxidation, in this region, occurs as removal of the NaO_2 film by exposing some of the conductive carbon cathode surface to the electrolyte. The following monotonous increase in C_{eff} indicates a gradual unblocking of the electrode surface during charge due to continuous oxidation of NaO_2 crystals, mediated by a solution mechanism, would lead to a gradual decrease in the crystal size. The ionic resistance (R_i) is observed to decrease during charge, most likely reflecting that larger NaO_2 crystals are removed from the pore volume in the cathode. At the end of charge, C_{eff} reaches a plateau at 3.11-3.77 μF/cm^2, depending on the current rate, and R_{CT} also dramatically increases. As the final C_{eff}'s after charge are lower than the initial value of a pristine cathode (~4.50 μF/cm^2), it suggests that some solid NaO_2 still remains on the surface of the cathode, possibly the larger NaO_2 crystals that have not yet been completely dissolved and/or that other low dielectric constant products (e.g. sodium carbonates) have accumulated on the electrode surface and blocks soluble NaO_2 oxidation. R_{CT} rapidly increases at sudden death on charge and is therefore likely a reflection of the depressed amount of dissolved NaO_2 in the electrolyte near the cathode surface as a consequence of the decrease in the amount of remaining solid NaO_2 at the cathode/electrolyte interface, which may have the consequence that an increasing fraction of the oxidation current is due to direct oxidation of NaO_2 (as suggested in ref.[11]).

Cell failure, in the presented cells, was caused by short circuits as dendrites formed through the glass fiber separators upon charge. This has previously also been reported by Hartmann et al.[1] and is an issue that limits cycle life. The solid electrolyte interphase (SEI) of the sodium anode, in non-aqueous electrolytes has been observed to be partly soluble, hence decreasing the Na/electrolyte interface stability[23]. The

observed decrease in R_{Na}, a concurrent continuous increase in C_{dl}^{Na}, and an initial drop in the exponent n of the Q equivalent circuit element indicates that the Na metal surface roughens or that sodium dendrites form during charge, as seen in **Figure 6**. The instability of the sodium anode is further demonstrated by monitoring the cathode and anode potential in relation to a third sodium reference electrode, where the largest overpotential in the plateau region is accounted for by the (~250 mV) anode and not the cathode (~10 mV), as illustrated in **Figure S4**.

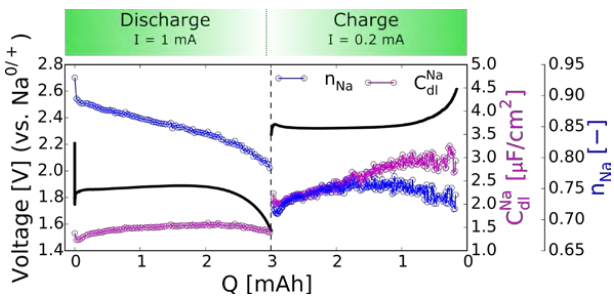

Figure 6: The *same* galvanostatic discharge and charge as of **Figure 5a**. Here the double-layer capacitance of the sodium anode is plotted versus the capacity. The exponent of the constant phase element, n, that is used to model the double-layer capacitance of the sodium anode is plotted in blue and the effective double-layer capacitance of the sodium anode under operation is plotted in purple.

In summary, we have presented electrochemical impedance spectroscopy-, pressure change-, and SEM results that show the degree to which mass transport or kinetic losses dominate the internal resistance of the porous carbon electrode at different stages of discharge and charge in Na-O_2 cells. The results show that the discharge impedances are highly dependent on the current density. At higher current densities, the surface capacitance indicates that NaO_2 immediately covers the surface of the cathode as some form of, possibly porous, NaO_2 film is formed initially. Cubic NaO_2 crystals are observed after discharge at all current densities investigated here. The size of the crystals increases with decreasing discharge currents. At lower

discharge current densities, the gradual decrease of the cathode surface capacitance indicates that the cathode surface is coated gradually with NaO_2, probably reflecting that the surface is blocked by growth of cubic crystals of NaO_2 on the electrode with a continuous NaO_2 film stretching in-between at sudden-death as visible from SEM images. The NaO_2 crystals become smaller and more of the deposit appears as a continuous film as the discharge current increases. Interestingly, the cathode surface capacitance decreases very rapidly upon discharge at high current, indicating that much more of the electrode surface is covered with a low dielectric constant product (NaO_2) at an early stage of discharge consistent with formation of some kind of thin film. Considering that the discharge can proceed long after this film is formed, and factoring in that NaO_2 has a very low electronic conductivity, this may be an indication that the film formed at short times at high discharge currents is porous in nature. On charge, three regions could be identified. Initially, a large part of the NaO_2 film is oxidized and removed from the cathode surface; secondly, the NaO_2 crystals are dissolved and oxidized and as the crystals decrease in size more of the initial carbon/electrolyte interface is regained; and lastly, the potential and R_{CT} dramatically increases, possibly due to a decreased amount of dissolved NaO_2 in the electrolyte near the cathode surface.

Associated Content

Materials and methods, equations used to normalize impedance parameters, supporting figures, including Nyquist and Bode plots, and additional discharge-charge under a closed headspace is included here.

Acknowledgments

The authors gratefully acknowledge financial support from the ReLiable project (project No. 11-116792) funded by the Danish Council for Strategic Research, Program Commission on Sustainable Energy and Environment. This material is based upon work supported by the National Science Foundation Graduate Research Fellowship Program under Grant No. DGE-1106400.

References

(1) Hartmann, P.; Bender, C.; Sann, J.; Dürr, A. K.; Jansen, M.; Janek, J.; Adelhelm, P. A comprehensive study on the cell chemistry of the sodium superoxide (NaO2) battery. *Phys. Chem. Chem. Phys.* **2013**, *15*,11661-11672.

(2) Højberg, J.; McCloskey, B. D.; Hjelm, J.; Vegge, T.; Johansen, K.; Norby, P.; Luntz, A. C. An Electrochemical Impedance Spectroscopy Investigation of the Overpotentials in Li–O2 Batteries. *ACS Appl. Mater. Interfaces* **2015**, 7, 4039–4047.

(3) Viswanathan, V.; Thygesen, K. S.; Hummelshøj, J. S.; Nørskov, J. K.; Girishkumar, G.; McCloskey, B. D.; Luntz, A. C. Electrical Conductivity in Li2O2 and Its Role in Determining Capacity Limitations in Non-Aqueous Li-O2 Batteries. *J. Chem. Phys.* **2011**, *135*, 214704–214704.

(4) Luntz, A. C.; Viswanathan, V.; Voss, J.; Varley, J. B.; Nørskov, j. K.; Scheffler, R.; Speidel, A. Tunneling and Polaron Charge Transport through Li2O2 in Li–O2 Batteries. *J. Phys. Chem. Lett.,* **2013**, *4,* 3494-3499.

(5) Knudsen, K. B.; Luntz, A. C.; Jensen, S. H.; Vegge, T.; Hjelm, J. A Redox Probing Study of the Potential Dependence of Charge Transport through Li2O2. *J. Phys. Chem. C* **2015**, *Just accepted*.

(6) Aetukuri, N. B.; McCloskey, B. D.; García, J. M.; Krupp, L. E.; Viswanathan, V.; Luntz, A. C. Solvating Additives Drive Solution-Mediated Electrochemistry and Enhance Toroid Growth in Non-Aqueous Li–O2 Batteries. *Nat. Chem.* **2015**, *7*, 50–56.

(7) Schwenke, K. U.; Metzger, M.; Restle, T.; Piana, M.; Gasteiger, H. A. The Influence of Water and Protons on Li2O2 Crystal Growth in Aprotic Li-O2 Cells. *J. Electrochem. Soc.* **2015**, *162*, A573–A584.

(8) Burke, C. M.; Pande, V.; Khetan, A.; Viswanathan, V.; McCloskey, B. D. Enhancing Electrochemical Intermediate Solvation through Electrolyte Anion Selection to Increase Nonaqueous Li–O2 Battery Capacity. *Proc. Natl. Acad. Sci.* **2015**,112, 9293-9298.

(9) Johnson, L.; Li, C.; Liu, Z.; Chen, Y.; Freunberger, S. A.; Ashok, P. C.; Praveen, B. B.; Dholakia, K.; Tarascon, J.-M.; Bruce, P. G. The Role of LiO2 Solubility in O2 Reduction in Aprotic Solvents and Its Consequences for Li–O2 Batteries. *Nat. Chem.* **2014**, *6*, 1091–1099.

(10) Hartmann, P.; Grübl, D.; Sommer, H.; janek, J.; Bessler, W. G.; Adelhelm, P. Pressure Dynamics in Metal–Oxygen (Metal–Air) Batteries: A Case Study on Sodium Superoxide Cells. *J. Phys. Chem. C*, **2014**, 118, 1461-1471.

(11) Hartmann, P.; Heinemann, M.; Bender, C. L.; Graf, K.; Baumann, R.-P.; Adelhelm, P.; Heiliger, C.; Janek, J. Discharge and Charge Reaction Paths in Sodium-Oxygen Batteries: Does NaO2 Form by Direct Electrochemical Growth or by Precipitation from Solution? *J. Phys. Chem. C* **2015**, *119,* 22778-22786.

(12) McCloskey, B. D.; Garcia, J. M.; Luntz, A. C. Chemical and Electrochemical Differences in Nonaqueous Li–O2 and Na–O2 Batteries. *J. Phys. Chem. Lett.* **2014**, *5*, 1230–1235.

(13) Yang, S.; Siegel, D. J. Intrinsic Conductivity in Sodium–Air Battery Discharge Phases: Sodium Superoxide vs Sodium Peroxide. *Chem. Mater.* **2015**, *27*, 3852–3860.

(14) De Levie, R.; Delahay, P. *Advances in Electrochemistry and Electrochemical Engineering*; 6th ed.; Wiley-Interscience: New York; **1967**.

(15) Bisquert, J.; Garcia-Belmonte, G.; Fabregat-Santiago, F.; Compte, A. Anomalous Transport Effects in the Impedance of Porous Film Electrodes. *Electrochem. Commun.* **1999**, *1*, 429–435.

(16) Bisquert, J.; Garcia-Belmonte, G.; Fabregat-Santiago, F.; Ferriols, N. S.; Bogdanoff, P.; Pereira, E. C. Doubling Exponent Models for the Analysis of Porous Film Electrodes by Impedance. Relaxation of TiO2 Nanoporous in Aqueous Solution. *J. Phys. Chem. B* **2000**, *104*, 2287–2298.

(17) Lasia, A. Impedance of Porous Electrodes. *J. Electroanal. Chem.* **1995**, *397*, 27–33.

(18) Nielsen, J.; Hjelm, J. Impedance of SOFC Electrodes: A Review and a Comprehensive Case Study on the Impedance of LSM:YSZ Cathodes. *Electrochim. Acta* **2014**, *115*, 31–45.

(19) Brug, G. J.; van den Eeden, A. L. G.; Sluyters-Rehbach, M.; Sluyters, J. H. The Analysis of Electrode Impedances Complicated by the Presence of a Constant Phase Element. *J. Electroanal. Chem. Interfacial Electrochem.* **1984**, *176*, 275–295.
(20) Hirschorn, B. Determination of Effective Capacitance and Film Thickness from Constant-Phase-Element Parameters. *Electrochim. Acta* **2010**, *55*, 6218–6227.
(21) Lasia, A. Electrochemical Impedance Spectroscopy and Its Applications. In *Modern Aspects of Electrochemistry*; Conway, B. E., Bockris, J. O., White, R. E.,1st Ed.; Modern Aspects of Electrochemistry; Springer US, **2002**.
(22) Devan, S.; Subramanian, V. R.; White, R. E. Analytical Solution for the Impedance of a Porous Electrode. *J. Electrochem. Soc.* **2004**, *151*, A905–A913.
(23) Iermakova, D. I.; Dugas, R.; Palacín, M. R.; Ponrouch, A. On the Comparative Stability of Li and Na Metal Anode Interfaces in Conventional Alkyl Carbonate Electrolytes. *J. Electrochem. Soc.* **2015**, *162*, A7060–A7066.

Supplementary Information

An Electrochemical Impedance Study of the Capacity Limitations in Na-O_2 Cells

Kristian B. Knudsen[a,b], Jessica E. Nichols[b,c], Tejs Vegge[a], Alan C. Luntz[d,e], Bryan D. McCloskey[b,c,*], Johan Hjelm[a,*]

[a] Department of Energy Conversion and Storage, Technical University of Denmark, 4000 Roskilde, Denmark

[b] Department of Chemical and Biomolecular Engineering, University of California, Berkeley, California 94720, United States

[c] Environmental Energy Technologies Division, Lawrence Berkeley National Laboratory, Berkeley, California 94720, United States

[d] SUNCAT Center for interface Science and Catalysis, Department of Chemical Engineering, Stanford University, 443 Via Ortega Stanford, California 94305-5025, United States

[e] SLAC National Accelerator Laboratory, 2575 Sand Hill Road, Menlo Park, California 94025, United States

[*] Corresponding authors: Bryan D. McCloskey, bmcclosk@berkeley.edu, +1 510-642-2295; and Johan Hjelm, johh@dtu.dk, +45 46 77 58 87

1.0 Experimental Methods

1.2-dimethoxyethane (BASF, DME) and sodium triflouromethanesulfonate (Sigma-Aldrich, NaOtf) were used as received. The prepared electrolytes, 0.5 M NaOtf in DME, had <30 ppm H_2O as measured by Karl Fisher titration (MetrOhm). Na metal was purchased from GalliumSource, Avcarb P50 was purchased from Fuel Cell Store and Whatman glass fiber filters (QM-A grade) were used as separators. Na anodes were prepared by roll pressing a piece of Na between two pieces of Celgard 2500 and 12 mm P50 discs were used as cathodes. The cathodes were washed repeatedly in acetone and isopropanol before being dried first at 110°C in vacuum and then at 200°C inside an Ar glovebox. The glass fiber separators were cleaned following similar procedure. Cell preparation has been described in detail in previous publications for similar Li-O_2 cells[1,2]. The BET surface area of the AvCarb P50 cathodes was determined to 86.32 cm^2/mg. An three-electrode EL-air cell (EL-cell) was also used to monitor the overpotentials of each electrode relative to the reference sodium electrode. The cell was modified with stainless steel in- and outlets as it comes with PEEK capillaries that are permeable towards H_2O.

All electrochemical measurements were performed on a Bio-Logic VSP potentiostat. Electrochemical Impedance Spectroscopy (EIS) was performed at OCV using an a.c. amplitude of 10 mV that was scanned from 100 kHz to 32 mHz with 9 points/decade and 10 cycles/frequency. EIS was also performed galvanostatically at with the dc current stated for the each cell and with an ac amplitude of 10 % of the dc current. This was scanned from 100 KHz to 320 mHz with 9 points/decade and 4 cycles/frequency until 1 V vs. $Na^{0/+}$ was reached.

The quality of the EIS data was evaluated by a linearized Kramers-Kroning test to ensure that the rules of causality, linearity, stability, and finiteness were kept[3]. Equivalent circuit models were fitted to the data using the Levenberg-Marquardt complex non-linear least squares algorithm using a software programmed in Python[4], which relies on parts of the scientific Python stack described in refs.[5–7].

All scanning electron microscopy (SEM) measurements were performed on P50 cathodes galvanostatically discharged in an open headspace (~1000 torr) of O_2 to 1.0 V vs. $Na^{0/+}$, using materials as described above. Following discharge, the cells were flushed with Ar and transferred to an Ar-filled glovebox (<0.1 ppm H_2O, <0.1 ppm O_2). The cathodes were extracted and placed in a clean glass vial, then rinsed briefly in DME to wash off electrolyte salts. The glass vial and cathode were transferred to a vacuum chamber connected to the glovebox and dried for ~5 min to remove residual solvent. Following drying, the vials were removed from the vacuum chamber to the glovebox, and the cathodes were mounted on an SEM sample holder. The pristine cathode was mounted as prepared for use in a cell, without exposure to electrolyte or rinsing in solvent. To prevent exposure to ambient atmosphere, the sample holder was stored in an airtight glass bottle under an Ar atmosphere for transport to the SEM facility, and then transferred rapidly into the SEM chamber. The time from opening the glass bottle to the commencement of loading chamber pump down was less than one minute. Though this exposure prohibits quantitative chemical analysis in the SEM, we assume the change in morphology of the NaO_2 discharge product was negligible during this brief time. Measurements were performed using a JEOL JSM-7500F SEM operating in gentle beam (GB) mode with an emission electron current of 10.0μA, an accelerating voltage of 1.00 kV, a sample bias voltage of 1.50 kV, and a work distance between 6.0mm and 8.0 mm. The images presented in this work were collected with a through-lens secondary electron detector.

2.0 Galvanostatic Discharges in an Open Headspace (~1000 Torr) of O_2

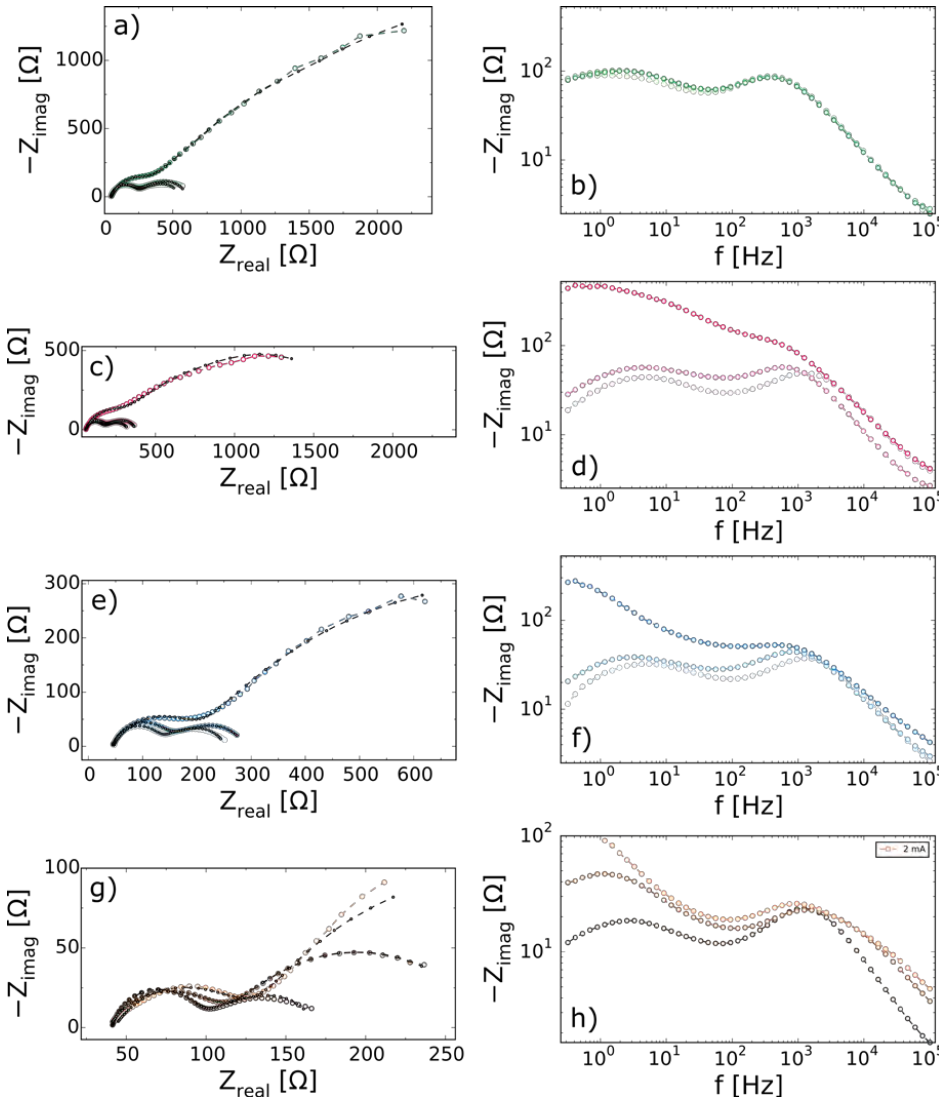

Figure S1: Summary of the electrochemical impedance spectroscopy performed during the galvanostatic discharges illustrated in F**igure S2**. For each current, a Nyquist- and Bode plot is depicted, hence a) and b) are the 0.1 mA discharge, c) and d) 0.5 mA discharge, e) and f) 1.0 mA discharge, and g) and h) are 2.0 mA discharge. Each current has three impedance spectra presented: lightest color represents the impedance

spectra nearest to Q = 0 mAh, the mid-color 1/2 ·Q_{full}, and the darkest color at Q_{full} *i.e.* at 1 V vs. $Na^{0/+}$ while the dotted lines (--) are the fitted equivalent circuits.

3.0 Galvanostatic Discharge in a Closed Headspace of O_2

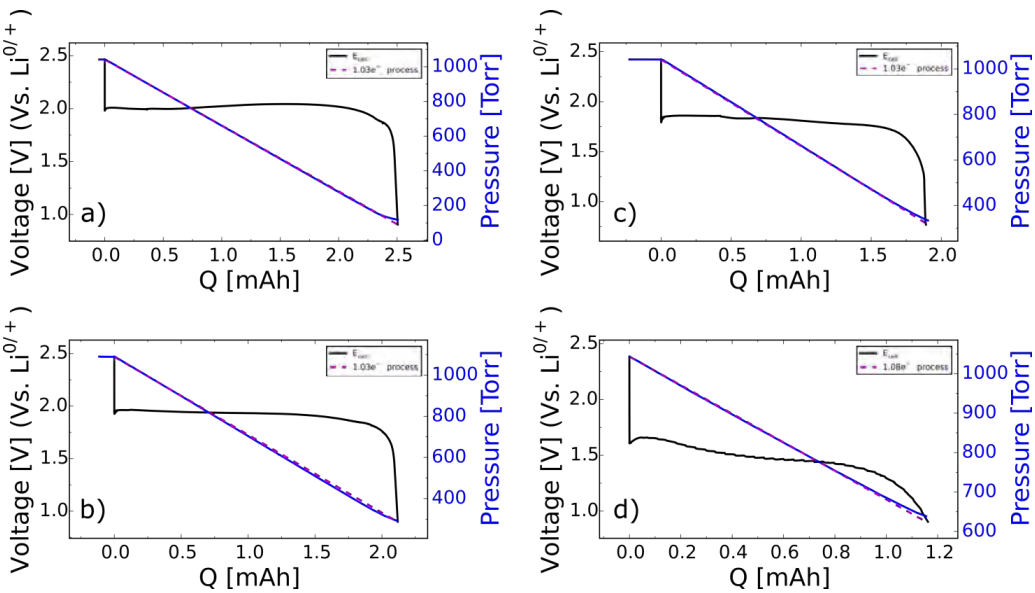

Figure S2: Galvanostatic discharges curve under a closed headspace of O_2 at a) 0.2 mA, b) 0.5 mA, c) 1.0 mA, and d) 2.0 mA.

4.0 Galvanostatic Charges

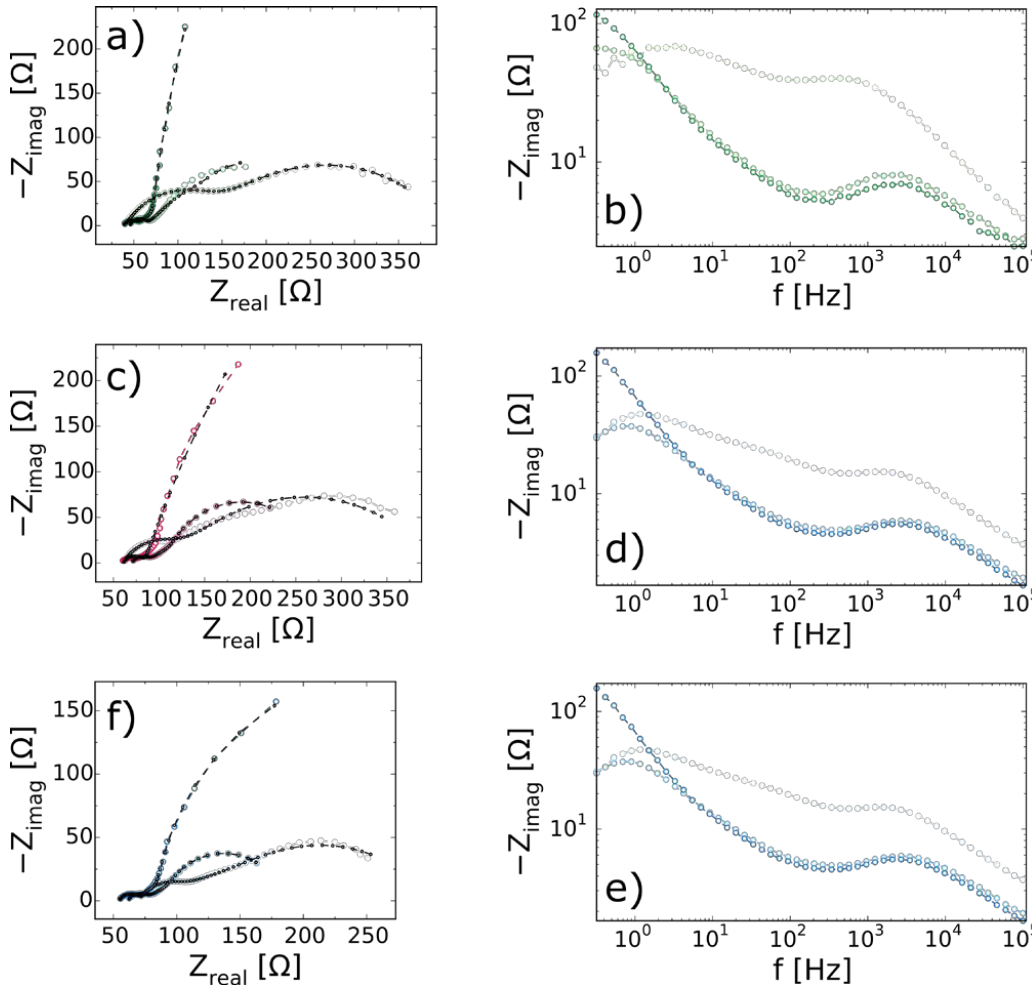

Figure S3: Summary of the electrochemical impedance spectroscopy (EIS) performed during galvanostatic charge. A Nyquist- and Bode plot is depicted for each current with three curves in each. The brightest curve illustrates the initial charge and the color darken as cell failure is reached at the darkest color, while the dotted lines (--) are the fitted equivalent circuits. a) and b) are the 0.1 mA charge, c) and d) 0.5 mA charge, e) and f) 1.0 mA discharge.

5.0 Galvanostatic discharge in Three-Electrode EL-cell

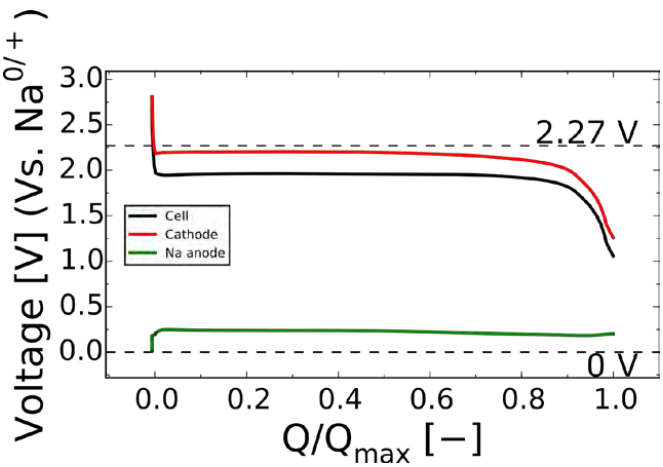

Figure S4: Illustrates a discharge in a three-electrode EL-cell air cell, where a third sodium reference electrode made it possible to measure the cell-, cathode-, and anode potential simultaneously. Here overpotential of 90-250 mV is observed at the anode during discharge and the sudden drop in cell potential is caused by the electrochemistry of the cathode.

6.0 References

(1) McCloskey, B. D. Solvents' Critical Role in Nonaqueous Lithium–Oxygen Battery Electrochemistry. *J. Phys. Chem. Lett.* **2011**, *2*, 1161–1166.

(2) McCloskey, B. D.; Valery, A.; Luntz, A. C.; Gowda, S. R.; Wallraff, G. M.; Garcia, J. M.; Mori, T.; Krupp, L. E. Combining Accurate O_2 and Li_2O_2 Assays to Separate Discharge and Charge Stability Limitations in Nonaqueous Li–O_2 Batteries. *J. Phys. Chem. Lett.* **2013**, *4*, 2989–2993.

(3) Boukamp, B. A. A Linear Kronig-Kramers Transform Test for Immittance Data Validation. *J. Electrochem. Soc.,* **1995**, *142,* 1885-1894.

(4) C. Graves, RAVDAV Data Analysis Software, Version 0.9.7, **2012**.

(5) Hunter, J. D. Matplotlib: A 2D Graphics Environment. *Comput. Sci. Eng.* **2007**, *9*, 90–95.

(6) Oliphant, J. O.; Peterson, P.; et al. Scipy: Open Source Scientific Tools for Python. ***2001***.

(7) Walt, S. van der; Colbert, S. C.; Varoquaux, G. The NumPy Array: A Structure for Efficient Numerical Computation. *Comput. Sci. Eng.* **2011**, *13*, 22–30.

IV

ECS Electrochemistry Letters, **4** (7) A63-A66 (2015)
2162-8726/2015/4(7)/A63/4/$33.00 © The Electrochemical Society

Reactions and SEI Formation during Charging of Li-O_2 Cells

Jonathan Højberg,[a,b,z] Kristian Bastholm Knudsen,[b] Johan Hjelm,[b,*] and Tejs Vegge[b]

[a]*Haldor Topsøe A/S, DK-2800 Kgs Lyngby, Denmark*
[b]*Department of Energy Conversion and Storage, Technical University of Denmark, DK 4000 Roskilde, Denmark*

In this letter we combine detailed electrochemical impedance measurements with quantitative measurements of O_2 evolution and Li_2O_2 oxidation to describe the charge mechanisms during charge of Li-O_2 batteries with porous carbon electrodes. We identify Li_2O_2 oxidation at 3.05 V and an apparent chemical formation of a solid electrolyte interface (SEI) layer as the first monolayer of Li_2O_2 is oxidized, leading to a voltage increase. The first electrochemical degradation reaction is identified between 3.3 V and 3.5 V, and the chemical degradation is limited above 3.5 V, suggesting that a chemically stable SEI layer has been formed.
 [DOI: 10.1149/2.0051507eel]

Manuscript submitted March 31, 2015; revised manuscript received May 4, 2015. Published May 13, 2015.

The non-aqueous Li-O_2 battery has received significant attention in the past years due to its potentially high specific energy and low cost, which makes it ideal for future electric vehicles. The combination of metallic lithium as the negative electrode and reduction of molecular oxygen at the positive electrode enable a theoretical energy density of 3.8 kWh/kg including the weight of lithium and oxygen.

During discharge, oxygen is consumed to form the insoluble Li_2O_2; a high bandgap product that will limit conduction of electrons and holes to the surface when the growing layer reaches a critical thickness.[1,2] Low overpotentials (<0.2 V) have been predicted for discharge and charge using density functional theory,[3–6] and supported experimentally by Luntz et al. using flat glassy carbon electrodes.[2] However, practical batteries with large surface area cathodes display large overpotentials.[7] This decreases the cycle efficiency significantly and open up potential dependent parasitic reactions during charge.[8]

Here, we focus on the initial part of the charge until a potential of 3.6 V to understand why the potential increases as the battery is charged. Understanding and ultimately solving this problem is an important step toward commercialization of the Li-O_2 technology. We have analyzed Li-O_2 batteries identical to a carbon based reference system used in a number of previous publications.[8–12] A differential capacity plot of a galvanostatic charge is used to identify the onset of at least eight electrochemical reactions during a full charge and using differential electrochemical mass spectrometry (DEMS), electrochemical impedance spectroscopy (EIS), and quantitative optical absorption spectroscopy; it was possible to explain why the initial low-overpotential oxidation of Li_2O_2 does not continue and why the voltage increases. The findings are illustrated in Figure 1a.

Experimental

All electrochemical measurements were performed using a 2-electrode Swagelok cell with XC72 carbon black cathodes (Vulcan XC72, Cabotcorp, GA), 1 M LiTFSI (Sigma-Aldrich) in 1,2-dimethoxyethane (BASF) electrolyte, a Whatman glass fiber separator and lithium anode. LiTFSI was dried at 180°C for 12 h and 1,2-dimethoxyethane was dried using 4 Å molecular sieves (Sigma-Aldrich). The carbon cathodes were manufactured by air-spraying a slurry of XC72 Carbon Black and PTFE (60 wt% dispersion in water) in a wt/wt ratio of 3:1 as described in Ref. 8.

Electrochemical impedance spectroscopy (EIS) and galvanostatic discharge-charge curves were measured using Bio-Logic VMP3 and MPG-2 potentiostats. Potentiostatic EIS measurements were performed at different charge potentials, U_{ch}, from 3.1 V to 3.6 V. Frequencies between 20 kHz and 10 mHz were investigated with 15 points per decade and an alternating current (AC) amplitude of 5 mV. All impedance measurements followed the procedure: a) discharge to 2.6 V at 130 mA/g_{carbon} followed by 150 min at 2.6 V, b) charge to U_{ch} at 130 mA/g_{carbon}, and c) continuous EIS measurements at U_{ch} until the current decreased to 13 mA/g_{carbon}. 130 mA/g_{carbon} was chosen because it is within a commercially interesting range and comparable to previous studies.[7–9] The voltage profile is presented in Figure S3 in the Supporting Information.

DEMS measurements were performed at 130–260 mA/g_{carbon} and the gas consumption and gas evolution were quantified using both pressure measurements and mass spectrometry. The applied in-house DEMS setup is similar in design to the setup used by McCloskey et al.[9]

To assess the amount of Li_2O_2 in the air electrode at different stages of charge, we used a spectrophotometric measurement to determine the concentration of a Ti-complex. Li_2O_2 was allowed to react with water to form H_2O_2 that oxidizes $TiOSO_4$ in the solution to form the Ti-complex. The concentration of the Ti-complex was determined by measuring the absorbance at around 408 nm. A detailed description of the method is included in the Supporting Information.

Results and Discussion

Figure 1b shows a typical charge curve, and Figure 2 shows differential capacity plots (dQ/dV) of such curves. The peaks correspond to voltage plateaus in the charge curve and thereby different processes, and from this, eight electrochemical processes can be identified at 3.05 V, 3.3 V, 3.4 V, 3.5 V, 3.85 V, 4.2 V, 4.3 V and 4.5 V. These potentials form the basis of the following discussion. Analyses of 10 charge measurements following a discharge to 2.6 V show a charge capacity below 3.15 V corresponding to 540 ± 80 $\mu mol_{Li_2O_2}/g_{carbon}$. This corresponds to 4.3% of the total discharge capacity or approximately one monolayer as calculated in the Supporting Information.

Quantification of Li_2O_2 and O_2 evolution.— Figure 3a shows the oxygen evolution (blue line) and the Li_2O_2 removal (red line) as the cathode is charged. The oxygen evolution is determined based on the DEMS measurements presented in Figure S1 in the Supporting Information and the Li_2O_2 removal is based on the optical absorption measurements presented in Figure S2 in the Supporting Information. The O_2 evolution and, in particular, the deviation from the theoretical value is in accordance with measurements presented by McCloskey et al.,[7] and suggests the presence of electrochemical degradation reactions, especially at potentials above 3.5 V. The Li_2O_2 is, however, disappearing more rapidly than expected from the electrochemistry, suggesting a significant chemical degradation. Figure 3b shows the amount of chemical and electrochemical reactions in different potential intervals, and it is clear that the chemical degradation is most significant in the potential ranges 2 V–3.1 V and 3.3 V–3.5 V. This effect is somewhat more pronounced than previously reported.[7]

Electrochemical impedance spectroscopy (EIS).— EIS was measured at 11 different potentials during the initial charge from 3.10 V to 3.60 V. Figure S4 in the Supporting Information shows a typical measurement, with the equivalent circuit fit and the determination of the resistance, $R_{Li_2O_2}$, and the pseudocapacitance. Both parameters are related to a combination of the charge transfer through Li_2O_2 and Li_2O_2

*Electrochemical Society Active Member.
zE-mail: jhoj@topsoe.dk

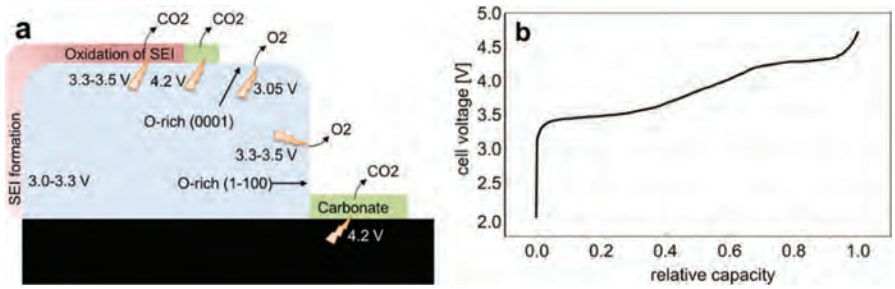

Figure 1. (a) Sketch of the reactions and SEI formation during charge of the Li-O_2 battery as discussed in this letter. The potentials in the figure are the proposed onset potentials. Li_2O_2 oxidation occurs at 3.05 V and an SEI layer is formed immediately on the freshly oxidized surface. At 3.3 V–3.5 V several reactions occur. Among these are gas evolution from the SEI layer and oxidation of other Li_2O_2 surfaces. (b) Charge of a Li-O_2 battery after a discharge to 2.6 V.

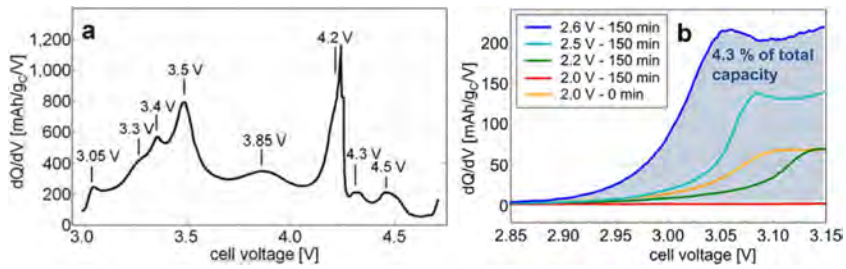

Figure 2. (a) Differential capacity plot (dQ/dV) of a representative battery charge. Each peak represents the onset of an electrochemical reaction. (b) Differential capacity plot of the initial part of the charge following a constant current 130 mA/g_{carbon} discharge to 2.0 V, 2.2 V, 2.5 V or 2.6 V, which was maintained for 150 min before charging. The measurement labeled *2.0 V–0 min* corresponds to charging immediately after discharge to 2.0 V.

oxidation.[8] Figure 4a shows the cathode resistance at selected voltages during charge, as determined by EIS. It is seen that the resistance increases from 3.10 V to 3.30 V, decreases at 3.33 V, increases until 3.50 V, and decreases again at 3.60 V. The resistance and corresponding pseudocapacitances at the marked cross section at 65 mA/g_{carbon} are shown in Figure 4b for all 11 potentials. Both the resistance and the pseudocapacitance change stepwise as a function of potential. The resistance increases monotonic until 2.27 V, then it drops and continue a second monotonic increase from 3.33 V to 3.50 V after which it drops. The pseudocapacitance is high at 3.10 V, decreases at 3.20 V, increases at 3.33 V and decreases again at 3.60 V. When keeping the potential at 3.10 V, it was observed that the capacitance decreased 60% from 0.7 mF/g_{carbon} at 130 mA/g_{carbon} to 0.28 mF/g_{carbon} at 13 mA/g_{carbon}. During the measurement, the current decreases and Li_2O_2 is removed. Both changes are expected to increase the capacitance, and the decreasing capacitance therefore clearly suggests that compounds are deposited during this initial charge, which is in line with the absorption measurements.

Identification of Li_2O_2 oxidation at 3.05 V.— We argue that the process identified at 3.05 V is oxidation of Li_2O_2 based on three observations. First, Figure S1 in the Supporting Information, shows that the e^-/O_2 ratio is between 2.0 (at 2 V) and 2.1 (at 3.2 V) in the beginning of the charge, which is exactly – or at least very close to – the expected value for Li_2O_2 oxidation. Second, Figure 2b shows how the onset potential of the process at around 3.05 V increases with the depth of discharge and the exposure time at low potentials. To understand this shift, it is noted that DEMS measurements show that the e^-/O_2 ratio is 2.0 during the entire discharge, and McCloskey et al. show that the Li_2O_2 yield is independent of the depth of discharge.[7] This means that the thickness, and thereby the conductivity, of the Li_2O_2 layer is the only parameter expected to change between the

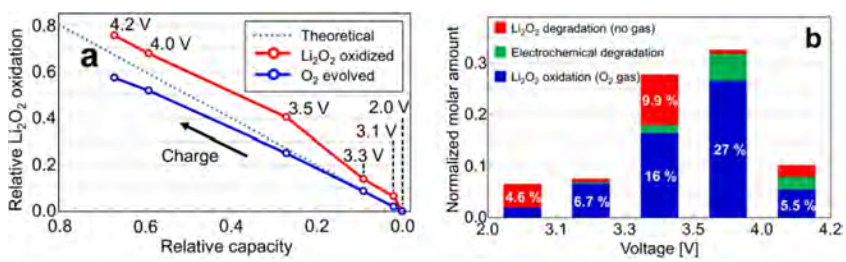

Figure 3. (a) Measurement of O_2 evolution using DEMS (blue) and Li_2O_2 removal (either chemical or electrochemical) determined spectrophotometrically (red). The dotted line corresponds to a pure electrochemical 2 e^-/O_2 oxidation of Li_2O_2 without any chemical degradation. (b) The amount of Li_2O_2 oxidation with and without gas evolution and electrochemical degradation in different potential intervals during charge. Values are normalized such that the sum of the electrochemical reactions (blue and green) equals the relative change in capacity in each interval and sum up to 1 for a full charge.

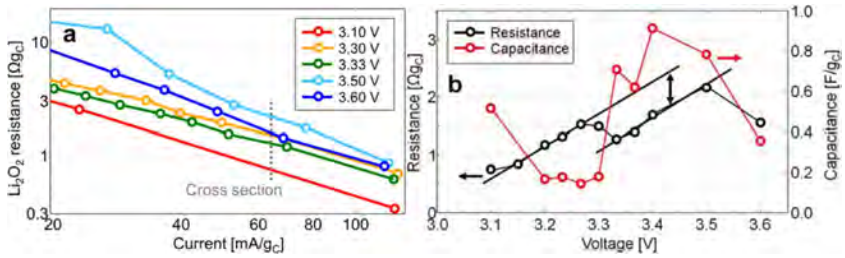

Figure 4. (a) The resistance related to the charge transfer through Li_2O_2 and Li_2O_2 oxidation measured at different potentials determined using EIS. The current decreases during the measurement. (b) Resistance and capacitance values at different potentials during charge. Guide lines have been inserted to illustrate the monotonic increases in the resistance.

measurements, and as the conductivity through the Li_2O_2 layer affects the onset potential of the reaction, it suggests that the reaction occurs at the Li_2O_2 surface. Third, the onset potential at the investigated current densities (~0.1 $\mu A/cm^2$ real surface area) is 2.9 V–3.0 V which corresponds well with the onset potential of Li_2O_2 oxidation measured by Viswanathan et al. using flat glassy carbon electrodes.[13]

SEI layer formation.— DEMS measurements show that all electrons come from the Li_2O_2 oxidation at the onset of the charge, until 3.1 V. In this interval, it was found from Figure 2b that 4.3% of the Li_2O_2 was oxidized electrochemically and in Figure 3b it is seen that another 4.6% was removed without gas evolution. Since all electrons are accounted for by the gas evolved, the reaction with no gas evolution must be chemical and it is interpreted as the formation of an SEI layer based on three observations. First, the amount of Li_2O_2 degradation is close to the amount of electrochemically oxidized Li_2O_2 in the initial part of the charge, and as the oxidation does not continue, it suggests that the electrochemical oxidation of Li_2O_2 exposes the surface such that the oxidation is followed by a chemical degradation of Li_2O_2, forming an SEI layer. Furthermore, the amount of oxidized and chemically degraded Li_2O_2 both correspond to approximately one monolayer, which suggest that the reaction occur on the entire surface of Li_2O_2. Second, the 60% decrease in capacitance at 3.1 V suggests a significant deposition of a dielectric compound that could be explained by the formation of an SEI layer. Third, the monotonic increase in Li_2O_2 resistance until 3.3 V suggests a decrease of available surface area or an increased electronic transport resistance. Both options could be explained by a growing SEI layer.

Electrochemical degradation.— Identification of the lowest potential without electrochemical degradation is important to identify a safe-voltage limit. We propose that at least one of the three separate processes identified in the differential capacity plot in the voltage range from 3.3 V to 3.5 V is an electrochemical degradation reaction as the e^-/O_2 ratio increases in this range. Two observations suggest that the reaction occurs at 3.3 V, but further investigation is needed to determine the onset potential definitively. First, EIS measurements show that the pseudocapacitance increases and the resistance decreases at 3.3 V. A sudden change like this suggests a new reaction pathway at this potential. Second, isotope measurements presented by McCloskey et al. using an identical system show that CO_2 evolution occurs from the electrolyte-Li_2O_2 interface from 3.3 V.[9] As the CO_2 evolution reaction depends on the potential, it is likely that this reaction is the new reaction pathway seen in the EIS measurements. To explain that three processes are identified in this voltage range, it is noted that DFT calculations from different groups show that onset potentials in this range could also be oxidation of another Li_2O_2 crystal plane like the oxygen rich (1–100) surface.[14,15]

Charge above 3.5 V.— At around 3.6 V, the resistance and the pseudocapacitance decrease again. The correspondence between impedance and overpotential is not straight forward, but the significant decrease in impedance as the voltage increases, is a strong indication of a shift in equilibrium potential caused by a mixed potential established between different oxidation reactions to maintain the constant current. The theory of a mixed a potential is further substantiated by measurements at higher potentials shown in a previous publication.[8]

Summary

The main results of this work are shown in Figure 1a. We have showed that Li_2O_2 is oxidized already at 3.05 V in porous carbon cathodes, but that this facile oxidation is limited to approximately one monolayer. Analysis of the chemical degradation and the change in double layer capacitance indicate that the Li_2O_2 surface reacts with the electrolyte to form a SEI layer as soon as the outermost layer is oxidized. The resistance increases as the SEI layer blocks the surface and the voltage increases to maintain the constant current.

Three reactions were identified between 3.3 V and 3.5 V. The interval is dominated by Li_2O_2 oxidation with a small amount of electrochemical degradation and significant chemical degradation of Li_2O_2. It is expected that the reactions in this region are a gas evolving degradation reaction in the Li_2O_2-electrolyte interface and oxidation of another Li_2O_2 crystal plane, possibly the O-rich (1–100) plane, among others. Above 3.5 V the chemical and electrochemical reactions become more complicated and a shift in equilibrium potential due to the establishment of a mixed potential is indicated as previously reported,[8] but further work would be needed to understand and distinguish these reactions fully.

In conclusion, the immediate formation of an SEI layer on the oxidized Li_2O_2 surface in the initial part of the charge is a significant problem that needs to be resolved before a viable Li-O_2 battery can be developed and an analysis of the very first part of the charge might serve as a suitable screening parameter in the search for better electrolytes.

Acknowledgments

The authors acknowledge support from the ReLiable project funded by the Danish Council for Strategic Research – Programme Commission on Sustainable Energy and Environment (project #11-116792).

References

1. V. Viswanathan, K. S. Thygesen, J. S. Hummelshøj, J. K. Nørskov, G. Girishkumar, B. D. McCloskey, and A. C. Luntz, *J. Chem. Phys.*, **135**, 214704 (2011).
2. A. C. Luntz, V. Viswanathan, J. Voss, J. B. Varley, A. Speidel, J. K. Nørskov, and R. Scheffler, *J. Phys. Chem. Lett.*, **4**, 3494 (2013).
3. J. S. Hummelshøj, J. Blomqvist, S. Datta, T. Vegge, J. Rossmeisl, K. S. Thygesen, A. C. Luntz, K. W. Jacobsen, and J. K. Nørskov, *J. Chem. Phys.*, **132**, 071101 (2010).
4. J. S. Hummelshøj, A. C. Luntz, and J. K. Nørskov, *J. Chem. Phys.*, **138**, 034703 (2013).
5. J. Chen, J. S. Hummelshøj, K. S. Thygesen, J. S. G. Myrdal, J. K. Nørskov, and T. Vegge, *Catal. Today*, **165**, 2 (2011).
6. D. J. Siegel and M. D. Radin, *Energy Environ. Sci.*, **6**, 2370 (2013).

7. B. D. McCloskey, A. Valery, A. C. Luntz, S. R. Gowda, G. M. Wallra, J. M. Garcia, T. Mori, and L. E. Krupp, *J. Phys. Chem. Lett.*, **4**, 2989 (2013).
8. J. Højberg, B. D. McCloskey, J. Hjelm, T. Vegge, K. Johansen, P. Norby, and A. C. Luntz, *ACS Appl. Mater. Interfaces*, **7**, 4039 (2015).
9. B. D. McCloskey, A. Speidel, R. Scheffler, D. Miller, V. Viswanathan, J. S. Hummelshøj, J. K. Nørskov, and A. C. Luntz, *J. Phys. Chem. Lett.*, **3**, 997 (2012).
10. B. D. McCloskey, D. S. Bethune, R. M. Shelby, G. Girishkumar, and A. C. Luntz, *J. Phys. Chem. Lett.*, **2**, 1161 (2011).
11. S. R. Gowda, A. Brunet, G. M. Wallraff, and B. D. McCloskey, *J. Phys. Chem. Lett.*, **4**, 276 (2013).
12. B. D. McCloskey, R. Scheffler, A. Speidel, D. S. Bethune, R. M. Shelby, and A. C. Luntz, *J. Am. Chem. Soc.*, **133**, 18038 (2011).
13. V. Viswanathan, J. K. Nørskov, A. Speidel, R. Scheffler, S. R. Gowda, and A. C. Luntz, *J. Phys. Chem. Lett.*, **4**, 556 (2013).
14. M. D. Radin, F. Tian, and D. J. Siegel, *J. Mater. Sci.*, **47**, 17 (2012).
15. J. S. G. Myrdal and T. Vegge, *Rsc Adv.*, **4**, 15671 (2014).

Supporting Information:

Reactions and SEI formation during charging of Li-O_2 cells

Jonathan Højberg[1,2,*], Kristian Bastholm Knudsen[2], Johan Hjelm[2], Tejs Vegge[2]

[1]Haldor Topsøe A/S, Nymøllevej 55, DK-2800 Kgs Lyngby, Denmark

[2]Department of Energy Conversion and Storage, Technical University of Denmark, Frederiksborgvej 399, DK-4000 Roskilde, Denmark

*Corresponding author

E-mail: jhoj@topsoe.dk

Tel.: (+45) 27292175

Fax: (+45) 45272999

DEMS measurements

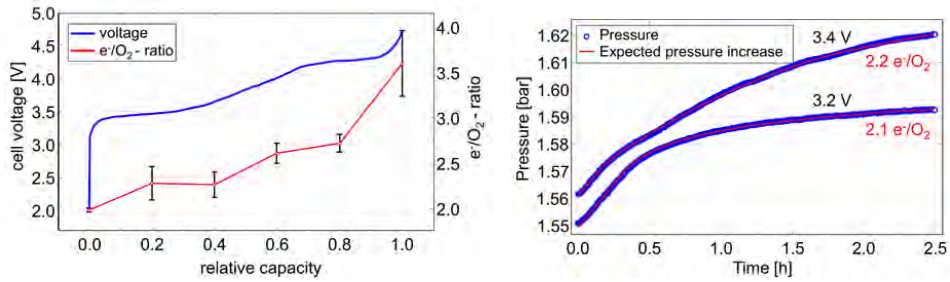

Figure S1. Left: Charge of a Li-O_2 battery after a discharge to 2.6 V. The e^-/O_2 ratio was calculated using an average of six DEMS measurements. The errorbars indicate one standard deviation. Right: Headspace pressure increase during charge at 130 mA/g_{carbon} constant current charge until a potential U_{ch} (noted in the figure) is reached. The charging is continued potentiostatic at U_{ch}, resulting in a decreasing current with time.

Calculation of monolayers

It is not possible to estimate the thickness of the Li_2O_2 layer, because the full BET area may not reflect the accessible surface area, as the use of binder has been shown to block the micropores of the carbon electrode.[1,2] Another approach is to use that it is generally accepted that the sudden death occur as the insulating Li_2O_2 layer reaches a thickness of ~5 nm at relevant current densities, and, using this thickness, the initial oxidation of 4.3 % correspond to a removal of 2.1 Å Li_2O_2. This is approximately one monolayer of Li_2O_2.

Chemical quantification of Li_2O_2

After electrochemical test of a Li-O_2 battery, the cell was purged with argon and transferred to a glovebox. The cell was carefully disassembled and the cathode was extracted. Each cathode was washed with 1,2-dimethoxyethane (BASF) dried using 4 Å molecular sieves (Sigma-Aldrich), and the cathodes were subsequently dried in vacuum. The cathodes were taken from the glovebox and immediately put into a 4 mL 0.063-0.07 % $TiOSO_4$ aqueous solution and the colored oxidized Ti-complex was seen immediately. The reactions occurring are listed in (S1) and (S2).[3]

$$Li_2O_2 + 2H_2O \rightarrow 2LiOH + H_2O_2 \qquad (S1)$$

$$Ti(IV)OSO_4 + H_2O_2 + 2H_2O \rightarrow 4H^+ + H_2Ti(VI)O_4 + OSO_4^{4-} \qquad (S2)$$

$H_2Ti(VI)O_4$ absorbs strongly at 408 nm. The solutions were left to react for 15-30 min and to remove carbon particles, which otherwise would interfere with the spectrophotometric measurement, samples were centrifuged and the supernatant was extracted yielding a clear colored liquid that was characterized using a Shimadzu UV-3600 PharmaSpec with 1 nm resolution and medium scan in absorbance mode.

The results from the absorption measurements are illustrated in Figure S2.

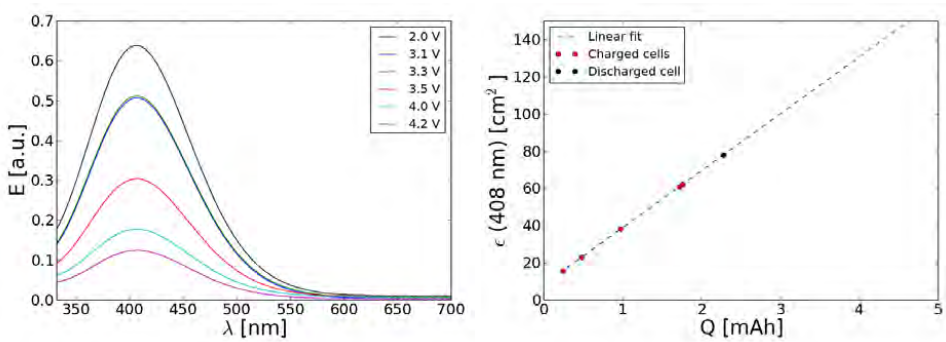

Figure S2. Optical absorption spectroscopy for the washed Li_2O_2 coated electrodes. Left: The extinction of the $H_2Ti(VI)O_4$ complex in aqueous solutions illustrating the amount of detected Li_2O_2. Right: Lambert-Beer type

calibration curve used to determine the amount of Li_2O_2 in the cathodes. The curve is made by measuring the absorbance of solutions with a known amount of peroxide. In the graph, the amount of Li_2O_2 is represented by a capacity equivalent.

The chemical quantification of Li_2O_2 using the Ti-complex presumes that Li_2O_2 reacts with water forming LiOH and H_2O_2. Another reaction is, however, possible

$$Li_2O_2 + H_2O \rightarrow \frac{1}{2}O_2 + 2LiOH \qquad (S3)$$

If this reaction takes place, the amount of Li_2O_2 would be underestimated, since the Ti() complex is only oxidized by H_2O_2 that is not formed during this reaction.

Experimentally we did not observe any O_2 evolution from cathodes submerged in H_2O and previous McCloskey et al. used a similar method to convert Li_2O_2 and LiO_2 from identical cathodes into H_2O_2, and detailed tests of the method showed that all Li_2O_2 was converted to H_2O_2.[4]

Electrochemical impedance spectroscopy

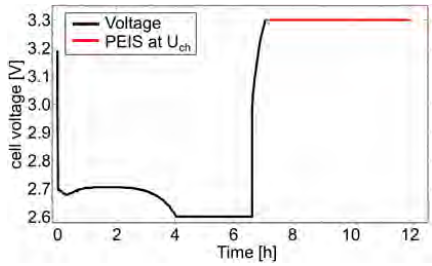

Figure S3. Typical voltage profile used to measure the impedance at specific potentials during charge. All impedance measurements follow the procedure: a) discharge to 2.6 V at 130 mA/g_{carbon} followed by 150 min at 2.6 V, b) charge to U_{ch} at 130 mA/g_{carbon}, and c) continuous EIS measurements at U_{ch} until the current decreased to 13 mA/g_{carbon}. The voltage profile show a measurement with U_{ch} = 3.30 V.

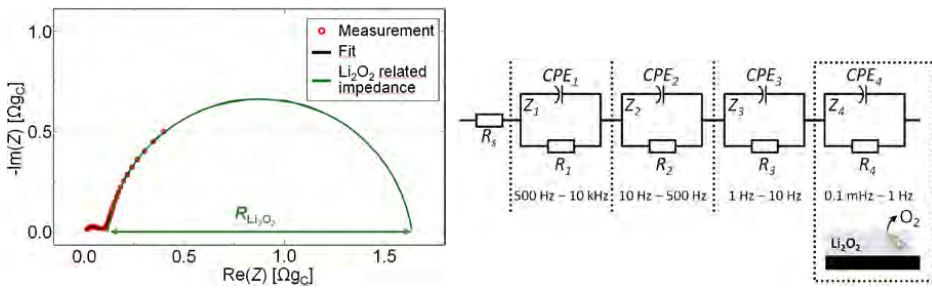

Figure S4. Left: Typical EIS measurement performed at a constant potential U_{ch}. The spectrum is dominated by the low frequency arc that has been shown to relate to the Li_2O_2 reduction during discharge and Li_2O_2 oxidation during charge.[5] Right: The equivalent circuit used to describe the impedance during charge. The allowed peak-frequency intervals of all processes are listed in the figure. As previously shown, Z_4 is related to the oxygen oxidation and double layer capacitance of the cathode.[5]

As discussed in a previous publication, the pseudocapacitance C^* is calculated using[5]

$$\boldsymbol{C^* = Q^{1/n}\left(\frac{R_\Omega R}{R_\Omega + R}\right)^{(1-n)/n}},$$

where R, Q and n are fitting parameters from the Voigt elements, and R_Ω is the DC resistance at the investigated frequency.

References

1. S. Meini, M. Piana, H. Beyer, J. Schwammlein, and H. A. Gasteiger, *J. Electrochem. Soc.*, **159**, A2135–A2142 (2012).

2. R. Younesi, N. Ingh, S. Urbonaite, and K. Edström, in *ECS transaction*,, p. 121–127 (2010).

3. G. Eisenberg, *Ind. Eng. Chem. Anal. Ed.*, **15**, 327–328 (1943).

4. B. D. McCloskey, A. Valery, A. C. Luntz, S. R. Gowda, G. M. Wallra, J. M. Garcia, T. Mori, and L. E. Krupp, *J. Phys. Chem. Lett.*, **4**, 2989–2993 (2013).

5. J. Højberg, B. D. McCloskey, J. Hjelm, T. Vegge, K. Johansen, P. Norby, and A. C. Luntz, *ACS Appl. Mater. Interfaces*, **7**, 4039–4047 (2015).

V

Communication: The influence of CO_2 poisoning on overvoltages and discharge capacity in non-aqueous Li-Air batteries

Yedilfana S. Mekonnen,[1,2] Kristian B. Knudsen,[1] Jon S. G. Mýrdal,[1] Reza Younesi,[1] Jonathan Højberg,[1] Johan Hjelm,[1] Poul Norby,[1] and Tejs Vegge[1,a)]
[1]*Department of Energy Conversion and Storage, Technical University of Denmark, Frederiksborgvej 399, DK-4000 Roskilde, Denmark*
[2]*Center for Atomic-scale Materials Design, Technical University of Denmark, DK-2800 Lyngby, Denmark*

(Received 31 January 2014; accepted 11 March 2014; published online 24 March 2014)

The effects of Li_2CO_3 like species originating from reactions between CO_2 and Li_2O_2 at the cathode of non-aqueous Li-air batteries were studied by density functional theory (DFT) and galvanostatic charge-discharge measurements. Adsorption energies of CO_2 at various nucleation sites on a stepped $(1\bar{1}00)$ Li_2O_2 surface were determined and even a low concentration of CO_2 effectively blocks the step nucleation site and alters the Li_2O_2 shape due to Li_2CO_3 formation. Nudged elastic band calculations show that once CO_2 is adsorbed on a step valley site, it is effectively unable to diffuse and impacts the Li_2O_2 growth mechanism, capacity, and overvoltages. The charging processes are strongly influenced by CO_2 contamination, and exhibit increased overvoltages and increased capacity, as a result of poisoning of nucleation sites: this effect is predicted from DFT calculations and observed experimentally already at 1% CO_2. Large capacity losses and overvoltages are seen at higher CO_2 concentrations. © *2014 AIP Publishing LLC*. [http://dx.doi.org/10.1063/1.4869212]

I. INTRODUCTION

As energy storage needs are growing rapidly, there is also an increase in research into high energy density materials for energy storage. Significant attention has been given to metal-air batteries, particularly Li-air batteries, as future environmentally friendly high energy density storage for vehicles, where the capacity offered by existing Li-ion technology is too low to solve the increasing demands on batteries.[1] The Li-O_2 couple is particularly attractive and could have ∼5–10 times greater specific energies than currently available Li-ion batteries, though there are severe scientific and technical challenges that need to be addressed.[2,3] Such as a clear understanding of the Li_2O_2 growth mechanisms, transport processes, interfacial phenomena, air impurities, and stability of the key components are vital parts of non-aqueous rechargeable Li-air cell research.[4]

As first reported by Abraham and Jiang in 1996, the Li-O_2 battery with aprotic solvent is shown to be rechargeable, when Li_2O_2 is formed during discharge at the cathode.[5] Detailed understanding of the Li_2O_2 growth mechanism is important to solve the problem associated with the practical limitations of the battery. Previous theoretical works by Hummelshøj *et al.*[6] and Radin *et al.*[7,8] showed that steps on a reconstructed $(1\bar{1}00)$surface could act as nucleation sites for low discharge overvoltage and facets such as (0001), $(1\bar{1}00)$, and $(11\bar{2}0)$ have similar surface energies. Hummelshøj *et al.*[9] have also shown that surfaces are potential dependent and vary during discharge and charge. According to G_0W_0 calculations, both Li_2O_2 and Li_2CO_3 are insulating materials with wide band gap of 4.9 and 8.8 eV, respectively.[10–12] Therefore, as these materials deposit at the cathode surface during discharge they will limit the electronic conduction and lead to sudden death during discharge within 5–10 nm thick Li_2O_2 deposits.[13,14] However, recent DFT calculations found that hole and electron polaronic transports at the surface and in bulk Li_2O_2 and Li_2CO_3 can take place. Using a PBE+U (Hubbard-corrected Perdew–Burke–Ernzerhof) exchange correlation functional, Garcia-Lastra *et al.*[11] revealed that the hole polarons have higher mobility than electron polarons and Li_2CO_3 exhibits lower conduction than Li_2O_2. Recent works by Luntz *et al.* have shown that hole tunneling should dominate and polaronic transport is only expected to be significant in Li_2O_2 at elevated temperatures and low current densities.[15,16]

Li_2CO_3 like crystalline species are formed by parasitic side reactions between the Li_2O_2 or LiO_2 and carbon sources from air impurities such as CO and CO_2 gases,[17] the graphite itself, or the decomposition of aprotic electrolytes. Younesi *et al.*[18,34] reported the degradation of various electrolytes by Li_2O_2 and documented Li_2CO_3 as a decomposition product from aprotic electrolytes. Likewise, McCloskey *et al.*[3] have shown that carbonates accumulate at the C-Li_2O_2 and Li_2O_2-electrolyte interfaces and are responsible for a large potential increase during recharge and a huge decrease in exchange current density. This makes growth of Li_2O_2 on Li_2CO_3 an equally important process to investigate, but this is beyond the scope of this communication. As reported by Siegfried *et al.*[19] and Myrdal and Vegge[20] adsorption of sulfur containing compounds on oxide surfaces could also control the electrochemical growth mechanism. Adsorbed species at surfaces can potentially block the nucleation sites, and therefore, alter the growth directions, overvoltages, and capacities.

In this communication, we address the influence of CO_2 contamination on the Li_2O_2 growth mechanism, discharge/charge overvoltages, and capacity in non-aqueous

a)E-mail: teve@dtu.dk

TABLE I. Adsorption energies of CO_2 in the gas phase at $(1\bar{1}00)$ Li_2O_2 surface.

Species	Sites	Adsorption energy (eV)
CO_2	Step valley	−0.73
	Terrace valley	−0.21
	Step ridge	−0.02

Li-air batteries using density functional theory (DFT) and galvanostatic measurements. Among other air contaminants, CO_2 is the most critical subject due to its high solubility in aprotic electrolytes and high reactivity with Li_2O_2 to form an insulating material Li_2CO_3.

II. COMPUTATIONAL RESULTS AND ANALYSIS

DFT[21–23] as implemented in the GPAW (grid-based projector-augmented wave method) code[24] is used to perform the presented calculations through the atomic simulation environment (ASE).[25] GPAW is built on real space grids and non-valence electrons are described by PAW (projector augmented-wave method).[26,27] Electron exchange and correlation is approximated by the revised Perdew–Burke–Ernzerhof (RPBE) functional.[28] The stepped $(1\bar{1}00)$ Li_2O_2 surface with a super cell consisting of a 56–64 atoms slab with a 18 Å vacuum layer between periodic images along the z-axis, see Fig. S1 in the supplementary material.[35] Since the oxygen rich (0001) facet will also be exposed, in particular under charging conditions,[9] and subsequent investigations should be performed to analyze the detailed mechanisms of CO_2 bonding to this facet. Recent computational DFT results for SO_2 adsorption on stepped (0001) and $(1\bar{1}00)$ surfaces do, however, show preferential bonding to the (1100) facets,[20] which is investigated here. The k-points are sampled with a (4,4,1) Monkhorst-Pack mesh and 0.15 grid points is used. Atomic energy optimization calculations are performed until all forces are less than 0.01 eV/Å. Energy barriers are calculated by the climbing image nudged elastic band (CINEB) method.[29–31]

Adsorption energies of CO_2 at various nucleation sites on a stepped $(1\bar{1}00)$ Li_2O_2 surface were determined, see Table I. CO_2 binds preferentially at the step valley site and weakly binds at the step ridge site. NEB calculations show that once CO_2 is adsorbed at step valley site, it is bound by barriers upwards of 3 eV, see Fig. S2 in the supplementary material,[35] since the CO_2 molecule is required to desorb from the surface prior to re-adsorbing at the step site. The detailed nature of a conversion of adsorbed CO_2 to Li_2CO_3 warrants further investigations, but we find the adsorption of a single CO_2 molecule forms a $Li_{\sim 3}CO_3$-type complex (Fig. 1(b)), which could act as a nucleation site for further growth of Li_2CO_3.

The computational lithium electrode approach is used in the free energy calculations.[6,32] Defined as, U = 0, when bulk Li anode and Li ions in solution ($Li^+ + e^-$) are at equilibrium. The free energy change of the reaction is shifted by $-neU$ at an applied bias, where n is the number of transferred electrons; other assumptions are listed in the supplementary material.[35] As reported by Hummelshøj *et al.*, kinks and steps sites of the stepped $(1\bar{1}00)$ Li_2O_2 surface are favorable nucleation sites for a low overvoltage Li_2O_2 growth mechanism. The influence of CO_2 poisoning on the Li_2O_2 growth mechanism is studied while CO_2 is already adsorbed at step valley site (Fig. 1(b)).

The free energy diagram in Fig. 2 shows a four steps, two formula units Li_2O_2 growth mechanism on the stepped $(1\bar{1}00)$ Li_2O_2 surface with and without CO_2. The first step in the presence of CO_2 is adsorption of LiO_2 species (Fig. 1(c)), and which reduces the binding energy by 0.44 V compared to the pure discharge. The next step is the addition of a second LiO_2 species (Fig. 1(d)), which is the potential limiting charge step that raises the binding energy by 0.20 V compared to pure Li_2O_2. This is followed by subsequent additions of two Li (Figs. 1(e) and 1(f)) with relatively small binding energies with respect to a pure discharge. In the pure O_2 discharge mechanism, unlike in the presence of CO_2, addition of the first Li is the limiting charge potential step. The $2Li_2O_2$ growth at the step surface effectively displaces CO_2 from the step to the less stable terrace site.

Hummelshøj *et al.* have reported that the pure Li_2O_2 growth mechanism follows a 4 steps reaction mechanism, where all reaction steps are electrochemical, similar to what is seen in the presence of CO_2. The equilibrium potential can be obtained as $U_0 = -\Delta G/2e$. The effective equilibrium potential on a pure surface becomes 2.73 V (experimental value, $U_{0,Exp} = 2.85$ V), while in the presence of CO_2, this is effectively reduced to 2.53 V for the first cycle due to the shift in binding energy of CO_2 from a step valley to terrace site. As a result, discharge at other facets may become activate.[9] At neutral bias all reaction steps are downhill, but at an applied potential, the free energy difference changes for each step calculated as

$$\Delta G_{i,U} = \Delta G_i - eU. \tag{1}$$

The lowest free energy step, $\Delta G_{i,min}$, along the reaction path becomes uphill first at an applied potential called limited discharge potential, $U_{discharge}$, while the largest free energy step, $\Delta G_{i,max}$, that is last to become downhill for the reversed reaction at an applied potential called limited charge potential, U_{charge}, obtained as

$$U_{discharge} = \min[-\Delta G_i/e] \text{ and } U_{charge} = \max[-\Delta G_i/e]. \tag{2}$$

In the presence (absence) of a single CO_2 molecule, this discharge occurs as described in Fig. 1, resulting in $U_{discharge} = 2.21$ V (2.66 V), and $U_{charge} = 2.97$ V (2.81 V) and the discharge and charge overvoltages in the presence (absence) of CO_2 are $\eta_{discharge} = 0.31$ V (0.07 V), and $\eta_{charge} = 0.44$ V (0.08 V). The calculated 0.44 V overvoltage for charge corresponds to low CO_2 concentrations, where only a single CO_2 molecule is adsorbed on the Li_2O_2 step forming a $Li_{\sim 3}CO_3$ type complex (see Fig. 1). Here, the charging process follows the same reaction steps as the discharge, but in reverse (from right to left in Fig. 2), i.e., the first two steps are desorption of two Li and followed by desorption of 2 LiO_2 species: in total desorbing 2 Li_2O_2 units from the surface and returning to the configuration in Fig. 1(b). Quantitative agreement with

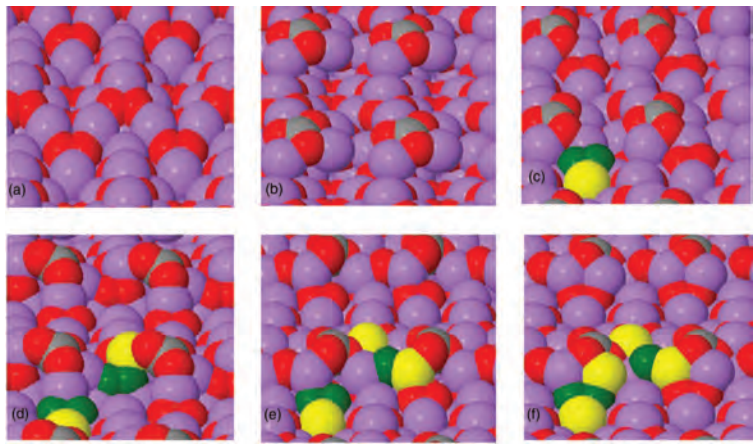

FIG. 1. Stepped Li_2O_2 ($1\bar{1}00$) surface before and after adsorption of CO_2 and 4 steps Li_2O_2 growth pathways during discharge. (a) Pure stepped Li_2O_2 surface. (b) CO_2 adsorbs to step valley site forming a $Li_{\sim 3}CO_3$ type complex. (c) 1st LiO_2 adsorbs. (d) 2nd LiO_2 adsorbs. (e) 1st Li. (f) 2nd Li adsorbs to the surface completing growth of 2 Li_2O_2 formula units. Atoms labeled as: C (gray), Li (purple), and O (red). Deposited atoms shown as: Li (yellow) and O (green).

experimental overvoltages can therefore only be expected for low concentrations of CO_2 (e.g., 1%). For higher CO_2 concentrations, the formation of crystalline Li_2CO_3 would be expected, resulting in significantly larger overvoltages.[3]

III. EXPERIMENTAL RESULTS AND ANALYSIS

Li-air batteries were constructed using a Swagelok design and assembled inside an Ar-filled glovebox ($\leq$3 ppm O_2 and H_2O). Each battery contained a 200 μl 1 M LiTFSI (99.95%, Sigma-Aldrich) and 1,2-dimethoxymethane, DME, (H_2O < 20 ppm, BASF) electrolyte. Cathodes consisted of P50 AvCarb carbon paper (Fuel cell store), which were sonicated using 2-propanol (99.5%, Sigma-Aldrich) and acetone ($\geq$99.8%, Sigma-Aldrich), introduced into a glovebox where they were rinsed with DME before drying in vacuum at 80 °C for 12 h. Cathodes were supported by a 316 steel mesh. A 10 mm diameter lithium foil (99.9%, Sigma-Aldrich) was used as anode. Two Celgard separators 2500 (Celgard) were placed in between the two electrodes. The separators were sonicated in EtOH (99.9%, Sigma-Aldrich), transferred to a glovebox, and rinsed with DME before drying in vacuum at 80 °C for 12 h. Experiments were performed using a Bio-Logic VMP3 Multichannel galvanostat (Bio-Logic, Claix, France). Batteries were operated in two galvanostatic modes: First, at 100 μA (127.3 μA/cm^2) where cells were discharged to 2 V and charged to 4.6 V vs. Li^+/Li. Second, at 50 μA (63.6 μA/cm^2) using the same potential limits.

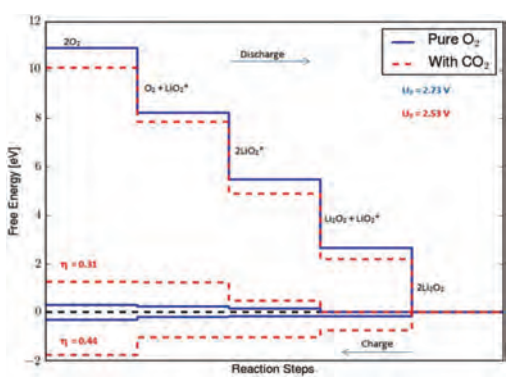

FIG. 2. Calculated free energy diagrams for a four steps discharge mechanism on a stepped (1100)Li_2O_2 surface with and without adsorbed CO_2.

To investigate the effect of gaseous CO_2, the assembled cells were purged with three different atmospheres: 0/100 CO_2/O_2, 1/99 CO_2/O_2, and 50/50 CO_2/O_2. Three individual batteries were assembled and investigated for each atmosphere and each curve presented in Figs. 3 and 4 is therefore an average of three cells with the equal atmosphere as shown in Fig. S3 in the supplementary material.[35] The lowest discharge capacity was observed for the 50% CO_2 cells and is likely caused by the high concentration of electrochemically inactive CO_2. A similar effect was observed, by Gowda *et al.*[17] for a pure CO_2 cell, where the cell potential immediately dropped. It should however be noted that Takechi *et al.*[33] observed, quite to the contrary of our observations, higher discharge capacities up to 70% CO_2 with respect to pure O_2 cells. Interestingly, a higher discharge capacity was observed for the 1% CO_2 cells in respect to the pure O_2 cells as shown in Fig. 3 (inset). A possible explanation is the dissolution of Li_2CO_3 species in DME and/or, as also suggested by Gowda *et al.*, or a change in deposition morphology compared to that deposited in the pure O_2 cells as suggested by Myrdal and Vegge.[20] Such morphological changes could increase the total electrodeposited layer and lead to higher capacities.

All CO_2 cells have higher discharge overvoltages compared to cells with pure O_2 at a discharge rate of 127.3 μA/cm^2, which may be caused by the blocking of the

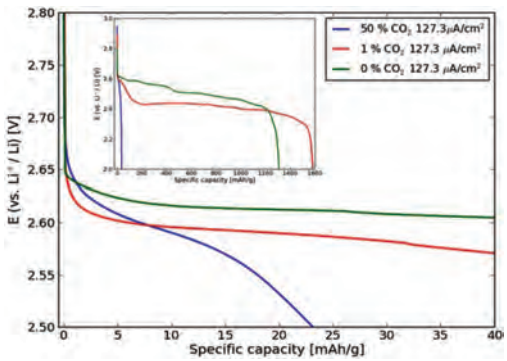

FIG. 3. Galvanostatic discharge profiles at 127.3 μA/cm^2 discharge at three different atmospheres: 50% CO_2, 1% CO_2, and 0% CO_2. Inset shows the increase in discharge capacity in 1% CO_2.

active nucleation sites by solubilized CO_2, forcing the reactions to follow pathways with higher overvoltages. This effect can even be seen at 1% CO_2, as illustrated in Fig. 3 above. The charge capacity, as seen in Fig. 4 and Fig. S4 in the supplementary material,[35] is very dependent on the CO_2 concentration, with high concentrations limiting charge capacity and thereby the cell reversibly. The 50% CO_2 cells reach the lower potential limit (2.0 V) early, at approximately 35 mAh/g, while 1% CO_2 cells and pure O_2 cells continued until capacities in the range 1150–1600 mAh/g were reached depending on current density. The low charge capacity at high CO_2 contaminations should be attributed to the poor Li-CO_2 electrochemistry, also reported by Gowda *et al.* The charging overvoltages are a function of both current density and the level of CO_2 contamination. While there is no significant difference in overvoltages between cells charge at 127.3 and 63.6 μA/cm^2 for 50% CO_2 cells, which again can be attributed to the poor Li-CO_2 electrochemistry. At 127.3 μA/cm^2, there is an increase in overvoltage of about 0.4 and 0.3 V for 1% CO_2 cells and 0% CO_2 cells, respectively. The general increase in overvoltages with increasing current density can be explained

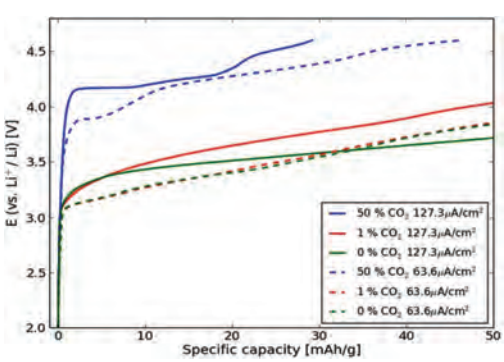

FIG. 4. Galvanostatic charge profiles at 127.3 (solid) and 63.6 (dotted) μA/cm^2 at three different atmospheres: 50% CO_2, 1% CO_2, and 0% CO_2.

by the Butler-Volmer model, while the larger overvoltage for the 1% CO_2 cells than 0% CO_2 cells is expectedly caused by the formation and oxidation of the carbonate like species (Fig. 1(b)). A second charge at 63.6 μA/cm^2 shows identical results for 1% and 0% CO_2. This can be ascribed to the evolution of CO_2 observed during the initial charge cycle, where CO_2 is released at 4.5 V, as shown in Fig. S5 in the supplementary material,[35] resulting in residual CO_2 in the electrolyte causing blocking of the step sites in subsequent charging experiments.

IV. CONCLUSIONS

Influences of CO_2 poisoning at a stepped $(1\bar{1}00)$ Li_2O_2 surface in non-aqueous Li-air battery were studied using DFT calculations and cells were characterized by electrochemical charge-discharge measurements. CO_2 preferentially binds at step valley site at the Li_2O_2 surface and the Li_2O_2 growth mechanism consists of four electrochemical steps, following the same sequence for both pure and contaminated systems. Accordingly, the first step of the growth mechanism is the adsorption of two LiO_2 species and followed by addition of two Li to form 2 Li_2O_2 at the cathode surface. For charge in the low CO_2 limit, a similar reaction will occur, but in reverse order.

Low concentrations of CO_2 (1%) effectively block the surface-active nucleation sites and alter the shape and growth directions of Li_2O_2 on the surface; resulting in an increased capacity of the battery at the expense of an increase in the overvoltage in the presence of CO_2. A similar behavior is seen in pure oxygen following charging to 4.5 V, resulting from decomposition reactions. The effective discharge potential is reduced by 0.20 V on a stepped $(1\bar{1}00)$ Li_2O_2 surface, shifting the reaction to alternate nucleation sites. In general, the DFT calculations and experimental results show that the recharging process is strongly influenced by CO_2 contamination, and exhibits significantly increased charging overvoltage, which is observed already with 1% CO_2 contamination, while at 50% CO_2 a large capacity loss is also seen.

ACKNOWLEDGMENTS

The authors acknowledge support of this work from the ReLiable project (Project No. 11-116792) funded by the Danish Council for Strategic Research Programme Commission on Sustainable Energy and Environment.

[1]D. Linden and T. Reddy, *Hand Book of Batteries*, 3rd ed. (McGraw Hill, New York, 2001).
[2]T. Ogasawara, A. Débart, M. Holzapfel, P. Novák, and P. G. Bruce, J. Am. Chem. Soc. **128**, 1390 (2006).
[3]B. D. McCloskey, A. Speidel, R. Scheffler, D. C. Miller, V. Viswanathan, J. S. Hummelshøj, J. K. Nørskov, and A. C. Luntz, J. Phys. Chem. Lett. **3**, 997 (2012).
[4]G. Girishkumar, B. D. McCloskey, A. C. Luntz, S. Swanson, and W. Wilcke, J. Phys. Chem. Lett. **1**, 2193 (2010).
[5]K. M. Abraham and Z. Jiang, J. Electrochem. Soc. **143**, 1 (1996).
[6]J. S. Hummelshøj, J. Blomqvist, S. Datta, T. Vegge, J. Rossmeisl, K. S. Thygesen, A. C. Luntz, K. W. Jacobsen, and J. K. Nørskov, J. Chem. Phys. **132**, 071101 (2010).
[7]M. D. Radin, J. F. Rodriguez, F. Tian, and D. J. Siegel, J. Am. Chem. Soc. **134**, 1093 (2011).

[8]M. D. Radin, F. Tian, and D. J. Siegel, J. Mat. Sci. **47**, 7564 (2012).
[9]J. S. Hummelshøj, A. C. Luntz, and J. K. Nørskov, J. Chem. Phys. **138**, 034703 (2013).
[10]P. Albertus, G. Girishkumar, B. D. McCloskey, R. S. Sanchez-Carrera, B. Kozinsky, J. Christensen, and A. C. Luntz, J. Electrochem. Soc. **158**(3), A343 (2011).
[11]J. M. Garcia-Lastra, J. S. G. Myrdal, K. S. Thygesen, and T. Vegge, J. Phys. Chem. C **117**, 5568 (2013).
[12]J. M. Garcia-Lastra, J. D. Bass, and K. S. Thygesen, J. Chem. Phys. **135**, 121101 (2011).
[13]V. Viswanathan, K. S. Thygesen, J. S. Hummelshøj, J. K. Nørskov, G. Girishkumar, B. D. McCloskey, and A. C. Luntz, J. Chem. Phys. **135**, 214704 (2011).
[14]J. Chen, J. S. Hummelshøj, K. S. Thygesen, J. S. G. Myrdal, J. K. Nørskov, and T. Vegge, Catal. Today **165**, 2 (2011).
[15]J. B. Varley, V. Viswanathan, J. K. Nørskov, and A. C. Luntz, Energy Environ. Sci. **7**, 720 (2014).
[16]A. C. Luntz, V. Viswanathan, J. Voss, J. B. Varley, J. K. Nørskov, R. Scheffler, and A. Speidel, J. Phys. Chem. Lett. **4**, 3494 (2013).
[17]S. R. Gowda, A. Brunet, G. M. Wallraff, and B. D. McCloskey, J. Phys. Chem. Lett. **4**, 276 (2013).
[18]R. Younesi, M. Hahlin, F. Björefors, P. Johansson, and K. Edström, Chem. Mater. **25**, 77 (2013).
[19]M. J. Siegfried and K. S. Choi, Adv. Mat. **16**, 1743 (2004).
[20]J. S. G. Myrdal and T. Vegge, "DFT study of selective poisoning of Li-Air batteries for increased discharge capacity," RSC Adv. (to be published).
[21]P. Hohenberg and W. Kohn, Phys. Rev. **136**, B864 (1964).
[22]W. Kohn and L. Sham, Phys. Rev. **140**, A1133 (1965).
[23]J. J. Mortensen, L. B. Hansen, and K. W. Jacobsen, Phys. Rev. B **71**, 035109 (2005).
[24]J. Enkovaara, C. Rostgaard, J. J. Mortensen, J. Chen, M. Dulak, L. Ferrighi, J. Gavnholt, C. Glinsvad, V. Haikola, H. A. Hansen, H. H. Kristoffersen, M. Kuisma, A. H. Larsen, L. Lehtovaara, M. Ljungberg, O. Lopez-Acevedo, P. G. Moses, J. Ojanen, T. Olsen, V. Petzold, N. A. Romero, J. Stausholm-Moller, M. Strange, G. A. Tritsaris, M. Vanin, M. Walter, B. Hammer, H. Hakkinen, G. K. H. Madsen, R. M. Nieminen, J. K. Nørskov, M. Puska, T. T. Rantala, J. Schiøtz, K. S. Thygesen, and K. W. Jacobsen, J. Phys. Condens. Matter **22**, 253202 (2010).
[25]S. R. Bahn and K. W. Jacobsen, Comput. Sci. Eng. **4**, 56 (2002).
[26]P. E. Blöchl, Phys. Rev. **50**, 17953 (1994).
[27]P. E. Blöchl, C. J. Först, and J. Schimpl, Bull. Mater. Sci. **26**, 33 (2003).
[28]B. Hammer, L. B. Hansen, and J. K. Nørskov, Phys. Rev. B **59**, 7413 (1999).
[29]H. Jonsson, G. Mills, and K. W. Jacobsen, *Classical and Quantum Dynamics in Condensed Phase Systems*, edited by B. J. Berne, G. Cicotti, and D. F. Coker (World Scientific, 1998).
[30]G. Henkelman and H. Jónsson, J. Chem. Phys. **113**, 9978 (2000).
[31]G. Henkelman, B. Uberuaga, and H. A. Jónsson, J. Chem. Phys. **113**, 9901 (2000).
[32]J. K. Nørskov, J. Rossmeisl, A. Logadottir, L. Lindqvist, J. R. Kitchin, T. Bligaard, and H. Jonsson, J. Phys. Chem. B **108**, 17886 (2004).
[33]K. Takechi, T. Shiga, and T. Asaoka, Chem. Commun. **47**, 3463 (2011).
[34]R. Younesi, P. Norby, and T. Vegge, ECS Electrochem. Lett. **3**, A15 (2014).
[35]See supplementary material at http://dx.doi.org/10.1063/1.4869212 for Figs. S1–S5.

VI

THE JOURNAL OF PHYSICAL CHEMISTRY C

Article

pubs.acs.org/JPCC

Instability of Ionic Liquid-Based Electrolytes in Li−O_2 Batteries

Supti Das,[†] Jonathan Højberg,[†,‡] Kristian Bastholm Knudsen,[†] Reza Younesi,[†,∥] Patrik Johansson,[§] Poul Norby,[†] and Tejs Vegge*[,†]

[†]Department of Energy Conversion and Storage, Technical University of Denmark, Frederiksborgvej 399, DK-4000 Roskilde, Denmark

[‡]Haldor Topsøe A/S, Nymøllevej 55, DK-2800 Kgs. Lyngby, Denmark

[§]Department of Applied Physics, Chalmers University of Technology, SE-412 96 Gothenburg, Sweden

[∥]Department of Chemistry-Ångström Laboratory, Uppsala University, SE-751 21 Uppsala, Sweden

Supporting Information

ABSTRACT: Ionic liquids (ILs) have been proposed as promising solvents for Li−air battery electrolytes. Here, several ILs have been investigated using differential electrochemical mass spectrometry (DEMS) to investigate the electrochemical stability in a Li−O_2 system, by means of quantitative determination of the rechargeability (OER/ORR), and thereby the Coulombic efficiency of discharge and charge. None of the IL-based electrolytes are found to behave as needed for a functional Li−O_2 battery but perform better than commonly used organic solvents. Also the extent of rechargeability/reversibility has been found to be strongly dependent on the choice of IL cation and anion as well as various impurities.

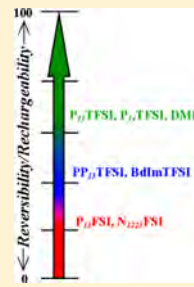

1. INTRODUCTION

The quest for alternative energy storage systems has led significant attention being paid to the Li−air (or Li−O_2) battery concept during the past decade.[1−10] An exceptionally high theoretical specific energy, comparable to gasoline, makes the Li−O_2 battery more appealing than other metal−ion or metal−air battery systems, while the practical energy density still is elusive. There are, however, many challenges identified as essential to bring this technology into practical and commercially viable applications. In the Li−O_2 battery, oxygen is reduced during discharge to form Li_2O_2 at the porous air electrode, while the metallic lithium electrode is oxidized. During charge, the formed Li_2O_2 is now oxidized and lithium is plated back onto the lithium electrode. In order to maintain the reversibility, the electrochemical reaction for an ideal Li−O_2 battery, $2\ Li^+ + 2\ e^- + O_2 \leftrightarrows Li_2O_2$, is needed to be a $2\ e^-$ process.[11] To ensure the rechargeability needed to sustain several hundreds or thousands of charge/discharge cycles of a practical battery, these reactions must be completely reversible with only insignificant losses in any competing/degradation reactions. The development of an electrolyte with sufficient stability toward Li_2O_2 and intermediate reaction products like the superoxide radical has been described as the biggest challenge for the Li−O_2 battery,[6] and so far no stable electrolyte has been identified.[1,12−15] Moreover, a suitable electrolyte for Li−O_2 cells should also have the following properties: compatibility with anode, low volatility to avoid solvent evaporation in open cell system, high oxygen solubility and diffusivity to enable sufficient oxygen transport to the air electrode to support the required currents, low viscosity to ensure fast kinetics of mass transport and a high ionic conductivity, and a suitably wide electrochemical stability window. Although many solvents have been investigated in this regard, none of them fulfill all these requirements.

Several groups have proposed ionic liquids (ILs) as suitable electrolytes due to their relatively high electrochemical and chemical stabilities against O_2^- radicals.[3,4,16−24] Other arguments for ILs are their suggested safety and environmental friendliness due to being nonvolatile.[4,17,24−26] With ILs, the physicochemical properties can be tuned by varying the cation and anion combination. Not all ILs are suitable as Li−O_2 battery electrolytes; for example, ILs with imidazolium-based cations are unstable against peroxide radical attack.[27] On the other hand, pyrrolidinium- and piperidinium-based cations combined with the bis(trifluoromethanesulfonyl)imide (TFSI) anion have been reported to be functional.[28−30] Bresser et al.[31] recently reviewed the utilization of ILs in Li−O_2 batteries and the new "LABOHR" Flow Cell Concept in order to overcome the mass transport limitation, especially for supplying oxygen to the cathode as reported by Monaco et al.[20] They used *N*-butyl-*N*-methyl-pyrrolidinium TFSI doped with LiTFSI (P_{14}TFSI−LiTFSI, 9:1) as an electrolyte in a novel Li−O_2

Received: May 24, 2015
Revised: July 5, 2015
Published: July 16, 2015

DOI: 10.1021/acs.jpcc.5b04950
J. Phys. Chem. C 2015, 119, 18084−18090

flow cell configuration by circulating the oxygen-saturated electrolyte through the cell. Indeed, the very first report on IL-based electrolytes for an Li−air battery was published by Kuboki et al. in 2005.[4] In their study, hydrophobic imidazolium-based ILs were investigated as electrolyte solvents for primary Li−air batteries. Mizuno et al.[29] studied the applicability of *N*-methyl-*N*-propyl-piperidinium TFSI (PP_{13}TFSI) as electrolyte solvent for Li−O_2 batteries, where they found a retention of the reversible capacity of ca. 60% of the initial capacity after 30 cycles. In a more recent study, Elia et al.[17] demonstrated the reversibility of a P_{14}TFSI−LiTFSI electrolyte with an energy efficiency of ca. 82% by using capacity-limited galvanostatic cycling. In another report, the stability of the very same P_{14}TFSI−LiTFSI electrolytes were investigated by Piana et al.[21] in different Li−O_2 cell configurations, showing P_{14}TFSI to be reduced on metallic lithium, but to work well in an especially designed configuration. Furthermore, poor cyclability was concluded to be due to insufficient long-term stability against superoxide (O_2^-) radicals. In all, these partly promising results have further reinforced the research efforts aiming toward developing stable IL-based electrolytes for Li−O_2 batteries.

Here, we investigate the rechargeability of a Li−O_2 cell using IL-based electrolytes based on five different cations and two different anions as shown in Figure 1. The main focus is *N*-methyl-*N*-alkyl-pyrrolidinium (P_{13} and P_{14}) and *N*-methyl-*N*-alkyl-pipiridinium (PP_{13})-based cations in combination with the TFSI anion, as these ILs have shown promising results as stable electrolytes in Li−O_2 batteries.[28−30] Primarily, we analyze the stability and hence reversibility using differential electrochemical mass spectrometry (DEMS) to quantitatively assess the amount of oxygen consumed during discharge and the types and amounts of gas evolved during charge. Complementary measurements to reveal the underlying chemical structural features determining the stability are made using ILs based on the bis(fluorosulfonyl)imide (FSI) anion or cations based on quaternary ammonium or imidazolium.

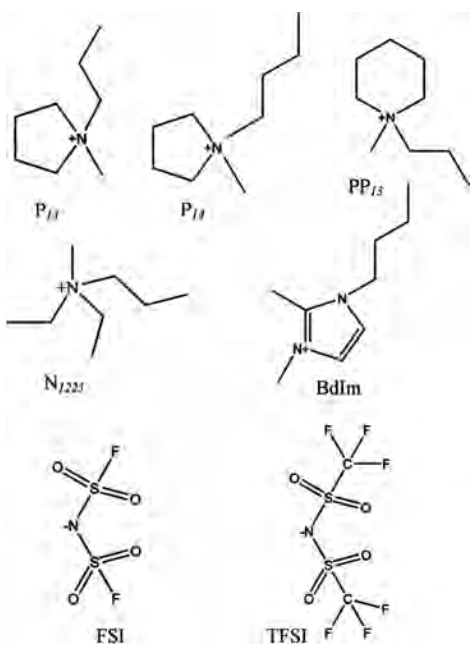

Figure 1. Chemical structures of the cations and anions used in this study.

2. EXPERIMENTAL MATERIALS AND METHODS

The following ILs were used: *N*-methyl-*N*-propylpyrrolidinium TFSI (P_{13}TFSI, 99.9%, Solvionic), P_{13}FSI (99.9%, Solvionic), *N*-methyl-*N*-propylpiperidinium TFSI (PP_{13}TFSI, 99.9%, Solvionic), *N*,*N*-diethyl-*N*-methyl-*N*-propyl-ammonium FSI (N_{1223}FSI, 99.9%, Solvionic), 1-butyl-2,3-dimethyl-imidazolium TFSI (BdImTFSI, 99.9%, Solvionic), and *N*-methyl-*N*-butyl-pyrrolidinium TFSI (P_{14}TFSI, 98.5%, Sigma-Aldrich). The chemical structures of the IL cations and anions are shown in Figure 1. All ILs were used as received. The corresponding lithium salts, LiTFSI (99.9%, Sigma-Aldrich) and LiFSI (99.9%, Suzhou Fluolyte), were preheated at 180 and 80 °C, respectively, prior to preparing ∼0.3 M LiX-IL (X = TFSI, FSI) electrolytes by mixing salt and IL and stirring overnight at room temperature to obtain homogeneous electrolytes. DME (1,2-dimethoxyethane) was purchased from Novolyte and dried using 4 Å molecular sieves (Sigma-Aldrich) for several days. The DME is used to create a DME-1 M LiTFSI organic reference electrolyte (cycled using a current density of 318.5 $\mu A/cm^2$).

Home-made carbon cathodes were manufactured by air-spraying a slurry of XC72 carbon black (Vulcan XC72, Cabotcorp, GA) and PTFE (60 wt % dispersion in water, Sigma-Aldrich) in a wt/wt ratio of 3:1 onto a 316SS stainless steel 150 mesh (Westcoast, Denmark) as previously described in detail in Højberg et al.[13] After air-drying for at least 1 h, the coated SS mesh was cut in 10 mm diameter cathodes. The cathodes were rinsed carefully using acetone and isopropanol and dried in vacuum for at least 30 min at room temperature followed by at least 12 h at 200 °C inside a glovebox. A home-built airtight Swagelok Li−O_2 cell was used for all studies. The cell was assembled with lithium as anode (HongKong Wisdom Tech Company), Whatman glass fiber separators, and an XC72 cathode. Approximately 60 μL of electrolyte was used for each experiment. The cells were all tested at room temperature (25 °C).

The possible presence of crystalline products on the electrodes after the first cycle (for discharge and charge, separately) and their nature were analyzed using a Rigaku Advance X-ray Diffractometer (2θ = 20−80°) working with Cu−Kα radiation (λ = 0.15418 nm). For this purpose, cathode materials were scratched from the electrode after disassembling inside the glovebox and inserted into a 0.7 mm diameter capillary, subsequently sealed with glue. For diffraction mesurement, all cells were discharged to a cutoff voltage of 2.2 V at a current density of 25.5 $\mu A/cm^2$.

DEMS measurements were performed at two different current densities, 25.5 and 63.7 $\mu A/cm^2$, and the gas consumption and gas evolution were quantified using both pressure measurements and mass spectrometry. The applied in-house DEMS setup[32] is similar in design to the setup used by McCloskey et al.[33] In this case, the cells were discharged to a voltage cutoff of 2.2 V and charged to 4.2 V using the same current density.

DOI: 10.1021/acs.jpcc.5b04950
J. Phys. Chem. C 2015, 119, 18084−18090

The saturation concentration and diffusion constant of oxygen, denoted as $[O_2]$ and D_{O_2}, respectively, in the ILs were determined by a chronoamperometric technique adapted from Shoup and Szabo.[34,35] Prior to this, the ILs were saturated with O_2 for 12 h. A 33 μm glassy-carbon (GC) microdisc electrode (Bio-Logic) was polished using 0.05 μm Al_2O_3 (Buehler). The electrochemical determinations were conducted using a minimal amount of the IL (a few drops) in a borosilicate glass vial. The vial was cleaned in boiling HNO_3 (Sigma-Aldrich), heated to 120 °C and brought into a glovebox, where the IL was added. The glass vial was taken out of the glovebox and rapidly put under an O_2 atmosphere with a Pt wire acting as both pseudoreference and counter electrode. The chronoamperometric experiments were performed using a Bio-Logic VMP3 potentiostat with a sample time of 0.01 s, by stepping the potential from OCV to a potential sufficiently low to reduce oxygen for 5 s.

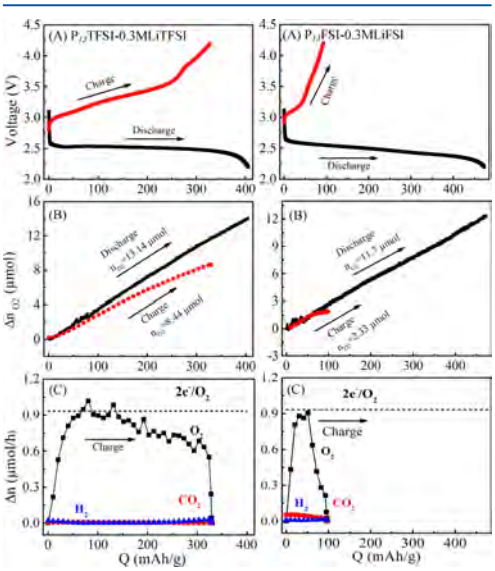

Figure 2. (A) Galvanostatic discharge−charge curves for cells utilizing P13TFSI-0.3MLiTFSI and P_{13}FSI-0.3MLiFSI (both at 63.7 $\mu A/cm^2$ discharge−charge). (B) Oxygen consumption (measured using pressure decay) during discharge and evolution (measured using DEMS) during charge. (c) Gas evolution rates for O_2, CO_2, and H_2.

3. RESULTS AND DISCUSSIONS

In the Figures 2 and 3 and Supporting Information Figures S1 and S2, the results of the DEMS measurements using the different IL-based electrolytes are shown. From these data, the e^-/O_2 ratio during both discharge and charge, the amount of oxygen reduced (ORR) during discharge compared to the oxygen evolved (OER) during charge, and the amount of CO_2 and H_2 evolved during charge are all determined. These key characteristics/parameters are crucial in order to determine if a Li−O_2 system is truly reversible[36] and are summarized in Table 1.

In Figure 2A, we show the first galvanostatic discharge−charge cycle curves (at 63.7 $\mu A/cm^2$) for electrolytes based on P_{13}TFSI and P_{13}FSI in Li−O_2 cells at room temperature. In Figure 2B, we present the total gas (O_2) consumed during discharge (ORR) and gas evolved during charge (OER). The value of the ratio (OER/ORR) should be exactly 1 if the cell is fully rechargeable. The measurement shows that the cells employing the P_{13}TFSI- and P_{13}FSI-based electrolytes are only ∼60% and ∼20% rechargeable, respectively, at potentials below 4.2 V. Finally, in Figure 2C we show DEMS measurements during charge where oxygen (m/z = 32) is identified as the main gaseous charging product in both the electrolytes. For P_{13}TFSI, the initial O_2 evolution rate is close to 2 e^-/O_2, which thus is consistent with Li_2O_2 oxidation. However, as the charging continues, the oxygen evolution rate gradually decreases with a higher e^-/O_2 of 3. The P_{13}FSI-based electrolytes also shows an initial 2 e^-/O_2 ratio, suggesting Li_2O_2 oxidation, but after charging approximately 10% of the full discharge capacity, the oxygen evolution decreases and the potential increases rapidly, resulting in a very small fraction of oxygen evolution during charge. This clearly indicates much better reversibility in P_{13}TFSI (>3×) than P_{13}FSI.

All results for cells with the P_{14}TFSI- and PP_{13}TFSI-based electrolytes are displayed in Figure 3. The oxygen gas evolution rate for the P_{14}TFSI-based electrolyte was close to $2e^-/O_2$ throughout most of the charging process and decreased only slightly at the end of charge (OER/ORR > 60%). For the PP_{13}TFSI-based electrolyte, on the other hand the battery was not able to sustain the current (at 63.7 $\mu A/cm^2$) for long, showing a premature cell death, and only very little oxygen gas evolved. At the lower current density (25.5 $\mu A/cm^2$), a capacity similar to the P_{14}TFSI-based electrolyte as measured at 63.7 $\mu A/cm^2$ was obtained. Although the electron count per oxygen is ∼2.09 during discharge, the charge revealed significant electrochemical degradation corresponding to more than half of measured the current. The poor reversibility in the PP_{13}TFSI-based electrolyte with an OER/ORR ratio of 40% is similar to the results obtained by McCloskey et al.[1]

XRD results of discharged cathodes using pure ILs as well as the corresponding DME-based electrolytes are depicted in Figure 4. Indeed, Li_2O_2 crystalline phases were observed in all the discharged cathodes except when using the electrolytes employing the FSI anion (e.g., P_{13}FSI-LiFSI, N_{1223}FSI-LiFSI; Figure 4, Figure S3). Moreover, LiF was identified in all electrolytes as one of the discharge products, attributed to the chemical decomposition of Li_2O_2 with Li-salt (LiTFSI). LiF has in the literature been found to be a major decomposition product from all fluorine containing salts.[36−38] However, no presence of Li_2CO_3 was observed from the XRD; also we did not detect any CO_2 evolving below 4.2 V in the DEMS measurements.

In Figure 5, we show the e^-/O_2 data obtained through six cycles for the electrolytes based on P_{14}TFSI and P_{13}TFSI. The amount of electrochemical degradation reactions increase during both discharge and charge as the batteries are cycled, which signifies that even though the first cycles might seem promising, the system is not really stable.

Effects of Anion Substitution (Discussion on P_{13}FSI versus P_{13}TFSI). The galvanostatic discharge−charge cycle curves for the electrolytes based on P_{13}TFSI and P_{13}FSI show that the FSI based provides a larger discharge capacity in the

DOI: 10.1021/acs.jpcc.5b04950
J. Phys. Chem. C 2015, 119, 18084−18090

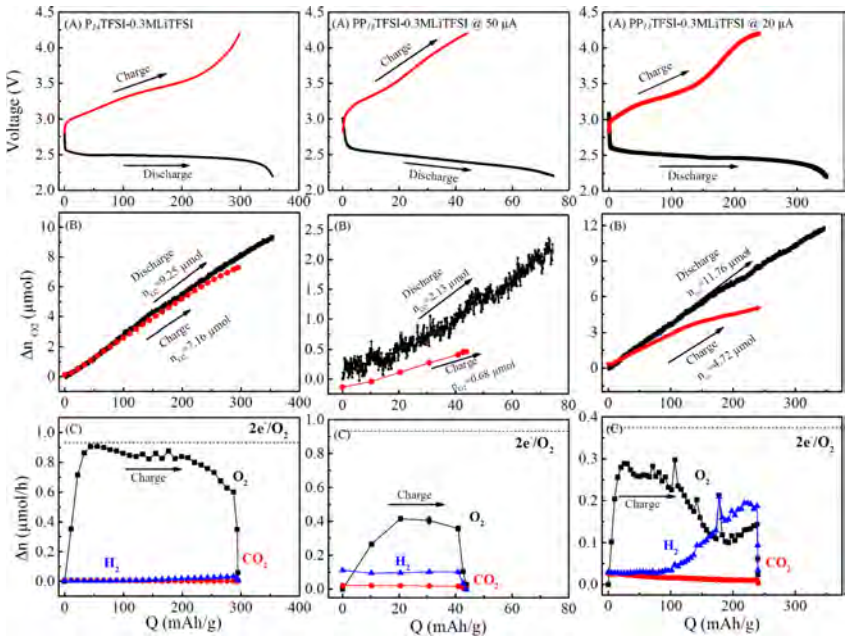

Figure 3. (A) Galvanostatic discharge−charge curves for cells employing P_{14}TFSI-0.3MLiTFSI (63.7 μA/cm^2 discharge−charge) and PP_{13}TFSI-0.3MLiTFSI (63.7 μA/cm^2 and 25.5 μA/cm^2 discharge−charge). (B) Oxygen consumption (measured using pressure decay) during discharge and evolution (measured using DEMS) during charge and (c) gas evolution rates for O_2, CO_2, and H_2.

Table 1. DEMS Result of Different Ionic Liquids and DME-Based Electrolytes

cathode	solvent	salt	OER/ORR	(e^-/O_2)dis	$(e-/O_2)$ch	CO_2/ORR	H_2/ORR[b]
XC72	P_{13}TFSI	LiTFSI	0.62[a] (±0.08)	2 (±0.14)	3.09 (±0.27)	0.005 (±0.001)	0.01
	P_{14}TFSI	LiTFSI	0.63[a] (±0.13)	2.03 (±0.12)	2.75 (±0.4)	0.004 (±0.001)	0.01
	PP_{13}TFSI	LiTFSI	0.40[a] (±0.12)	2.09 (±0.05)	4.02 (±0.08)	0.03	0.18 (±0.09)
	BdImTFSI	LiTFSI	0.45[a] (±0.15)	2.14 (±0.1)	8.26	0.02 (±0.01)	0.008 (±0.006)
	P_{13}FSI	LiFSI	0.19[a] (±0.004)	2.51 (±0.1)	3.4	0.04 (±0.03)	0.01 (±0.01)
	N_{1223}FSI	LiFSI	0.19[a] (±0.06)	2.45 (±0.117)	4.06	0.005 (±0.002)	0.003 (±0.001)
	DME	LiTFSI	0.78 (±0.05) 0.66[a]	1.99 (±0.02)	2.62 (±0.12)	0.08	0.03

[a]Based on charge to 4.2 V. [b]Indicates noncalibrated data. The H_2 intensities were not calibrated and can only be used to compare H_2 evolution between the different electrolytes.

first cycle than all other electrolytes but the rechargeable capacity to be very low. This indicates that the extra capacity is due to a significant electrochemical degradation during discharge. Our preliminary CV results reveal other electrochemical reduction processes along with the reduction of O_2 (cf. Supporting Information, Figure S5). An analysis of Figure 2 clearly shows some parasitical electrochemistry attributable to oxidation/degradation of the electrolyte or to the oxidation electrolyte degradation products.[1,32] The combination of DEMS and XRD measurements suggests that only a negligible fraction of the discharge product in cells employing FSI is Li_2O_2, whereas Li_2O_2 is the primary discharge product when employing TFSI. A caveat is that the O_2 evolution rate for P_{13}FSI−LiFSI, where the charging capacity is very low, is highly dependent on the background correction made (Supporting Information, Figure S4). Moving to the DEMS results these clearly show differences in performance by changing the anion. In the literature, it has been shown[39] that the O_2 solubility of the IL might be enhanced by choosing a suitable anion, although the oxygen mobility may simultaneously decrease. Monaco et al.[39] demonstrated an increase in the O_2 solubility to be coupled to an increased fluorine content in the anion and also increased anion size has been suggested.[40] The larger O_2 solubility in TFSI-based ILs as compared to FSI-based (Table 2) corroborates these observations as TFSI is both larger and contains more fluorine and may be the underlying cause of the better reversibility of P_{13}TFSI-based electrolytes.

Effects of Cation Substitution (Discussion on P_{14}TFSI versus PP_{13}TFSI). In Figure 3, we show that the reversibility differs a lot depending on the choice of cation; all electrolytes based on TFSI provide an e^-/O_2 ratio of approximately 2 during discharge, but during charge the different cations employed result in very different electrochemistry. The PP_{13}TFSI-based electrolyte shows an OER/ORR of 40% at

DOI: 10.1021/acs.jpcc.5b04950
J. Phys. Chem. C 2015, 119, 18084−18090

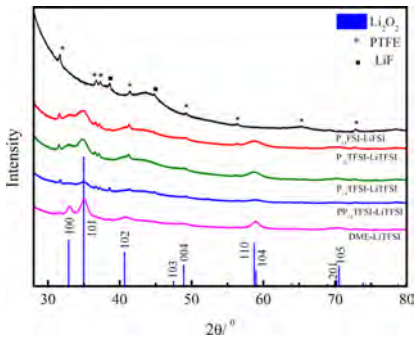

Figure 4. XRD diffractograms of discharged XC72 carbon cathodes using various electrolytes. Symbols * indicates peaks due to the binder (polytetrafluoroethylene, PTFE).

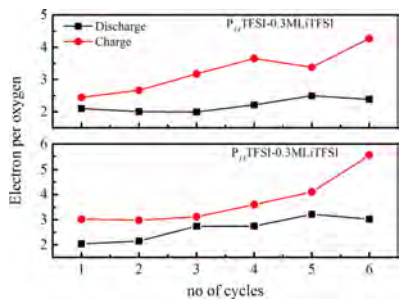

Figure 5. Cycling behavior of cells using the P_{14}TFSI- and P_{13}TFSI-based electrolytes.

Table 2. Concentration $[O_2]$ and Diffusion of Oxygen, D_{O_2}, in the ILs

IL	D_{O_2} [cm²/s]	$[O_2]$ [mM]	η [mPa·s]
P_{13}FSI	2.57×10^{6}	8.17	52.70[a]
P_{13}TFSI	9.17×10^{7}	11.71	71.23[a]
P_{14}TFSI	$(1.8 \pm 0.2) \times 10^{6}$	14	89 (3)
BdImTFSI	1.22×10^{6}	18.81	115.22[a]
N_{1223}FSI	1.22×10^{6}	7.71	NA
DME	4×10^{5}	8.76	0.42 (41,42)

[a]Viscosity data from Solvionic product information.

4.2 V, whereas P_{13}TFSI and P_{14}TFSI are 62−63%, the latter close to DME at 4.2 V (Table 1). The amount of electrochemical degradation is also different from 4.0 $(e^-/O_2)_{ch}$ in the PP_{13}TFSI-based electrolytes to 2.8 $(e^-/O_2)_{ch}$ in the P_{14}TFSI-based electrolytes at a current density of 63.7 μA/cm². The DEMS measurements depict that the oxygen evolution rate behavior during charge at low current density (25.5 μA/cm²) show a ratio higher than 2 e^-/O_2 (~3) in the beginning but also gradually changes to a ~4 electron process in case of piperidinium (PP_{13}TFSI)-based electrolytes. However, using the higher current density (63.7 μA/cm²) the ratio is ~4 throughout the charging process. Therefore, it could be inferred that different chemical/electrochemical reactions are occurring extensively, leading to the instability of electrolyte. From Figure 3, it can be seen that the PP_{13}TFSI-based electrolyte is developing a significant amount of H_2 (~27%**, ** indicates noncalibrated data) during charge−which is a clear indication of water present. The existence of trace amounts of water was also detected in our preliminary results of solubility measurement, but more experiments (like Karl Fischer titration, NMR) are needed to quantify the effect. The presence of water could be an important reason for the observed differences between the cations employed.

Piana et al.[21] assembled a cell with a pure lithium metal anode and Vulcan XC72 as the cathode and found alkene and amines as degradation products of P_{14}TFSI-based electrolytes by OEMS (Online Electrochemical Mass Spectrometry) and ^{1}H NMR. When we here use a similar cell configuration, we find only a ~62% reversibility in the first cycle by DEMS, which clearly indicates parasitic electrochemical reactions taking place during discharge and charge, but we could however not detect any alkenes or amines.

General Discussion. Both DME and other IL-based electrolyte compositions are presented in the Supporting Information (Figures S1 and S2) in order to enable more extensive analysis of and comparisons with the IL-based electrolytes on which we primarily focus. A comparison of the first galvanostatic discharge−charge cycles of the DME−LiTFSI and P_{14}TFSI−LiTFSI electrolytes show the electrochemical stabilities and discharge capacities to be comparable even P_{14}TFSI is better than DME and any difference likely related to the difference in current density. In more detail, the charging voltage increases sharply for the DME-based electrolyte and while more than 15% of the capacity is obtained below 3.15 V for the P_{14}TFSI-based electrolyte, the corresponding amount is 4.3% for the DME-based electrolyte. Both electrolytes show $(e^-/O_2)_{ch}$ ratios close to 2 during both discharge and charge.

Small, but significant parasitical reactions are observed for the P_{13}TFSI-, P_{14}TFSI-, and PP_{13}TFS-based electrolytes where the $(e^-/O_2)_{dis}$ ratios are all fairly close to 2, while for BdImTFSI-, P_{13}FSI-, and N_{1223}FSI-based electrolytes the ratios are much larger (Table 1). As mentioned above, the DME-based electrolyte also display a high degree of reversibility but we find a much larger part of the reaction to occur at lower potentials when using the P_{14}TFSI- and P_{13}TFSI-based electrolytes as compared to the DME based. In general, all electrolytes show much higher $(e^-/O_2)_{ch}$ ($\gg$2.0) ratios, which implies that parasitical electrochemical reactions always occur during the charging process. The evolution of other gases (e.g., CO_2, H_2) during cell operation was very low (below the detection level) for all electrolytes except for the electrolyte based on PP_{13}TFSI. As we have observed substantial amounts of H_2 in the DEMS study of PP-based electrolytes and detected trace amounts of water in both the PP_{13}TFSI and BdImTFSI ILs during the solubility measurements, these impurities might cause the significant differences observed.

Although the two electrolytes based on the ILs P_{13}TFSI and P_{14}TFSI have been observed to be the best in terms of stability, these are still not sufficiently stable for any long-term application (Figure 5). The observed increases in the e^-/O_2 ratios during cycling agrees well with the results of McCloskey et al.[1] for DME-based electrolytes and Piana et al.[21] for P_{14}TFSI-based electrolytes.

4. CONCLUSIONS

By employing detailed DEMS, we have demonstrated that the extent of Li−O_2 battery rechargeability is highly dependent on

DOI: 10.1021/acs.jpcc.5b04950
J. Phys. Chem. C 2015, 119, 18084−18090

the choice of cation and anion for the ILs employed as the solvent. We observed that none of the studied ILs-based electrolytes behaves as needed for a functional Li−O_2 battery, even though P_{14}TFSI performs better than DME. The TFSI anion was found to be more stable than the FSI anion, and the pyrrolidinium and TFSI (P_{13}TFSI, P_{14}TFSI) based ILs have a better rechargeability below 4.2 V (OER/ORR > 60%) than pyrrolidinium and FSI (P_{13}FSI) and piperidinium and TFSI (PP_{13}TFSI) based IL. In contrast, electrolytes based on imidazolium and quaternary ammonium cations are much more unstable in Li−O_2 battery application. Further investigations are required to determine whether the differences observed for the various ILs are inherent to the type of cation or if they are due to the level of various impurities.

■ ASSOCIATED CONTENT

Supporting Information

Additional figures of galvanostatic discharge−charge curves, XRD patterns, and cyclic voltammetry. The Supporting Information is available free of charge on the ACS Publications website at DOI: 10.1021/acs.jpcc.5b04950.

■ AUTHOR INFORMATION

Present Address

(P.J.) LRCS/CNRS UMR7314, Université de Picardie Jules Verne, 33 rue Saint Leu, 80039 Amiens, France.

Notes

The authors declare no competing financial interest.

■ ACKNOWLEDGMENTS

The authors acknowledge support from the ReLiable project (project nr. 11-116792/0603-00462B) funded by the Danish Council for Strategic Research - Programme Commission on Sustainable Energy and Environment under the Danish Innovation Foundation.

■ REFERENCES

(1) McCloskey, B.; Bethune, D.; Shelby, R.; Mori, T.; Scheffler, R.; Speidel, A.; Sherwood, M.; Luntz, A. Limitations in Rechargeability of Li-O_2 Batteries and Possible Origins. *J. Phys. Chem. Lett.* **2012**, *3*, 3043.

(2) Lu, J.; Li, L.; Park, J.-B.; Sun, Y.-K.; Wu, F.; Amine, K. Aprotic and Aqueous Li−O_2 Batteries. *Chem. Rev.* **2014**, *114*, 5611.

(3) Katayama, Y.; Sekiguchi, K.; Yamagata, M.; Miura, T. Electrochemical Behavior of Oxygen/Superoxide Ion Couple in 1-Butyl-1-Methylpyrrolidinium Bis (Trifluoromethylsulfonyl) Imide Room-Temperature Molten Salt. *J. Electrochem. Soc.* **2005**, *152*, E247.

(4) Kuboki, T.; Okuyama, T.; Ohsaki, T.; Takami, N. Lithium-Air Batteries Using Hydrophobic Room Temperature Ionic Liquid Electrolyte. *J. Power Sources* **2005**, *146*, 766.

(5) Ogasawara, T.; Débart, A.; Holzapfel, M.; Novák, P.; Bruce, P. G. Rechargeable Li_2O_2 Electrode for Lithium Batteries. *J. Am. Chem. Soc.* **2006**, *128*, 1390.

(6) McCloskey, B.; Bethune, D.; Shelby, R.; Girishkumar, G.; Luntz, A. Solvents' Critical Role in Nonaqueous Lithium−Oxygen Battery Electrochemistry. *J. Phys. Chem. Lett.* **2011**, *2*, 1161.

(7) Myrdal, J. S. G.; Vegge, T. Selective Poisoning of Li-Air Batteries for Increased Discharge Capacity. *RSC Adv.* **2014**, *4*, 15671.

(8) Garcia-Lastra, J. M.; Myrdal, J. S. G.; Christensen, R.; Thygesen, K. S.; Vegge, T. DFT+U Study of Polaronic Conduction in Li_2O_2 and Li_2CO_3: Implications for Li-Air Batteries. *J. Phys. Chem. C* **2013**, *117*, 5568.

(9) Chen, J.; Hummelshøj, J. S.; Thygesen, K. S.; Myrdal, J. S. G.; Nørskov, J. K.; Vegge, T. The Role of Transition Metal Interfaces on the Electronic Transport in Lithium-Air Batteries. *Catal. Today* **2011**, *165*, 2.

(10) Storm, M. M.; Johnsen, R. E.; Younesi, R.; Norby, P. Capillary Based Li-Air Batteries for in situ Synchrotron X-ray Powder Diffraction Studies. *J. Mater. Chem. A* **2015**, *3*, 3113.

(11) Hummelshøj, J. S.; Blomqvist, J.; Datta, S.; Vegge, T.; Rossmeisl, J.; Thygesen, K. S.; Luntz, A. C.; Jacobsen, K. W.; Nørskov, J. K. Communications: Elementary Oxygen Electrode Reactions in the Aprotic Li-Air Battery. *J. Chem. Phys.* **2010**, *132*, 071101.

(12) Mekonnen, Y. S.; Knudsen, K. B.; Mýrdal, J. S. G.; Younesi, R.; Højberg, J.; Hjelm, J.; Norby, P.; Vegge, T. Communication: The Influence of CO_2 Poisoning on Overvoltages and Discharge Capacity in Non-Aqueous Li-Air Batteries. *J. Chem. Phys.* **2014**, *140*, 121101.

(13) Højberg, J.; McCloskey, B. D.; Hjelm, J.; Vegge, T.; Johansen, K.; Norby, P.; Luntz, A. C. An Electrochemical Impedance Spectroscopy Investigation of the Overpotentials in Li−O_2 Batteries. *ACS Appl. Mater. Interfaces* **2015**, *7*, 4039.

(14) Younesi, R.; Urbonaite, S.; Edström, K.; Hahlin, M. The Cathode Surface Composition of a Cycled Li−O_2 Battery: A Photoelectron Spectroscopy Study. *J. Phys. Chem. C* **2012**, *116*, 20673.

(15) Younesi, R.; Norby, P.; Vegge, T. A New Look at the Stability of Dimethyl Sulfoxide and Acetonitrile in Li-O_2 Batteries. *ECS Electrochem. Lett.* **2014**, *3*, A15.

(16) Balaish, M.; Kraytsberg, A.; Ein-Eli, Y. A Critical Review on Lithium−Air Battery Electrolytes. *Phys. Chem. Chem. Phys.* **2014**, *16*, 2801.

(17) Elia, G. A.; Hassoun, J.; Kwak, W.-J.; Sun, Y.-K.; Scrosati, B.; Mueller, F.; Bresser, D.; Passerini, S.; Oberhumer, P.; Tsiouvaras, N. An Advanced Lithium−Air Battery Exploiting an Ionic Liquid-Based Electrolyte. *Nano Lett.* **2014**, *14*, 6572.

(18) Ara, M.; Meng, T.; Nazri, G.-A.; Salley, S. O.; Ng, K. S. Ternary Imidazolium-Pyrrolidinium-Based Ionic Liquid Electrolytes for Rechargeable Li-O_2 Batteries. *J. Electrochem. Soc.* **2014**, *161*, A1969.

(19) Allen, C. J.; Mukerjee, S.; Plichta, E. J.; Hendrickson, M. A.; Abraham, K. Oxygen Electrode Rechargeability in an Ionic Liquid for the Li−Air Battery. *J. Phys. Chem. Lett.* **2011**, *2*, 2420.

(20) Monaco, S.; Soavi, F.; Mastragostino, M. Role of Oxygen Mass Transport in Rechargeable Li/O_2 Batteries Operating with Ionic Liquids. *J. Phys. Chem. Lett.* **2013**, *4*, 1379.

(21) Piana, M.; Wandt, J.; Meini, S.; Buchberger, I.; Tsiouvaras, N.; Gasteiger, H. A. Stability of a Pyrrolidinium-Based Ionic Liquid in Li-O_2 Cells. *J. Electrochem. Soc.* **2014**, *161*, A1992.

(22) Soavi, F.; Monaco, S.; Mastragostino, M. Catalyst-Free Porous Carbon Cathode and Ionic Liquid for High Efficiency, Rechargeable Li/O_2 Battery. *J. Power Sources* **2013**, *224*, 115.

(23) Allen, C. J.; Hwang, J.; Kautz, R.; Mukerjee, S.; Plichta, E. J.; Hendrickson, M. A.; Abraham, K. Oxygen Reduction Reactions in Ionic Liquids and the Formulation of a General ORR Mechanism for Li−Air Batteries. *J. Phys. Chem. C* **2012**, *116*, 20755.

(24) Lewandowski, A.; Świderska-Mocek, A. Ionic Liquids as Electrolytes for Li-Ion Batteries—An Overview of Electrochemical Studies. *J. Power Sources* **2009**, *194*, 601.

(25) Grande, L.; Paillard, E.; Kim, G.-T.; Monaco, S.; Passerini, S. Ionic Liquid Electrolytes for Li−Air Batteries: Lithium Metal Cycling. *Int. J. Mol. Sci.* **2014**, *15*, 8122.

(26) Kar, M.; Simons, T. J.; Forsyth, M.; MacFarlane, D. R. Ionic Liquid Electrolytes as a Platform for Rechargeable Metal−Air Batteries: A Perspective. *Phys. Chem. Chem. Phys.* **2014**, *16*, 18658.

(27) Hayyan, M.; Mjalli, F. S.; Hashim, M. A.; AlNashef, I. M. An Investigation of the Reaction between 1-Butyl-3-Methylimidazolium Trifluoromethanesulfonate and Superoxide Ion. *J. Mol. Liq.* **2013**, *181*, 44.

(28) Hayyan, M.; Mjalli, F. S.; Hashim, M. A.; AlNashef, I. M.; Al-Zahrani, S. M.; Chooi, K. L. Long Term Stability of Superoxide Ion in Piperidinium, Pyrrolidinium and Phosphonium Cations-Based Ionic Liquids and its Utilization in the Destruction of Chlorobenzenes. *J. Electroanal. Chem.* **2012**, *664*, 26.

(29) Mizuno, F.; Takechi, K.; Higashi, S.; Shiga, T.; Shiotsuki, T.; Takazawa, N.; Sakurabayashi, Y.; Okazaki, S.; Nitta, I.; Kodama, T. Cathode Reaction Mechanism of Non-Aqueous Li−O_2 Batteries with

DOI: 10.1021/acs.jpcc.5b04950
J. Phys. Chem. C 2015, 119, 18084−18090

Highly Oxygen Radical Stable Electrolyte Solvent. *J. Power Sources* **2013**, *228*, 47.
(30) Takechi, K.; Higashi, S.; Mizuno, F.; Nishikoori, H.; Iba, H.; Shiga, T. Stability of Solvents against Superoxide Radical Species for the Electrolyte of Lithium-Air Battery. *ECS Electrochem. Lett.* **2012**, *1*, A27.
(31) Bresser, D.; Paillard, E.; Passerini, S. Ionic Liquid-Based Electrolytes for Li Metal/Air Batteries: A Review of Materials and the New 'LABOHR' Flow Cell Concept. *J. Electrochem. Sci. Technol.* **2014**, *5*, 37.
(32) Højberg, J.; Knudsen, K. B.; Hjelm, J.; Vegge, T. Reactions and SEI Formation during Charging of Li-O_2 Cells. *ECS Electrochem. Lett.* **2015**, *4*, A63.
(33) McCloskey, B. D.; Speidel, A.; Scheffler, R.; Miller, D. C.; Viswanathan, V.; Hummelshøj, J. S.; Nørskov, J. K.; Luntz, A. C. Twin Problems of Interfacial Carbonate Formation in Nonaqueous Li−O_2 Batteries. *J. Phys. Chem. Lett.* **2012**, *3*, 997.
(34) Shoup, D.; Szabo, A. Chronoamperometric Current at Finite Disk Electrodes. *J. Electroanal. Chem. Interfacial Electrochem.* **1982**, *140*, 237.
(35) Xiong, L.; Aldous, L.; Henstridge, M. C.; Compton, R. G. Investigation of the Optimal Transient Times for Chronoamperometric Analysis of Diffusion Coefficients and Concentrations in Non-Aqueous Solvents and Ionic Liquids. *Anal. Methods* **2012**, *4*, 371.
(36) Luntz, A. C.; McCloskey, B. D. Nonaqueous Li−Air Batteries: A Status Report. *Chem. Rev.* **2014**, *114*, 11721.
(37) McCloskey, B. D.; Valery, A.; Luntz, A. C.; Gowda, S. R.; Wallraff, G. M.; Garcia, J. M.; Mori, T.; Krupp, L. E. Combining Accurate O_2 and Li_2O_2 Assays to Separate Discharge and Charge Stability Limitations in Nonaqueous Li-O_2 Batteries. *J. Phys. Chem. Lett.* **2013**, *4*, 2989.
(38) Nasybulin, E.; Xu, W.; Engelhard, M. H.; Nie, Z.; Burton, S. D.; Cosimbescu, L.; Gross, M. E.; Zhang, J.-G. Effects of Electrolyte Salts on the Performance of Li-O_2 Batteries. *J. Phys. Chem. C* **2013**, *117*, 2635.
(39) Monaco, S.; Arangio, A. M.; Soavi, F.; Mastragostino, M.; Paillard, E.; Passerini, S. An Electrochemical Study of Oxygen Reduction in Pyrrolidinium-Based Ionic Liquids for Lithium/Oxygen Batteries. *Electrochim. Acta* **2012**, *83*, 94.
(40) Hu, Y.-F.; Liu, Z.-C.; Xu, C.-M.; Zhang, X.-M. The Molecular Characteristics Dominating the Solubility of Gases in Ionic Liquids. *Chem. Soc. Rev.* **2011**, *40*, 3802.
(41) Saleh, M. A.; Akhtar, S.; Ahmed, M. S. Density, Viscosity and Thermodynamics for Viscous Flow of Water + 1,2-Dimethoxyethane. *Phys. Chem. Liq.* **2008**, *46*, 140.
(42) Hayamizu, K.; Aihara, Y. Ion and Solvent Diffusion and Ion Conduction of PC-DEC and PC-DME Binary Solvent Electrolytes of $LiN(SO_2CF_3)_2$. *Electrochim. Acta* **2004**, *49*, 3397.

DOI: 10.1021/acs.jpcc.5b04950
J. Phys. Chem. C 2015, 119, 18084−18090

Supporting information

Instability of Ionic Liquid Based Electrolytes in Li-O_2 Batteries

Supti Das, [1] *Jonathan Højberg,*[1,2] *Kristian Bastholm Knudsen,*[1] *Reza Younesi,*[1,5] *Patrik Johansson,*[3,4] *Poul Norby*[1] *and Tejs Vegge* *[1]

[1]Department of Energy Conversion and Storage, Technical University of Denmark, Frederiksborgvej 399, DK-4000 Roskilde, Denmark

[2]Haldor Topsøe A/S, Nymøllevej 55, DK-2800 Kgs. Lyngby, Denmark

[3]Department of Applied Physics, Chalmers University of Technology, SE-412 96 Gothenburg, Sweden

[4]Current position: Visiting professor at LRCS/CNRS UMR7314, Université de Picardie Jules Verne, 33 rue Saint Leu, 80039 Amiens, France

[5]Department of Chemistry-Ångström Laboratory, Uppsala University, SE-751 21 Uppsala, Sweden

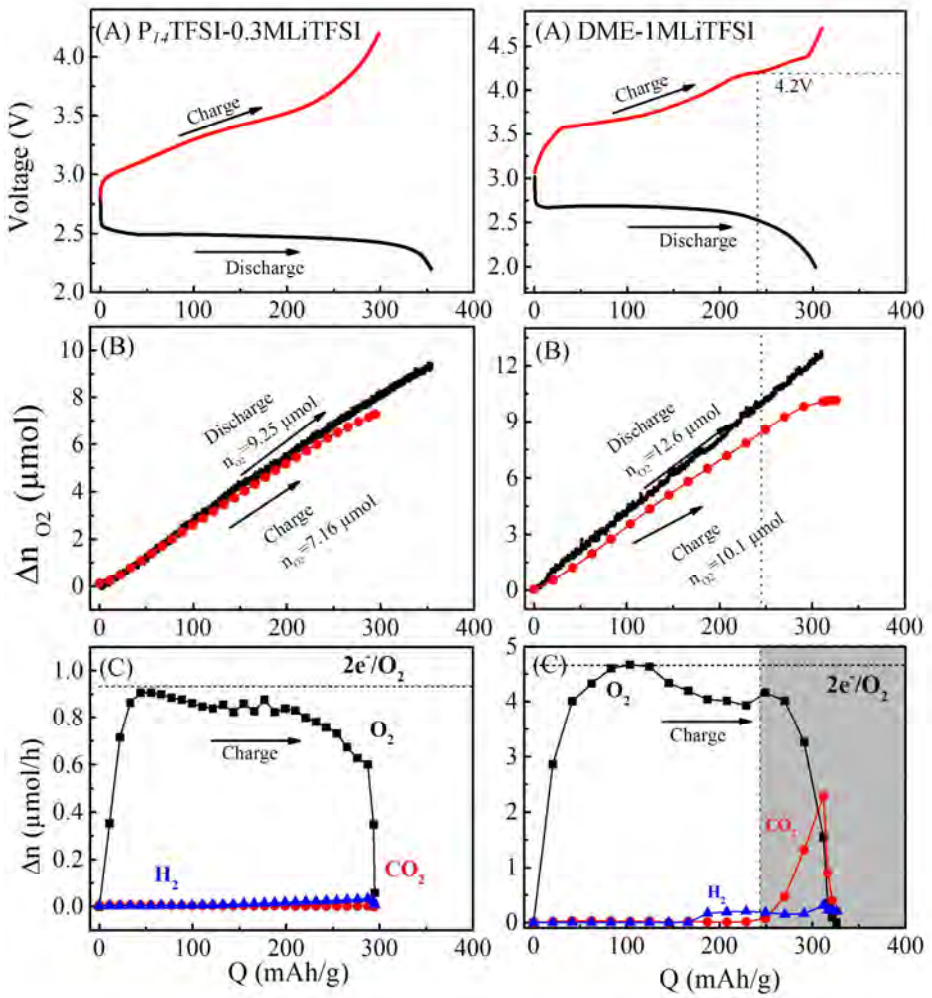

Figure S1: (A) Galvanostatic discharge−charge curves for cells utilizing P_{14}TFSI-0.3M LiTFSI (at 63.7 μA/cm^2 discharge-charge) and DME-1MLiTFSI (at 318.5 μA/cm^2 discharge-charge). (B) Oxygen consumption (measured using pressure decay) during discharge and evolution (measured using DEMS) during charge. (c) Gas evolution rates for O_2, CO_2, and H_2.

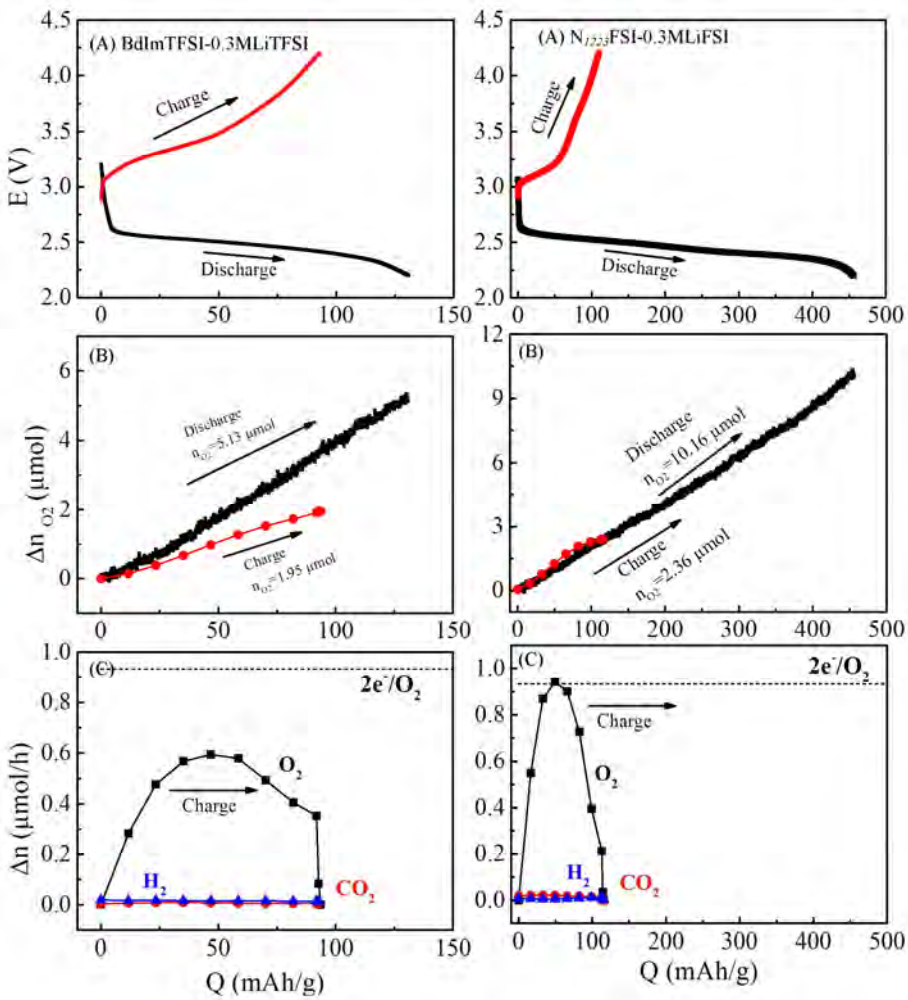

Figure S2: (A) Galvanostatic discharge–charge curves for cells utilizing BdImTFSI-0.3M LiTFSI and N_{1223}FSI-0.3MLiFSI (both at 63.7 µA/cm^2 discharge-charge). (B) Oxygen consumption (measured using pressure decay) during discharge and evolution (measured using DEMS) during charge. (c) Gas evolution rates for O_2, CO_2, and H_2.

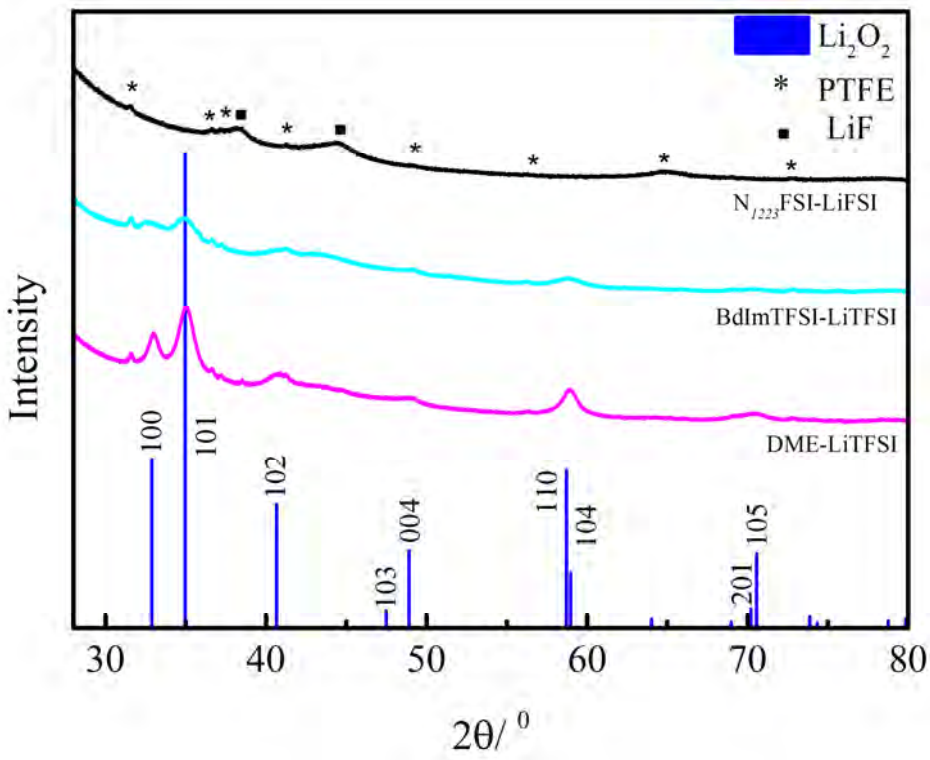

Figure S3: XRD patterns of discharged XC72 carbon cathodes of various electrolytes.

The symbol * indicates peaks for polytetrafluoroethylene (PTFE).

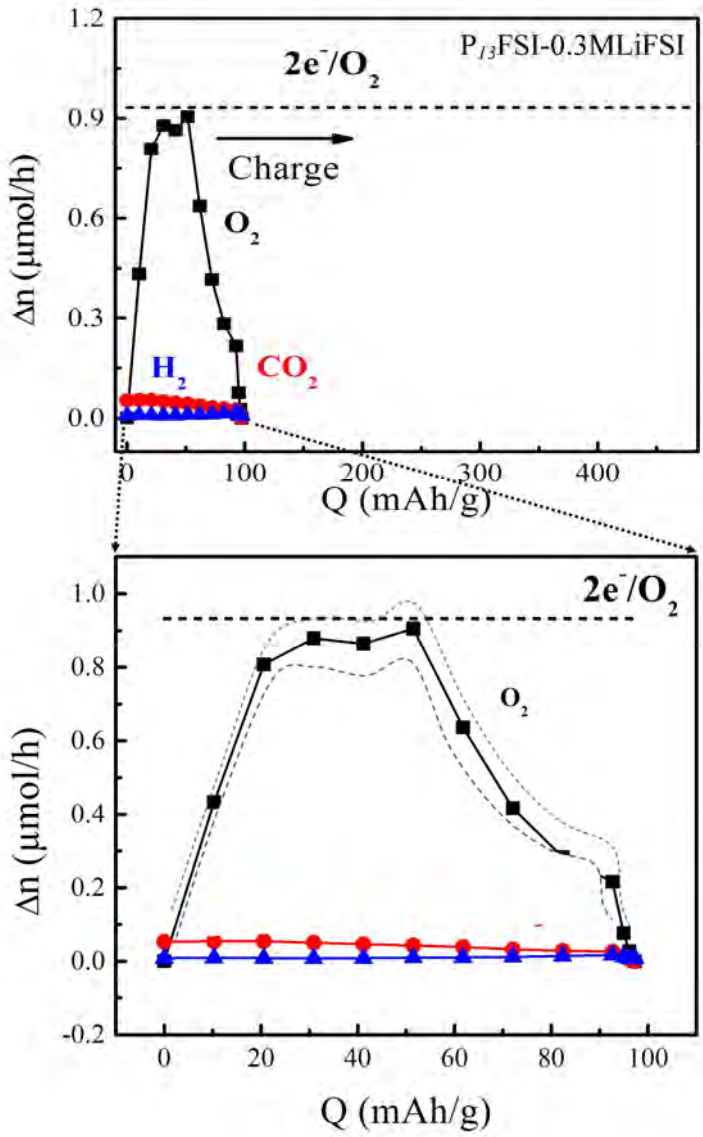

FigureS4: Backgound correction in P_{13}FSI-0.3MLiFSI depending upon choice of baseline.

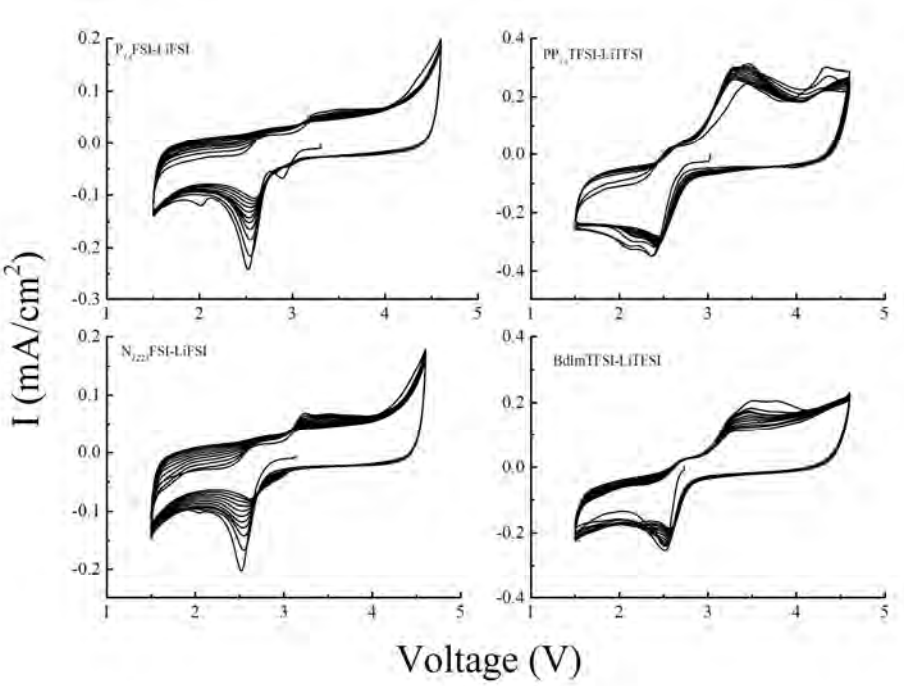

Figure S5: Cyclic voltammetry of Li-O_2 cells utilizing different electrolytes at a scan rate of 0.5 mV/s. The cathodic peak, found at ~2.5 V for all electrolytes corresponds to the reduction of O_2 to LiO_2, whereas further reduction of LiO_2 to Li_2O_2 (at ~2.27 V) was observed only for the TFSI based electrolytes. For the FSI systems the appearance of other small cathodic peaks indicates other parallel reactions (possibly electrochemical degradation). During the anodic scan two peaks corresponding to the oxidation of LiO_2 (~2.67 V) and Li_2O_2 (~3.2-3.3 V) are observed for all electrolytes, although the intensities are very low for the FSI based. Continuous decreases in the intensity of both cathodic and anodic currents for each cycle was easily noticed in FSI based ILs, whereas rather slow for the TFSI based. This could be attributed to the accumulation of insoluble reduction products (Li_2O_x) passivating the electrode surface for the latter. These preliminary results also indicates less reversibility and more degradation for the FSI based electrolytes.